

Experimental Determination and Thermodynamic Modelling of Phase Diagrams for High Temperature Materials



By Sebastian Jonathan Fox
School of Metallurgy and Materials
University of Birmingham

A thesis submitted to
the University of Birmingham
for the degree of:
DOCTOR OF PHILOSOPHY
August 2019

UNIVERSITY OF
BIRMINGHAM

University of Birmingham Research Archive

e-theses repository

This unpublished thesis/dissertation is copyright of the author and/or third parties. The intellectual property rights of the author or third parties in respect of this work are as defined by The Copyright Designs and Patents Act 1988 or as modified by any successor legislation.

Any use made of information contained in this thesis/dissertation must be in accordance with that legislation and must be properly acknowledged. Further distribution or reproduction in any format is prohibited without the permission of the copyright holder.

Abstract

As outlined in Chapter 1: Introduction; Nickel based superalloys with FCC_A1 (γ) matrix/FCC_L1₂ (γ') precipitate microstructures are the primary high temperature materials for gas turbine applications. Since they were first invented in the 1950s, ongoing research has resulted in steady improvements to their physical properties, leading to increases in aero engine power and efficiency. However, these alloys appear to be starting to plateau in terms of improvements in maximum operating temperatures, therefore the impetus to search for the next generation of superalloy is beginning to grow.

This work focuses on studying and modelling the phase equilibria of the Ta-Al-Co, and Ti-Fe-Mo systems in order to investigate their potential as base systems for disordered BCC_A2 (β) matrix, ordered BCC_B2, D0₃, or L2₁ (β') superlattice precipitate strengthened alloys for structural applications. Chapter 2 contains a detailed literature review of the available data on these two ternaries, which was collected and reviewed as the first step towards performing CALPHAD assessments, and producing thermodynamic databases for the two systems.

Prior to this work, the Ta-Al-Co system was poorly understood, however, the limited data available indicated that it contained several ternary intermetallic phases, one of which was thought to potentially be in equilibrium with the BCC A2 Ta phase. Chapter 3 consists of a detailed experimental investigation into the phase equilibria of this system, followed by the production of ternary isothermal sections at temperatures of 1000°C and 1150°C. Unfortunately, the Ta-Al-Co system does not appear to contain a disordered BCC_A2 Ta to ordered BCC intermetallic two phase field, which rules out the possibility that this ternary could be used as a base system for a two phase precipitation strengthened Ta alloy. However,

this system is still an important ternary subsystem of both Ni, and Co based superalloys, so the experimental data and phase diagrams produced by this study could still be useful for the purposes of alloy design in the future.

Significantly more literature data exists for the Ti-Fe-Mo ternary, with recent work establishing phase diagrams for the system that contain a large BCC_A2 + BCC_B2 two phase region.[1]–[3] This allows for the production of high strength β/β' precipitate strengthened Ti-Fe-Mo alloys that could potentially be used for structural applications. It was not necessary to perform further experiments, on this system, as the required data for the assessment was produced by Knowles et al.[1]–[3]

Chapters 4 and 5 detail the process of performing CALPHAD assessments, and producing thermodynamic databases for the two systems utilising the Thermo-Calc software package.[4] Appropriate models and coefficients were selected to describe the Gibbs energy of each phase in the systems based on their crystal structures and physical behaviour. The coefficients of these models were then fitted to the most accurate experimental phase diagram and thermodynamic data available to produce thermodynamic descriptions for the two systems. Phase diagrams calculated from the databases produced were in good agreement with those plotted based on experimental data. It is envisaged that these ternary CALPHAD databases could potentially be adapted and incorporated into existing multicomponent superalloy design databases, in order to improve the accuracy of modelling calculations for alloy design and processing applications.

This work was supported by the Rolls-Royce/EP SRC Strategic Partnership under EP/H022309/1.

Acknowledgements

Firstly, I would like to thank my academic supervisor Dr. Nils Warnken for his advice and support during this project. I would also like to thank my industrial supervisor Mr. Neil Glover from Rolls-Royce plc. who also provided useful advice and discussions.

I am additionally grateful to numerous other people who helped with and or contributed to this work. Thanks go to Dr. H.J. Stone, Dr. N.G. Jones, and Dr. A.J. Knowles who produced the initial framework for the selection of potential of β/β' superlattice precipitate strengthened alloy systems at the University of Cambridge. They also provided useful advice and discussions throughout the project, and helped to facilitate the production of a batch of 9 arc melted Ta-Al-Co alloys at Cambridge. In addition, Dr A.J. Knowles performed the experimental work on the Ti-Fe-Mo ternary that was used for the CALPHAD modelling of this system in the present work. Thanks also go to Dr S. McCain, Dr. S. Li, Dr. N. Atkins and Mr G. Sutton at the University of Birmingham, who assisted with the production of numerous Ta-Al-Co alloys for me via laser, and arc melting. And Dr. Jing Wu who provided advice and helpful discussions on solving SEM sample conductivity problems.

I would also like to thank Dr. Nathalie Dupin of Calcul Thermodynamique, who kindly offered to teach me some CALPHAD modelling skills after my solo struggles hit numerous walls. It is unlikely that I would have been able to complete this work without her generosity and guidance.

In addition, I would like to acknowledge the technical staff at the School of Metallurgy and Materials, specifically Mr. S. Williams for glassblowing and sample encapsulation, Mr. J. Singh for advice on sample preparation, and Mr P. Stanley and Ms. T. Morris for advice and training on the SEMs.

Moreover, I would like to thank my friends and colleagues in The Materials Modelling Group, The Netshape Building, and The School of Metallurgy and Materials for keeping me sane during my PhD.

And finally, I am grateful to the Engineering and Physical Science Research Council and Rolls-Royce plc. for financially supporting this research.

Contents

Abstract

Acknowledgements

Chapter 1: Introduction.....	1
Chapter 2: Literature Review.....	4
2.1: The Aluminium Cobalt (Al-Co) System.....	4
2.2: The Aluminium Tantalum (Al-Ta) System.....	13
2.3: The Cobalt Tantalum (Co-Ta) System.....	25
2.4: The Tantalum Aluminium Cobalt (Ta-Al-Co) System.....	34
2.5: The CALPHAD Method.....	38
2.5.1: Background.....	38
2.5.2: CALPHAD Models.....	41
2.5.3: From Gibbs Energy to Phase Diagrams.....	50
Chapter 3: Experimental Determination of Phase Equilibria in the Ta-Al-Co system.....	53
3.1: Introduction.....	53
3.2: Methods for Experimental Determination of Phase Equilibria in the Ta-Al-Co system.....	58
3.2.1: Introduction.....	58
3.2.2: Ta-Al-Co Alloy Sample Production.....	60
3.2.3: Ta-Al-Co Alloy Heat Treatments.....	62
3.2.4: Ta-Al-Co Alloy Sample Analysis.....	64
3.3: Results.....	67
3.3.1: Introduction.....	67
3.3.2: Bulk Ta-Al-Co Alloy Compositions.....	67
3.3.3: Ta-Al-Co Alloy Microstructures and Initial Phase Identification.....	69
3.3.4: Ta-Al-Co Phase Equilibria and Phase Diagrams.....	97
3.4: Discussion.....	115
3.5: Conclusions.....	130
3.6: Future Work.....	131
Chapter 4: Thermodynamic Assessment of the Ta-Al-Co System.....	133
4.1: Introduction.....	133
4.2: Method.....	134

4.2.1: The CALPHAD Method	134
4.2.2: Thermodynamic Modelling and the Model Set Up File	139
4.3: Results.....	153
4.4: Discussion.....	173
4.5: Conclusions.....	177
4.6: Future work.....	178
Chapter 5: Thermodynamic Assessment of the Ti-Fe-Mo System	180
5.1: Introduction.....	180
5.2: Method.....	184
5.2.1: Introduction to the Method.....	184
5.2.2: Thermodynamic Modelling and the Model Set Up File	187
5.3: Results.....	194
5.4: Discussion.....	206
5.5: Conclusions.....	211
5.6: Future Work.....	212
Chapter 6: Conclusions.....	213
6.1: Conclusions on the Experimental Determination of the Ta-Al-Co System.....	213
6.2: Conclusions on the Thermodynamic Assessment of the Ta-Al-Co System.....	214
6.3: Conclusions on the Thermodynamic Assessment of the Ti-Fe-Mo System.....	215
References.....	216
Appendix 1: SEM EDX Sampling Volume Dimensions and Quantification Procedure.....	224
Appendix 1.1: SEM EDX Point Analysis Sampling Volume Dimensions.....	224
Appendix 1.2: SEM EDX Acquisition and Quantification.....	236
Appendix 2: Thermodynamic Parameters for the Optimised Ta-Al-Co Description Produced in ‘this Work’ (TW).....	242
Appendix 3: Thermodynamic Parameters for the Optimised Ti-Fe-Mo Description Produced in ‘this Work’ (TW).....	252
Appendix 4: .tdb Thermo-Calc database for the optimised Ta-Al-Co description produced in this work	258
Appendix 5: .tdb Thermo-Calc database for the optimised Ti-Fe-Mo description produced in this work	282

Chapter 1: Introduction

Nickel based superalloys with FCC_A1 (γ) /FCC_L1₂ (γ') microstructures are the primary high temperature materials for gas turbine applications, and have been since they were first developed in the early 1950s. Over the last 60 years their properties have been steadily improved, resulting in increases in aero engine power and efficiency. However, these alloys appear to be starting to plateau in terms of improvements in maximum operating temperatures, therefore the impetus to search for the next generation of superalloy is beginning to grow.

Phase diagrams are maps of the equilibrium state of a material as a function of temperature, composition, and pressure. They are used as a guide to the relationship between a materials chemical composition, processing conditions, microstructure, and physical properties.[5], making them an important tool for new alloy design. The experimental determination of phase diagrams for multi-component alloys has always been a costly, time consuming and labour intensive process. However due to recent advances in computational methods, accurate phase diagrams can now be produced more rapidly, and at lower costs.

The primary aims of this project are to study and model the phase equilibria of the Ta-Al-Co, and Ti-Fe-Mo systems in order to investigate their potential as base systems for disordered BCC_A2 (β) matrix, ordered BCC_B2, D0₃, or L2₁ (β') superlattice precipitate strengthened alloys for aerospace applications. At present, the Ta-Al-Co system is poorly understood, however, the limited data available indicates that it contains several ternary intermetallic phases, one of which could potentially be in equilibrium with the BCC_A2 (β) Ta phase, which raises the possibility that there could be β/β' two phase field present in the Ta corner of the diagram.

Significantly more literature data exists for the Ti-Fe-Mo ternary, with recent work establishing phase diagrams for the system that contain a large BCC_A2 (β) + BCC_B2 (β') two phase region.[1]–[3] This allows for the production of high strength β/β' precipitate strengthened Ti-Fe-Mo alloys that could potentially be used for structural applications.

The equilibrated alloy method has been chosen as the method of choice for experimental determination of the phase equilibria of the two systems. This method consists of producing a number of different alloys with compositions at specific points of interest on the phase diagram. These alloys are then annealed for times and temperatures chosen for the purposes of enabling the alloys to get as close as practically possible to their equilibrium state. This is followed by rapidly quenching them back to room temperature to ‘lock in’ the equilibrium state. The alloys can then be analysed by techniques such as scanning electron microscopy (SEM), energy dispersive X-ray spectroscopy (EDX) and X-ray diffraction (XRD) in order to identify the phases present, and their compositional boundaries at the specified equilibrium temperatures.

Modelling work will be carried out using the 'Calculation of Phase Diagrams' (CALPHAD) method, complemented by experimental investigations on selected equilibrated alloys. The basic principles of this approach are to select appropriate models and coefficients to describe the Gibbs energy of each phase in the system of interest based on their crystal structures and physical behaviour. The coefficients of these models are then fitted to the most accurate experimental phase diagram and thermodynamic data available to produce a thermodynamic description of the system that accurately represents its real life behaviour. If realistic descriptions are created for the necessary unary, binary and ternary systems, based on accurate experimental data, these descriptions can then be combined to produce a credible extrapolated description of a multicomponent system, without the need for any new

multicomponent experimental data. This multicomponent description can then be used for practical applications, such calculating phase diagrams for use in alloy design, or providing input data for materials production and processing simulations. It is envisaged that by creating accurate thermodynamic databases for these alloy systems this work may contribute towards the development of potential new materials for gas turbine and other aerospace applications.

Chapter 2: Literature Review

2.1: The Aluminium Cobalt (Al-Co) System

One of the earliest recorded experimental investigations of the Al-Co system was carried out by Guillet, who published a liquidus for the system over a century ago in 1902 [6][7]. Since then numerous other studies of this system have been performed. The first full Al-Co phase diagram was produced by Gwyer in 1908 [8], from time versus temperature cooling curve studies and metallographic analysis of around thirty different alloys spanning the composition range of the system. Gwyer's phase diagram, displayed in Figure 2.1, shows three different intermetallic phases; $\text{Al}_{13}\text{Co}_3$, Al_5Co_2 and AlCo , with melting temperatures of 943°C , 1175°C , and 1630°C respectively.

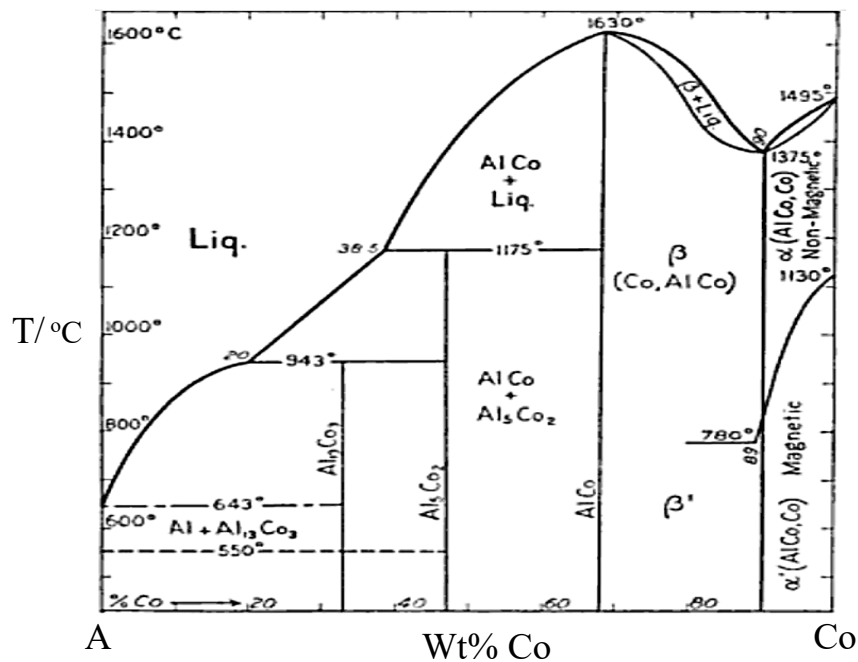


Figure 2.1: Gwyer's Al-Co phase diagram [8]

After Guillet [6][7] and Gwyer,[8] a number of other researchers also used thermal analysis techniques to perform more detailed investigations of the Al-Co system over specific composition ranges. Starting from the aluminium end of the phase diagram: Fink and Freche, 1932 [9], studied samples between 0.01 and 15.68 weight % (wt%) cobalt during cooling, with a significant focus on samples between 0.01 and 3.64% cobalt; Gödecke, 1971 [10], investigated alloys with compositions between 10 and 40 atomic % (at%) cobalt during heating; Köster, 1933 [11], analysed samples from 51.6 to 89.7at% cobalt during cooling; and Schramm, 1941 [12], examined alloys from 78 to 86at% cobalt during heating and cooling. In addition, all four researchers performed metallographic examinations via optical microscopy and Schramm also carried out X-ray diffraction (XRD) studies.

A 1989 review by McAlister[13] evaluated and consolidated these and other studies to produce an updated phase diagram for the Al-Co system. This diagram is shown in Figure 2.2, and is the version currently accepted by the ASM handbook [14]. The liquidus from 0 to 25at% cobalt is based on the data of Fink and Freche [9], and Gödecke [10], and from 71 to 86at% cobalt it is based on the results of Schramm [12]. This data was reasoned to be more reliable than that of Gwyer [8] and Köster [11], [15] based on probable sample purity and perceived experimental care [13]. The liquidus from 25 to 71 and 86-100 at% cobalt is based on the more questionable data of Gwyer and Köster, which generally lies slightly below that of the other studies, and is therefore tentatively drawn with dotted lines.

For the terminal solubility values, the solubility of cobalt in FCC α -aluminium at 655°C was concluded to be between 0.00045 and 0.00090 at% by Fink and Freche [9], and the maximum solubility of aluminium in FCC α -cobalt was determined to be around 16at%, at approximately 1400°C by Schramm [12]. The FCC α -cobalt solvus has been studied using a range of techniques, including metallography [12], electron probe microanalysis (EPMA)

[16], [17], electromotive force (EMF) measurements [18], and XRD [17]. This data is fairly consistent and was used to map the FCC α -cobalt solvus.

At the time of McAlister's review, five different intermetallic phases had been found to exist in the Al-Co system: Al_9Co_2 , $\text{Al}_{13}\text{Co}_4$, Al_3Co , Al_5Co_2 , and AlCo [13]. The melting points and crystal structures of the aluminium rich, peritectically formed phases: Al_9Co_2 [9], [10],[19],[20], $\text{Al}_{13}\text{Co}_4$ [10], [21], [22] and Al_5Co_2 [10], [21], [23], [24] are all fairly well established, but the structure of Al_3Co has not yet been identified. The composition range of Al_5Co_2 is thought to be on the order of the order of 0.5 at%, with the other three peritectic phases having a negligible composition range [10]. The existence and structure of the AlCo phase has been confirmed by a number of independent studies [8], [16], [21], [25]. However, at the time McAlister considered the available data on its melting behaviour to be unreliable [13]. Further support for this assertion is provided Panteleimonov et al, 1974 [26], whose work was not included in McAlister's review. Their experimental investigation produced a complete phase diagram that gave a higher melting temperature of 1645°C for the AlCo phase, compared to the values of 1630°C from Gwer [8] and 1628°C and 1620°C from Köster [11], [15] that were considered by McAlister. With regards to the available data on the composition range of this phase, only one point on the aluminium rich single phase boundary has been reported at 46.4 at% cobalt and 1000°C [27], whereas the cobalt rich boundary had been extensively studied using metallography [12], EPMA [16], [17], EMF measurements [28], and XRD [12], [25]. The crystal structure data collected by McAlister for all phases is listed in Table 2.1, and their composition ranges and transformation temperatures can be seen in Figure 2.2.

Table 2.1: Crystal structure data for the phases in the Al-Co system [13]

Phase	Composition, at% Co	Pearson symbol	Space Group	Struktur- bericht designation	Prototype	Ref
α -Al	0	cF4	$Fm\bar{3}m$	A1	Cu	[29]
Al ₉ Co ₂	18.1	mP22	P2 ₁ /a	[20]
Al ₁₃ Co ₄	23.5	mC93	Cm	[22]
Al ₃ Co	25.6	[10], [22]
Al ₅ Co ₂	28.6	hP28	P6 ₃ /mmc	D8 ₁₁	Co ₂ Al ₅	[23], [24]
AlCo	≈48 to 75.5	cP2	$Pm\bar{3}m$	B2	CsCl	[16]
α -Co	84 to 100	cF4	$Fm\bar{3}m$	A1	Cu	[29]
ε -Co	100	hP2	P6 ₃ /mmc	A3	Mg	[29]

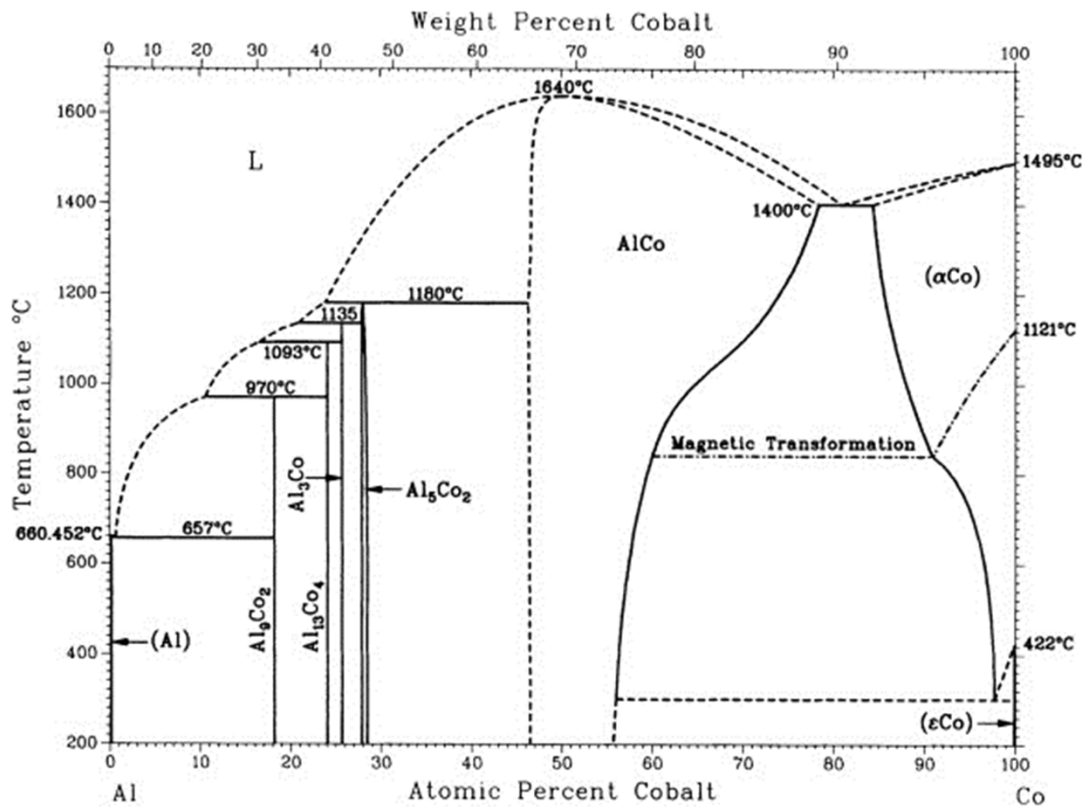


Figure 2.2: McAlister's reviewed Al-Co phase diagram [13]

The first thermodynamic assessment of the Al-Co system was carried out by Dupin and Ansara in 1998 [30]. This study reviewed all of the information considered by McAlister [13], combined with data from a number of more recent investigations, including those of Kimura et al, 1994 [31], Gödecke and Ellner, 1996 [32], and Grusco, 1996 [33]. Kimura, et al [31], used differential thermal analysis (DTA) and energy dispersive X-ray spectroscopy (EDS) to study the eutectic reaction that occurs between the AlCo and FCC α -cobalt phases, and provided new information about the phase field boundaries in this region. This data was included in the models of Dupin and Ansara [30], along with Gödecke and Ellner's [32] results on the liquidus and melting temperatures of all four well established aluminium peritectic phases: Al₉Co₂, Al₁₃Co₄, Al₃Co, Al₅Co₂. Gödecke and Ellner [32], and Grushco [33] also

reported the existence of three new intermetallic phases with compositions close to $\text{Al}_{13}\text{Co}_4$. However, the data on the composition and temperature ranges of these phases is quite contentious; therefore, Dupin and Ansara[30] rejected this information and simply modelled a single $\text{Al}_{13}\text{Co}_4$ phase in this region.

A second thermodynamic assessment of this system was recently performed by Stein et al in 2013 [34], to update the first according to the results of their latest experimental work. Using DTA in an argon atmosphere, they measured the liquidus temperatures of samples ranging from 30 to 60 at% cobalt, and found the maximum congruent melting temperature of the BCC_B2_AlCo phase to be $1673 \pm 3^\circ\text{C}$. This value is significantly higher than those previously measured; however they are confident about the accuracy of this measurement due to their sample purity and more advanced experimental instrumentation.

All of the previously discussed data was considered by Stein et al [34], and those results judged to be most accurate were incorporated into their models. The experimentally measured invariant reaction points, and the sublattice models used in this assessment are given in Tables 2.2, and 2.3 respectively, and the Al-Co phase diagram calculated from their optimised thermodynamic description is shown in Figure 2.3. Although partially reliant on the judgement of the authors, this assessment likely represents the best description of the Al-Co system currently available.

Table 2.2: The experimentally measured invariant points used by Stein et al [34], The values for x_i are in mole fraction Co and correspond to the order that the phases appear in the invariant reactions.

Invariant reaction	Reaction type	T_{exp} (°C)	T_{exp} (K)	X_1	X_2	X_3
$L \leftrightarrow \text{AlCo}$	Congruent	1673	1946	0.5	0.5	N/A
$L \leftrightarrow \alpha\text{-Co}^{\text{para}}$	Melting	1495	1768	1	1	N/A
$L \leftrightarrow \text{AlCo} + \alpha\text{-Co}^{\text{para}}$	Eutectic	1400	1673	0.81	0.785	0.844
$L + \text{AlCo} \leftrightarrow \text{Al}_5\text{Co}_2$	Peritectic	1180	1453	0.238	0.463	0.28
$L + \text{Al}_5\text{Co}_2 \leftrightarrow \text{Al}_3\text{Co}$	Peritectic	1153	1426	0.208	0.278	0.256
$\alpha\text{-Co}^{\text{para}} \leftrightarrow \alpha\text{-Co}^{\text{ferro}}$	Magnetic	1127	1400	1	1	N/A
$L + \text{Al}_3\text{Co} \leftrightarrow \text{Al}_{13}\text{Co}_4$	Peritectic	1093	1366	0.165	0.256	0.24
$L + \text{Al}_{13}\text{Co}_4 \leftrightarrow \text{Al}_9\text{Co}_2$	Peritectic	970	1243	0.105	0.24	0.181
$\alpha\text{-Co}^{\text{para}} \leftrightarrow \alpha\text{-Co}^{\text{ferro}} + \text{AlCo}$	Magnetic	865	1138	0.94	0.915	0.59
$L \leftrightarrow \alpha\text{-Al}$	Melting	660.452	933.452	0	0	N/A
$L \leftrightarrow \alpha\text{-Al} + \text{Al}_9\text{Co}_2$	Peritectic	657	930	0.05	0.181	0
$\alpha\text{-Co}^{\text{ferro}} \leftrightarrow \varepsilon\text{-Co}$	Allotropic	422	695	1	1	N/A
$\alpha\text{-Co}^{\text{ferro}} \leftrightarrow \text{AlCo} + \varepsilon\text{-Co}$	Eutectoid	300	573	0.98	0.56	1

Table 2.3: The sublattice models and crystal structure data used by Stein et al [34]

Phase	Sublattice Model	Comp at% Co	Pearson symbol	Space group	Strukturbericht	Proto-type	Ref
α -Al	(Al,Co)	0	cF4	$Fm\bar{3}m$	A1	Cu	[29]
Al ₉ Co ₂	(Al)9(Co)2	18.1	mP22	P2 ₁ /a	[20]
Al ₁₃ Co ₄	(Al)13(Co)4	23.5	mC93	Cm	[22]
Al ₃ Co	(Al)3(Co)	25.6	[10], [22]
Al ₅ Co ₂	(Al)5(Co)2	28.6	hP28	P6 ₃ /mmc	D8 ₁₁	Co ₂ Al ₅	[23], [24]
AlCo	(Al,Co,Va)0.5 (Al,Co,Va)0.5	≈ 48 to 75.5	cP2	$Pm\bar{3}m$	B2	CsCl	[16]
α -Co	(Co,Al)	84 to	cF4	$Fm\bar{3}m$	A1	Cu	[29]
ϵ -Co	(Co,Al)	100	hP2	P6 ₃ /mmc	A3	Mg	[29]

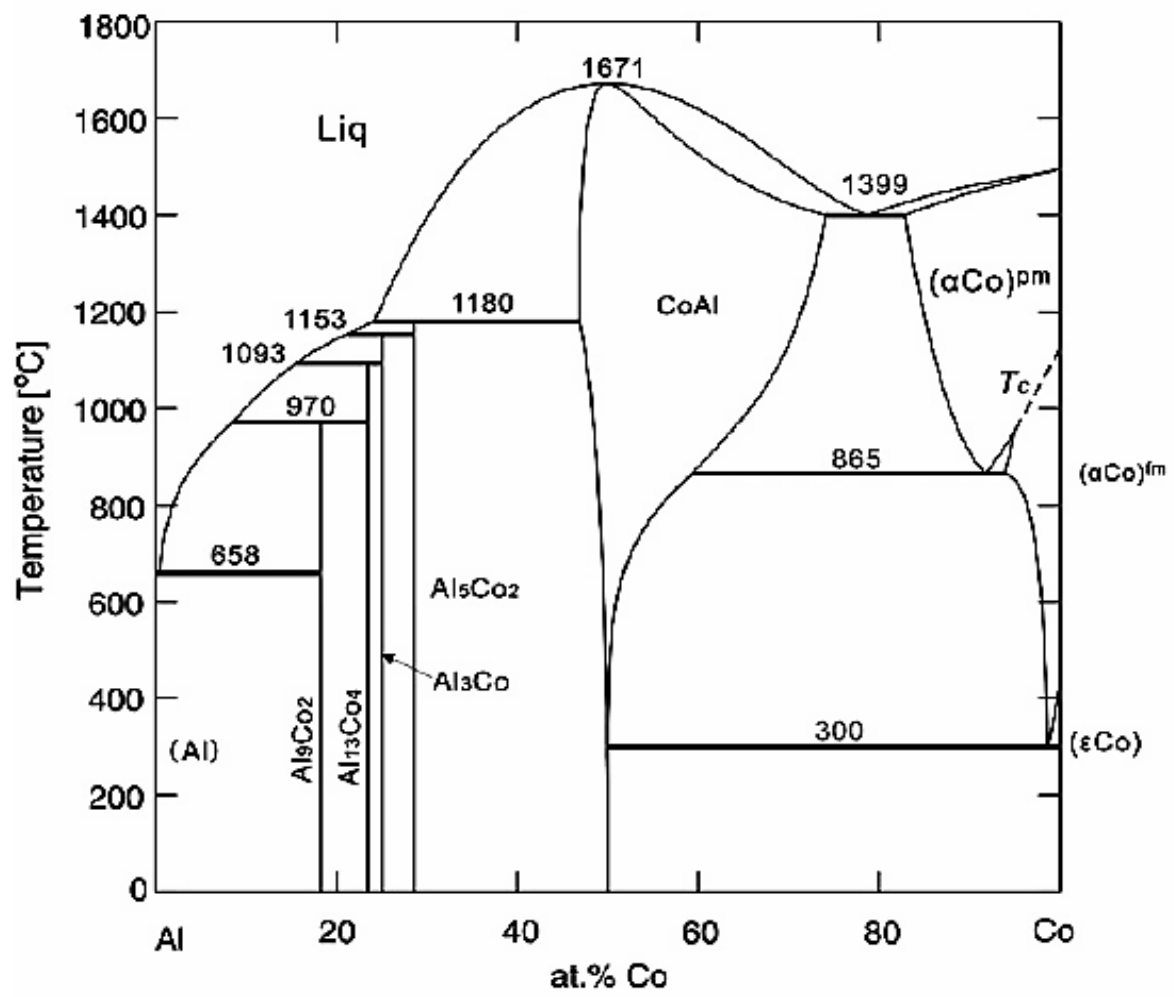


Figure 2.3: Stein et al's calculated Al-Co phase diagram [34]

2.2: The Aluminium Tantalum (Al-Ta) System

Research into the Al-Ta system only started relatively recently, with the 1956 and 1959 works of Glazov et al [35], [36] being among the first to investigate the phase equilibria in this system. Glazov et al [35], [36] performed XRD and microhardness tests, and found that the solubility of tantalum in aluminium ranges from 0.010at% at 25°C to 0.033at% at 640°C. They also used DTA to determine the temperature of the invariant reaction: $L + \epsilon\text{-Al}_3\text{Ta} \leftrightarrow \alpha\text{-Al}$ to be 668°C. Yeremenko, 1976 [37], later added further information on the liquidus at the aluminium end of the phase diagram reporting solubility values of tantalum in aluminium between 0.016 at% at 700°C to 0.055at% at 900°C.

The first full Al-Ta phase diagram was produced by Kimura et al, in 1973 [38], who studied 16 as cast alloys spanning the composition range of the system using metallography, XRD and optical pyrometry. Kimura et al's phase diagram displayed in Figure 2.4 provides a tentative liquidus for the system, shows the terminal solubilities of the constituent elements, and gives the positions of two intermetallic phases, $\epsilon\text{-Al}_3\text{Ta}$ and $\sigma\text{-AlTa}_2$. However, it is also clear from the figure, that the melting point data of Kimura et al exhibits fairly significant scatter, which is most probably due to their use of as cast samples.

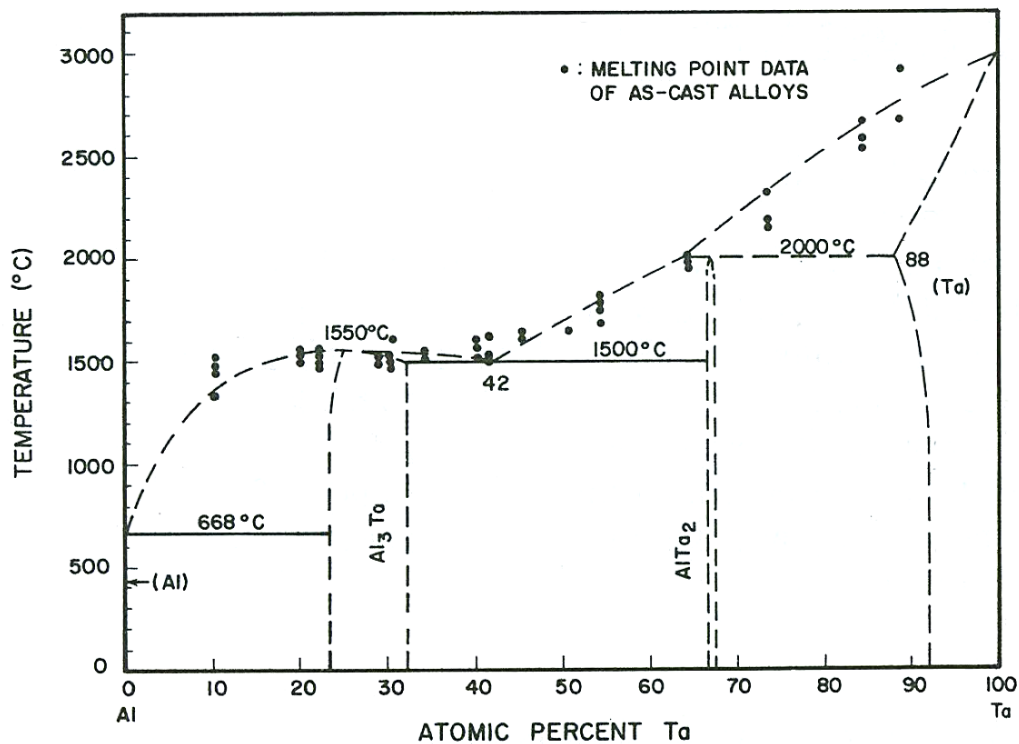


Figure 2.4: Kimura et al's Al-Ta phase diagram [38]

Later investigations by Schuster in 1985 [39], and Subramanian et al in 1990 [40], utilised arc melting in argon to produce homogenous samples, which were then annealed at temperatures just below the values of the appropriate phase transitions for between 100 and 1000 hours in an effort to achieve equilibrium. Schuster's work [39] focussed on alloys with compositions between 25 and 65at% tantalum, and provided new information about the liquidus and two of the intermetallic phases in that region. Firstly, he identified that the ϵ -Al₃Ta phase actually occurs at 25at% Ta, melts at 1627°C, and has a negligible homogeneity range; and secondly he discovered that another intermetallic phase, Al₃Ta₂ also exhibiting negligible homogeneity exists at around 38at% tantalum. In addition, this new phase; Al₃Ta₂ was found to exhibit a polymorphic phase transformation at 1225°C before finally melting at 1575°C.

Using Schuster's findings to inform their choice of annealing times and temperatures, Subramanian et al [40] then studied heat treated samples with compositions between 21.5 and 60at% tantalum via EPMA, XRD, and DTA. They then combined their results with the available literature data to produce an updated phase diagram for the system. Subramanian et al's [40] phase diagram, shown in Figure 2.5, is the version currently accepted by the ASM handbook [14]. This diagram shows a different liquidus than previous versions, with a cascade of peritectic reactions occupying the central region instead of the eutectic type reaction predicted by Kimura [38] and Schuster [39]. It also shows four intermediate phases; the negligible homogeneity range peritectics, ϵ -Al₃Ta, Al₂Ta, and AlTa and the σ -phase, AlTa₂, which extends from 56 to 80at% tantalum.

Kimura's [38], Schuster's [39], and Subramanian et al's [40] results clearly differ in terms of the intermetallic phases that they have identified to exist across the central region of the phase diagram. In fact, at the time of Subramanian et al's work there were a number of conflicting reports with regards to the stoichiometries, crystal structures, and melting behaviour of the intermediate phases that had been reported to exist in the composition range between 20 and 80at% tantalum. Subramanian et al [40] reviewed the available information, and attempted to clarify the situation with their experimental work. The comparison of their results with previous literature data given in Table 2.4 shows good agreement in terms of the existence and proposed structures of the ϵ -Al₃Ta phase at 25at% Ta, and the σ -AlTa₂ phase in the region of 60-80at% Ta. However, it does not provide definitive answers with regards to the phases that have been reported in the region of 25 to 60at% Ta.

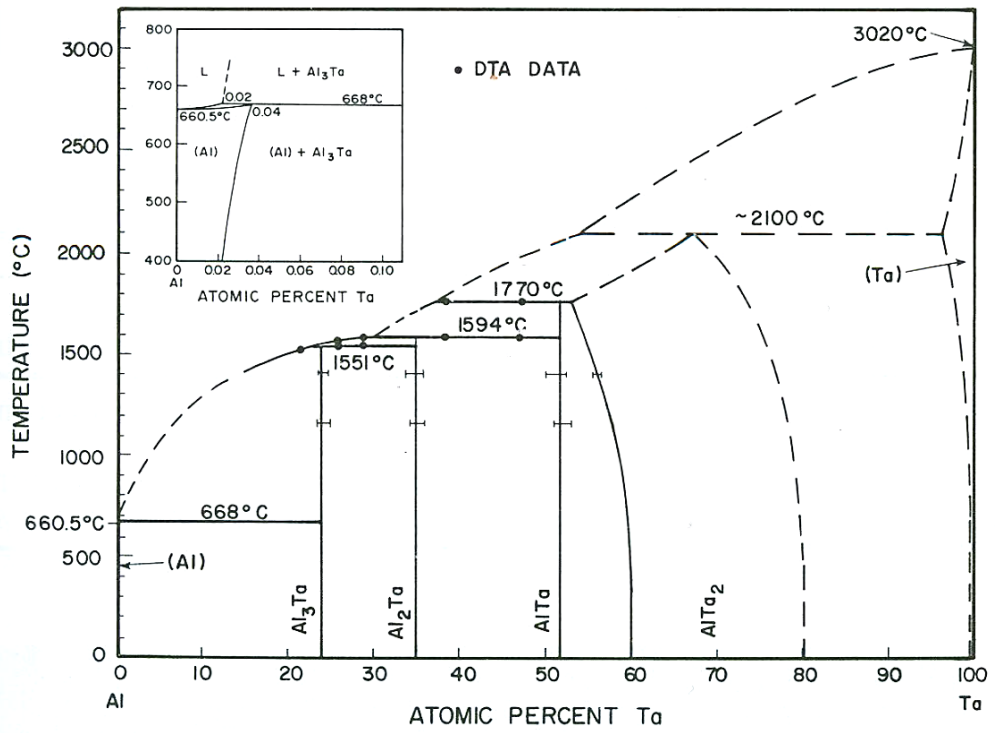


Figure 2.5: Subramanian et al's Al-Ta phase diagram [40]

Table 2.4: Subramanian et al's results (highlighted in bold) and reviewed data on the intermetallic phases reported in the Al-Ta system between 20 and 80at% Ta [40]

Phase	Crystal structure	Comp. at% Ta	Melting reaction	Melting/ Decomp. Temp. (°C)	Ref
ϵ-Al₃Ta	Al ₃ Ti (tetragonal)	≈25±X	Peritectic	1500	[41]
	Al ₃ Ti (tetragonal)	25 to 32	Congruent	1550	[38]
	Al ₃ Ti (tetragonal)	25	Congruent	1627	[39]
	D0₂₂	25	Peritectic	1551	[40]
Al₂Ta	Orthorhombic or tetragonal	≈34	[42]
		≈33	[43]
		34.5 to 35	Peritectic	1594	[40]
Al ₃ Ta ₂	Hexagonal	≈40	[44]
	orthorhombic	≈38-40	Peritectic	≈1570	[39]
Al ₁₇ Ta ₁₂	Complex cubic	≈42	[45]
AlTa	...	≈50	[43]
		≈52	Peritectic	1770	[40]
Al ₁₂ Ta ₁₇	α -Mn (cubic)	≈60	[45], [46]
Al ₃ Ta ₅	...	62.5	[43]
σ-AlTa₂	σ-CrFe (tetragonal)	66.7±X	Peritectic	2100	[41]
		60 to 80	[42], [45], [47]
		66.7	Peritectic	2000	[38]
		≈56 to 80	[40]
AlTa ₃	...	75	[43]

In order to shed further light on this central region of the Al-Ta system, Mahne et al [48]–[50] performed detailed XRD analyses of single crystal alloy samples. They initially found that the phases previously identified as Al_2Ta , Al_3Ta_2 , and $\text{Al}_{17}\text{Ta}_{12}$, and highlighted in blue in Table 2.4, are actually a single cubic phase with stoichiometry $\text{Al}_{69}\text{Ta}_{39}$ and Pearson symbol cF432 [49]. However, they later concluded that this new phase, $\text{Al}_{69}\text{Ta}_{39}$ undergoes three peritectoid decomposition reactions as it cools to form phases with approximate compositions of $\text{Al}_{1.5}\text{Ta}/\text{Al}_3\text{Ta}_2$, $\text{Al}_{1.4}\text{Ta}/\text{Al}_7\text{Ta}_5$, and AlTa , stating that “the phase relations in the range between $\epsilon\text{-Al}_3\text{Ta}$ and $\sigma\text{-AlTa}_2$ are significantly more complex than first thought”. [50] In addition, a further analysis of the phases in this region was later conducted by Boulineau et al, in 2006 [51] using synchrotron XRD. They concluded that the phases previously identified as AlTa , $\text{Al}_{12}\text{Ta}_{17}$, Al_3Ta_5 , and highlighted in green in Table 2.4, is actually a single monoclinic, mP86, phase of stoichiometry $\text{Al}_{38}\text{Ta}_{48}$. These investigations have at least partially clarified some of the discrepancies between the previous reports on the intermetallic phases present in this system.

To date, three thermodynamic assessments of the Al-Ta system have been performed. The first was carried out by Kaufman in 1991 [52] and produced a very similar phase diagram to that of Subramanian et al [40]. This is probably due to Subramanian et al’s investigation in 1990 being the most up to date experimental work available at that time. The second was performed by Du and Schmid-Fezer in 1996 [53]. This assessment is based on a large amount of literature data, but gave a particularly high weight to the results of Mahne et al [48]–[50], and was performed prior the work of Boulineau et al [51]. Consequently, the central part of their phase diagram, which is displayed in Figure 2.6 fits closely with the data of Mahne et al [48]–[50], and shows the newly identified $\text{Al}_{69}\text{Ta}_{39}$ phase undergoing three peritectoid decomposition reactions to form Al_3Ta_2 , Al_7Ta_5 , and AlTa . In addition, the stability range of

the σ -AlTa₂ is reduced to around 66 to 80at% tantalum at 1500°C, and is even less at lower temperatures. Moreover, they have also reinstated the central eutectic reaction at around 46at% tantalum, and 1499°C, being in general agreement with the results of Kimura et al [38], Schuster [39] and Mahne et al [50] on this point, rather than those of Subramanian et al [40]. The third and most recent thermodynamic assessment was carried out by Witusiewicz et al [54] in 2010. Before modelling the system, they performed a detailed review of the available literature, including the work of Boulineau et al [51], coupled with an analysis of seven different alloys with compositions ranging from 20.5 to 88at% tantalum via DTA, pyrometry, EDS, electron backscattered diffraction (EBSD), XRD and metallography. Their calculated phase diagram is shown in Figure 2.7, and a calculated invariant reaction scheme for the system is given in Table 2.5. Table 2.6 shows their results, plus a summary of their review on the crystallographic structures of the intermetallic phases that have been reported to exist in the Al-Ta system.

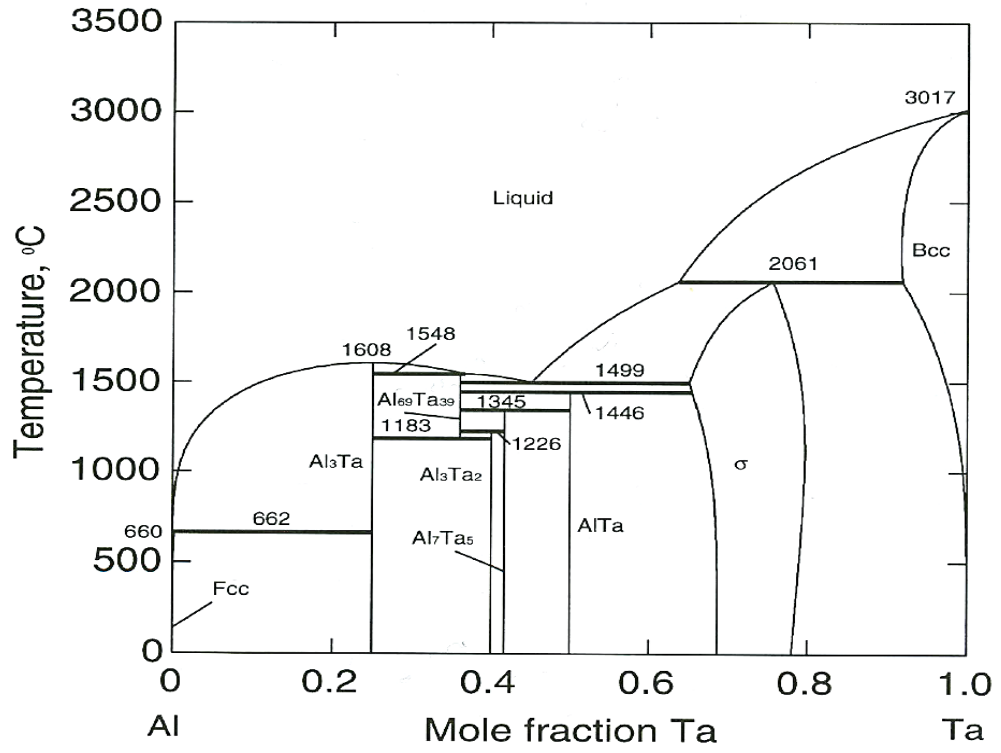


Figure 2.6: Du and Schmid-Fezer's calculated Al-Ta phase diagram [53]

Table 2.5: Witusiewicz's et al's invariant reaction scheme for the Al-Ta system, the values for x_i are in mole fraction Ta and correspond to the order that the phases appear in the invariant reactions [54]

Invariant reaction	Reaction type	T_{exp} (°C)	T_{exp} (K)	X_1	X_2	X_3
$L \leftrightarrow \beta\text{-Ta}$	Melting	3017	3290	1	1	N/A
$L \leftrightarrow \beta\text{-Ta} + \sigma\text{-AlTa}_2$	Peritectic	2074	2347	0.678	0.930	0.759
$L + \sigma\text{-AlTa}_2 \leftrightarrow \text{Al}_{69}\text{Ta}_{39}$	Peritectic	1612	1885	0.327	0.51	0.378
$\sigma\text{-AlTa}_2 \leftrightarrow \phi\text{-Al}_{38}\text{Ta}_{48}$	Congruent	1581	1854	0.552	0.552	N/A
$L + \text{Al}_{69}\text{Ta}_{39} \leftrightarrow \varepsilon\text{-Al}_3\text{Ta}$	Peritectic	1541	1814	0.237	0.355	0.244
$\sigma\text{-AlTa}_2 \leftrightarrow \text{Al}_{69}\text{Ta}_{39} + \phi\text{-Al}_{38}\text{Ta}_{48}$	Eutectoid	1464	1737	0.511	0.376	0.522
$\text{Al}_{69}\text{Ta}_{39} \leftrightarrow \varepsilon\text{-Al}_3\text{Ta} + \phi\text{-Al}_{38}\text{Ta}_{48}$	Eutectoid	1098	1371	0.368	0.25	0.524
$L + \varepsilon\text{-Al}_3\text{Ta} \leftrightarrow \alpha\text{-Al}$	Peritectic	660.7	933.7	0.000038	0.247	0.00038

Table 2.6: Witusiewicz's et al's results and reviewed data on the crystal structures of the phases in the Al-Ta system [54]

Phase	Comp at% Co	Pearson symbol	Space group	Struktur -bericht	Prototype	Ref
α -Al	0-0.038	cF4	$Fm\bar{3}m$	A1	Cu	[29]
ε -Al ₃ Ta	25	tI8	$I4/mmm$	D0 ₂₂	TiAl ₃	[55]
Al₆₉Ta₃₉ (Previously reported Al ₂ Ta Al _{1.5} Ta Al ₃ Ta ₂ Al ₇ Ta ₅ Al _{1.4} Ta Al ₁₇ Ta ₁₂)	35.5- 37.5	cF432	$F4\bar{3}m$...	Al ₆₉ Ta ₃₉	[49]
ϕ -Al ₃₈ Ta ₄₈ (Previously reported AlTa Al ₁₂ Ta ₁₇ Al ₃ Ta ₅)	52-58	mP86	P2 ₁ /c	[51]
σ -AlTa ₂ (Previously reported AlTa ₃)	51-80.5	tP30	P4 ₂ /mmm	D8 ₆	CrFe	[47]
β -Ta	93-100	cI2	$Im\bar{3}m$	A2	W	[29]

Witusiewicz et al [54], identified four intermetallic phases to exist across the Al-Ta system: ϵ -Al₃Ta, Al₆₉Ta₃₉, ϕ -Al₃₈Ta₄₈, and σ -AlTa₂. The crystal structures and composition ranges of these phases are shown in Table 2.6 and Figure 2.7. They did not find any evidence of the Al_{1.5}Ta/Al₃Ta₂, Al_{1.4}Ta/ Al₇Ta₅ phases that were reported to form peritectically from the decomposition of Al₆₉Ta₃₉ by Mahne et al [50], and therefore excluded these phases from their models. Apart from the ϕ -Al₃₈Ta₄₈ phase behaviour and the decomposition of the Al₆₉Ta₃₉ phase at 1371K/1098°C, Witusiewicz et al [54], found their results on the liquidus to be in good agreement with those of Subramanian [40], and gave these two sets of results a higher weight than those of Kimura et al [38], Schuster [39] and Mahne et al [50]. Consequently their phase diagram features a similar cascade of peritectic and congruent reactions occupying the central region to that of Subramanian et al [40] instead of the eutectic type reaction favoured by Du and Schmidt-Fezer [53] and others [38], [39], [50]. Witusiewicz et al's assessment [54] likely represents the best description of the Al-Ta system currently available. However, it seems that further research is required to settle the discrepancies between previous reports, and definitively describe the phase equilibria that take place between the ϵ -Al₃Ta and ϕ -Al₃₈Ta₄₈ phases of the system.

2.3: The Cobalt Tantalum (Co-Ta) System

The first recorded experimental investigation of the Co-Ta system was performed by Hashimoto in 1937 [56], who measured the phase boundaries across the entire composition range via thermal analysis and magnetic measurements during heating and cooling. These results yielded a liquidus for the system, and provided information on the terminal solid solutions and an intermetallic phase, CoTa, which was stable from about 48 to 52at% tantalum. Köster et al, 1938 [57], also used thermal analysis, and measured the phase boundaries between 0 and 30at% tantalum. Their measured liquidus is in agreement with that of Hashimoto. Further information on the system was provided by Wallbaum in 1941 [58], [59], when he used XRD to identify two new binary intermetallic phases with compositions close to Co₂Ta. The first was a Laves C36 phase, with an MgNi₂, hP24 structure, and the second was a Laves C15 phase, with a Cu₂Mg, cF24 structure. Later XRD studies by Korchynsky et al, 1959 [60], and Dragsdorf et al, 1960 [61], confirmed the observations of Wallbaum [58], [59], and also reported the existence of two further binary phases in the form of a Co₃Ta/Co₇Ta₂ phase that forms peritectically at around 990°C and 25at% tantalum, and a third Co₂Ta Laves phase of C14, hP12, MgZn₂ structure.

In 1967, Raman [62] performed thermal analysis, XRD and metallography studies of alloy samples across the entire composition range after heat treatments at 1000°C and 1200°C. His results were in agreement with the previously discussed works with regards to the composition, structure and position of the intermediate phases: Co₃Ta/Co₇Ta₂, and the three off stoichiometry Co₂Ta, Laves phases C36, C15, and C14. However, he also found two other phases: μ -Co₇Ta₆, and CoTa₂. The μ -Co₇Ta₆ phase, first referred to as CoTa by Hashimoto [56], was identified to form congruently from the melt at around 1750°C and was stable

between 48 and 55at% tantalum. The CoTa_2 phase also formed congruently, but at a higher temperature of 1930°C, and with a stability range of 64 to 68at% tantalum. On the basis of these results, Raman [62] proposed a full phase diagram for the Co-Ta system. This diagram was later refined by Petkov et al [63], [64], who performed detailed DTA, XRD, and metallography analyses of alloys between 0 and 40at% tantalum. Petkov et al's [63], [64] results agreed with those of Raman [62] in terms of the phases present, their general positions, and their crystal structures; however they provided more detailed information on the phase equilibria of the three Laves phases. Further revisions to Raman's [62] phase diagram were made by Bernard et al in 1976 [65], after their investigation of the Co-Ta system between 40 to 100at% tantalum, again via DTA, XRD, and metallography. They reported melting temperatures for the $\mu\text{-Co}_7\text{Ta}_6$ and CoTa_2 phases of 1620°C and 1700°C respectively, which are much lower than those of Raman [62]. Moreover, they also differ with Raman [62] in terms of the compositional stabilities reported for these phases, stating that $\mu\text{-Co}_7\text{Ta}_6$ is stable from 44 to 56at% tantalum, and that CoTa_2 forms peritectically and has a negligible homogeneity range about 66.67at% tantalum. A 1986 review by Barabash and Koval [66] evaluated the aforementioned studies to produce a complete phase diagram for the Co-Ta system, which is shown in Figure 2.8, and a summary of the crystal structure data for the phases, which is given in Table 2.7. This phase diagram was later redrawn by Okamoto [67] and is the version currently accepted by the ASM handbook [14].

Table 2.7: Composition and crystal structure data for the solid phases in the Co-Ta system

[66]

Phase	Comp at% Co	Pearson symbol	Space group	Struktur- bericht	Proto- type
α -Co	0-4	cF4	$Fm\bar{3}m$	A1	Cu
ε -Co	0-?	hP2	$P6_3/mmc$	A3	Mg
Co_7Ta_2	22.2
λ_3 -Laves, Co_2Ta	27.5-29	hP24	$P6_3/mmc$	C36	$MgNi_2$
λ_2 -Laves, Co_2Ta	29.9-36	cF24	$Fd\bar{3}m$	C15	Cu_2Mg
λ_1 -Laves, Co_2Ta	37	hP12	$P6_3/mmc$	C14	$MgZn_2$
μ - Co_7Ta_6	44-56	hR13	$R\bar{3}m$	D8 ₅	Fe_7W_6
$CoTa_2$	66.7	tI12	$I4/mcm$	C16	Al_2Cu
β -Ta	80-100	cI2	$Im\bar{3}m$	A2	W

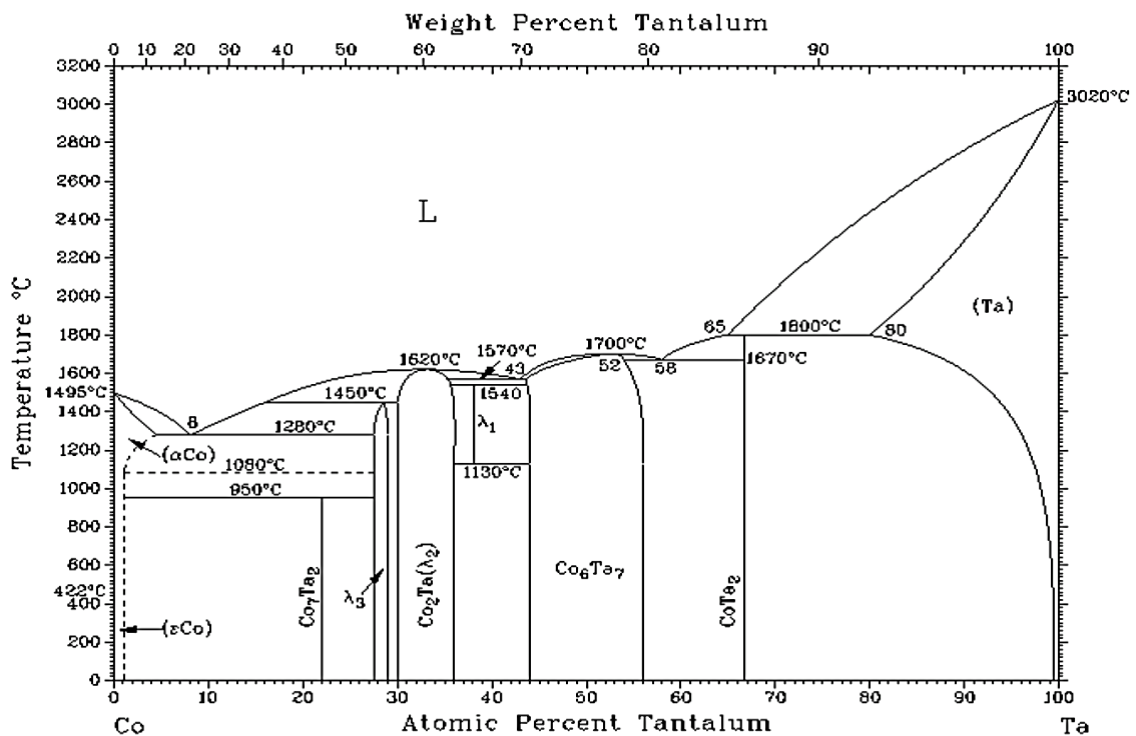


Figure 2.8: Barabash and Koval's reviewed Co-Ta phase diagram [66]

To date, four thermodynamic assessments have been performed on the Co-Ta system. The first was carried out by Kaufman in 1991 [66], but was based on the ASM's pre-Barabash and Koval data, which described most of the intermediate phases as stoichiometric line compounds. The second was performed by Liu and Chang, in 1999 [68], and considered all of the previously discussed data, with the addition of the Gibbs energy of formation data of Rezhikhina et al [69], and the calculated enthalpy of formation data of Niessen et al [70], and Colinet et al [71]. Their calculated phase diagram is shown in Figure 2.9, and closely replicates the experimentally determined version of Barabash and Koval [66]. However their inclusion of the extra thermodynamic data has enabled them to calculate more realistic descriptions of the terminal solubility boundaries, which were previously poorly described due to a lack of traditional experimental phase diagram data in these regions.

The third thermodynamic assessment of this system was carried out by Hari-Kumar et al. in 2002 [72], as part of a larger assessment of the ternary Co-Nb-Ta system. They considered much of the same data as Liu and Chang [68], but with the addition of an extra study on the α -FCC to ε -HCP transition at the Co rich end of the composition range by Zhao [73]. Their phase diagram, shown in Figure 2.10 replicates the experimental diagram shown in Figure 2.8 quite well, and appears to provide the most realistic looking terminal solubility and λ_2 -Laves C15 phase boundaries of any of the three diagrams presented for this system so far. Their calculated invariant reaction scheme is also shown in Table 2.8. The one drawback of this assessment is their use of Co_3Ta and $\text{Co}_{16}\text{Ta}_9$ stoichiometric line compounds to represent the λ_3 -Laves C14, and λ_1 -Laves C36 phases, when the C14 phase has already been shown to have a small compositional stability range. This issue was considered by Hari-Kumar et al [72], however they preferred to use the stoichiometric models for these phases in their Co-Ta description, to maintain compatibility with an assessment of the Co-Nb system

that they planned to combine it with. Ironically, experimental studies have now determined that all three Laves phases in the Co-Nb system also have compositional stability ranges [74], [75]. The fourth and most recent thermodynamic assessment of the Co-Ta system was performed by Shinagawa et al in 2014 [76]. They considered all of the previously discussed data, but also performed their own experiments to map the phase boundaries across the system, analysing alloys heat treated at specific temperatures between 1300°C and 900°C, for times ranging from 96 to 672 hours, via EPMA, scanning and transmission electron microscopy (SEM & TEM), XRD and DSC. Their calculated phase diagram displayed in Figure 2.11, seems to map the stability ranges of the terminal cobalt, and intermediate phases more precisely than any of the previously published versions. This diagram shows that the CoTa₂ phase has a compositional stability range of about 64-67%at tantalum, similar to that first reported by Raman [62], and also gives a particularly detailed map of the phase equilibria that take place between the liquid, the three Laves phases, and the μ -Co₇Ta₆ phase. These equilibria are also remarkably similar those that take place in the Co-Nb phase diagram shown in Figure 2.12, which was produced by a recent experimental investigation by Stein et al [74]. On the available evidence, it is likely that Shinagawa et al's [76] thermodynamic assessment is the best description of the Co-Ta system currently available.

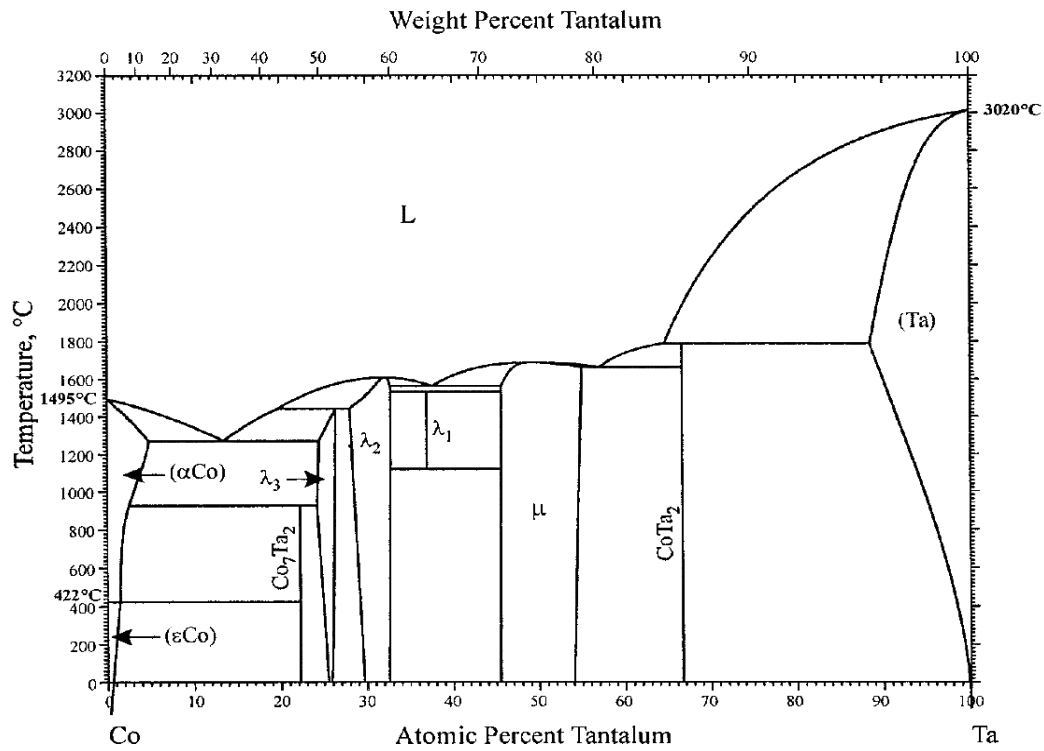


Figure 2.9: Liu and Chang's calculated Co-Ta phase diagram [68]

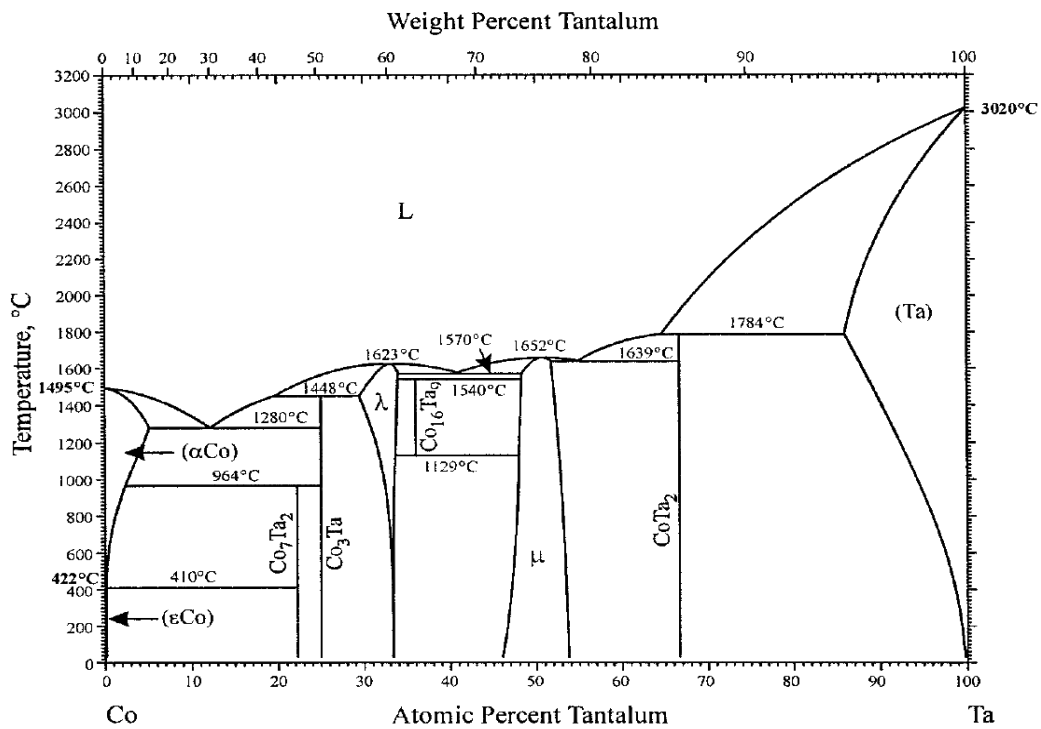


Figure 2.10: Hari-Kumar et al's calculated Co-Ta phase diagram [72]

Table 2.8: Hari-Kumar et al's invariant reaction scheme for the Al-Ta system, the values for x_i are in mole fraction Ta and correspond to the order that the phases appear in the invariant reactions [72]

Invariant reaction	Type	T_{exp} (°C)	T_{exp} (K)	X_1	X_2	X_3
$L \leftrightarrow \beta\text{-Ta}$	Melting	3020	3293	1	1	N/A
$L \leftrightarrow \beta\text{-Ta} + \text{CoTa}_2$	Peritectic	1784	2057	0.6462	0.8606	0.6667
$L \leftrightarrow \mu\text{-Co}_7\text{Ta}_6$	Congruent	1652	1925	N/A	0.51	N/A
$L \leftrightarrow \mu\text{-Co}_7\text{Ta}_6 + \text{CoTa}_2$	Eutectic	1639	1912	0.5508	0.5191	66.67
$L \leftrightarrow \lambda_2\text{-Laves C15}$	Congruent	1623	1896	N/A	0.3283	N/A
$L \leftrightarrow \lambda_2\text{-Laves C15} + \mu\text{-Co}_6\text{Ta}_7$	Eutectic	1570	1843	0.469	0.3389	0.484
$\lambda_2\text{-Laves C15} + \mu\text{-Co}_7\text{Ta}_6 \leftrightarrow \lambda_3\text{-Laves C14}$	Peritectoid	1540	1813	0.3386	0.4837	0.36
$L \leftrightarrow \alpha\text{-Co}^{\text{para}}$	Melting	1495	1768	0	0	N/A
$L + \lambda_2\text{-Laves C15} \leftrightarrow \lambda_1\text{-Laves C36}$	Peritectic	1451	1724	0.1917	0.2941	0.25
$L \leftrightarrow \alpha\text{-Co}^{\text{para}} + \lambda_1\text{-Laves C36}$	Eutectic	1280	1553	0.1238	0.0526	0.25
$\lambda_3\text{-Laves C14} \leftrightarrow \lambda_2\text{-Laves C15} + \mu\text{-Co}_7\text{Ta}_6$	Eutectoid ordering	1129	1402	0.36	0.335	0.4807
$\alpha\text{-Co}^{\text{para}} \leftrightarrow \alpha\text{-Co}^{\text{ferro}}$	Magnetic ordering	1127	1400	0	0	N/A
$\alpha\text{-Co}^{\text{para}} + \lambda_1\text{-Laves C36} \leftrightarrow \alpha\text{-Co}^{\text{para}} + \text{Co}_7\text{Ta}_2$	Peritectoid	964	1237	0.0234	0.25	0.2222
$\alpha\text{-Co}^{\text{ferro}} \leftrightarrow \varepsilon\text{-Co}$	Allotropic transformation	422	695	0	0	N/A
$\alpha\text{-Co}^{\text{ferro}} \leftrightarrow \varepsilon\text{-Co} + \text{Co}_7\text{Ta}_2$	Eutectoid	410	683	0.00125	1.38E ⁻⁶	0.2222

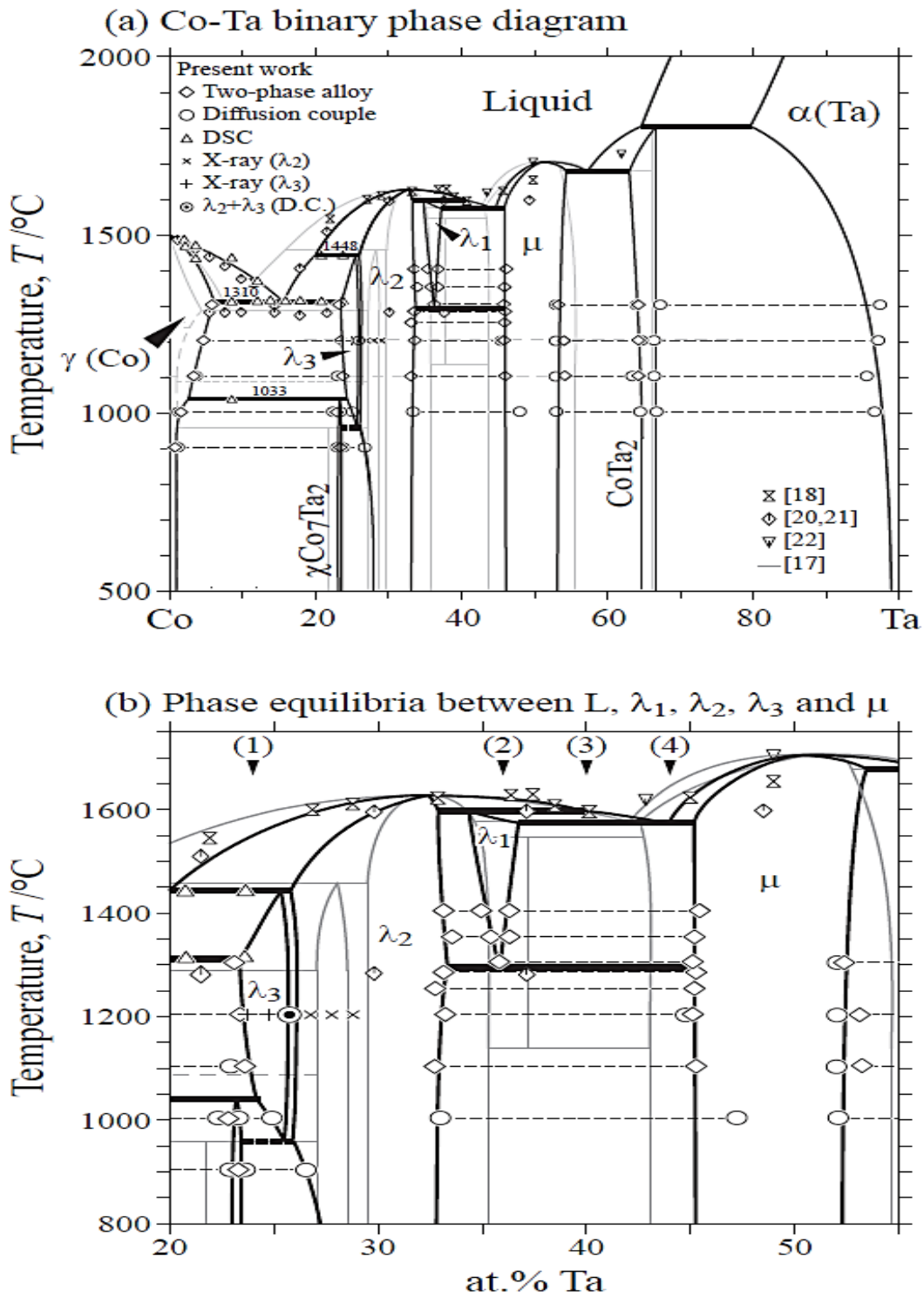


Figure 2.11a: Shinagawa et al's calculated Co-Ta phase diagram and experimentally measured data points [76]. The faint grey lines show the phase boundaries of Barabash and Koval's [66] previous diagram.

Figure 2.11b: A more detailed look at the phase equilibria between the L, λ_3 , λ_2 , λ_1 , and μ phases [76]

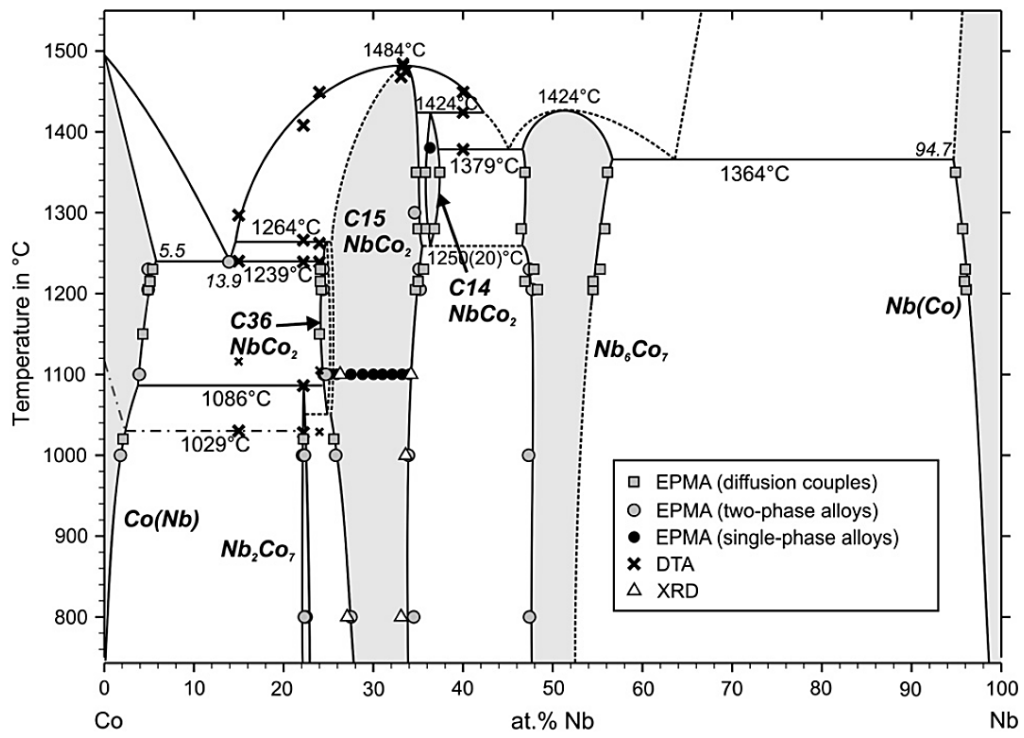


Figure 2.12: Stein et al's experimentally determined Co-Nb phase diagram [74]

2.4: The Tantalum Aluminium Cobalt (Ta-Al-Co) System

There is currently very little information available on the Ta-Al-Co ternary, as only a few experimental studies have been performed on the system to date. Most of the data that is available comes from the 1968 investigation of Hunt and Raman [77] who used XRD to analyse the phases present in five different Al-Co-Ta alloys. Prior to analysis, their samples were created via arc melting in an argon atmosphere, then annealed at 1000°C for 168 hours in evacuated silica capsules and left to air cool. Their results yielded a partial isothermal section at 1000°C, which is shown in Figure 2.13. The compositions of the alloy samples they studied are also marked on this figure. Further information is provided by the work of Markiv [78], and Buschow et al [79], who used XRD to investigate a range of aluminium containing, AlCu₂Mn type Heusler alloys, after annealing at 900°C for 240 hours followed by water quenching. Both studies confirmed the existence of an AlCo₂Ta ternary phase in this system.

The aforementioned investigations were later reviewed by Ferro et al in 1991 [80], who added the AlCo₂Ta ternary Heusler phase identified by Markiv [78], and Buschow et al [79] to Hunt and Raman's [77] isothermal section as shown in Figure 2.13. They also produced a summary of the crystal structure data for the solid phases found in the system, which is listed in Table 2.9. However, this table is currently incomplete, as a full list of the solid phases present in the system would include all of those found in its constituent binaries, listed in Tables 2.3, 2.6, and 2.7, plus any new ternary phases. From these tables we can conclude that there are at least nineteen binary solid phases, and so far, only five of them are listed in Table 2.9 as having been experimentally observed in the Ta-Al-Co ternary system. These are β -Ta, CoTa₂, μ -Co₇Ta₆, λ_1 -Laves C36-Co₂Ta, and σ -AlTa₂. Of these five phases, three have been identified to extend into the ternary diagram due to their significant ternary

solubilities, namely, μ -Co₇Ta₆, λ_1 -Laves C36-Co₂Ta, and σ -AlTa₂. In addition, two ternary solid phases have also been discovered: μ' -Al₂₃Co₂₃Ta₅₄, and the Heusler AlCo₂Ta phase. Thus far, no three phase equilibria have been reported.

The presence of these two ternary phases in the Ta-Al-Co system, with the AlCo₂Ta Heusler phase having an ordered L2₁ crystal structure, raised the possibility that if the μ' phase had an ordered BCC_B2, D0₃, or L2₁ (β') structure, then a BCC_A2 (β)/ β' two phase field may be present in the tantalum corner of the diagram. If this is the case then the ternary could be a potential base system for a β/β' precipitation strengthened high melting point alloy. Hunt and Raman [77] suggest that the μ' phase may be related to the μ phase, but provide no crystallographic data on this compound, so its structure is currently unknown. In any case, the Ta-Al-Co ternary is also an important superalloy subsystem, and its phase equilibria are very poorly understood. Therefore it has been decided that the system merits further study.

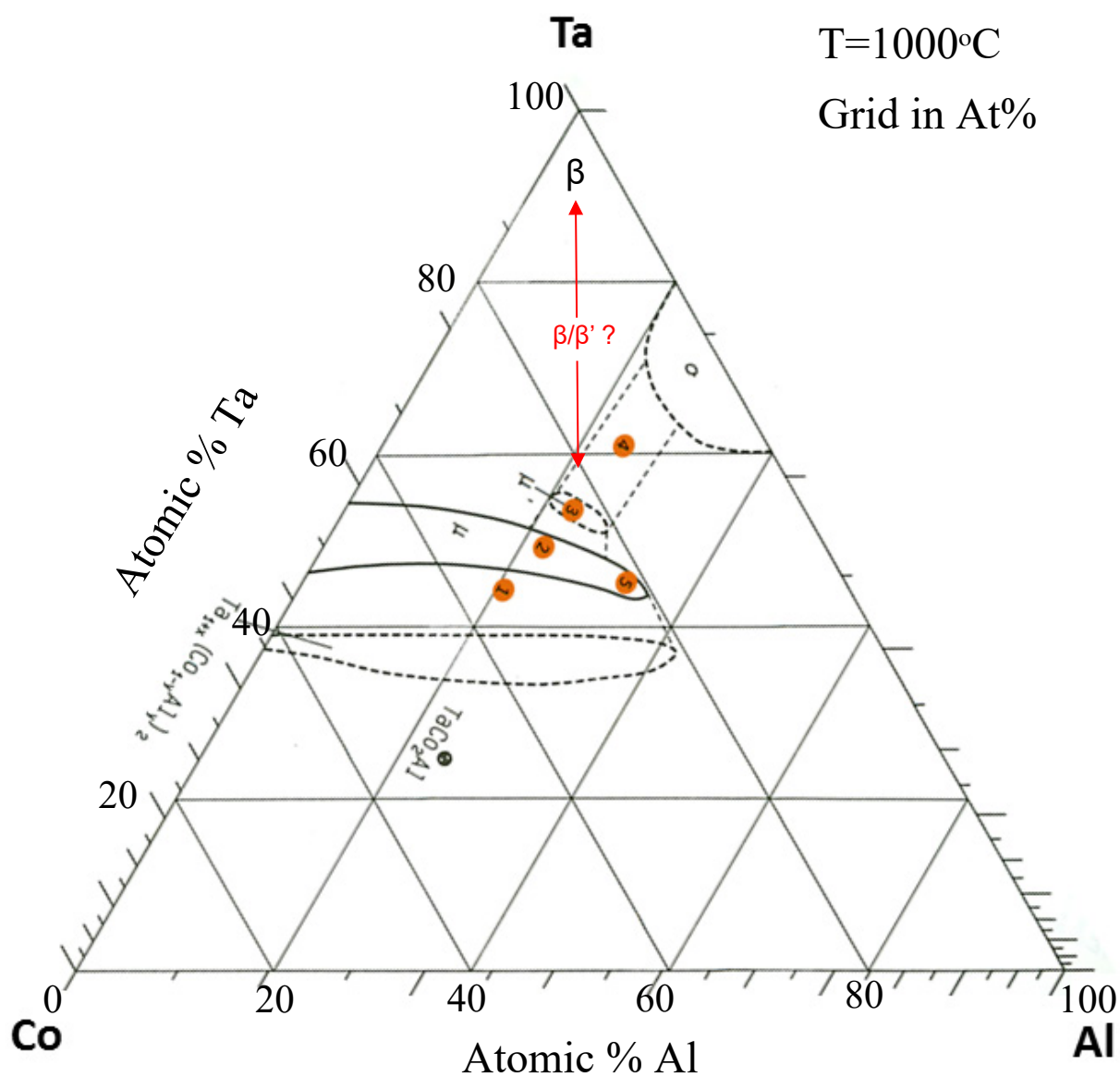


Figure 2.13: Hunt and Raman's [77] isothermal section of the Al-Co-Ta system at 1000°C. The orange markers show the compositions of the alloys investigated. In addition, the composition of the AlCo_2Ta ternary Heusler phase studied by Markiv [78], and Buschow et al [79] has been added by Ferro et al [80].

Table 2.9: Composition and crystal structure data for the phases in the Al-Co-Ta system [80]

Phase/ Temperature Range (°C)	Pearson Symbol/ Prototype	Lattice Parameters (pm)	Comments
Ta	cI2 W	a = 330.25	[V-C]
Ta ₂ Co	tI12 CuAl ₂	a = 611.6 c = 496.9	[V-C]
μ , Ta _{6+x} (Co _{1-y} Al _y) _{7-x}	hR39 W ₆ Fe ₇		$-0.15 \leq x \leq 1.28$ at $y=0$ $0 \leq y \leq 0.61$
Ta ₆ Co ₇		a = 490.0 c = 2642 a = 494.7 c = 2657 a = 498.7 c = 2719 a = 499.4 c = 2738	x = 0, y = 0 x = 1, y = 0 x = 0.37, y = 0.43 x = -0.28, y = 0.61 [68Hun]
Ta _{1+x} (Co _{1-y} Al _y) ₂	hP12		x \approx 0.22, y \leq 0.65 [68Hun]
α TaCo ₂	MgZn ₆	a = 479.7 c = 782.7	x \approx 0.22, y = 0 [V-C]
σ , Ta _{2+x} (Co _y Al _{1-y}) _{1-x}	tP30 CrFe		$-0.2 \leq x \leq 0.4$ [68Hun] $0 \leq y \leq 0.25$ at x = 0, y = 0 [V-C]
* μ' , \approx Ta ₅₄ Co ₂₃ Al ₂₃	related to hR39 W ₆ Fe ₇		[68Hun]
* TaCo ₂ Al	cF16 MnCu ₂ Al	a = 592.7 a = 593.0	[65Mar] [81Bus] annealed 10 days at 900°C

2.5: The CALPHAD Method

2.5.1: Background

Phase diagrams are maps of the equilibrium state of a material as a function of temperature, composition, and pressure. They are used as a guide to the relationship between a materials chemical composition, processing conditions, microstructure, and physical properties.[5] This makes them useful tools in the areas of alloy design and thermo-mechanical process development. CALPHAD is an acronym for the CALculation of PHase Diagrams, and is a proven method of producing a self-consistent thermodynamic description of a given alloy system from different types of materials data.[5]

The fundamental principles describing thermodynamics and phase equilibria were first established by Gibbs in the 1870s [81], [82]. This work laid the mathematical foundations that enabled Van Laar [83], [84] to develop solution models, and produce the first calculated prototype binary phase diagrams in 1908. Van Laar's models demonstrated that the topological features of binary phase diagrams are dependent upon the relative thermodynamic stabilities of the phases involved. More than 40 years later, in the 1950s, Meijering [85], [86] extended the work of Van Laar [83], [84] to calculate prototype phase diagrams for ternary and quaternary systems. Over the next 20 years or so, gradual progress was made as Kaufman et al [87] started using computers to systematically calculate phase diagrams for real binary and ternary systems. In 1970, Kaufman and Bernstein described the modern CALPHAD approach in their book: Computer Calculation of Phase diagrams [87]. They also organised the first meeting of the international CALPHAD group in 1973, and the first issue of the CALPHAD journal followed soon after in 1977. Since then, the efforts of these early researchers, coupled with modern developments in modelling and computational technology

have driven rapid progress in the field. The CALPHAD method can now be used to calculate accurate descriptions of multicomponent systems that can be used for practical applications, such as alloy design, or process simulations [88], [89]. Modern comprehensive guides on the subject have been written by Saunders and Miowdownnik [90], and Lukas et al [5].

The basic principles of this approach are to select appropriate models and coefficients to describe the Gibbs energy of each phase in the system of interest based on their crystal structures and physical behaviour. The coefficients of these models are then fitted to the most accurate experimental phase diagram and thermodynamic data available to produce a thermodynamic description of the system that accurately represents its real life behaviour. This fitting process, also known as optimisation, is an iterative technique that utilises the least squares method to simultaneously adjust the Gibbs energy curves of all the phases in the system to the values that best fit with the selected experimental data. If accurate descriptions are created for the necessary unary, binary and ternary systems, based on good experimental data, these descriptions can then be combined to produce a credible extrapolated description of a multicomponent system, without the need for any new multicomponent experimental data. A summary flow chart describing this process is shown in Figure 2.14.

Gaining an accurate description of an unknown multicomponent alloy containing ten or more different elements, from only experimental data on its unary, binary and ternary subsystems is a very attractive prospect indeed, because it would take a ridiculously large amount of time to investigate such a system using conventional experimental methods. Yet, the CALPHAD method can be used to explore the phase equilibria over the full composition range of a multicomponent alloy in just a fraction of the time, allowing researchers to save resources by focussing their experimental efforts on only the most promising areas of the phase diagram [88], [89]. Other advantages of this method are that it can combine and summarise

large amounts of different types of experimental data into a single self-consistent description of a system, and that it can also be used to provide input data for predictive materials production or processing simulations. The main drawback of the CALPHAD method is that although it can be used to extrapolate the stability ranges of all known phases, it won't predict the presence of any new unassessed phases. This is why all of the binary and ternary phases must be accurately described prior to extrapolation. If quaternary, and quinary phases are present in the system, they must also be assessed, and added to the thermodynamic description, or they will not be included in the multicomponent extrapolation. Quaternary metallic compounds are not that common, and quinary phases are rarer still, however the possibility that they may be present should still be considered.

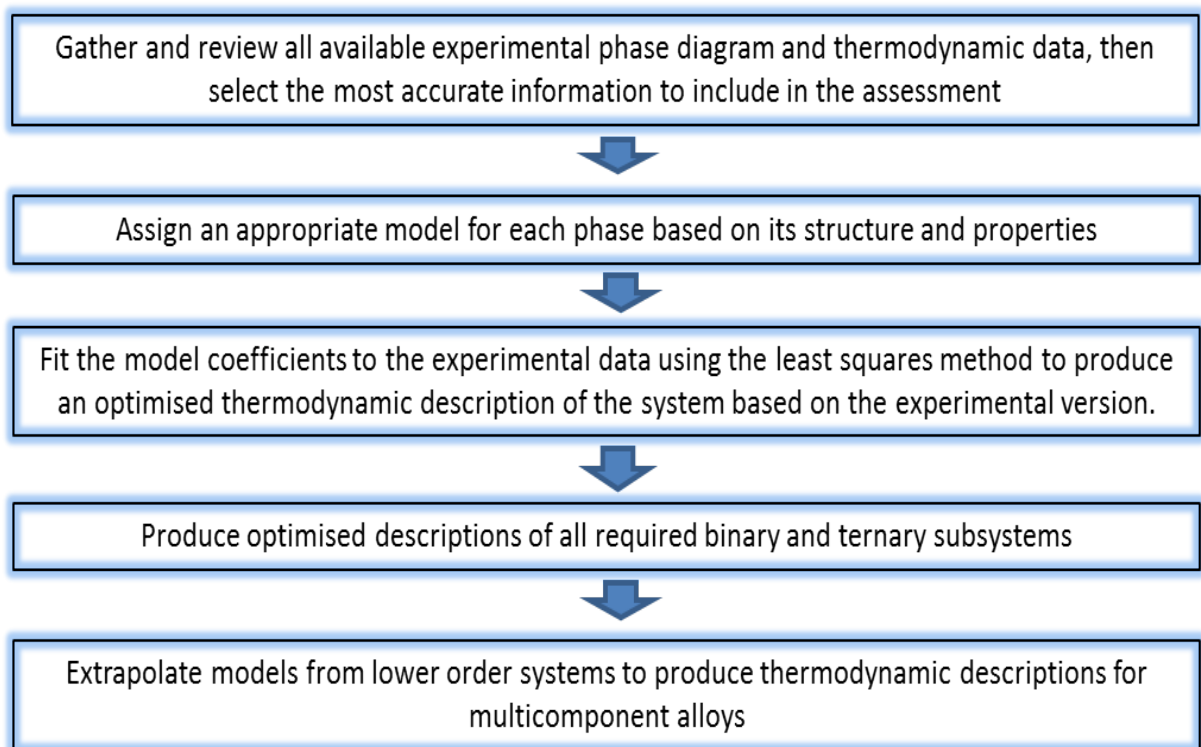


Figure 2.14: Summary of the CALPHAD process

2.5.2: CALPHAD Models

In the CALPHAD method the Gibbs energy of each phase in the selected system is described by an appropriate model in order to produce a complete thermodynamic description for the material in question. The Gibbs energy is used as the quantity on which to model the phases, because if its value is known along with the temperature, pressure and composition of the system, then most other important thermodynamic quantities can also be calculated. Using these models the equilibrium state of the system can be determined by finding the minimum total Gibbs energy for the system, G^{Sys} , which is equal to the minimum value of the sum of the number of moles of every phase in the system, n_i , multiplied their respective Gibbs energies, G_i^φ , as shown in equation 2.1 [5], [88], [90].

$$G^{Sys} = \sum_i n_i G_i^\varphi = \text{minimum} \quad (2.1)$$

The Gibbs energy for each phase, G^φ , is dependent upon the temperature, pressure, and composition of the system. It is also partially dependent upon any physical phenomena that may occur, such as magnetism. Thus in order to model the Gibbs energy of a phase, each of these contributions must be considered, as shown in equation 2.2. [5], [88], [90]

$$G^\varphi = G_T^\varphi(T, x) + G_p^\varphi(p, T, x) + G_{Mag}^\varphi(T_C, \beta_0, T, x) \quad (2.2)$$

Where $G_T^\varphi(T, x)$ is the contribution of the temperature and composition, $G_p^\varphi(p, T, x)$ is the contribution of the pressure, and $G_{Mag}^\varphi(T_C, \beta_0, T, x)$ is the magnetic contribution of the Curie temperature (T_C), and the average magnetic moment per atom (β_0). For condensed systems at normal pressures, as is the case for most metal alloys below their boiling point, the pressure contribution term, $G_p^\varphi(p, T, x)$, can be ignored. In addition, the contribution of physical

phenomena, such as magnetism, $G_{Mag}^{\phi}(T_C, \beta_0, T, x)$, need only be considered in cases where such phenomena are present. Thus many of the phases present in metallic systems can be modelled by considering the simplest case, whereby the Gibbs energy of the phase can be accurately described by the contributions of the temperature, and composition, $G_T^{\phi}(T, x)$, with the other contributions only being added for the specific cases where they are required.

To model the Gibbs energy of a multicomponent phase, G^{ϕ} , as a function of composition and temperature, $G_T^{\phi}(T, x)$, three distinct contributions must be taken into account. These are given in equation 2.3, and displayed graphically in Figure 2.15. [5], [88], [90]

$$G^{\phi} = G_T^{\phi}(T, x) = G^0 + G^{ideal} + G^{xs} \quad (2.3)$$

The first term, G^0 corresponds to the Gibbs energy of a mechanical mixture of the elemental phase constituents, before any atomic mixing has taken place. The second term, G^{ideal} is the contribution of the ideal configurational entropy of mixing, and the third term, G^{xs} , is the excess energy that results from any non-random mixing. The Gibbs energy models for many different types of phase are based on this primary equation, which will be discussed further when these models are introduced.

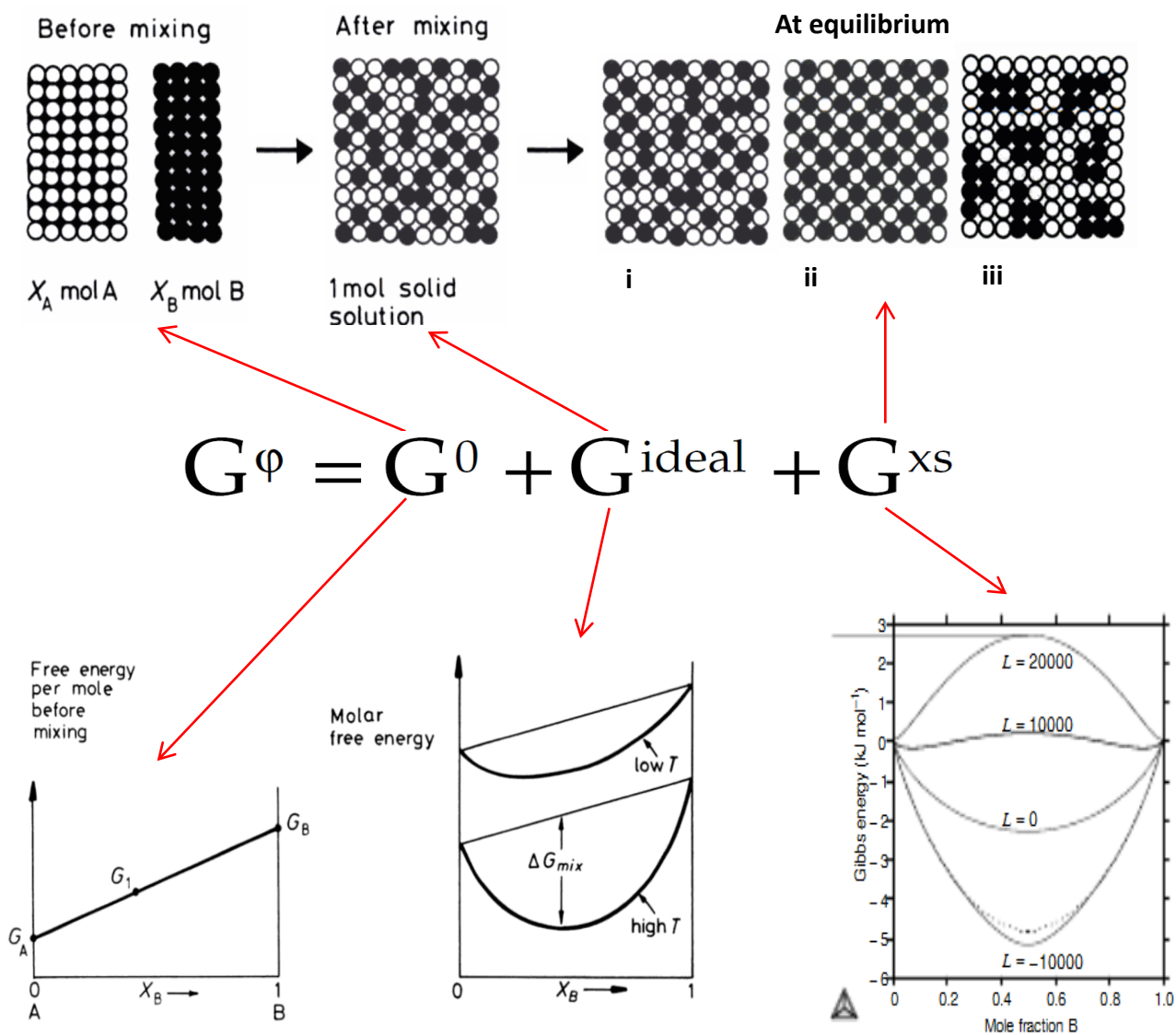


Figure 2.15: The contributions to the Gibbs energy of a multicomponent phase, as a function of temperature and pressure. Modified from Porter et al [91], and Lukas et al [5]

The temperature dependence of a phase with fixed composition, G_{AB} , such as a pure component, end member, or stoichiometric phase is usually described by the power series given in equation 2.4, which substitutes into the G^0 and G^{xs} terms of equation 2.3 in many of the Gibbs energy models.

$$G_{AB} - x_A H_A^{SER} - x_B H_B^{SER} = a + bT + cT \ln T + dT^2 + eT^{-1} + fT^3 + \dots \quad (2.4)$$

In this equation, x_A and x_B are the mole fractions of components A and B, H_A^{SER} and H_B^{SER} are the enthalpies of components A and B under standard conditions, and a to f are model coefficients to be fitted to experimental data. [5], [88], [90]

The Gibbs energy models for a binary stoichiometric phase, a disordered solution phase, and an ordered solution or intermetallic phase are all given by various modifications of equation 2.3, as described below.

$$G^\varphi = G^0 + G^{ideal} + G^{xs} \quad (2.3)$$

For a binary stoichiometric compound of composition A_xB_y :

$$G^0 = x_A G_A + x_B G_B$$

$$G^{ideal} = 0$$

$$G^{xs} = \Delta G_{AB}^f \quad (2.5)$$

Where x_A , and x_B are the mole fractions of components, A and B, G_A and G_B are the Gibbs energies of the pure components, A and B, at temperature, T_x , as described by equation 2.4, and ΔG_{AB}^f is the Gibbs energy of formation of compound A_xB_y . [5], [88], [90]

For disordered solution phases, such as the liquid, FCC, BCC, or HCP phases with a random atomic arrangement, the Redlich-Kister subregular solution model[92] is normally used. In this model:

$$\begin{aligned}
 G^0 &= x_A G_A + x_B G_B \\
 G^{ideal} &= RT(x_A \ln x_A + x_B \ln x_B) \\
 G^{xs} &= x_A x_B \sum_{i=0}^n {}^i L_{AB} (x_A - x_B)^i \quad (2.6)
 \end{aligned}$$

Where, x_A and x_B are the mole fractions of components A and B, G_A and G_B are the Gibbs energies of the pure components A and B, at temperature, T_x , as described by equation 2.4, R is the ideal gas constant, ${}^i L_{AB}$ is the i th interaction parameter, which combines with the Redlich-Kister polynomial: $(x_A - x_B)^i$ to describe the Gibbs energy contribution resulting from any non-ideal interactions between the atoms of components A and B. [5], [88], [90], [92]

For an ordered phase, or an intermetallic with an appreciable solubility range, the more complex sublattice model is required. The basic principle behind this model is that a sublattice is assigned to each distinct site in the crystal structure as shown for three common metallic structures in Figure 2.16. Current CALPHAD software can handle up to a maximum of five sublattices, although many phases can often be modelled with less. For example, in the case of the BCC_B2 ordered phase shown in Figure 2.17, A atoms fill positions 1 and 2, and B atoms fill positions 3 and 4, so a four sublattice model for this phase of $(A,B)_{0.25} (A,B)_{0.25} (A,B)_{0.25} (A,B)_{0.25}$ would give the same result as a two sublattice model of $(A,B)_{0.5} (A,B)_{0.5}$, therefore the simpler model is sufficient to describe this phase.

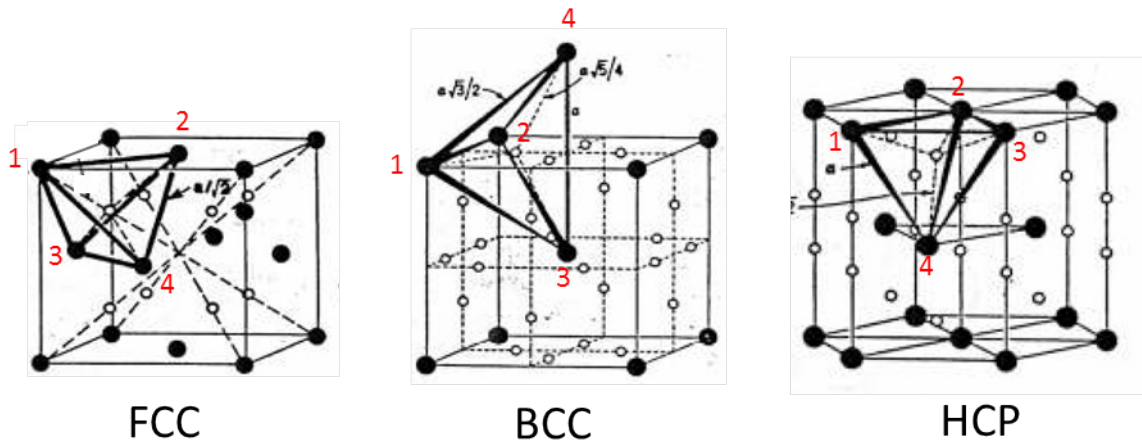


Figure 2.16: The four different sublattice sites of the FCC, BCC, and HCP structures. Modified from Cullity [93]

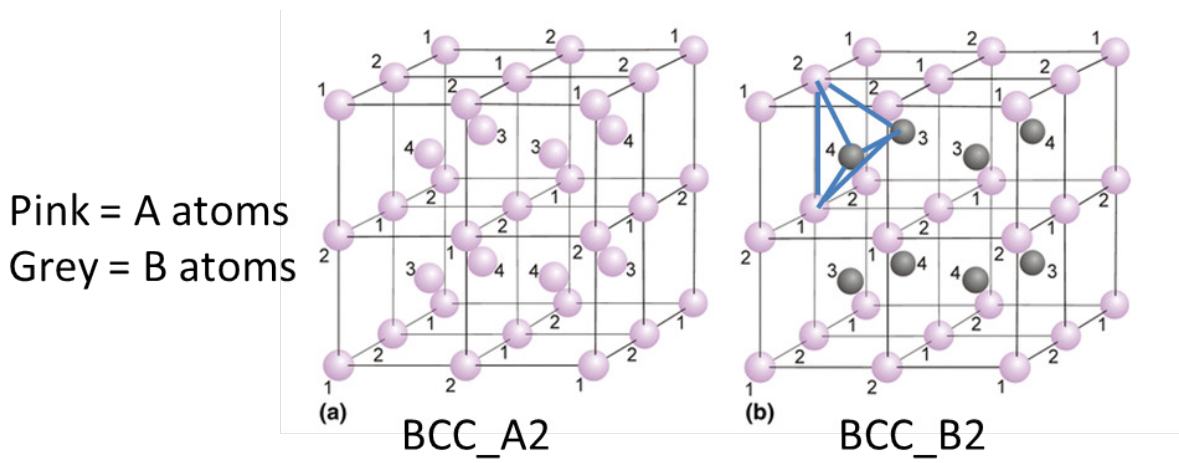


Figure 2.17: The BCC_B2 ordered phase. Modified from Witusiewicz et al [94]

For this type of ordered phase, the reciprocal solutions Redlich-Kister sublattice model is normally used. In this model:

$$\begin{aligned}
G^0 &= y_A^1 y_A^2 G_{AA} + y_A^1 y_B^2 G_{AB} + y_B^1 y_A^2 G_{BA} + y_B^1 y_B^2 G_{BB} \\
G^{ideal} &= RT \{ a^1 (y_A^1 \ln y_A^1 + y_B^1 \ln y_B^1) + a^2 (y_A^2 \ln y_A^2 + y_B^2 \ln y_B^2) \} \\
G^{xs} &= y_A^1 y_B^1 y_A^2 \sum_{i=0}^{n_{A,B:A}} {}^i L_{A,B:A} (y_A^1 - y_B^1)^i + y_A^1 y_B^1 y_B^2 \sum_{i=0}^{n_{A,B:B}} {}^i L_{A,B:B} (y_A^1 - y_B^1)^i + \\
&\quad y_A^1 y_A^2 y_B^2 \sum_{i=0}^{n_{A:A,B}} {}^i L_{A:A,B} (y_A^2 - y_B^2)^i + y_B^1 y_A^2 y_B^2 \sum_{i=0}^{n_{B:A,B}} {}^i L_{B:A,B} (y_A^2 - y_B^2)^i + \\
&\quad y_A^1 y_B^1 y_A^2 y_B^2 {}^0 L_{A,B:A,B}
\end{aligned} \tag{2.7}$$

Where, G_{AA} , G_{AB} , G_{BA} , G_{BB} are the Gibbs energy of the endmembers AA, AB, BA, and BB, at temperature, Tx, as described by equation 2.4, R is the ideal gas constant, a^1 and a^2 are the site fractions of sublattices 1 and 2, y_A^1 , y_B^1 , y_A^2 and y_B^2 are the constituent fractions of elements A and B on sublattices 1 and 2, and the ${}^i L_{...}$ values are the i th interaction parameters, which combine with the Redlich Kister polynomials to describe the Gibbs energy contribution resulting from any interactions between the atoms on each sublattice. In addition, the model notation uses a colon to separate the different sublattices, and a comma to separate the components on a specific sublattice. [5], [88], [90]

In the case of magnetic phases, the magnetic contribution to the Gibbs energy, $G_{Mag}^\varphi(T_C, \beta_0, T, x)$, first referred to in equation 2.2, must be added to the contributions of the temperature and composition, $G_T^\varphi(T, x)$, described in equations 2.2 to 2.4, yielding the following model:

$$G^\varphi = G_T^\varphi(T, x) + G_{Mag}^\varphi(T_C, \beta_0, T, x) = G^0 + G^{ideal} + G^{xs} + G_{Mag}^\varphi \quad (2.8)$$

with:

$$G_{Mag}^\varphi = RT \ln(\beta_0^\varphi + 1) \cdot f(\tau^\varphi) \quad (2.9)$$

Where, β_0^φ is the average Bohr magneton number per atom in the phase, $f(\tau^\varphi)$ is the integral of a function fitted to the magnetic contribution to the heat capacity, and

$$\tau^\varphi = \frac{T}{T_C^\varphi} \quad (2.10)$$

With T_C^φ , being the Curie temperature of the phase. [5], [88], [90]

Both β_0^φ and T_C^φ are composition dependant and can be described in a similar manner to that of a standard non-magnetic excess energy:

$$\beta_0^\varphi = x_A \beta_{0A} + x_A x_B \sum_{i=0}^n {}^i \beta_{0A,B} (x_A - x_B)^i \quad (2.11)$$

and

$$T_C^\varphi = x_A T_{CA} + x_A x_B \sum_{i=0}^n {}^i T_{CA,B} (x_A - x_B)^i \quad (2.12)$$

Where A is the magnetic element, and B is non-magnetic, β_{0A} and T_{CA} are the Bohr magnetic moment, and Curie temperature for element A, and $\beta_{0A,B}$ and ${}^i T_{CA,B}$ are parameters describing

the interaction between A and B atoms. It should be noted that if element B is also magnetic then an extra term, which is similar to the first term in both equations for element A, should also be added to these equations for element B. The integral function $f(\tau^\varphi)$ in equation 2.9, can be described by the following polynomial expressions that were derived by Hillert and Jarl [95]:

$$\begin{aligned}
 & \text{for } \tau < 1 & f(\tau^\varphi) \\
 & = 1 - \frac{1}{D} \left[\frac{79\tau^{-1}}{140p} + \frac{474}{497} \left(\frac{1}{p} - 1 \right) \left(\frac{\tau^3}{6} + \frac{\tau^9}{135} + \frac{\tau^{15}}{600} \right) \right] & (2.13)
 \end{aligned}$$

$$\begin{aligned}
 & \text{for } \tau \geq 1 & f(\tau^\varphi) \\
 & = -\frac{1}{D} \left(\frac{\tau^{-5}}{10} + \frac{\tau^{-15}}{315} + \frac{\tau^{-25}}{1500} \right) & (2.14)
 \end{aligned}$$

where:

$$D = \frac{518}{1125} + \frac{11692}{15975} \left(\frac{1}{p} - 1 \right) \quad (2.15)$$

and $p = 0.4$ for BCC structures, and 0.28 for FCC, and HCP structures.

Other models may also be used to describe different types of ordering and different physical phenomena, depending on the situation, however, the models given by equations 2.1 to 2.15 are the standard models commonly used for the CALPHAD assessments of metallic systems. Further information about these models can be found in the works of Saunders and Miowdownnik [90], and Lucas et al [5].

2.5.3: From Gibbs Energy to Phase Diagrams

Gibbs energy, G , is a measure of the maximum available work that can be extracted from any system under conditions of constant temperature, T , and pressure, P . Changes in Gibbs energy, ΔG , as the system goes from one state to another are highly informative, since we know that if $\Delta G (= G_{\text{final state}} - G_{\text{initial state}})$ is negative, then the observed change liberates energy and will occur spontaneously.

By using the CALPHAD models described in Section 2.5.2 to calculate the Gibbs energies for all of the phases in a system as a function of temperature and composition, Gibbs energy curves for these phases can be produced, from which the most stable phases at each temperature and composition can be identified. Essentially, the phases with the lowest, or most negative Gibbs energy, at each temperature and composition, will be the ones that are the most thermodynamically stable under those conditions. Therefore, these Gibbs energy curves can be used to create a phase diagram for the system of interest. Figure 2.18, below, shows the relationship between the Gibbs energy curves for the phases, and the resulting phase diagrams for two hypothetical binary systems.[14]

At temperatures, T_1 and T_2 in Figure 2.18(i)(a&b) the liquid phase has the lowest Gibbs energy at all compositions across the range from element A to element B. Consequently, at these temperatures and compositions the liquid phase is the most stable, which is reflected in the phase diagram in Figure 2.18(i)(f). However, at temperature, T_2 in Figure 2.18(i)(b) the Gibbs energy for the liquid and α phase are equal at a composition of 100% A, therefore this must be the position of the liquid and α phase boundary at this temperature and composition, which again is marked on the phase diagram in Figure 2.18(i)(f).

At temperature, T_3 in Figure 2.18(i)(c) the Gibbs energy for the α phase is lower at compositions closer to element A, and the Gibbs energy for the liquid phase is lower for compositions closer to element B. Thus in the phase diagram in Figure 2.18(i)(f), each of these phases is stable in the region where it has the lowest Gibbs energy. The positions of the boundaries between the α phase, the α + liquid two phase region, and the liquid phase, are determined by the positions at which the cotangent between the Gibbs energy curves for the two phases intersects the curve for each respective phase. I.e. the position of the α phase boundary occurs at the position where the cotangent between the Gibbs energy curves for both phases intersects the Gibbs energy curve for the α phase, and the position of the liquid phase boundary occurs at the position where the cotangent between the Gibbs energy curves for both phases intersects the Gibbs energy curve for the liquid phase. These boundaries are marked on the phase diagram in Figure 2.18(i)(f).

At temperatures, T_4 and T_5 in Figure 2.18(i)(d&e) the α phase has the lowest Gibbs energy at all compositions across the range from element A to element B. And thus, at these temperatures and compositions the α phase is the most stable, which is reflected in the phase diagram in Figure 2.18(i)(f). However, at temperature, T_4 in Figure 2.18(i)(d) the Gibbs energy for the liquid and α phase are equal at a composition of 100% B, and therefore this must be the position of the liquid and α phase boundary at this temperature and composition.

This is how the phase diagram for the system, shown in Figure 2.18(i)(f), can be constructed from the Gibbs energy curves for its phases as a function of temperature and composition, shown in Figures 2.18(i)(a&e). Figure 2.18(ii) also shows how a slightly more complex binary eutectic phase diagram can also be constructed from the Gibbs energy curves of its constituent phases as a function of temperature and pressure, using the same principles as described for Figure 2.18(i).

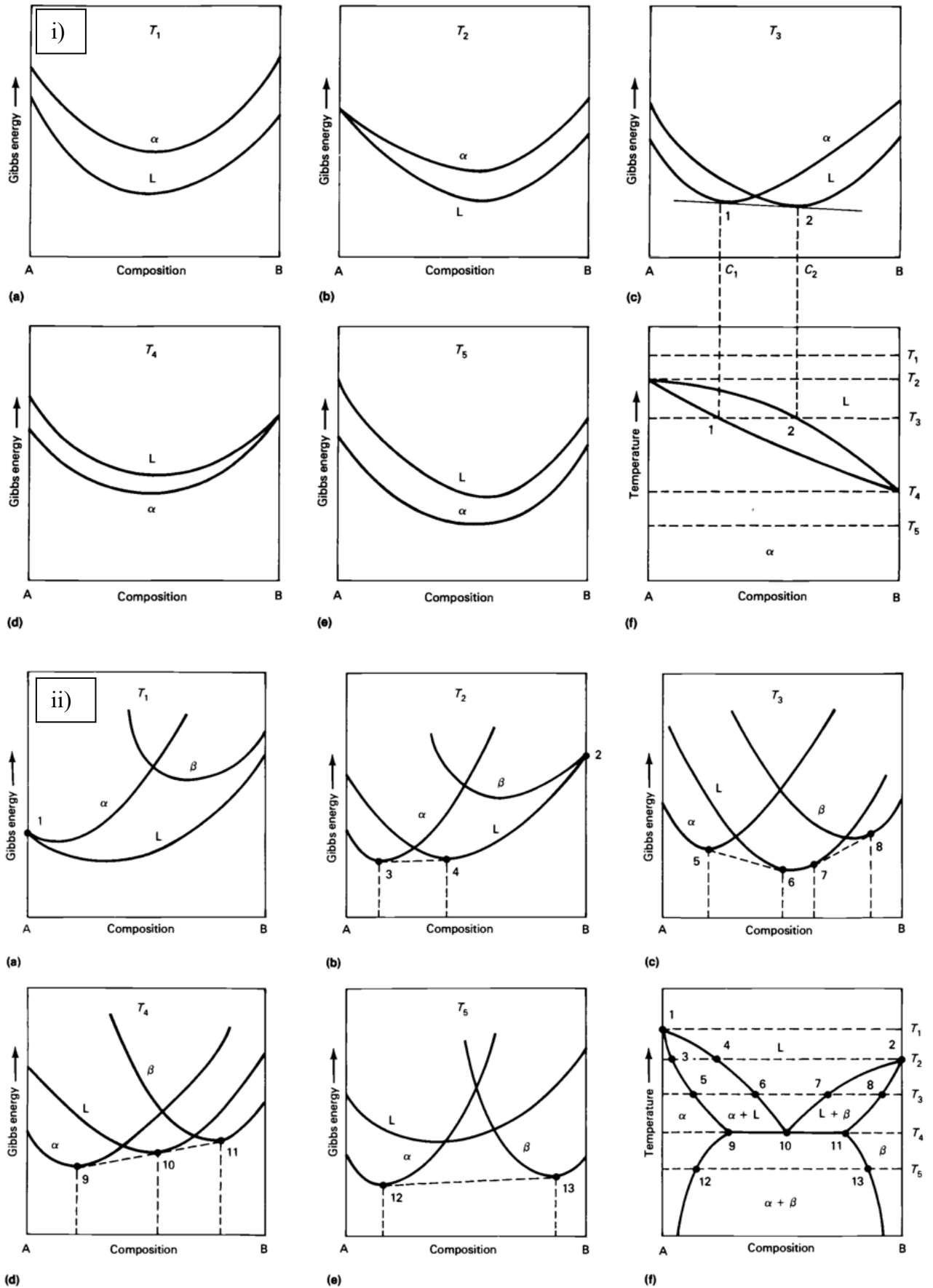


Figure 2.18: i) Use of Gibbs energy curves to construct a binary phase diagram that shows miscibility in both the liquid and solid states. And ii) Use of Gibbs energy curves to construct a binary eutectic phase diagram.[14]

Chapter 3: Experimental Determination of Phase Equilibria in the Ta-Al-Co system

3.1: Introduction

The Ta-Al-Co ternary has been identified as a system that merits further study to assess its potential as a base system for a refractory metal, BCC_A2-Ordered intermetallic, precipitate strengthened alloy. This would require the presence of a two phase field between the BCC_A2 Ta phase and an ordered ternary intermetallic that is crystallographically coherent with it, such as a B2, D0₃ or L2₁ phase. As discussed previously in Section 2.4, the Ta-Al-Co system is relatively unexplored at present. Its binary sub-systems have been investigated in some detail, [30], [34], [76], [96], [97], [40], [48]–[50], [53], [67], [68], [72] but the only ternary experimental data currently available appears to be the very limited partial isothermal section at 1000°C shown in Figure 3.1(a).[77] This was produced by Hunt and Raman,[77] who reported that a ternary intermetallic phase of undetermined crystal structure was present just above the Mu_D8₅ phase at a composition of around 55At%Ta/Nb-22.5At%Al-22.5At%Co, and a temperature of 1000°C in both the Ta-Al-Co and Nb-Al-Co systems. They named this phase Mu prime. Their findings raise the possibility that there may indeed be a two phase field between the BCC_A2 Ta phase and a ternary intermetallic compound in the Ta-Al-Co system. Conversely, a more recent study of the Nb-Al-Co system by Dovbenko et al.[75] did not find any evidence for the presence of the ternary Mu prime phase. However, they did find a ternary, ordered L2₁, Co₂AlNb phase at a composition of around 21At%Nb-28At%Al-51At%Co that is stable in the temperature range of 800°C to 1250+°C. At present it is unclear if the required two phase field is present in the Ta-Al-Co ternary, therefore further investigation would be required to clarify this point.

Since there is so little ternary experimental data available on the Ta-Al-Co system, a detailed investigation into its phase equilibria, followed by the production a ternary phase diagram would be a big step forward in our knowledge of this system. There are a number of reasons why such an investigation would be worthwhile. Firstly, it would enable us to evaluate the potential of this ternary as a possible base system for a practical high temperature alloy. Secondly, the Ta-Al-Co system is an important ternary subsystem for current multicomponent Ni and Co based superalloys, so improving our understanding of this ternary would also be beneficial to research into these alloys. And thirdly, it would advance our fundamental knowledge of a previously poorly understood alloy system. Therefore the aim of this chapter of the current work is to carry out an experimental investigation in to the phase equilibria of the Ta-Al-Co system, and produce complete ternary isothermal sections for the system at temperatures of 1000°C and 1150°C.

Due to the lack of ternary experimental data on the Ta-Al-Co system, a good starting point is to combine the limited data that is available from Hunt and Raman,[77] with all of the data on the three binary subsystems, and any other potential alternative sources of information in order to build the best possible base upon which to build a further investigation. Such alternative sources include thermodynamic models for the Ta-Al-Co system from the Ni superalloy databases; TTNI8,[98] and TCNI8,[99] and also experimental data on other similar ternary systems, such as the Nb-Al-Co system.

In terms of thermodynamic models; the Ni superalloy databases; TTNI8,[98] and TCNI8,[99] do both contain descriptions for the Ta-Al-Co ternary. However, given that so little experimental data is available on this system, it is unclear what data these assessments are based on. Figure 3.1(b) shows that the TTNI8 database does not have an accurate assessment for the Ta-Al-Co ternary. Conversely, the ternary isothermal section calculated

for this system from the TCNI8 database shown in Figure 3.1(c) appears to match up fairly well with the experimental diagram of Hunt and Raman,[77] shown in Figure 3.1(a), and also with the binary subsystem data from the literature,[54], [76], [96] with the exception of a couple of phases. [54] The TCNI8 database does not contain the ternary Mu prime phase, and it is also missing the $\text{Phi_Al}_{38}\text{Ta}_{48}$ phase which is stable at approximately 50-55at% Ta in the Al-Ta system. This database does list the Ta-Al-Co system as one of its assessed ternaries, but given the lack of available experimental data currently available on the ternary space of this system, it is likely that there are some gaps in the data that this assessment was based on.

Looking at the available experimental data on systems that are similar to the Ta-Al-Co ternary, it appears the most similar system is the Nb-Al-Co ternary. Fortunately, Dovbenko et al.[75] have recently performed a detailed experimental determination of this system.[75] A comparison of Figure 3.1(d); Dovbenko et al.'s[75] ternary isothermal section for the Nb-Al-Co system at 1000°C to Figure 3.1(a); Hunt and Raman's[77] partial isothermal section for the Ta-Al-Co system at the same temperature, clearly shows that there are considerable similarities between these two ternary systems. This is not unsurprising since they both contain the Al-Co binary, and out of the two remaining subsystems that differ, there are considerable similarities between the Al-Nb and Al-Ta binaries, and also between the Co-Nb, and Co-Ta binaries. Since there are numerous similarities between the constituent binary subsystems of these ternaries, in terms of the phases present, and also the positions and composition boundaries of these phases, it is reasonable to expect that there would also be considerable similarities between the two ternary systems as well.

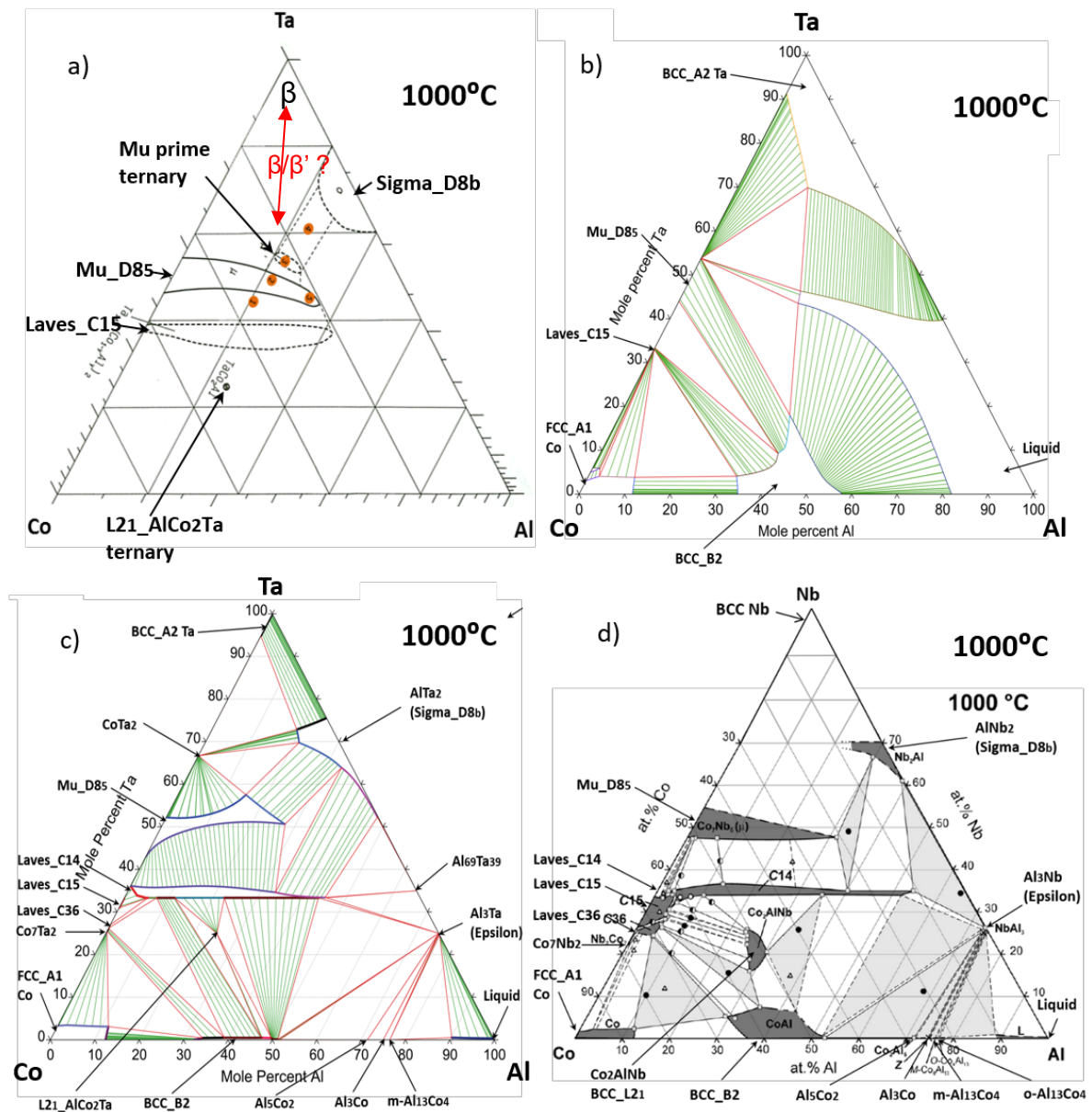


Figure 3.1: A comparison of Hunt and Raman’s partial isothermal section for the Ta-Al-Co system at 1000°C (a),[77] with the temperature matched ternary isothermal sections for the Ta-Al-Co system calculated using TTNi8 (b),[98] and TCNi8 (c) [99] databases, and Dovbenko et al.’s experimentally determined isothermal section for the Nb-Al-Co system (d).[75] Phase boundary compositions for the binary phases from the most recent binary descriptions of the Al-Co,[96] Al-Ta, [97] and Co-Ta [100] binaries are marked along the binary edges the calculated diagrams in (b) and (c) to compare how well the TTNi8 and TCNi8 databases match the most recent data on the binary subsystems of the Ta-Al-Co system

However, despite the many similarities that these ternary systems share, there are also a number of important differences between them too. Most notably that since Ta has a much higher melting point (3017°C) compared to Nb (2477°C) many of the Ta containing phases also have much higher melting points than their respective Nb containing equivalents. In addition, the Ta-Al-Co system also contains a number of phases that are not present in the Nb-Al-Co system. These are: $\text{CoTa}_2\text{C}_{16}$, which is stable at around 66at% Ta in the Co-Ta system,[76] and $\text{Al}_{69}\text{Ta}_{39}$, Al_7Ta_5 , and $\text{Phi_Al}_{38}\text{Ta}_{48}$, which are stable at approximately 36-38at% Ta, 42at% Ta, and 50-55at% Ta respectively in the Al-Ta system.[48]–[50] In addition, as previously mentioned Hunt and Raman[77] reported that a ternary phase that they named Mu prime was present at around 22.5At%Al-22.5At%Co-55At%Ta/Nb and 1000°C in both the Ta-Al-Co and Nb-Co-Al systems. However, Dovbenko et al.[75] did not find any evidence for the existence of the Mu prime phase, despite investigating the same region of the Nb-Co-Al phase diagram.

Regardless of these differences, the many similarities that these two ternary systems share means that the Nb-Al-Co phase diagram can be used as a reasonable initial starting point, and rough guide to inform an experimental investigation into the Ta-Al-Co system. And given the lack of ternary experimental data on the Ta-Al-Co system, and the differences between it and the Nb-Al-Co system, it is clear that such an investigation will be necessary in order to produce an accurate phase diagram for the Ta-Al-Co ternary.

3.2: Methods for Experimental Determination of Phase Equilibria in the Ta-Al-Co system

3.2.1: Introduction

The equilibrated alloy method[101] was chosen as the method of choice for the determination of the Ta-Al-Co phase diagram. This method consists of producing a number of different alloys with compositions at specific points of interest on the phase diagram. Then annealing these alloys for times and temperatures chosen for the purposes of enabling the alloys to get as close as practically possible to their equilibrium state. This is followed by rapidly quenching them back to room temperature to ‘lock in’ the equilibrium state. The alloys can then be analysed by techniques such as scanning electron microscopy (SEM), energy dispersive X-ray spectroscopy (EDX) and X-ray diffraction (XRD) in order to identify the phases present, and their compositional boundaries at the specified equilibrium temperatures. If the compositions of the different alloys chosen lie in all of the unique multiple phase fields across the compositional space of the system at the selected temperature, it should then be possible to produce a complete compositional map of the isothermal section for the alloy system at this temperature.

Due to the lack of experimental data on the Ta-Al-Co system, and it’s high degree of similarity with the Nb-Al-Co system, combined information from Hunt and Raman’s Ta-Al-Co,[77] and Dovbenko et al.’s Nb-Al-Co[75] phase diagrams were used as a guide to aid in selecting the best alloy compositions to investigate in order to map the mostly unknown Ta-Al-Co ternary. A list of the final 30 Ta-Al-Co alloy samples produced is given in Figure 3.2, and the compositions of these samples are plotted in ternary space on top of Dovbenko et al.’s Nb-Al-Co ternary isothermal section at 1000°C[75] In order to maximise

the information that could be gained from each sample, alloy compositions that were likely to be in key regions of the phase diagram, such as two and three phase regions were selected for production.

Alloy Sample Numbers and Bulk Compositions

(Numbers start in the Ta/Nb corner, moving to the Al, and then Co corners. Compositions are in At%, rounded to the nearest whole number).

◆ 1) 00Al - 10Co - 90Ta	◆ 11) 27Al - 19Co - 54Ta	◆ 21) 36Al - 46Co - 18Ta
◆ 2) 04Al - 07Co - 89Ta	◆ 12) 33Al - 12Co - 55Ta	◆ 22) 37Al - 51Co - 13Ta
◆ 3) 03Al - 24Co - 73Ta	◆ 13) 39Al - 10Co - 51Ta	◆ 23) 34Al - 51Co - 16Ta
◆ 4) 07Al - 15Co - 77Ta	◆ 14) 25Al - 28Co - 46Ta	◆ 24) 31Al - 56Co - 14Ta
◆ 5) 13Al - 21Co - 65Ta	◆ 15) 38Al - 25Co - 38Ta	◆ 25) 20Al - 63Co - 17Ta
◆ 6) 16Al - 23Co - 61Ta	◆ 16) 46Al - 13Co - 40Ta	◆ 26) 21Al - 63Co - 17Ta
◆ 7) 18Al - 14Co - 69Ta	◆ 17) 51Al - 05Co - 44Ta	◆ 27) 19Al - 67Co - 14Ta
◆ 8) 23Al - 13Co - 64Ta	◆ 18) 63Al - 04Co - 33Ta	◆ 28) 20Al - 70Co - 09Ta
◆ 9) 11Al - 33Co - 56Ta	◆ 19) 59Al - 11Co - 30Ta	◆ 29) 10Al - 79Co - 11Ta
◆ 10) 17Al - 29Co - 54Ta	◆ 20) 66Al - 30Co - 04Ta	◆ 30) 09Al - 79Co - 12Ta

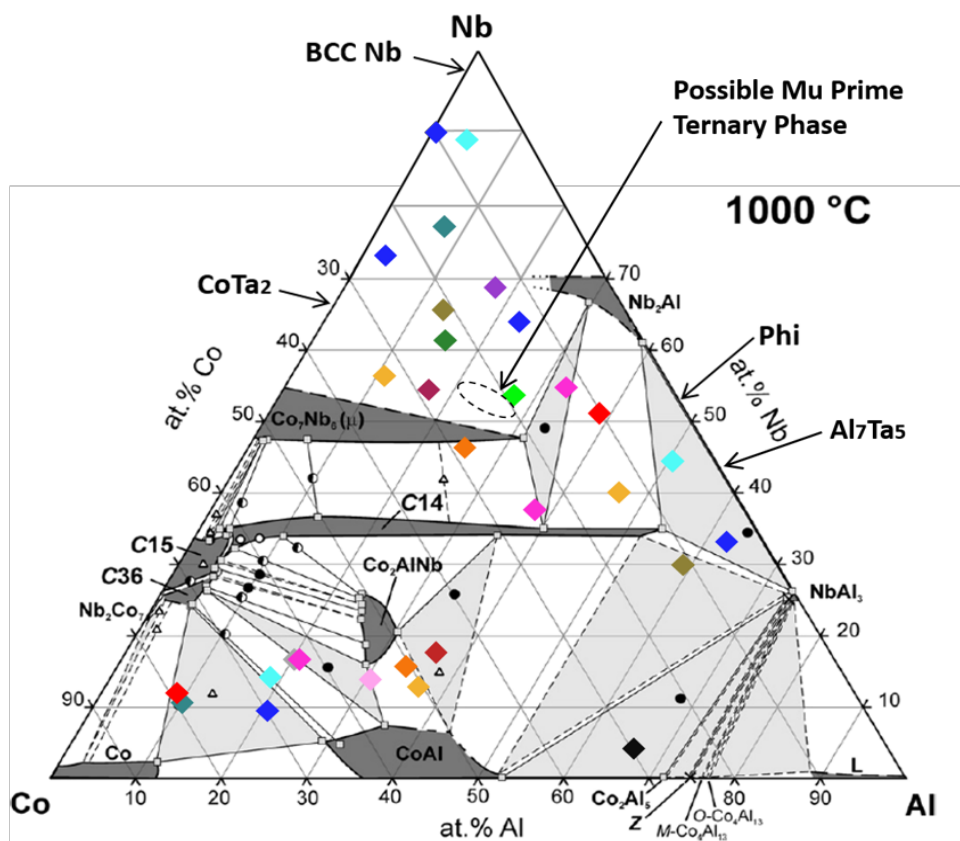


Figure 3.2: A list of the final 30 Ta-Al-Co alloy samples produced. In addition the compositions of these alloy samples are plotted in ternary space on top of Dovbenko et al.'s Nb-Al-Co isothermal section at 1000°C.[75] Extra phases that are present in the Ta-Al-Co system have been added from Hunt and Raman,[77] and also other studies on the on the Al-Ta,[48]–[50], [97] and Co-Ta binaries.[68], [72], [76], [100]

3.2.2: Ta-Al-Co Alloy Sample Production

Alloy compositions of interest in atomic percent were converted to weight percent, to enable the appropriate quantities of each of the required elements to be weighed out. This was performed on a microbalance that is accurate to 1mg. The sum total of the weighed component elements was 40g per alloy for the first batch of alloys, and 20g per alloy for all subsequent batches. To achieve the required masses, small pieces of elemental stock in shot or pellet form were used. In order to produce high quality alloys without impurities, the following grades of elemental stock were used; Ta of 99.9% purity, Al of 99.999% purity and Co of 99.99% purity.

Alloys were produced via electrical arc melting on a water cooled copper hearth under an Ar atmosphere using an Edmund Buhler arc melting furnace. In order to ensure the compositional homogeneity of each sample, the ingots were tipped upside-down and re-melted at least four times. A total of 30 alloys were produced, with average ingot dimensions of approximately 30x30x7mm for the first batch of 9 alloys, and 15x10x7mm for the following three batches that produced a further 21 alloys. Typical examples of the alloy ingots produced are shown below in Figure 3.3.

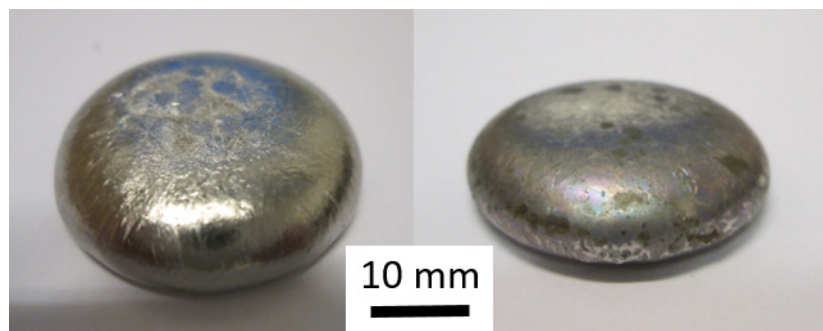


Figure 3.3: Typical examples of the arc melted Ta-Al-Co alloy ingots.

The first batch of arc melted alloys had aluminium compositions that were approximately 15-20at% below their initial target compositions. This was due to a certain amount of Al boiling off of the melt pool before it could mix with the other elements, since Ta has a melting point of 3017°C and Al has a boiling point of 2470°C. As a result, it was necessary to develop correction factors to compensate for this Al loss in the following production batches. These Al correction factors were based on the differences between the initial alloy target compositions and their actual measured compositions, and were generally in the +15wt%Al to +20wt%Al range. The amount of Al lost depends on the melt pool temperature and the heating time, so it is important to try to use consistent heating times for all alloys in order to produce alloys that closely match their target compositions.

Post production, each alloy ingot was sectioned into three roughly equally sized samples using a Struers Accutom-5 slow speed circular saw with a SiC blade, so that each of the 30 unique alloys could then be investigated in three different temperature conditions. The conditions chosen were:

- 1) The as cast condition
- 2) Equilibrated at 1000°C then water quenched
- 3) Equilibrated at 1150°C then water quenched

3.2.3: Ta-Al-Co Alloy Heat Treatments

The first step in planning appropriate heat treatments was to decide the temperatures to equilibrate the alloys at. The second was to select suitable annealing times to enable the alloys to get as close as practically possible to their equilibrium state. Temperatures of 1000°C, and 1150°C were chosen, in order to produce ternary isothermal sections that would be directly comparable with literature data on other similar systems, particularly those of Hunt and Raman,[77] and Dovbenko et al.[75] In addition, Dovbenko et al.[75] noted that they initially experienced issues with oxidation and the formation of impurity stabilised phases when heat treating Nb-Al-Co alloys at temperatures at 1200°C and above. Therefore a decision was made to stick to temperatures under 1200°C. The annealing times were selected as 1000 hours for the 1000°C heat treatment, and 500 hours for the 1150°C treatment, based on literature data from studies carried out on alloys containing similar elements.[75], [101], [102] In preparation for the planned heat treatments all samples were ultrasonically cleaned in ethanol, and air dried. They were then wrapped in Ta foil to protect them from oxidation, and prevent them from reacting with the walls of the quartz ampoule container vessels at the treatment temperatures. The wrapped samples were divided into groups of 4-6 specimens, which were then double encapsulated inside quartz ampoules that were first purged of air, then backfilled with argon, before finally being sealed to ensure that the heat treatments would be carried out in an argon atmosphere. The ampoules were made from 99.9% purity quartz tubes, and the double encapsulation was carried out as insurance to ensure that the argon atmosphere would still be maintained around the samples, even if one of the ampoules was to fail during the heat treatment. Figure 3.4 shows an example of a group of samples after double encapsulation inside two argon filled quartz ampoules.

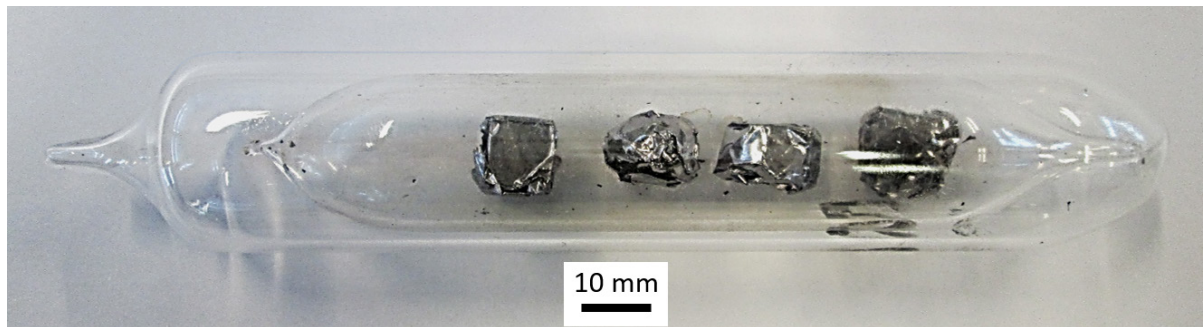


Figure 3.4: A group of samples double encapsulated inside two argon filled quartz ampoules.

For the samples to be heat treated at 1150°C, a 1cm³ piece of Ti sponge wrapped in Ta foil was added to each ampoule along with the alloy samples, to act as a getter for any residual O₂ molecules. Care was taken to ensure that there was a reasonable spacing between the each of the samples, and also between the samples and the Ti sponge to prevent any inter sample or sample/Ti sponge diffusion from occurring.

For the heat treatments themselves, the quartz ampoules containing the alloy samples were then placed at the centre of an Elite TSH12/100/940 horizontal tube furnace for isothermal holds of either a) 1000 hours at 1000°C or b) 500 hours at 1150°C. After each of the specified heat treatments the furnace was opened, and the ampoules were immediately dunked into a large steel bucket of cold water, and broken open so that the samples would be rapidly quenched to below room temperature. Samples were then dried and sorted for analysis.

3.2.4: Ta-Al-Co Alloy Sample Analysis

In preparation for SEM analysis, slices of approximately 5mm in width were cut from all alloy samples using a Struers Accutom-5 slow speed circular saw with a SiC blade. These sample slices were then mounted in conductive bakelite, and ground and polished to a surface finish of 0.25 μ m. Samples were then analysed using Jeol 6060 and Jeol 7000 SEM's, with Oxford INCA 300 EDX systems.

For EDX analysis an accelerating voltage of 20 KV was used, with a spot size setting of between 64-68, as the best possible compromise between limiting the interaction volume to the smallest possible size, whilst still generating sufficient X-rays from the elements of interest, and also minimising the effects of any sample charging. For bulk alloy composition measurements, EDX area scans were carried out on 5 different 962x725 μ m areas of the sample at 130x magnification. The mean of these 5 measurements was then taken as the bulk alloy composition for the sample. For phase composition measurements, 5-10 EDX point analysis measurements were carried out on specific phases at a magnification of 5000X, at a number of different areas of the sample. Again, the mean of these measurements was then taken as the composition for that phase.

The sampling volume for each of these EDX point analysis measurements was dependent upon the electron beam/sample interaction volume. And the dimensions of this sampling volume for the phases analysed during this work were calculated using approximations based on Castaing's[103] model for X-ray generation depth during SEM EDX, as described on page 231 in Appendix A1.1. These approximation models yielded EDX point analysis sampling dimensions ranging between 0.71 μ m in depth, and 0.54 μ m in width, for the densest element analysed, Ta, to 4.36 μ m in depth, and 3.36 μ m in width, for the least

dense element analysed, Al. Calculations of approximate EDX point analysis sampling dimensions as a function of density for the various Ta-Al-Co phases analysed in the present work were also performed using the same models, and are listed in Table A1.1 on page 228, in Appendix A1.1.

In order to measure tie lines and tie triangles, and therefore phase composition boundaries, these EDX point analysis measurements were carried out in pairs or triplets at points on each phase that were as close as possible to the interface between adjoining phases. Measurements were taken at these interfaces because this is where the phases should be in local equilibrium with each other. Care was taken to ensure that these point analysis measurements were carried out at the edges of individual phases, but also that they avoided sampling any of the adjoining phase in the same measurement. This is because measurements of phases too far away from their edges would yield composition results for positions further inside the phases rather than at their boundaries. And measurements that sampled adjoining phases would yield results for positions on the other side of the single phase boundary, in either two or three phase regions.

Initially there were a few problems with sample charging and scan drift during high magnification SEM/EDX on some of the heat treated intermetallic samples. This was thought to be due to a combination of oxide at the sample edges reducing sample conductivity, and some intermetallic compounds in certain samples just not being sufficiently conductive. These issues were managed by the application of conductive silver dag paint to sample edges, and around the surfaces of the bakelite mount, which significantly reduced the charging and scan drift. There were no significant problems for the lower magnification, larger area EDX scans that were used to measure bulk alloy compositions. However, for the smaller area EDX point analysis, phase composition measurements at magnifications of 5000X, a reduction of the

EDX scan time from 120 seconds to 60 seconds was still required with some samples in order to ensure scan completion before any scan drift occurred. This reduced the number of X-ray counts from an average of around 20,000 to an average of around 10,000 for these intermetallic samples. Therefore, an accuracy test was carried out where the compositional measurements from five scans on a sample with 20,000 counts were compared to those of 5 scans with 10,000 counts. There appeared to be no significant differences between the results of the scans at the two different scan times. So the 60 second scan time was judged to be the best compromise between maximising the number of EDX counts, and maximising the EDX scan resolution by ensuring that the scan was completed before any significant scan drift occurred.

EDX spectra were collected in the range of 0-10 KeV for all scans, and the processing options selected for the quantification were to quantify all selected elements, and to normalise the quantitative results. The quantification was non-standardised, in that it compared the measured EDX spectra to the Oxford INCA Energy software's default virtual standards[104] for X-ray emission lines in order to identify and quantify the various X-ray emission peaks in the spectra. The process followed for the acquisition and quantification of all EDX scans performed in this work is described in more detail on page 235 in Appendix A1.2.

3.3: Results

3.3.1: Introduction

30 different Ta-Al-Co alloys were investigated via SEM EDX as described in Section 3.2.4. Alloy samples were first investigated and analysed individually, before secondly being grouped together based on the specific phase fields that they appeared to occupy. This grouping was done for two reasons: 1) to allow the comparison of results from all of the samples within the same phase field, and 2) to enable typical representative samples to be chosen from each phase field, in order to avoid redundant detailed discussion of specific individual samples in cases where multiple samples essentially yielded the same results. The next step after this was to plot all of the bulk alloy and phase boundary composition data at each temperature together, and use it to create experimentally determined isothermal sections for the system at temperatures of 1000°C and 1150°C.

3.3.2: Bulk Ta-Al-Co Alloy Compositions

The bulk compositions of the 30 alloy samples in at%, measured via SEM EDX after an isothermal hold for either 1000Hrs at 1000°C, or 500Hrs at 1150°C, both followed by a water quench, are given in Table 3.1. Barring a couple of exceptions, the deviations between measurements made at different locations on the samples were generally less than 2.5%, thus it was concluded that most of the alloys were sufficiently homogenised.

Table 3.1: Bulk compositions in at% for all 30 alloy samples measured by SEM EDX after an isothermal hold for either 1000Hrs at 1000°C, or 500 Hrs at 1150°C, both followed by a water quench. Each composition listed is the average of at least 5 measurements.

Alloy Sample No	Heat Treatment Condition for Measurement	Measured Composition		
		At% Al	At% Co	At% Ta
1	1150°C	0.00 ± 0.00	9.75 ± 1.82	90.25 ± 2.13
2	1000°C &1150°C	4.07 ± 0.09	6.72 ± 1.00	89.21 ± 0.91
3	1000°C	2.67 ± 0.11	24.32 ± 0.04	73.01 ± 0.06
4	1000°C	7.43 ± 0.29	15.39 ± 1.21	77.18 ± 1.40
5	1000°C &1150°C	13.26 ± 0.21	21.31 ± 0.87	65.43 ± 1.09
6	1150°C	15.55 ± 1.28	23.25 ± 1.09	61.20 ± 1.23
7	1000°C &1150°C	17.65 ± 1.13	13.94 ± 1.33	68.41 ± 0.92
8	1150°C	22.87 ± 0.05	13.30 ± 0.73	63.83 ± 0.77
9	1000°C &1150°C	10.85 ± 0.38	32.93 ± 1.83	56.22 ± 1.45
10	1000°C &1150°C	17.10 ± 0.51	28.68 ± 2.11	54.22 ± 1.75
11	1000°C	27.46 ± 0.98	18.99 ± 0.41	53.55 ± 1.39
12	1000°C	33.06 ± 2.85	12.36 ± 1.45	54.59 ± 1.40
13	1000°C &1150°C	38.67 ± 0.68	10.29 ± 2.05	51.05 ± 2.72
14	1000°C	25.33 ± 1.46	28.47 ± 0.82	46.20 ± 0.63
15	1150°C	37.82 ± 0.68	24.61 ± 0.81	37.57 ± 1.01
16	1150°C	46.49 ± 0.60	13.47 ± 1.73	40.03 ± 1.14
17	1000°C	50.69 ± 0.12	4.94 ± 0.29	44.37 ± 0.22
18	1000°C	62.64 ± 0.98	4.27 ± 1.13	33.09 ± 0.78
19	1000°C	59.21 ± 0.54	11.01 ± 0.59	29.77 ± 1.12
20	1000°C	66.16 ± 0.77	29.62 ± 0.10	4.22 ± 0.68
21	1150°C	36.32 ± 1.63	46.07 ± 1.44	17.61 ± 1.17
22	1000°C &1150°C	36.68 ± 2.03	50.61 ± 5.03	12.71 ± 6.59
23	1000°C &1150°C	33.76 ± 5.23	50.56 ± 6.81	15.68 ± 3.96
24	1150°C	30.55 ± 1.13	55.71 ± 0.94	13.74 ± 1.07
25	1000°C &1150°C	20.10 ± 0.17	63.31 ± 0.96	16.59 ± 1.12
26	1000°C &1150°C	20.52 ± 0.50	63.02 ± 0.77	16.46 ± 0.42
27	1000°C &1150°C	18.58 ± 0.71	67.24 ± 0.50	14.19 ± 0.36
28	1000°C	20.49 ± 1.08	70.29 ± 1.65	9.22 ± 0.76
29	1000°C	10.08 ± 1.03	79.40 ± 1.65	10.51 ± 0.61
30	1000°C &1150°C	8.37 ± 1.87	79.03 ± 1.48	12.60 ± 1.78

3.3.3: Ta-Al-Co Alloy Microstructures and Initial Phase Identification

3.3.3.1: Alloy Samples 3 and 1.

Table 3.1 lists the average bulk compositions of samples 3 and 1 as 2.67%Al-24.32%Co-73.01%Ta and 0.00%Al-9.75%Co-90.25%Ta respectively, and Figure 3.5 indicates that they both appear to occupy the same two phase field in the Ta-Al-Co phase diagram. The SEM BSE micrographs in Figure 3.5(a-i) show that both alloys have two phase microstructures consisting of a light phase and a darker phase. Micrographs (a-c) show that the microstructure of sample 3 in the as cast condition consists of a high volume fraction of the darker phase, and a lower volume fraction of dendritic light phase. Micrographs (d-f) indicate that even after an isothermal hold for 1000Hrs at 1000°C, followed by water quench, sample 3 still has a fairly similar microstructure to when it was in the as cast state. Although the light phase dendrites do look slightly finer in terms of their size in the heat treated sample. It appears that the heat treatment started to partially break down the light phase dendrites, but was not sufficient to completely destroy the dendritic structure.

Figure 3.5(g-i) shows that the microstructure of sample 1 after an isothermal hold for 500Hrs at 1150°C, followed by water quench, consists almost entirely of the light phase with only a small volume fraction of dark phase that weaves thin circuitous pathways around larger slabs of light phase. The two phases have boundary compositions of 0.21%Al-3.77%Co-96.02%Ta for the light phase and 4.16%Al-29.75%Co-66.09%Ta for the dark phase in sample 3 after the 1000°C heat treatment. And 0.00%Al-3.78%Co-96.22%Ta for the light phase and 0.00%Al-36.47%Co-63.53%Ta for the dark phase in sample 1 after the 1150°C heat treatment. These phase boundary compositions are marked as tie lines on modified temperature matched isothermal sections of the Nb-Al-Co system[48]–[50], [68],

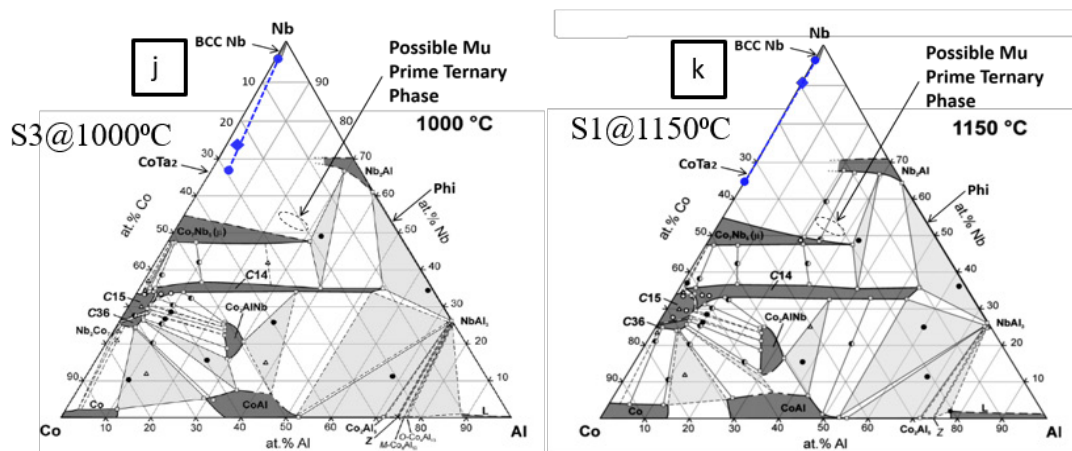
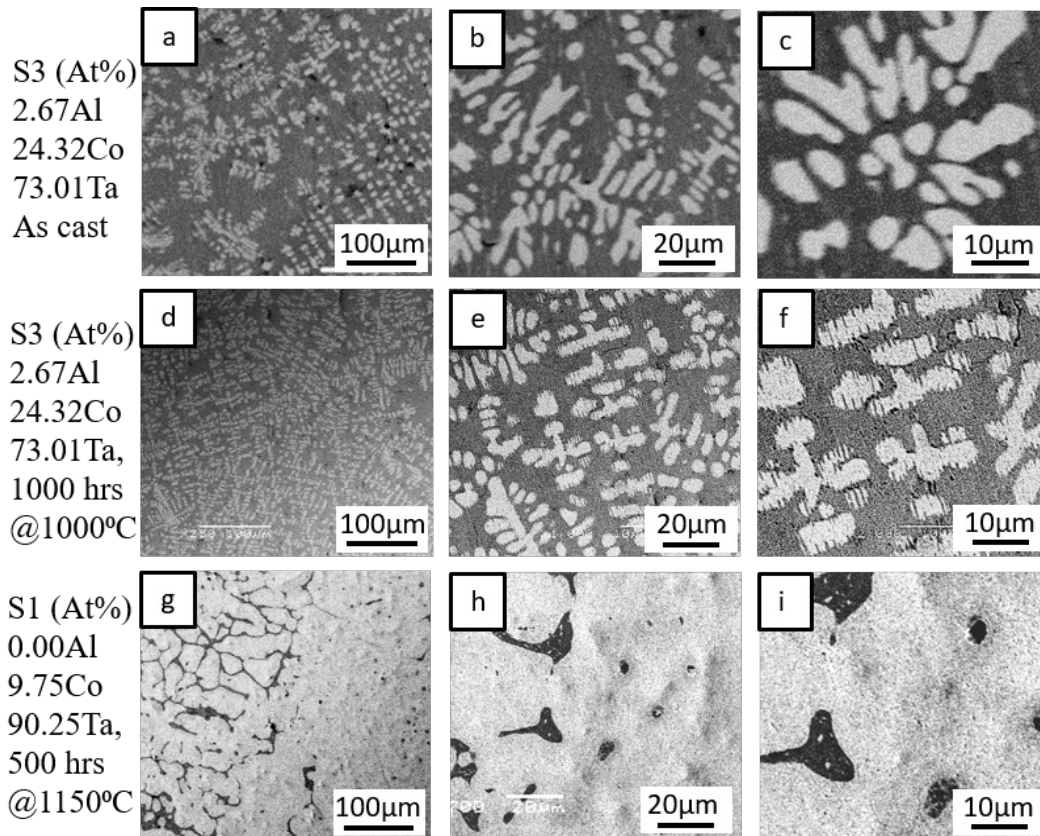
[72], [75]–[77], [97], [100] in Figure 3.5(j&k) to assist with phase identification in the Ta-Al-Co system. The Nb-Al-Co isothermal sections were modified from Dovbenko et al.[75] by using additional labels to mark the positions of any extra phases that are present in the Ta-Al-Co system using data from Hunt and Raman,[77] and also other studies on the on the Al-Ta,[48]–[50], [97] and Co-Ta binaries.[68], [72], [76], [100] Comparing the tie lines for sample 3 at 1000°C, and sample 1 at 1150°C to the modified temperature matched isothermal sections of the Nb-Al-Co system[48]–[50], [68], [72], [75]–[77], [97], [100] shown in Figure 3.5(j&k) we can conclude with a high degree of certainty that the light phase in these samples is BCC_A2 Ta, and the darker phase is CoTa₂_C16.

3.3.3.2: Alloy Sample 2

The average bulk composition of sample 2 is listed in Table 3.1 as 4.07%Al-6.72%Co-89.21%Ta. The SEM BSE micrographs in Figure 3.6(a-i) show that this alloy has a two phase microstructure consisting of a high volume fraction of a light phase and a much lower volume fraction of a darker phase. Micrographs (a-c) show that in the as cast condition alloy sample 2 has a lamellar microstructure with thick laths of the light phase alternating with much thinner laths of the darker phase. Micrographs (d-i) show that after isothermal holds of 1000Hrs at 1000°C, and 500Hrs at 1150°C, both followed by water quenches, the microstructure of alloy sample 2 changes to a coarser structure where many of the lamellae have joined to form a thick irregular network of interconnected light phase with small amounts of the darker phase filling the thin spaces in between.

The boundary compositions of the two phases in sample 2 after the isothermal holds at 1000°C and 1150°C are listed in Figure 3.6(j&k) and are marked as tie lines on the modified temperature matched isothermal sections of the Nb-Al-Co system[48]–[50], [68], [72], [75]–

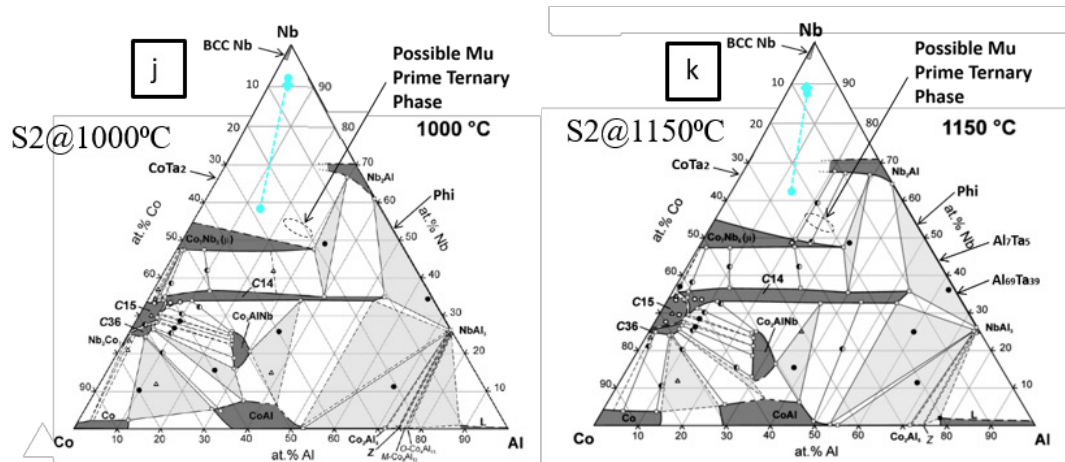
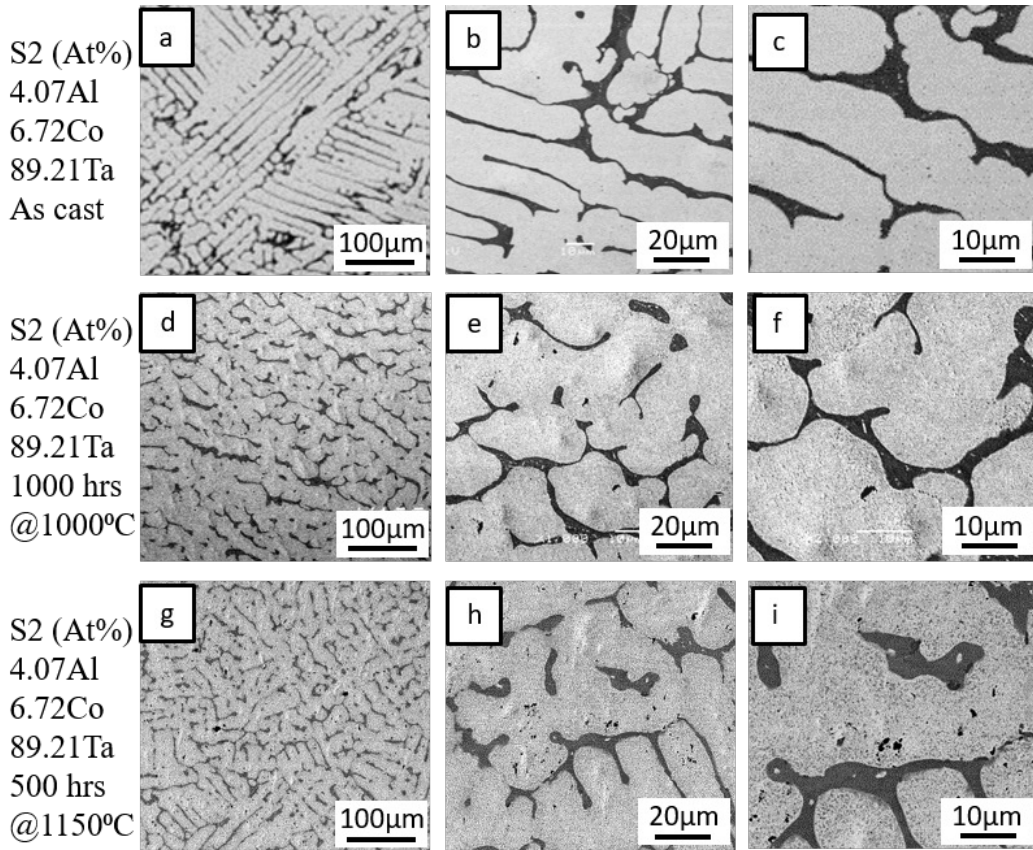
[77], [97], [100] It seems clear that the light phase is highly likely to be BCC_A2 Ta, but the dark phase is not as easy to identify. The two most likely possibilities are that the dark phase could either be the Mu_D8₅ phase or it could also be an unidentified ternary phase. The Mu_D8₅ phase originates at around the 50at%Ta mark in the Co-Ta binary, and is thought to extend out along the 50% Ta composition line to an Al At% of at least 30%.[75], [77] If the ternary solubility of Ta in this phase was slightly higher in the Ta-Al-Co system than it is in the Nb-Al-Co system, such that its boundary was slightly higher in Ta as it extends out towards the Al-Ta binary, then it would be a good match for our dark phase. If not then the dark phase may indeed be a ternary phase. Since further information is required to confirm the identity of this phase, it will be discussed in more detail in Section 3.4, in conjunction with the results from other alloy samples.



Light Phase: 0.21Al -3.77Co -96.02Ta,
BCC_A2 Ta
Grey Phase: 4.16Al -29.75Co -66.09Ta,
CoTa₂_C16

Light Phase: 0.00Al -3.78Co -96.22Ta,
BCC_A2 Ta
Dark Phase: 0.00Al -36.47Co -63.53Ta,
CoTa₂_C16

Figure 3.5: SEM BSE images of alloy sample 3 in the as cast condition (a-c), and after an isothermal hold for 1000Hrs at 1000°C, followed by water quench (d-f), and of alloy sample 1 after an isothermal hold for 500Hrs at 1150°C, followed by water quench (g-i). Bulk alloy, and phase boundary compositions from sample 3 after the 1000°C hold and sample 1 after the 1150°C hold were measured via SEM EDX and used to create tie lines, which were plotted on modified temperature matched isothermal sections of the Nb-Al-Co system[48]–[50], [68], [72], [75]–[77], [97], [100] in images (j) and (k) to assist with phase identification in the Ta-Al-Co system.



Light Phase: 3.46Al -4.64Co -91.90Ta,
BCC_A2 Ta
Grey Phase: 13.90Al -28.16Co -57.94Ta,
Mu D8₅?

Light Phase: 4.61Al -8.20Co -87.19Ta,
BCC_A2 Ta
Grey Phase: 14.03Al -24.62Co -61.35Ta,
Mu D8₅?

Figure 3.6: SEM BSE images of alloy sample 2 in the as cast condition (a-c), after an isothermal hold for 1000Hrs at 1000°C, followed by water quench (d-f), and after an isothermal hold for 500Hrs at 1150°C, followed by water quench, (g-i). Bulk alloy, and phase boundary compositions from sample 2 after the 1000°C and 1150°C isothermal holds were measured via SEM EDX and used to create tie lines, which were plotted on modified temperature matched isothermal sections of the Nb-Al-Co system[48]–[50], [68], [72], [75]–[77], [97], [100] in images (j) and (k) to assist with phase identification in the Ta-Al-Co system.

3.3.3.3: Alloy Samples 4 & 5

Alloy samples 4 and 5 have average bulk compositions of 7.43%Al-15.39%Co-77.18%Ta and 13.26%Al-21.31%Co-65.43%Ta respectively. These samples were identified as both occupying the same phase field, and both alloys exhibit fairly similar microstructures. Sample 5 was chosen as the example representative for its phase field, since the bulk composition of this sample is closer to the phase boundary composition of the dark phase in Sample 2 listed in Figure 3.6(j & k) above. Therefore the dark phase in sample 5 should be the same phase as the dark phase in sample 2, and the results from sample 5 may help to clarify those from sample 2.

Figure 3.7(a-c) shows that in the as cast state alloy sample 5 initially appears to exhibit a two phase microstructure with dendrites of a light phase surrounded by a higher volume fraction of a dark grey phase. However, Figure 3.7(f & i) show that after isothermal holds for 1000Hrs at 1000°C, and 500Hrs at 1150°C, both followed by water quenches, sample 5 actually exhibits a three phase microstructure. This is particularly evident in Figure 3.7(i), where a light phase, a light grey phase, and a dark grey phase are all clearly visible in the microstructure. These three phases are also present in Figure 3.7(f), but it is difficult to distinguish the light phase from the light grey phase due to the image size, and its contrast levels.

The boundary compositions of the three phases in sample 5 after the isothermal holds at 1000°C and 1150°C are listed in Figure 3.7(j & k) and are marked in gold, as tie triangles on the modified temperature matched isothermal sections of the Nb-Al-Co system[48]–[50], [68], [72], [75]–[77], [97], [100] Again it seems clear that the light phase is BCC_A2 Ta, and the light grey phase appears to be Sigma_d8_b in both temperature conditions. Since in the Ta-Al-Co system the Sigma_d8_b phase spans from around 62at% Ta to around 82at% Ta along

the Al-Ta binary border, and then also extends quite significantly into the ternary.[54], [77] This phase has a more limited composition range in the Nb-Al-Co system, due to the presence of the Delta_Nb₃Al phase just above it, at around 77-80at% Nb. Whereas this Delta phase is not present in the Ta-Al-Co ternary, which enables the Sigma_d8_b phase to stretch a lot further up into the Ta corner of this system. In the 1000°C temperature condition, the dark grey phase sits exactly on the Mu_D8₅ phase boundary of Dovbenko et al.'s temperature matched Nb-Al-Co isothermal section. This makes it highly likely that the dark phase in both alloy samples 2 and 5 in the 1000°C temperature condition is actually the Mu_D8₅ phase and not some unknown ternary phase. In the 1150°C condition, the dark phase in sample 5 could either be the Mu_D8₅ phase, or an unknown ternary phase. Although, it may simply be the case that the Mu_D8₅ phase simply has a slightly wider solubility range in the Ta-Al-Co system than in the Nb-Al-Ta system, especially at 1150°C. In that case the dark phase could also be the Mu_D8₅ phase in sample 5 in the 1150°C condition too, however this has not been confirmed as yet.

3.3.3.4: Alloy Samples 6, 7, 8, 9, 10 & 11

Alloy Samples 6, 7, 8, 9, 10 & 11 have all been identified as occupying the same phase field. The reason that so many alloys were produced with compositions in this region is that this is the area of the phase diagram where Hunt and Raman[77] reported the existence of the ternary 'Mu prime' phase in the Ta-Al-Co system. These samples will be discussed in more detail in Section 3.4, however in order to avoid redundantly showing the microstructures of six similar alloys, sample 7 has been chosen as a representative example for this phase field.

Sample 7 has a bulk composition of 17.65%Al-13.94%Co-68.41%Ta, and is situated approximately 14at% Ta directly above the reported position of the Mu prime ternary phase.

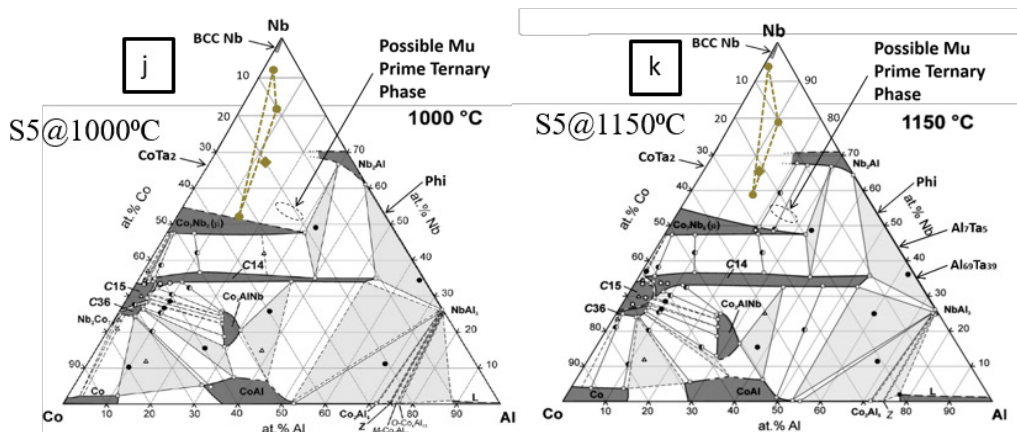
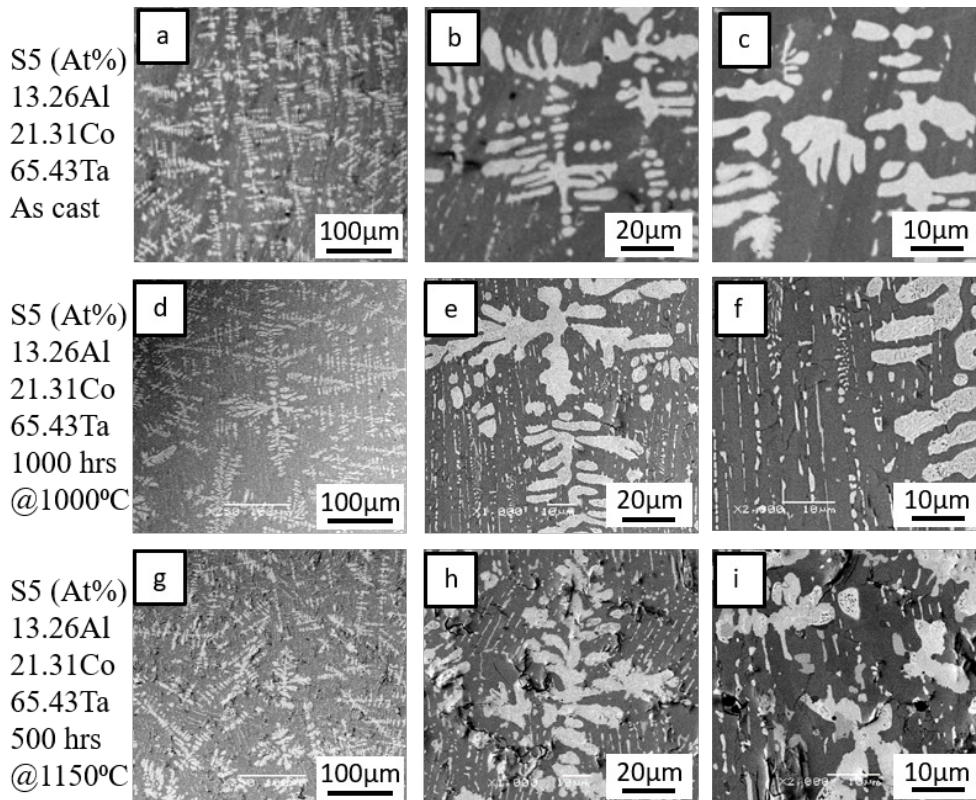
Figure 3.8(a-f) shows that after the isothermal holds at both 1000°C and 1150°C, alloy sample 7 has a two phase microstructure with a high volume fraction of a light phase surrounded by a darker phase. The average bulk alloy, and phase boundary compositions in sample 7 in the 1000°C and 1150°C temperature conditions are listed in Figure 3.8, and are marked as tie lines on the modified temperature matched isothermal sections of the Nb-Al-Co system in images g and h.[48]–[50], [68], [72], [75]–[77], [97], [100] The light phase appears to be Sigma_d8b, although its ternary composition boundary seems to be at a much higher Ta composition in the Ta-Al-Co system than it is in the Nb-Al-Co system. The average dark phase composition boundary is situated directly at the boundary of where the ternary Mu prime phase was reported to be by Hunt and Raman,[77] so it could indeed be this ternary Mu prime phase. However, one other possibility is that the Mu_D85 phase is simply wider in the Ta-Al-Co ternary than the Nb-Al-Co ternary, and that the top of the ternary boundary for this phase is simply slightly higher in terms of its Ta composition. If the dark phase in alloy samples 2 and 5 is indeed the Mu_D85 phase, then it does appear to have a ternary boundary somewhere in the 52-60at% Ta region, so the dark phase in sample 7 could also simply be the Mu_D85 phase, rather than the Mu prime phase.

3.3.3.5: Alloy Sample 13

Alloy sample 13 had slightly different measured average bulk compositions for the two specimens that were heat treated at 1000°C and 1150°C, despite these specimens both being cut from the same ingot. The specimen that was heat treated at 1000°C had an average bulk composition of 38.67%Al-10.29%Co-51.05%Ta, and has a three phase microstructure, as shown in Figure 3.9(a-c). This consists of a mix of partially destroyed light phase dendrites mixed with finer and more uniformly distributed light phase, and a very small amount of light

grey phase, surrounded by a darker phase. Figure 3.9(g) indicates that the light phase is likely to be Sigma_d8_b, which again has its ternary composition boundary at a higher Ta composition in the Ta-Al-Co system than it is in the Nb-Al-Co system. The light grey phase is likely to be Mu_D8₅, as its average composition boundary matches well with that of the same phase in the Nb-Al-Co system.[75] However, it could also possibly be the ternary Mu prime phase. And the dark phase is likely to be Laves_C14, since its composition boundary also matches well with that of the Laves_C14 phase in the Nb-Al-Co system.[75]

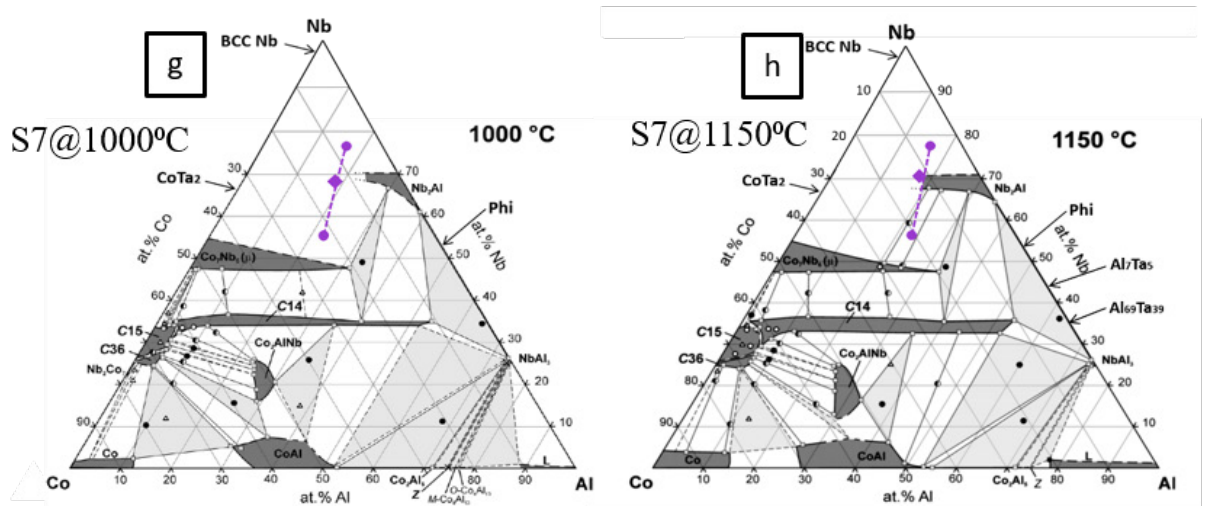
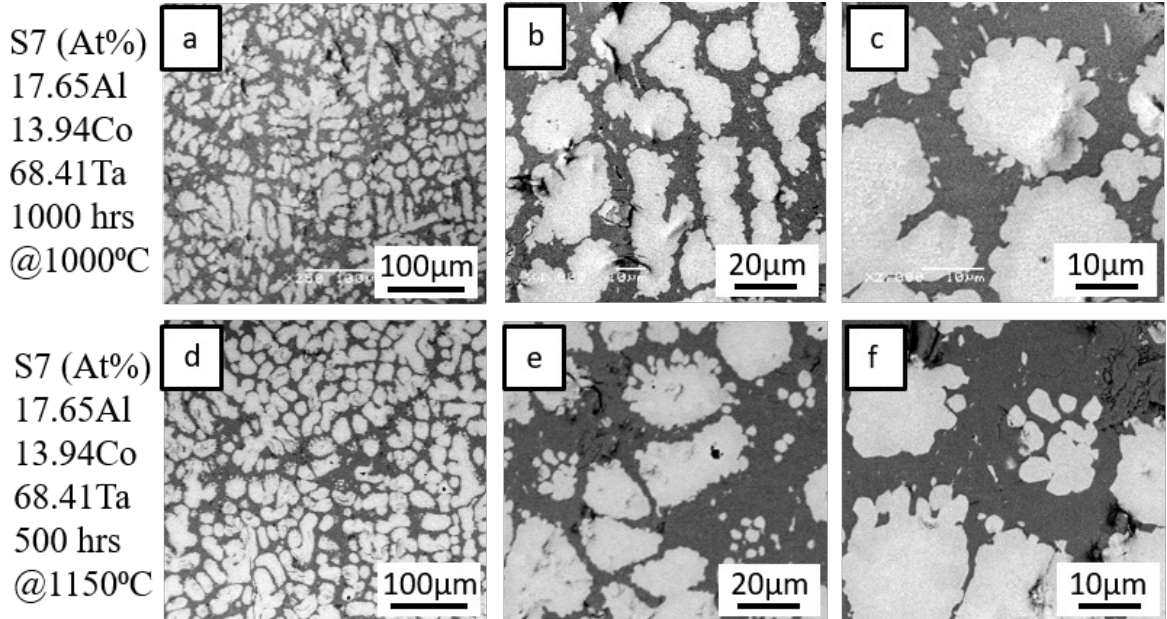
The alloy 13 specimen that was heat treated at 1150°C had an average bulk composition of 37.99%Al-8.24%Co-53.77%Ta, and has a two phase microstructure, as shown in Figure 3.9(d-f). This consists of light phase dendrites, which have started to break down into areas of finer and more uniformly distributed light phase, surrounded by a darker phase. So it appears that the slight shift in average bulk composition combined with a different heat treatment means that this alloy is just outside of the Sigma_d8_b - Mu_D8₅ - Laves_C14 tie triangle, and is instead situated in the Sigma_d8_b - Laves_C14 two phase region, as shown in Figure 3.9(h).



Light Phase: 2.58Al -6.71Co -90.71Ta,
BCC_A2 Ta
Light Grey Phase: 7.30Al -9.92Co -82.78Ta,
Sigma_D8b?
Dark Grey Phase, 14.42Al -33.96Co -51.62Ta,
Mu_D85?

Light Phase: 0.90Al -5.44Co -93.66Ta,
BCC_A2 Ta
Light Grey Phase: 11.12Al -10.88Co -82.78Ta,
Sigma_D8b?
Grey Phase: 15.23Al -26.96Co -57.81Ta,
Mu_D85?

Figure 3.7: SEM BSE images of alloy sample 5 in the as cast condition (a-c), after an isothermal hold for 1000Hrs at 1000°C, followed by water quench (d-f), and after an isothermal hold for 500Hrs at 1150°C, followed by water quench, (g-i). Bulk alloy, and phase boundary compositions from sample 5 after the 1000°C and 1150°C isothermal holds were measured via SEM EDX and used to create tie triangles, which were plotted on modified temperature matched isothermal sections of the Nb-Al-Co system[48]–[50], [68], [72], [75]–[77], [97], [100] in images (j) and (k) to assist with phase identification in the Ta-Al-Co system.



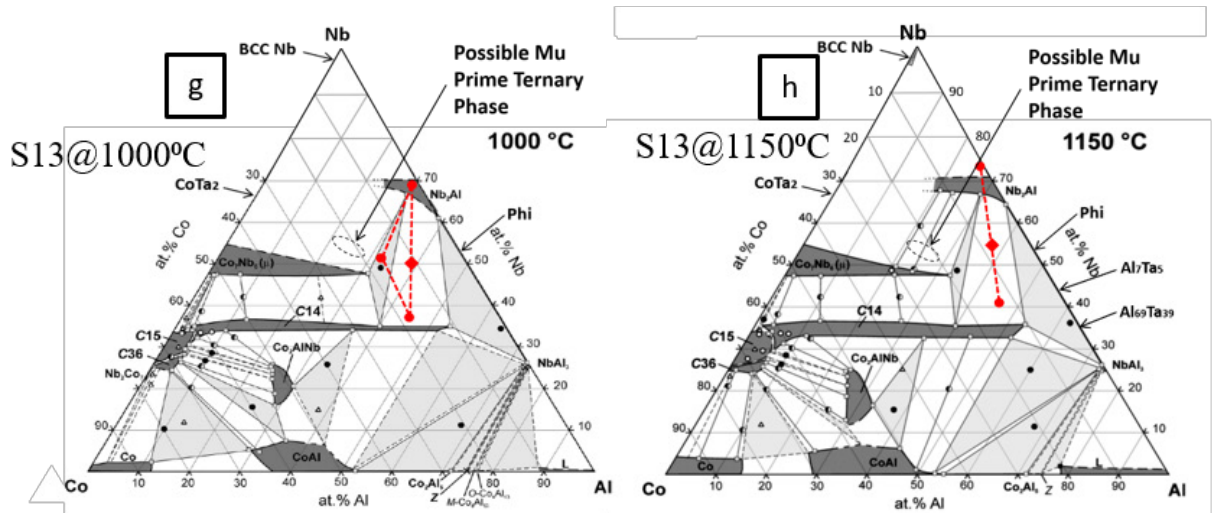
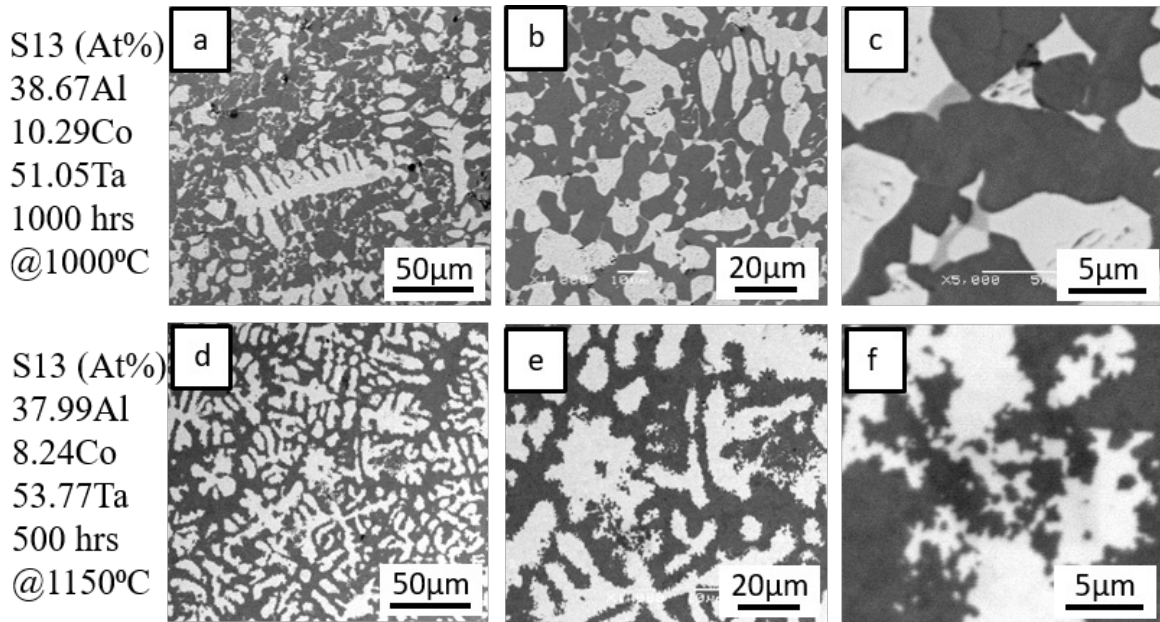
Light Phase: 16.61Al -7.39Co -75.99Ta,
Sigma_D8b?

Grey Phase: 22.74Al -22.36Co -54.90Ta,
Mu_D8s?

Light Phase: 16.44Al -6.94Co -76.61Ta,
Sigma_D8b?

Grey Phase: 23.46Al -21.21Co -55.32Ta,
Mu_D8s?

Figure 3.8: SEM BSE images of alloy sample 7 after an isothermal hold for 1000Hrs at 1000°C, followed by water quench (a-c), and after an isothermal hold for 500Hrs at 1150°C, followed by water quench (d-f). Bulk alloy, and phase boundary compositions from sample 7 after the 1000°C and 1150°C isothermal holds were measured via SEM EDX and used to create tie lines, which were plotted on modified temperature matched isothermal sections of the Nb-Al-Co system[48]–[50], [68], [72], [75]–[77], [97], [100] in images (g) and (h) to assist with phase identification in the Ta-Al-Co system.



Light Phase: 29.82Al -1.91Co -68.27Ta,
Sigma_D8b

Light Grey Phase: 32.48Al -16.52Co -50.99Ta,
Mu_D85

Dark Grey Phase, 45.02Al -18.10Co -36.88Ta,
Laves_C14

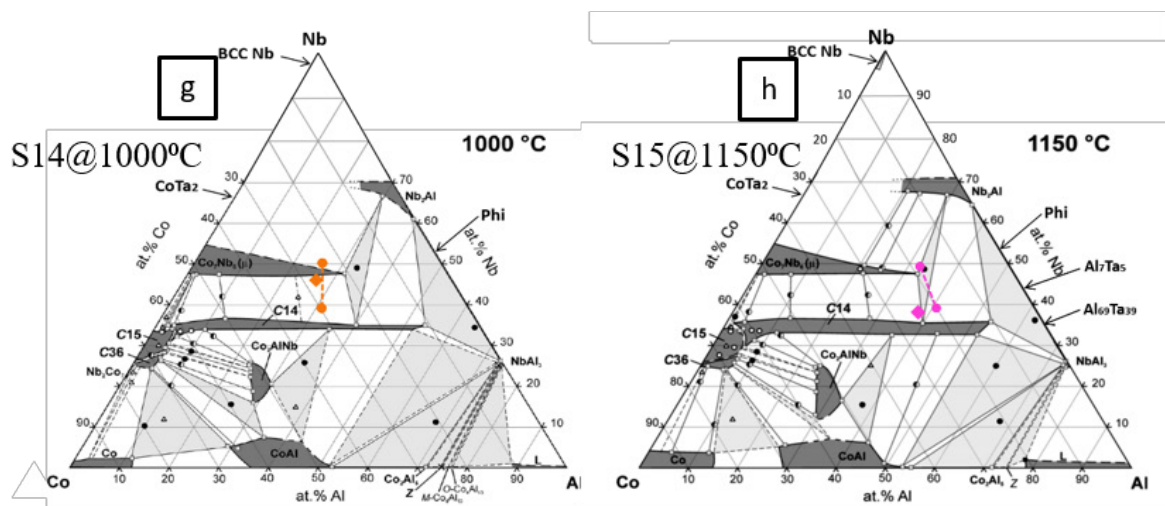
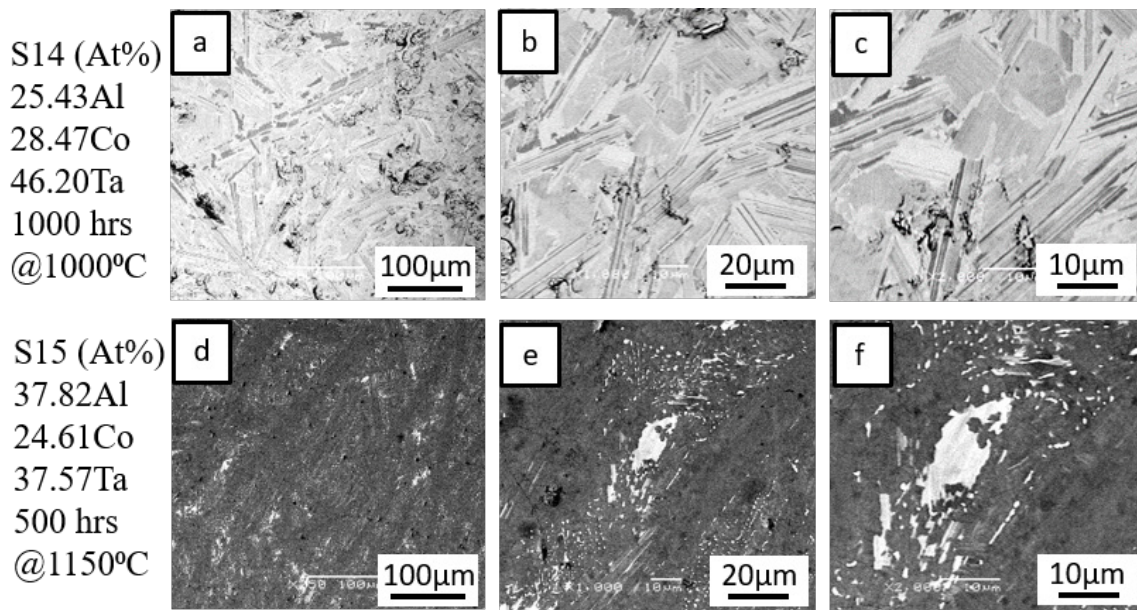
Light Phase: 26.62Al -0.98Co -72.40Ta,
Sigma_D8b?

Grey Phase: 46.23Al -13.46Co -40.31Ta,
Laves_C14

Figure 3.9: SEM BSE images of alloy sample 13 after an isothermal hold for 1000Hrs at 1000°C, followed by water quench (a-c), and after an isothermal hold for 500Hrs at 1150°C, followed by water quench (d-f). Bulk alloy, and phase boundary compositions from sample 13 after the 1000°C and 1150°C isothermal holds were measured via SEM EDX and used to create tie lines, which were plotted on modified temperature matched isothermal sections of the Nb-Al-Co system[48]–[50], [68], [72], [75]–[77], [97], [100] in images (g) and (h) to assist with phase identification in the Ta-Al-Co system.

3.3.3.6: Alloy Samples 14 & 15

Alloy samples 14 and 15 had average bulk compositions of 25.43%Al-28.47%Co-46.20%Ta, and 37.82%Al-24.61%Co-37.57%Ta respectively, and were identified as both occupying the same phase field. Figure 3.10(a-c) shows that after an isothermal hold for 1000Hrs at 1000°C, followed by a water quench, sample 14 exhibits a two phase lamellar microstructure. This consists of a very high volume fraction of light phase laths, separated by a smaller volume fraction of thin plates of dark phase. Figure 3.10(d-f) shows that after an isothermal hold for 500Hrs at 1150°C, followed by a water quench, sample 15 also exhibits a two phase microstructure, which appears to be an inverted version of that of sample 14. In the 1150°C condition the microstructure of sample 15 consists almost entirely of the dark phase, with a very volume fraction of finely distributed light phase precipitates. Figure 3.10(g&h) indicate that the light phase is highly likely to be Mu_D8₅, and the dark phase is probably Laves_C14.



Light Phase: 25.90Al -24.37Co -49.73Ta,
 Mu_D8s
 Grey Phase: 31.17Al -29.82Co -39.01Ta,
 Laves_C14

Light Phase: 32.46Al -18.75Co -48.78Ta,
 Mu_D8s
 Grey Phase: 40.90Al -20.29Co -38.80Ta,
 Laves_C14

Figure 3.10: SEM BSE images of alloy sample 14 after an isothermal hold for 1000Hrs at 1000°C, followed by water quench (a-c), and of alloy sample 15 after an isothermal hold for 500Hrs at 1150°C, followed by water quench (d-f). Bulk alloy, and phase boundary compositions from sample 14 after the 1000°C hold and sample 15 after the 1150°C hold were measured via SEM EDX and used to create tie lines, which were plotted on modified temperature matched isothermal sections of the Nb-Al-Co system[48]–[50], [68], [72], [75]–[77], [97], [100] in images (g) and (h) to assist with phase identification in the Ta-Al-Co system.

3.3.3.7: Alloy Sample 17

Alloy sample 17 has an average bulk composition of 50.69%Al-4.94%Co-44.37%Ta, as listed in Table 3.1. Figure 3.11(a-c) shows that after an isothermal hold for 1000Hrs at 1000°C, followed by a water quench, this sample exhibits a three phase microstructure, which consists of a light phase, a light grey phase and a dark phase. Figure 3.11(d) indicates that the light phase is likely to be Phi_Al₃₈Ta₄₈, the light grey phase likely to be Al₇Ta₅, and the dark phase is probably Laves_C14. The positions of these phases are slightly off of those found by Dovbenko et al.[75], but match up reasonably well with those found by Mahne et al.[48], [50]

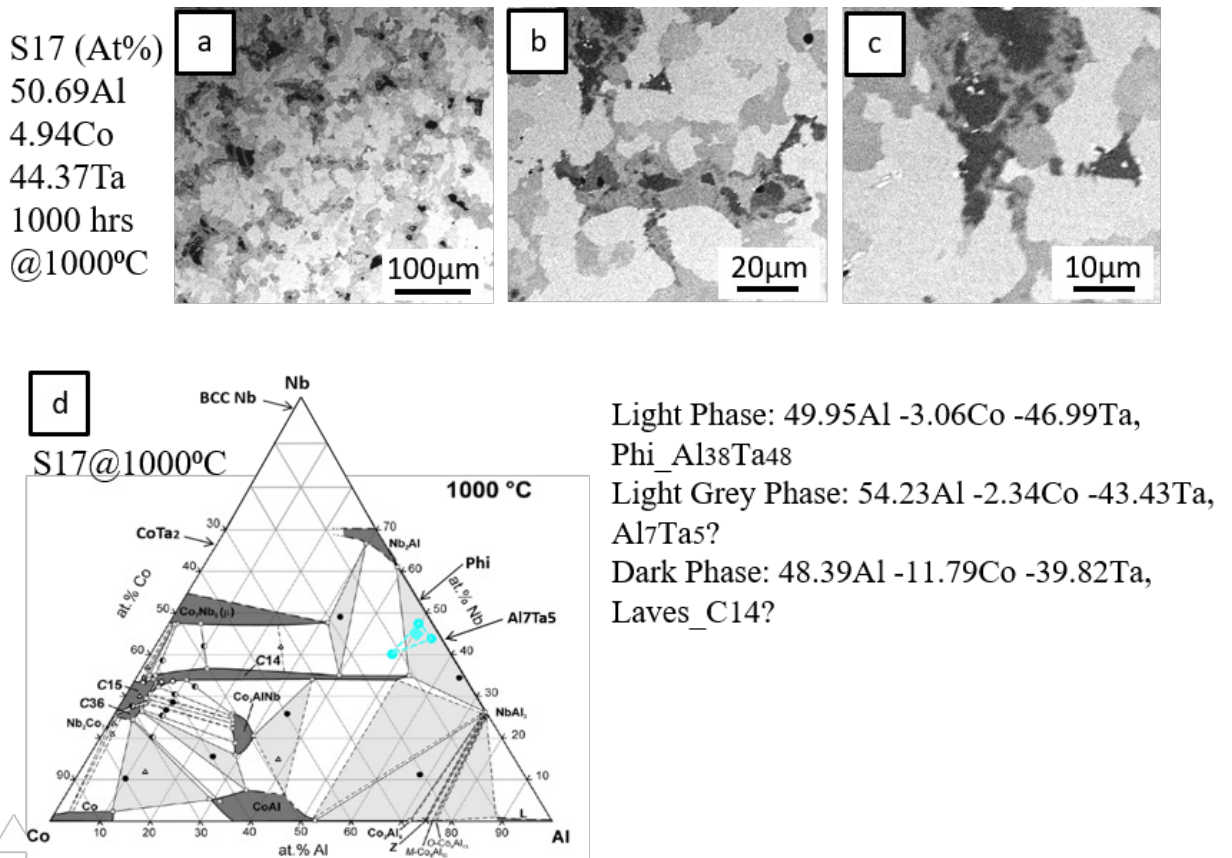


Figure 3.11: SEM BSE images of alloy sample 17 after an isothermal hold for 1000Hrs at 1000°C, followed by water quench (a-c). Bulk alloy, and phase boundary compositions from sample 17 after this 1000°C isothermal hold were measured via SEM EDX and used to create a tie triangle, which was plotted on a modified temperature matched isothermal section of the Nb-Al-Co system[48]–[50], [68], [72], [75]–[77], [97], [100] in image (d) to assist with phase identification in the Ta-Al-Co system.

3.3.3.8: Alloy Sample 18

Alloy sample 18 has an average bulk composition of 62.64%Al-4.27%Co-33.09%Ta, as listed in Table 3.1. Figure 3.12(a-c) illustrates that after an isothermal hold for 1000Hrs at 1000°C, followed by a water quench, this sample also exhibits a three phase microstructure. This consists of a network of evenly distributed light and light grey phase precipitates surrounded by a dark phase. Figure 3.12(d) indicates that the light phase is likely to be Al_7Ta_5 , the light grey phase likely to be Laves_C14, and the dark phase is probably Epsilon_Al₃Ta_D0₂₂. The positions of these phases are slightly off of those found by Dovbenko et al.,[75] but are in reasonable agreement with those found by Mahne et al.,[48], [50] and Kimura et al.[38]

3.3.3.9: Alloy Sample 19

Alloy sample 19 has an average bulk composition of 59.21%Al-11.01%Co-29.77%Ta. Figure 3.13(a-c) shows that after an isothermal hold for 1000Hrs at 1000°C, followed by a water quench, this sample has a three phase microstructure, which consists of a light phase, a light grey phase and a dark phase. Figure 3.13(d) indicates that the light phase is likely to be Laves_C14, the light grey phase likely to be Epsilon_Al₃Ta_D0₂₂, and the dark phase is likely to be Al₃Co. The positions of these phases are again slightly off of those found by Dovbenko et al.,[75] but are in good agreement with those found by Mahne et al.,[48], [50] and Kimura et al.[38] Figure 3.13(d) also shows that the positions of the tie triangles in the Al corner of the Ta-Al-Co system appear to be quite different to those found in the Nb-Al-Co system.

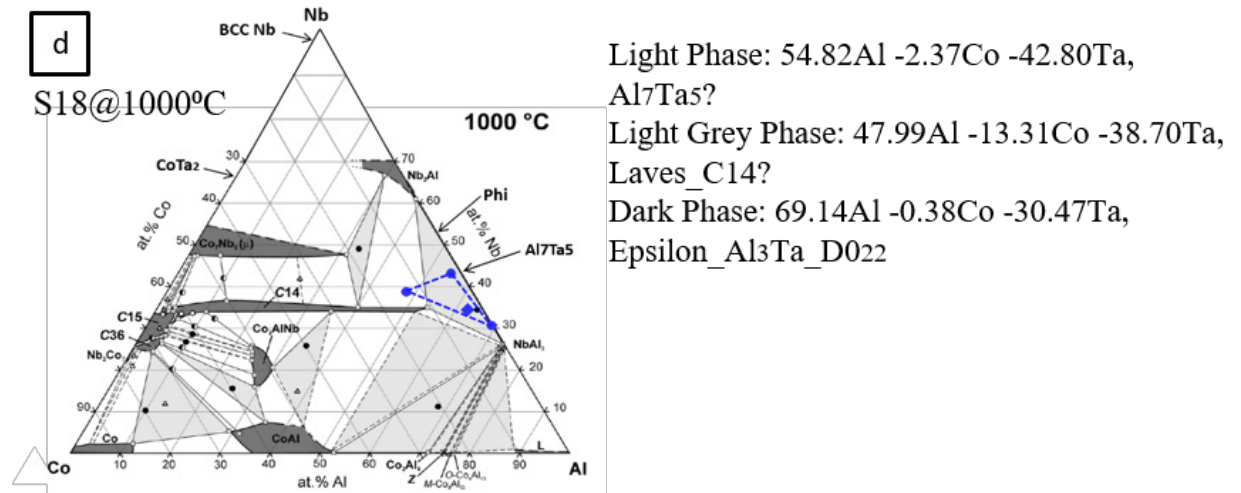
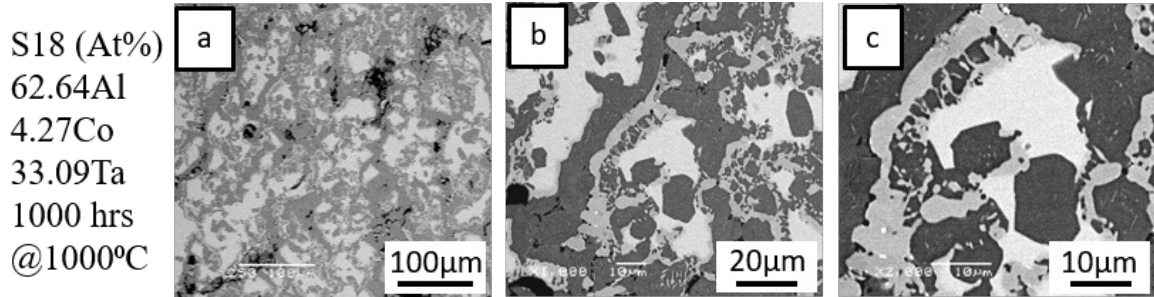
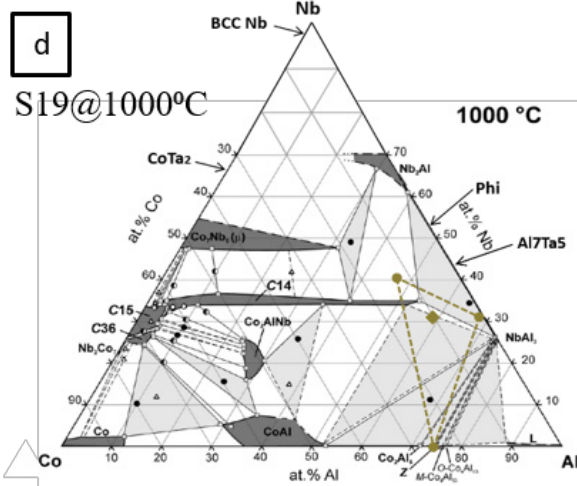
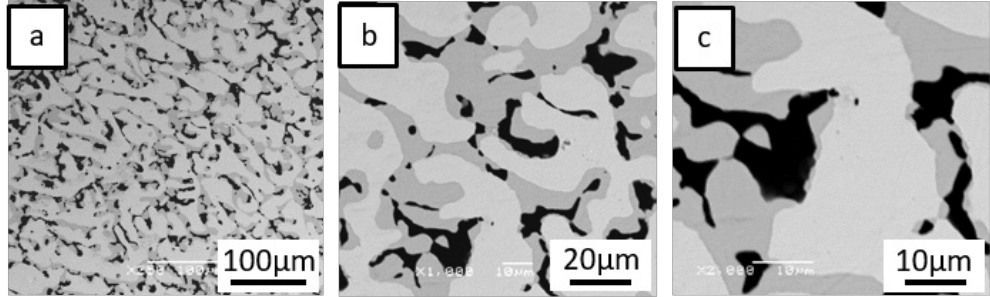


Figure 3.12: SEM BSE images of alloy sample 18 after an isothermal hold for 1000Hrs at 1000°C, followed by water quench (a-c). Bulk alloy, and phase boundary compositions from sample 18 after this 1000°C isothermal hold were measured via SEM EDX and used to create a tie triangle, which was plotted on a modified temperature matched isothermal section of the Nb-Al-Co system[48]–[50], [68], [72], [75]–[77], [97], [100] in image (d) to assist with phase identification in the Ta-Al-Co system.

S19 (At%)
 59.21Al
 11.01Co
 29.77Ta
 1000 hrs
 @1000°C



Light Phase: 47.25Al -11.66Co -41.09Ta,
 Laves_C14?
 Light Grey Phase: 67.57Al -1.14Co -31.27Ta,
 Epsilon_Al3Ta_D022
 Dark Phase: 74.61Al -25.39Co -0.00Ta,
 Al3Co

Figure 3.13: SEM BSE images of alloy sample 19 after an isothermal hold for 1000Hrs at 1000°C, followed by water quench (a-c). Bulk alloy, and phase boundary compositions from sample 19 after this 1000°C isothermal hold were measured via SEM EDX and used to create a tie triangle, which was plotted on a modified temperature matched isothermal section of the Nb-Al-Co system[48]–[50], [68], [72], [75]–[77], [97], [100] in image (d) to assist with phase identification in the Ta-Al-Co system.

3.3.3.10: Alloy Sample 20

Alloy sample 20 has an average bulk composition of 66.16%Al-29.62%Co-4.22%Ta. Figure 3.14(a-c) shows that after an isothermal hold for 1000Hrs at 1000°C, followed by a water quench, this sample has a two phase microstructure, which consists of a light phase and a dark phase. Figure 3.14(d) indicates that the light phase is likely to be Laves_C14, and the dark phase is probably Al₅Co₂. This figure also shows that the results from sample 20 are in good agreement with those from sample 19 in terms of the positions of the tie triangles in the Al corner of the Ta-Al-Co system. In fact the results from alloy samples 14 to 20 are all in good agreement with each other with regards to the positions of the phase boundaries in this region of the phase diagram.

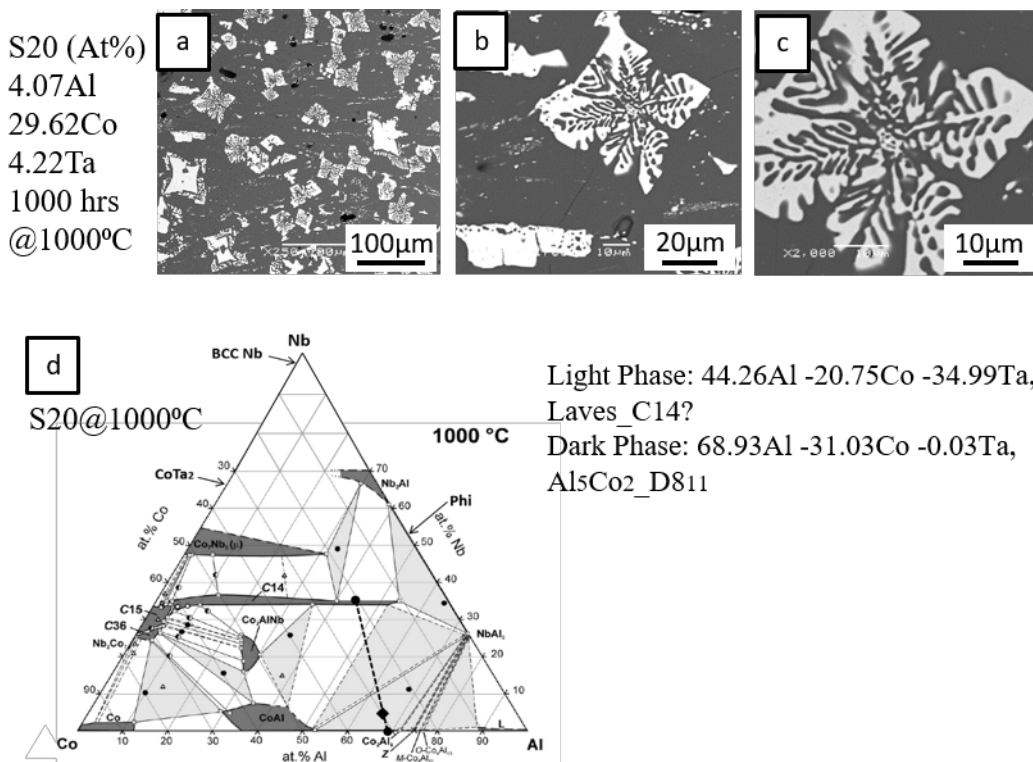


Figure 3.14: SEM BSE images of alloy sample 20 after an isothermal hold for 1000Hrs at 1000°C, followed by water quench (a-c). Bulk alloy, and phase boundary compositions from sample 20 after this 1000°C isothermal hold were measured via SEM EDX and used to create a tie triangle, which was plotted on a modified temperature matched isothermal section of the Nb-Al-Co system[48]–[50], [68], [72], [75]–[77], [97], [100] in image (d) to assist with phase identification in the Ta-Al-Co system.

3.3.3.11: Alloy Samples 23 and 21

Alloy sample 23 had slightly different measured average bulk compositions for the two specimens that were heat treated at 1000°C and 1150°C, despite these specimens both being cut from the same ingot. The specimen that was heat treated at 1000°C had an average bulk composition of 31.40%Al-52.77%Co-15.83%Ta, and has a two phase microstructure, as shown in Figure 3.15(a-c). This consists of blocks of a dark phase surrounded by an interconnected network of light phase. Figure 3.15(j) indicates that the light phase is likely to be the ternary L₂₁ phase, and the dark phase is probably the BCC_B2 phase.

The specimen that was heat treated at 1150°C had an average bulk composition of 26.17%Al-45.96%Co-19.79%Ta, and has a very different microstructure to the specimen that was heat treated at 1000°C, due to the composition difference between them. Figure 3.15(d-f) shows that this specimen is composed of a very high volume fraction of the ternary L₂₁ phase, with only a very small volume fraction of the BCC_B2 phase present.

Alloy sample 21 had an average bulk composition of 36.32%Al-53.07%Co-17.61%Ta, and appears to have a 3 phase microstructure, as shown in Figure 3.15(g-i). This consists of blocks of a dark phase surrounded by a circuitous interconnected network of light grey phase, with some tiny flecks of light phase. The light phase precipitates were too small to accurately measure via SEM EDX measurements, but attempted measurements indicated that their composition was close to that of the Laves_C14 phase. Figure 3.15(k) shows that the light grey phase is highly likely to be the ternary L₂₁ phase. The dark phase could potentially either be a new ternary phase, or it could also simply be the BCC_B2 phase. SEM EDX measurements of the dark phase in both alloy samples 23 and 21 exhibited significant scatter, and it is thought that the circuitous network of light grey phase that surrounds it may have prevented accurate measurements of the dark phase in these samples. Attempts to measure

the dark phase may have inadvertently also sampled some of the light, and light grey phases, which would have the effect of pulling the measured compositions away from the dark phase boundary, and up into the two/three phase regions between the dark phase and the lighter phases as shown in Figure 3.15(j&k).

3.3.3.12: Alloy Samples 22 and 24

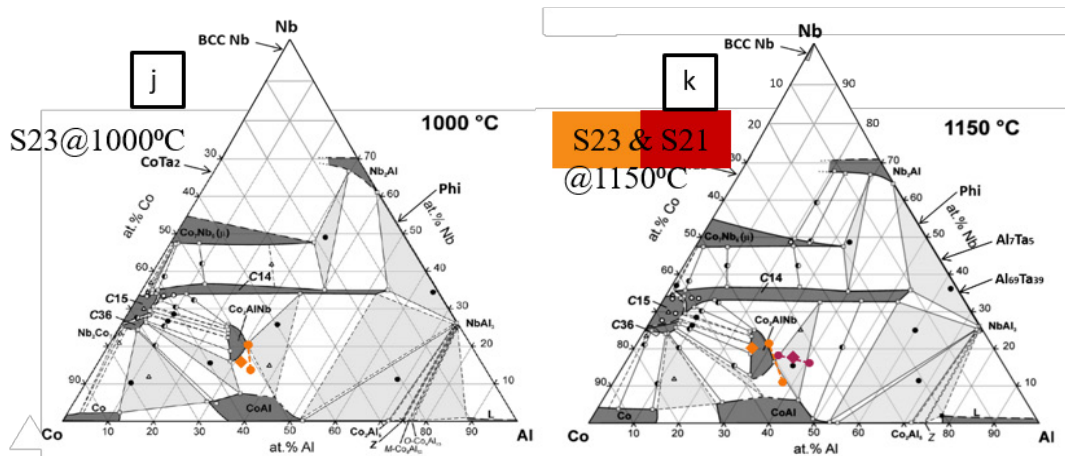
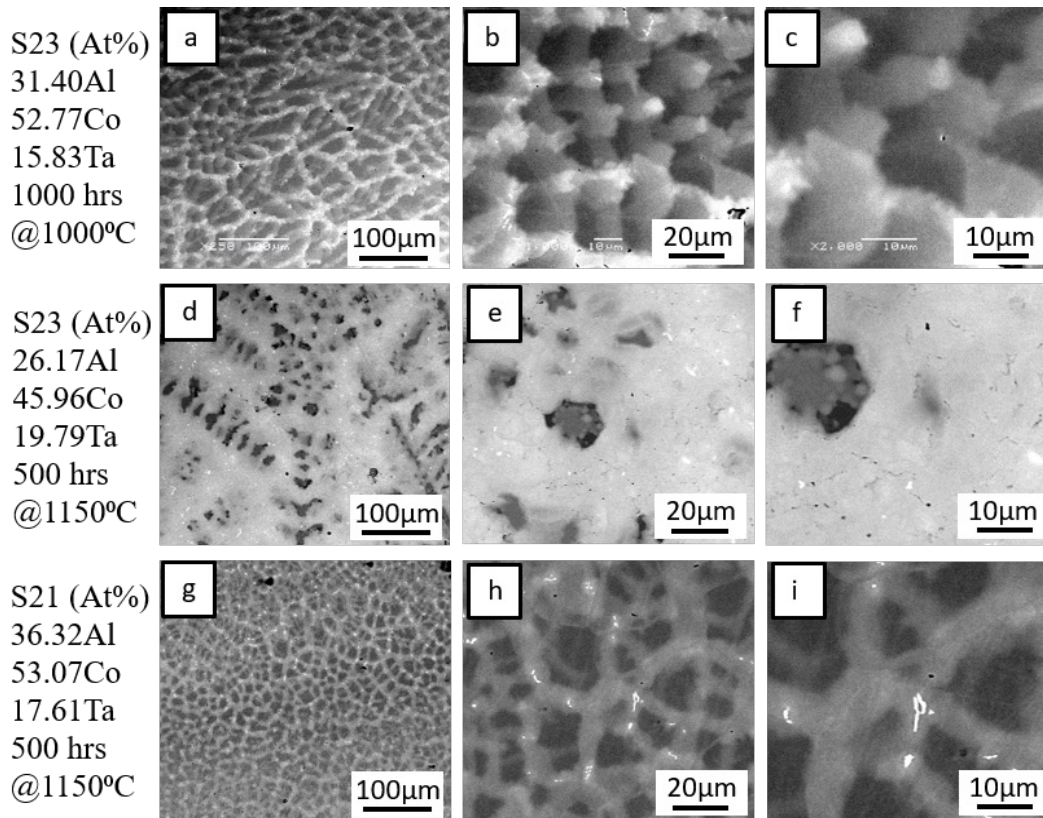
Alloy sample 22 also had slightly different measured average bulk compositions for the two specimens that were heat treated at 1000°C and 1150°C. The specimen that was heat treated at 1000°C had an average bulk composition of 36.68%Al-50.61%Co-12.71%Ta. This specimen was initially thought to have a two phase eutectic microstructure, with a light phase surrounded by a dark phase as shown in Figure 3.16(a-c). However, closer examination also revealed the presence of tiny 1-2 μm long needles of a light grey phase in the spaces between the light and dark phase eutectic structure as illustrated in Figure 3.16(c&d). So the alloy could potentially have a three phase microstructure instead. Figure 3.16(k) indicates that the light and dark eutectic phases are likely to be Laves_C14 and BCC_B2 respectively. The width of the light grey needles is well below the approximate sampling volume for the SEM EDX point analysis measurements for phases of this density, of just over $1\mu\text{m}^3$. So the dimensions of these precipitates make them too small to accurately measure their compositions on the SEMs used in this work. Based on the composition of this alloy it is possible that they could potentially be $L2_1$ phase precipitates, however this has not been proven as yet.

The alloy 22 specimen that was heat treated at 1150°C had an average bulk composition of 38.34%Al-55.64%Co-6.12%Ta, and has a very different microstructure to the specimen that was heat treated at 1000°C, due to the composition difference between them.

Figure 3.16(e-g) shows that this specimen is composed of a very high volume fraction of the dark BCC_B2 phase, with only a small volume fraction of the light Laves_C14 phase present.

Alloy sample 24 had an average bulk composition of 30.55%Al-55.71%Co-13.74%Ta, and was heat treated at 1150°C only. This alloy exhibited a very similar eutectic microstructure to that of alloy 22 in the 1000°C condition, as shown in Figure 3.16(h-j). Figure 3.16(l) indicates that the light phase in alloy 24 is likely to be Laves_C14 phase and the dark phase is almost certainly BCC_B2, just like in alloy 22.

The fact that the dark phase in alloys 22 and 24 is almost certainly BCC_B2 adds further weight to the hypothesis that the dark phase in sample 21 is also BCC_B2, and not some new ternary phase. It seems likely that the measured composition boundary for the dark phase in sample 21 was simply shifted due to sampling some of some of the Laves_C14 phase and also some of the circuitous L2₁ phase network that weaves its way through the dark BCC_B2 phase in this sample.



Light Phase: 30.60Al -49.06Co -20.34Ta,
L21
Dark Phase: 34.41Al -51.69Co -13.90Ta,
BCC_B2

Light Grey Phase: 29.32Al -49.63Co -21.05Ta
& 33.09Al -48.93Co -17.98Ta, L21
Dark Phase: 37.55Al -51.62Co -10.84Ta &
40.87Al -43.04Co -16.09Ta, BCC_B2

Figure 3.15: SEM BSE images of alloy sample 23 after and an isothermal hold for 1000Hrs at 1000°C, followed by water quench (a-c), and after and an isothermal hold for 500Hrs at 1150°C, followed by water quench (d-f), and also of alloy sample 21 after an isothermal hold for 500Hrs at 1150°C, followed by water quench (g-i). Bulk alloy, and phase boundary compositions from sample 23 after the 1000°C and 1150°C holds, and sample 21 after the 1150°C hold were measured via SEM EDX and used to create tie lines, which were plotted on modified temperature matched isothermal sections of the Nb-Al-Co system[48]–[50], [68], [72], [75]–[77], [97], [100] in images (j) and (k) to assist with phase identification in the Ta-Al-Co system.

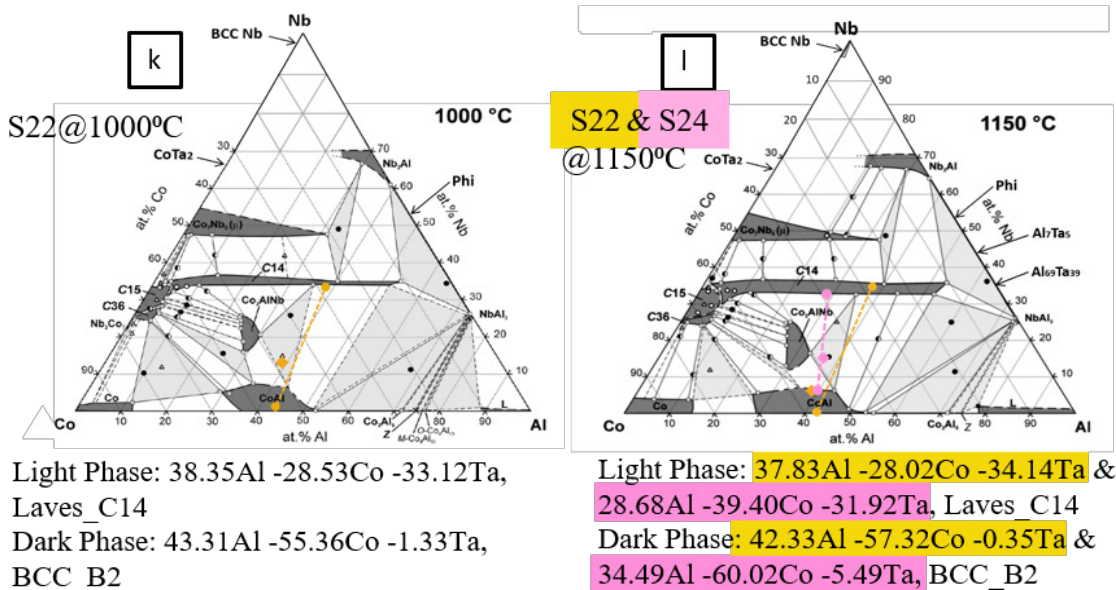
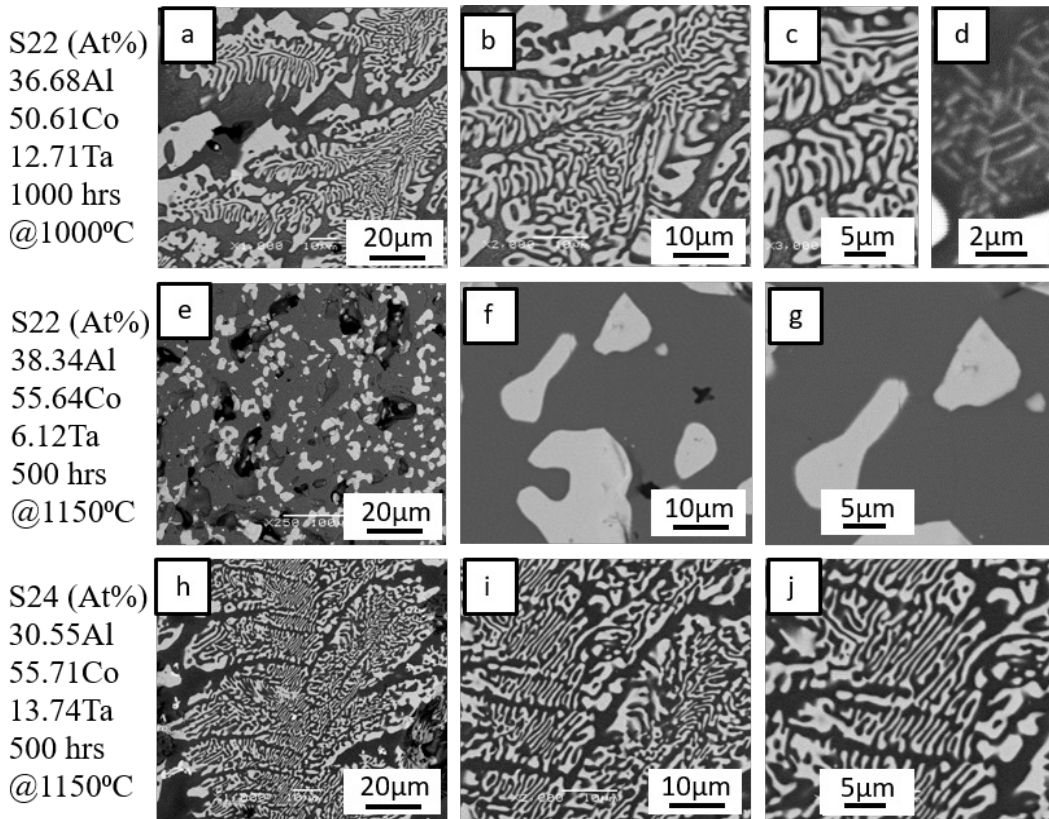


Figure 3.16: SEM BSE images of alloy sample 22 after and an isothermal hold for 1000Hrs at 1000°C, followed by water quench (a-d), and after and an isothermal hold for 500Hrs at 1150°C, followed by water quench (e-g), and also of alloy sample 24 after an isothermal hold for 500Hrs at 1150°C, followed by water quench (h-j). Bulk alloy, and phase boundary compositions from sample 22 after the 1000°C and 1150°C holds, and sample 24 after the 1150°C hold were measured via SEM EDX and used to create tie lines, which were plotted on modified temperature matched isothermal sections of the Nb-Al-Co system [48]–[50], [68], [72], [75]–[77], [97], [100] in images (k) and (l) to assist with phase identification in the Ta-Al-Co system.

3.3.3.13: Alloy Sample 26

Alloy sample 26 had an average bulk composition of 20.52%Al-63.02%Co-16.46%Ta, as listed in Table 3.1. Figure 3.17 shows the microstructures of this alloy in the as cast condition (a-c), after the 1000°C heat treatment (d-f), and after the 1150°C heat treatment (g-i). In the as cast condition the alloy microstructure appears to consist of grains of a grey phase, encircled by a network of light phase and dark areas around the grain boundaries. It is unclear if the dark areas are a distinct third phase, or if they are simply Ta depleted zones around the light phase grain boundary precipitates.

In the 1000°C condition the alloy microstructure consists of grains of dark phase containing numerous evenly distributed 1-2 μm long needles of a light phase, surrounded by an intergranular network of light phase. In Figure 3.17(j) the light phase is identified as likely to be Laves_C15 and the dark phase as likely to be BCC_B2. The light phase needles were too small to accurately measure via EDX, but attempted measurements gave compositions that lay on the Laves_C15 - BCC_B2 tie line. So it was concluded that the light phase needles were also likely to be the Laves_C15 phase, just like the larger intergranular light phase precipitates, and not L2₁, or some other phase. Therefore it appears that this alloy has a two phase Laves_C15 - BCC_B2 microstructure in the 1000°C condition.

Figure 3.17(g-i) shows that alloy 26 also has a two phase microstructure in the 1150°C condition. However, at this temperature the microstructure consists of grains of grey phase, with either very few or no small light phase needle precipitates, which are again surrounded by an intergranular network of light phase. In Figure 3.17(k) the light phase is identified as likely to be Laves_C15 and the grey phase as likely to be L2₁. So it seems that the bulk composition of this alloy is situated in a different phase field at 1150°C than it is at 1000°C.

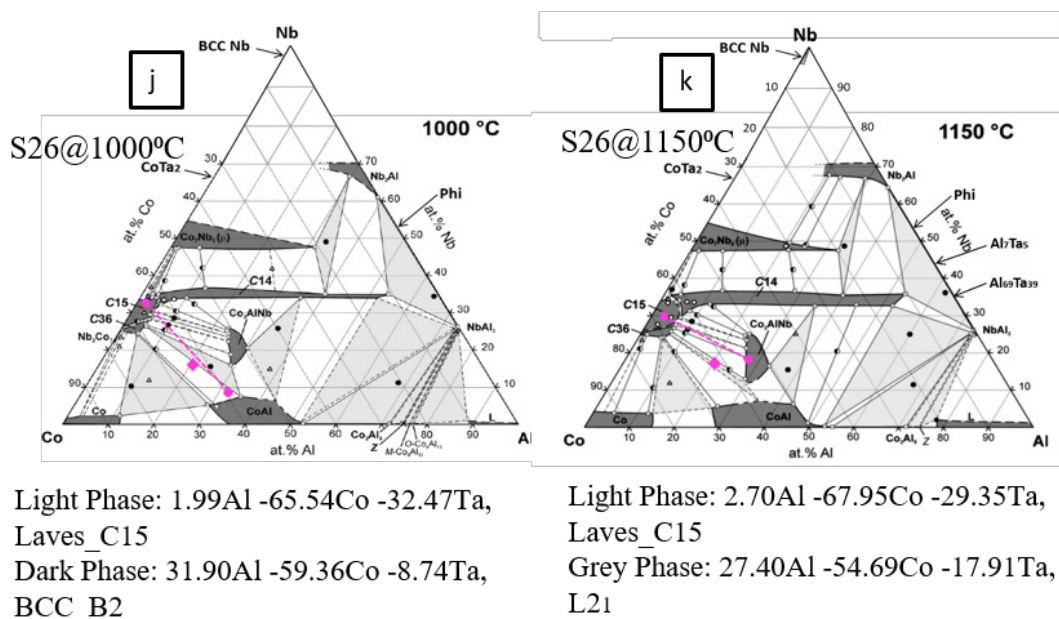
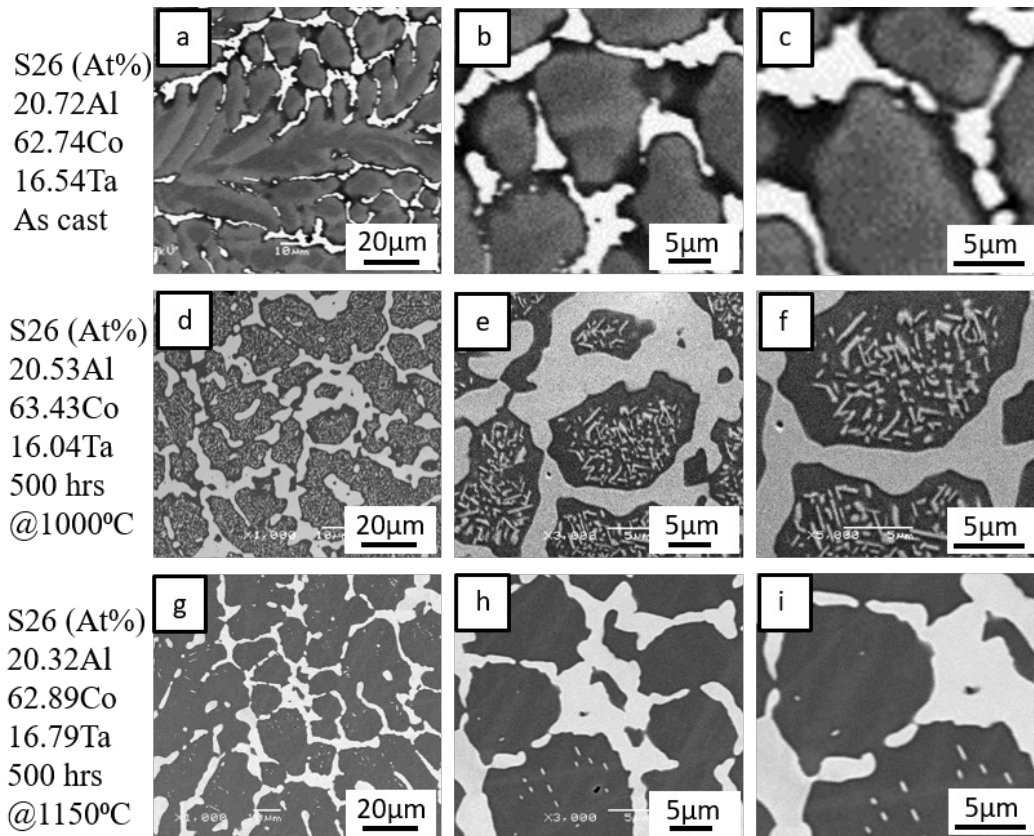


Figure 3.17: SEM BSE images of alloy sample 26 in the as cast condition (a-c), after an isothermal hold for 1000Hrs at 1000°C, followed by water quench (d-f), and after an isothermal hold for 500Hrs at 1150°C, followed by water quench, (g-i). Bulk alloy, and phase boundary compositions from sample 26 after the 1000°C and 1150°C isothermal holds were measured via SEM EDX and used to create tie lines, which were plotted on modified temperature matched isothermal sections of the Nb-Al-Co system[48]–[50], [68], [72], [75]–[77], [97], [100] in images (j) and (k) to assist with phase identification in the Ta-Al-Co system.

3.3.3.14: Alloy Sample 30

Alloy sample 30 had an average bulk composition of 8.37%Al-79.03%Co-12.60%Ta, as listed in Table 3.1. Figure 3.18 shows the microstructures of this alloy in the as cast condition (a-c), after the 1000°C heat treatment (d-f), and after the 1150°C heat treatment (g-i). In the as cast condition alloy 30 appears to have a two phase microstructure that consists of larger light phase dendrites and globular dark grey phase precipitates surrounded a fine eutectic mix of light and dark grey phases. Based on SEM EDX measurements the light phase was thought to be either Laves_C15, or Laves_C36, and the dark grey phase was identified as FCC_A1 Co.

In the 1000°C condition alloy 30 exhibits a three phase microstructure that consists of a mix of light phase, light grey phase and dark grey phase. It is difficult to clearly distinguish between the two grey phases due to the lack of contrast between them, but close examination of the right side of Figure 3.18(f) shows that the 4µm oval shaped light grey precipitate has a clearly demarcated border with the surrounding dark grey phase. Figure 3.18(j) illustrates that the light phase is likely to be Laves_C15, the light grey phase is BCC_B2, and the dark grey phase is FCC_A1 Co.

Figure 3.18(g-i) shows that in the 1150°C condition alloy 30 also has a three phase microstructure that consists of light phase, light grey phase and dark grey phase precipitates. However at this temperature the microstructure is coarser, and the precipitates of each phase are larger. Also, the contrast between the light grey and dark grey phases is clearer in these micrographs. Again, Figure 3.18(k) shows that the light phase is likely to be Laves_C15, the light grey phase is BCC_B2, and the dark grey phase is FCC_A1 Co.

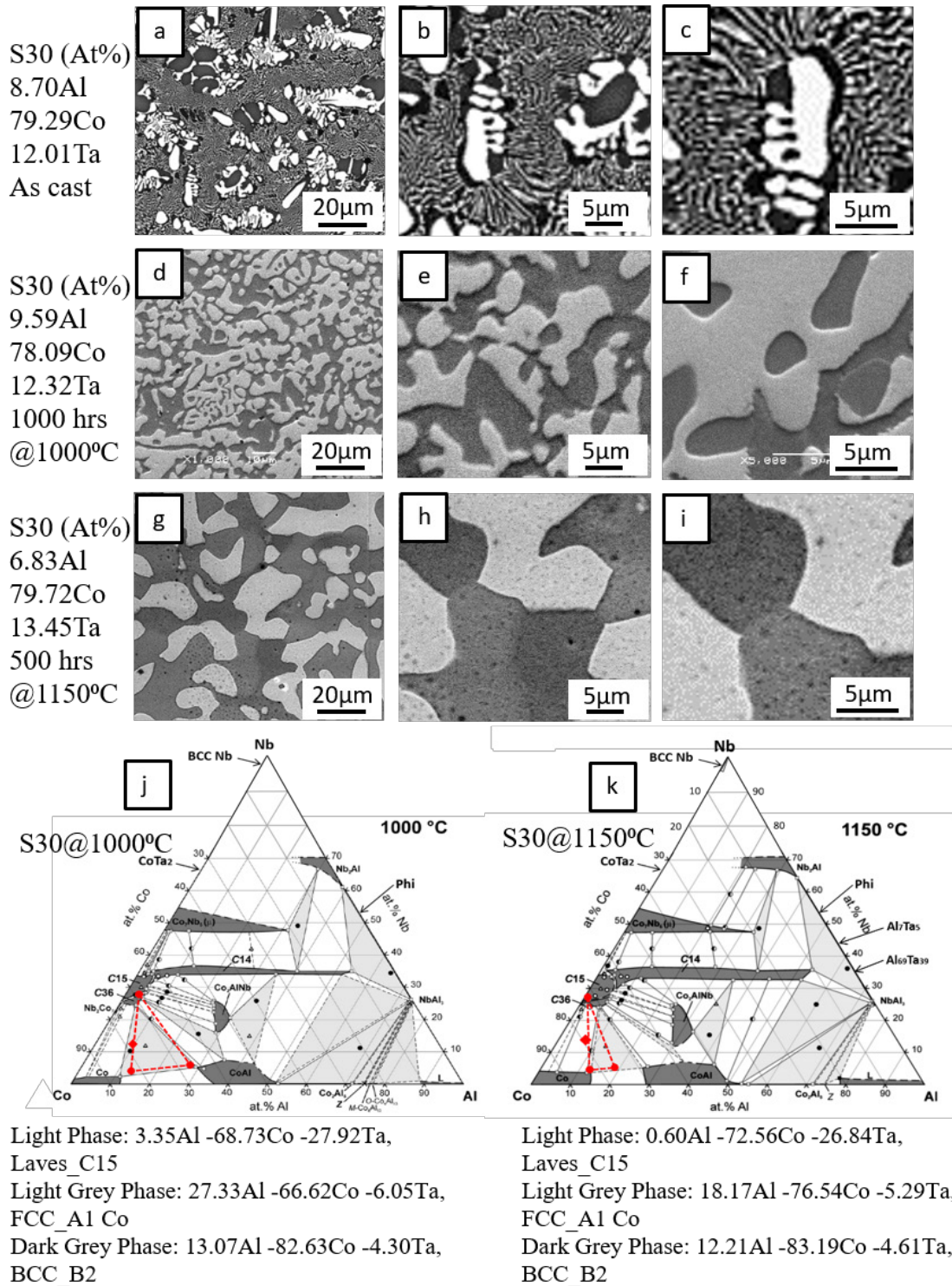


Figure 3.18: SEM BSE images of alloy sample 30 in the as cast condition (a-c), after an isothermal hold for 1000Hrs at 1000°C, followed by water quench (d-f), and after an isothermal hold for 500Hrs at 1150°C, followed by water quench, (g-i). Bulk alloy, and phase boundary compositions from sample 30 after the 1000°C and 1150°C isothermal holds were measured via SEM EDX and used to create tie triangles, which were plotted on modified temperature matched isothermal sections of the Nb-Al-Co system[48]–[50], [68], [72], [75]–[77], [97], [100] in images (j) and (k) to assist with phase identification in the Ta-Al-Co system.

3.3.4: Ta-Al-Co Phase Equilibria and Phase Diagrams

The average phase boundary compositions measured via SEM EDX for all phases in all Ta-Al-Co alloy samples equilibrated at 1000°C are listed in Tables 3.2a, and 3.2b. Since these boundary compositions were measured as tie lines and tie triangles, they could be plotted as such on a ternary isothermal section for the system at this temperature, along with the average bulk alloy composition data for all samples listed in Table 3.1. This ternary phase boundary data was also combined with the temperature matched binary phase boundary data for the Al-Co,[96] Al-Ta,[48]–[50], [97] and Co-Ta,[72], [76], [100] systems to produce a complete experimentally determined ternary isothermal section for the Ta-Al-Co system at 1000°C, which is shown in Figure 3.19.

From this figure it can be seen that at 1000°C the BCC_A2 Ta phase exhibits negligible solubility for Al in the Al-Ta binary, as found by Glazov et al.[35], [36] and has a solubility of around 3 at% for Co in the Co-Ta binary, as reported by Shinagawa et al.[76]

It extends from these binary edge points to a composition of approximately 2%Al-3.8%Co-94.2%Ta, based on the results from alloy samples 2, 3, 4, & 5, which are listed in Table 3.2a, and plotted on Figure 3.19. For the solubility of Co in BCC_A2 Ta, the results of sample 3 (plotted in royal blue), were given more weight than those of samples 2, 4, & 5, since they are more in line with literature data. The BCC_A2 Ta phase forms equilibria with the CoTa₂_C16, Mu_D8₅, and Sigma_D8_b phases as shown in the figure.

At 1000°C, the CoTa₂_C16 phase exhibits an approximate solubility range of 66-67at% Ta in the Co-Ta binary,[100] and extends from here out into the ternary to a composition of 4.16%Al-29.75%Co-66.09Ta, based on the results from sample 3. This phase forms equilibria with the BCC_A2 Ta and Mu_D8₅ phases.

Table 3.2a: Average phase boundary compositions measured via SEM EDX for all phases in alloy samples 2-17 that were exposed to an isothermal hold for 1000Hrs at 1000°C, followed by water quench. Each composition listed is the average of at least 5 measurements. (Continued overleaf in Table 3.2b for samples 18-30).

Alloy Sample No	Phase	Measured composition		
		At% Al	At% Co	At% Ta
1
2	BCC_A2 Ta	3.46 ± 1.33	4.64 ± 0.68	91.90 ± 1.81
	Mu_D8 ₅	13.90 ± 1.08	28.16 ± 2.70	57.94 ± 2.30
3	BCC_A2 Ta	0.21 ± 0.36	3.77 ± 0.81	96.02 ± 0.59
	CoTa ₂ C16	4.16 ± 0.24	29.75 ± 0.87	66.09 ± 0.91
4	BCC_A2 Ta	2.41 ± 2.05	4.72 ± 1.71	92.87 ± 3.14
	Sigma_D8 _b	9.93 ± 0.42	12.34 ± 1.55	77.73 ± 1.56
	Mu_D8 ₅	13.58 ± 1.09	27.87 ± 3.85	58.55 ± 2.97
5	BCC_A2 Ta	2.58 ± 0.94	6.71 ± 2.64	90.71 ± 3.53
	Sigma_D8 _b	7.30 ± 1.70	9.92 ± 1.06	82.78 ± 1.80
	Mu_D8 ₅	14.42 ± 0.65	33.96 ± 0.70	51.62 ± 0.50
6
7	Sigma_D8 _b	16.61 ± 0.81	7.39 ± 0.73	75.99 ± 0.99
	Mu_D8 ₅	22.74 ± 1.52	22.36 ± 3.26	54.90 ± 1.73
8
9	?	12.12 ± 0.87	28.70 ± 2.78	59.18 ± 2.15
	Mu_D8 ₅	11.28 ± 0.99	34.62 ± 2.90	54.11 ± 2.02
10	Sigma_D8 _b	10.97 ± 0.54	12.29 ± 0.75	76.74 ± 1.17
	Mu_D8 ₅	15.43 ± 1.31	32.44 ± 1.19	52.13 ± 0.29
11	Sigma_D8 _b	21.22 ± 1.98	7.27 ± 2.60	71.51 ± 4.24
	Mu_D8 ₅	27.43 ± 1.61	19.86 ± 3.11	52.71 ± 1.68
12	Sigma_D8 _b	25.19 ± 1.12	3.33 ± 1.30	71.47 ± 1.41
	Laves_C14	38.52 ± 0.48	25.22 ± 0.89	36.26 ± 0.86
13	Sigma_D8 _b	29.82 ± 1.30	1.91 ± 0.76	68.27 ± 1.09
	Mu_D8 ₅	32.48 ± 2.73	16.52 ± 1.75	50.99 ± 1.75
	Laves_C14	45.02 ± 0.30	18.10 ± 0.33	36.88 ± 0.37
14	Mu_D8 ₅	25.90 ± 1.01	24.37 ± 1.74	49.73 ± 1.71
	Laves_C14	31.17 ± 0.95	29.82 ± 1.57	39.01 ± 1.69
15
16
17	Phi_Al ₃₈ Ta ₄₈	49.95 ± 0.36	3.06 ± 0.67	46.99 ± 0.74
	Al ₇ Ta ₅	54.23 ± 1.05	2.34 ± 1.56	43.43 ± 1.08
	Laves_C14	48.39 ± 0.65	11.79 ± 1.82	39.82 ± 1.17

Table 3.2b: Average phase boundary compositions measured via SEM EDX for all phases in alloy samples 18-30 that were exposed to an isothermal hold at for 1000Hrs at 1000°C, followed by water quench. Each composition listed is the average of at least 5 measurements. (Continued from Table 3.2a for samples 2-17).

Alloy Sample No	Phase	Measured composition		
		At% Al	At% Co	At% Ta
18	Al ₇ Ta ₅	54.82 ± 0.66	2.37 ± 0.56	42.80 ± 0.29
	Laves_C14	47.99 ± 0.07	13.31 ± 0.33	38.70 ± 0.27
	Epsilon_Al ₃ Ta_D0 ₂₂	69.14 ± 0.16	0.38 ± 0.19	30.47 ± 0.25
19	Laves_C14	47.12 ± 0.93	12.68 ± 1.23	40.21 ± 1.32
	Epsilon_Al ₃ Ta_D0 ₂₂	68.08 ± 0.59	1.18 ± 0.17	30.75 ± 0.53
	Al ₃ Co	73.99 ± 1.16	26.01 ± 1.16	0.00 ± 0.00
20	Laves_C14	44.26 ± 1.05	20.75 ± 1.18	34.99 ± 1.25
	Al ₅ Co ₂ _D8 ₁₁	68.93 ± 1.41	31.03 ± 1.38	0.03 ± 0.04
21
22	Laves_C14	38.35 ± 0.61	28.53 ± 0.41	33.12 ± 0.62
	BCC_B2	43.31 ± 1.05	55.36 ± 2.20	1.33 ± 1.69
23	L2 ₁	30.60 ± 1.34	49.06 ± 2.72	20.34 ± 2.06
	BCC_B2	34.41 ± 1.50	51.69 ± 2.04	13.90 ± 1.39
24
25	Laves_C36	1.17 ± 0.11	75.46 ± 0.21	23.37 ± 0.13
	BCC_B2	22.98 ± 0.48	65.43 ± 0.58	11.59 ± 0.44
26	Laves_C15	1.99 ± 0.16	65.54 ± 0.68	32.47 ± 0.84
	BCC_B2	31.90 ± 1.59	59.36 ± 2.03	8.74 ± 0.54
27	Laves_C36	1.22 ± 0.17	75.62 ± 0.43	23.16 ± 0.56
	BCC_B2	25.61 ± 0.42	65.79 ± 0.29	8.60 ± 0.16
28	Laves_C15	2.23 ± 0.79	68.71 ± 2.50	29.06 ± 3.29
	BCC_B2	31.84 ± 6.04	60.27 ± 6.88	7.89 ± 1.28
29	Laves_C15	1.17 ± 0.21	70.88 ± 0.34	27.95 ± 0.54
	BCC_B2	27.47 ± 2.63	66.43 ± 3.27	6.10 ± 0.65
	FCC_A1 Co	12.63 ± 1.00	83.38 ± 1.28	3.99 ± 0.32
30	Laves_C15	3.35 ± 1.34	68.73 ± 2.19	27.92 ± 2.61
	BCC_B2	27.33 ± 0.88	66.62 ± 0.92	6.05 ± 0.21
	FCC_A1 Co	13.07 ± 0.42	82.63 ± 0.37	4.30 ± 0.34

Sample Number (Starting from Ta corner, moving to Al, then Co)

- | | |
|--|---|
| 1 Not analysed at 1000°C | 16 Not analysed at 1000°C |
| 2 BCC_A2 Ta - Mu_D85 Tie Line | 17 Phi_Al38Ta48 - Al7Ta5 - Laves_C14 Tie Triangle |
| 3 BCC_A2 Ta - CoTa2_C16 Tie Line | 18 Al7Ta5 - Laves_C14 - Epsilon_Al3Ta_D022 Tie Triangle |
| 4 BCC_A2 Ta - Sigma_D8b - Mu_D85 Tie Triangle | 19 Laves_C14 - Epsilon_Al3Ta_D022 - Al3Co Tie Triangle |
| 5 BCC_A2 Ta - Sigma_D8b - Mu_D85 Tie Triangle | 20 Laves_C14 - Al5Co2_D811 Tie Line |
| 6 Not analysed at 1000°C | 21 Not analysed at 1000°C |
| 7 Sigma_D8b - Mu_D85 Tie Line | 22 Laves_C14 - BCC_B2 Tie Line |
| 8 Not analysed at 1000°C | 23 L21 - BCC_B2 Tie Line |
| 9 ? - Mu_D85 Tie Line | 24 Not analysed at 1000°C |
| 10 Sigma_D8b - Mu_D85 Tie Line | 25 Laves_C36 - BCC_B2 Tie Line |
| 11 Sigma_D8b - Mu_D85 Tie Line | 26 Laves_C15 - BCC_B2 Tie Line |
| 12 Sigma_D8b, Laves_C14 | 27 Laves_C36 - BCC_B2 Tie Line |
| 13 Sigma_D8b - Mu_D85 - Laves_C14 Tie Triangle | 28 Laves_C15 - BCC_B2 Tie Line |
| 14 Mu_D85 - Laves_C14 Tie Line | 29 FCC_A1 Co - BCC_B2 - Laves_C15 Tie Triangle |
| 15 Not analysed at 1000°C | 30 FCC_A1 Co - BCC_B2 - Laves_C15 Tie Triangle |

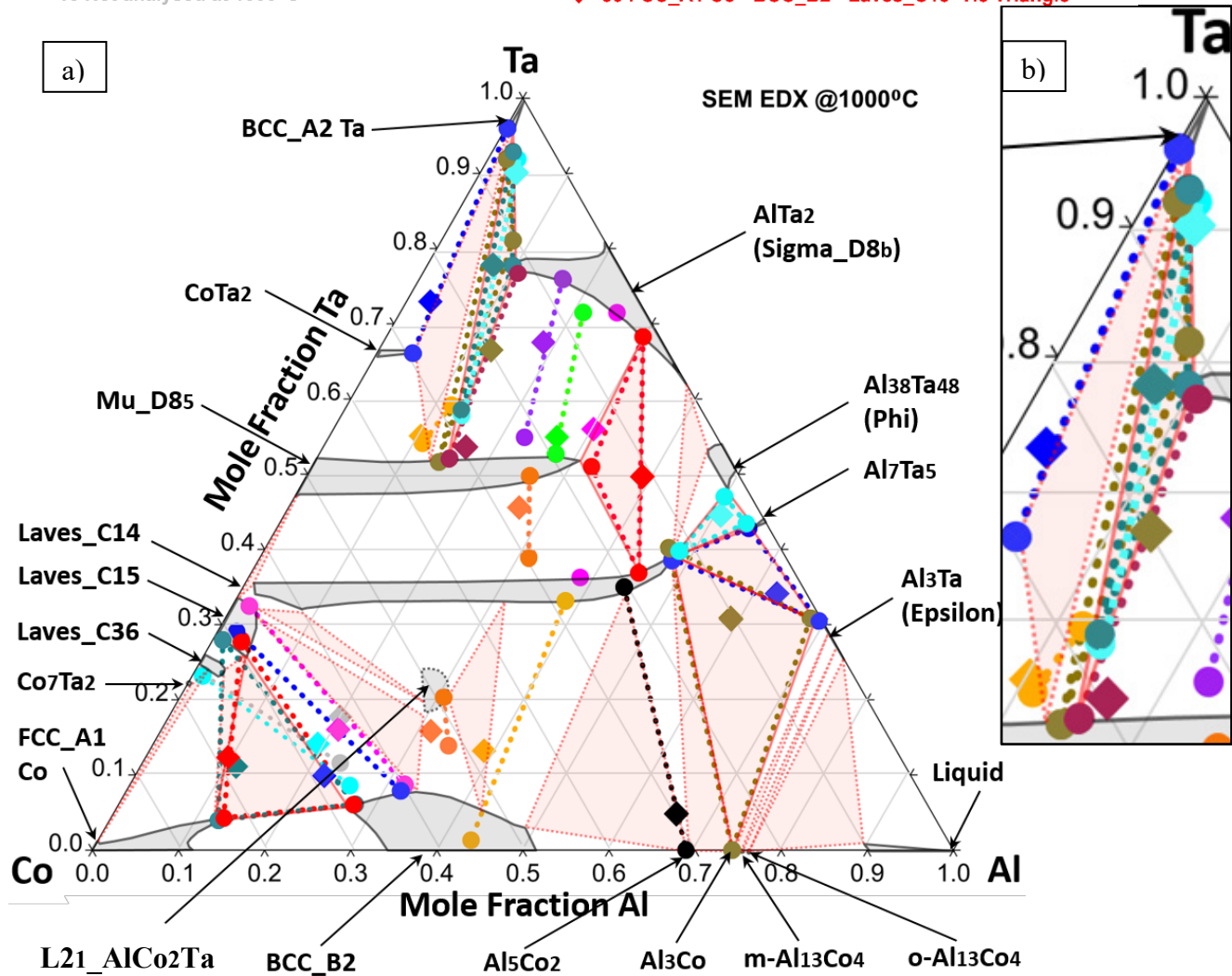


Figure 3.19: a) A ternary isothermal section for the Ta-Al-Co system at 1000°C, determined using SEM EDX analysis of 23 of the 30 different alloy samples after they were exposed to an isothermal hold for 1000Hrs at 1000°C, followed by a water quench. Average bulk alloy compositions from Table 3.1 are marked as solid diamonds, and average phase boundary compositions from Tables 3.2a & 3.2b are marked as solid circles. Tie lines and tie triangles are marked using thick dotted lines. b) A magnified image of the tie triangles in the Ta corner of the system.

Sample Number (Starting from Ta corner, moving to Al, then Co)

- | | |
|--|---|
| 1 Not analysed at 1000°C | 16 Not analysed at 1000°C |
| 2 BCC_A2 Ta - Mu_D85 Tie Line | 17 Phi_Al38Ta48 - Al7Ta5 - Laves_C14 Tie Triangle |
| 3 BCC_A2 Ta - CoTa2_C16 Tie Line | 18 Al7Ta5 - Laves_C14 - Epsilon_Al3Ta_D022 Tie Triangle |
| 4 BCC_A2 Ta - Sigma_D8b - Mu_D85 Tie Triangle | 19 Laves_C14 - Epsilon_Al3Ta_D022 - Al3Co Tie Triangle |
| 5 BCC_A2 Ta - Sigma_D8b - Mu_D85 Tie Triangle | 20 Laves_C14 - Al5Co2_D811 Tie Line |
| 6 Not analysed at 1000°C | 21 Not analysed at 1000°C |
| 7 Sigma_D8b - Mu_D85 Tie Line | 22 Laves_C14 - BCC_B2 Tie Line |
| 8 Not analysed at 1000°C | 23 L21 - BCC_B2 Tie Line |
| 9 ? - Mu_D85 Tie Line | 24 Not analysed at 1000°C |
| 10 Sigma_D8b - Mu_D85 Tie Line | 25 Laves_C36 - BCC_B2 Tie Line |
| 11 Sigma_D8b - Mu_D85 Tie Line | 26 Laves_C15 - BCC_B2 Tie Line |
| 12 Sigma_D8b, Laves_C14 | 27 Laves_C36 - BCC_B2 Tie Line |
| 13 Sigma_D8b - Mu_D85 - Laves_C14 Tie Triangle | 28 Laves_C15 - BCC_B2 Tie Line |
| 14 Mu_D85 - Laves_C14 Tie Line | 29 FCC_A1 Co - BCC_B2 - Laves_C15 Tie Triangle |
| 15 Not analysed at 1000°C | 30 FCC_A1 Co - BCC_B2 - Laves_C15 Tie Triangle |

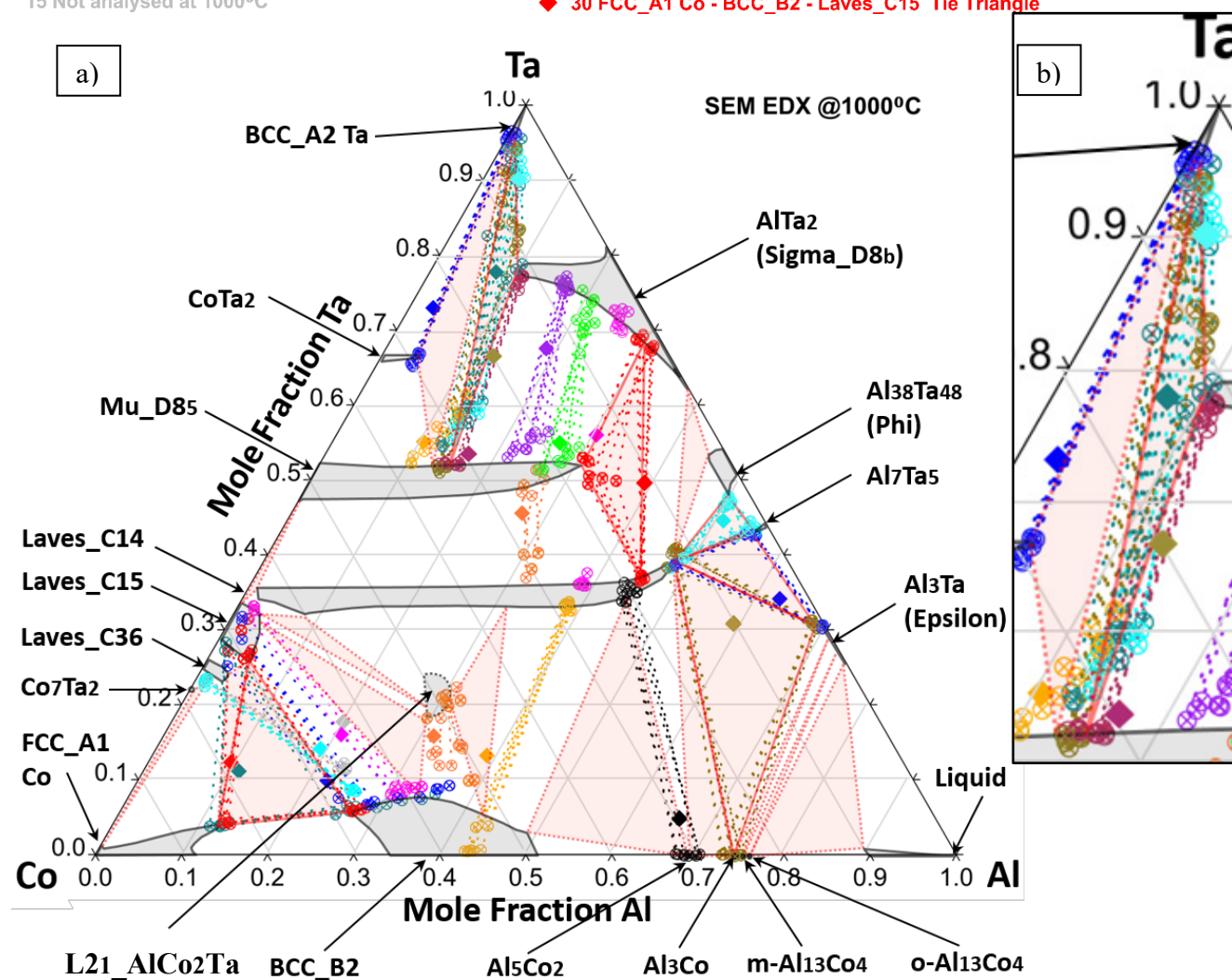


Figure 3.20: a) A ternary isothermal section for the Ta-Al-Co system at 1000°C, determined using SEM EDX analysis of 23 of the 30 different alloy samples after they were exposed to an isothermal hold for 1000Hrs at 1000°C, followed by a water quench. Average bulk alloy compositions from Table 3.1 are marked as solid diamonds, and all raw individually measured phase boundary compositions are marked as circles containing a cross. Tie lines and tie triangles are marked using dotted lines. b) A magnified image of the tie triangles in the Ta corner of the system.

Based on the results of a number of previous studies,[39], [40], [42], [45], [51] the thermodynamic assessment of Witusiewicz et al.,[97] yielded that the Sigma_D8_b phase has a solubility range that spans from approximately 62at% Ta to 81at% Ta in the Al-Ta binary at 1000°C. In Figure 3.19 the Sigma_D8_b phase extends out from these binary edge points, and along the ternary phase boundary points measured in samples 4, 5, 7, & 10-13, which are plotted on the figure, and also listed in Table 3.2a. The ternary extension of this phase is skewed upward towards higher Ta contents, and has a maximum ternary solubility of 9.93%Al-12.34%Co-77.73%Ta as measured in sample 4 (plotted in turquoise). The Sigma_D8_b phase forms equilibria with multiple other phases, as shown in Figure 3.19.

The Mu_D8₅ phase has a solubility range of approximately 47.5at% Ta to 52.5at% Ta in the Co-Ta binary at 1000°C.[72], [76], [100] This phase extends significantly into the Ta-Al-Co ternary along the phase boundary points measured in samples 2, 4, 5, 7, & 9-14, which are plotted on Figure 3.19, and also listed in Table 3.2a. The ternary extension of this phase was found to curve slightly upwards towards higher Ta contents, and not slightly downwards as reported by Hunt and Raman.[77] The Mu_D8₅ phase has a maximum ternary solubility of 32.48%Al-16.52%Co-50.99%Ta as measured in sample 13 (plotted in red).

The possibility that the ternary Mu prime phase reported by Hunt and Raman,[77] could be present above the Mu_D8₅ phase at a composition of around 22.5%Al-22.5%Co-55%Ta and a temperature of 1000°C was initially considered. This was based on the fact that in Figure 3.19, alloy samples 2, 4, 7, and 9 all show average phase boundary compositions that are slightly higher in Ta than the average phase boundary compositions found for the Mu_D8₅ phase in samples 5, 10, 11 & 13. However, looking at the at the raw data for each individual phase boundary composition measurement in Figure 3.20, it was concluded that the presence of the ternary Mu prime was unlikely, and that it was

more likely that the phase boundary compositions measured in this area in these samples simply corresponded to the boundary of the Mu_D8₅ phase. This was based on the rationale that the individual raw phase boundary composition points from samples 2, 4, 7, and 9 actually do stretch down close to top of the Mu_D8₅ phase boundary. It's just that these data points exhibit a significant amount of scatter, which when averaged, result in mean phase boundary compositions that are skewed upwards to slightly higher Ta contents, which are above the Mu_D8₅ phase boundary that they are supposed to represent. The reasons for this scatter are discussed in further detail in Section 3.4, but the net outcome is that these results do not seem to support the presence of the ternary Mu prime phase. This conclusion is in agreement with the findings of Dovbenko et al.,[75] rather than those of Hunt and Raman.[77]

In the Co-Ta binary, the Laves_C14 phase has a maximum solubility range of approximately 35at% Ta to 37at% Ta at 1390°C, and is only stable within the temperature range of 1300°C to 1600°C.[76] Figure 3.19 shows that despite not being present in the Co-Ta binary at 1000°C, this phase exhibits extensive ternary solubility at this temperature in the Ta-Al-Co system, as it stretches most of the way across the phase diagram, from an approximate composition of 1%Al-63%Co-36%Ta to a composition of 48%Al-12%Co-40%Ta. In this figure, the phase boundary of the Laves_C14 phase close to the Co-Ta binary has been estimated based on Dovbenko et al.'s findings for this phase in the Nb-Al-Co system.[75] However, as we move further from the Co-Ta binary edge, the boundary of the Laves_C14 phase in the Ta-Al-Co system at 1000°C has been plotted on the diagram based on the SEM EDX measurements of this boundary in alloy samples 13, 14, 17-20, & 22 from the present work.

The Phi_Al₃₈Ta₄₈ phase has a solubility range of 50.5at% Ta to 54at% Ta in the Al-Ta binary at 1000°C.[48], [50], [97] Figure 3.19 shows that this phase extends just over 3at%

into the Ta-Al-Co ternary to an average composition of 49.95%Al-3.06%Co-46.99%Ta, as measured in sample 17 (plotted on the diagram in light blue). The Al_7Ta_5 phase was also measured in sample 17, and also extends approximately 3at% into the ternary from approximately 42at% Ta in the Al-Ta binary at 1000°C.[50]

The Epsilon_ Al_3Ta_2 phase was measured in samples 18 and 19 to exhibit little to no ternary solubility, and to be present at a composition of 30%Ta-70%Al in the Al-Ta binary at 1000°C. A number of literature studies report that this phase has a composition of 25%Ta-75%Al in the Al-Ta binary at this temperature.[39], [40], [42], [50], [97] However, there is one study that reports this phase to have a maximum composition range spanning from 25 to 32at% Ta,[38] which is consistent with the results of the present work.

The boundaries of the liquid phase and the two peritectic compounds o- $\text{Al}_{13}\text{Co}_{14}$, and m- $\text{Al}_{13}\text{Co}_{14}$ at 1000°C in Figure 3.19, were taken from literature data on the Al-Co system,[96] and the boundaries of the other two peritectic compounds Al_3Co and Al_5Co_2 _D8₁₁ were measured from alloy samples 19 & 20 respectively. All four of these peritectic phases exhibit little to no binary or ternary solubility, and are considered to be stoichiometric compounds.

The BCC_B2 phase exhibits a solubility range of 34.5at% Al to 51.5at% Al in the Al-Co binary at 1000°C,[34], [96] and extends into the Ta-Al-Co ternary as shown in Figures 3.19 and 3.20. Its maximum ternary solubility is reached at around 8at% Ta, at a composition of approximately 34%Al-58%Co-8%Ta. These figures show that in the Ta-Al-Co system, the BCC_B2 phase is in equilibrium with many other phases at 1000°C. These are the: Al_5Co_2 _D8₁₁, Laves_C14, AlCo_2Ta _L2₁, Laves_C15, and FCC_A1 Co phases.

The AlCo_2Ta _L2₁ phase is a ternary Heusler type phase.[75] The centre of this phase is situated at a composition of around 29%Al-50%Co-21%Ta, in the Ta-Al-Co system at

1000°C, and the phase exhibits a solubility range of approximately 4at% in its Al and Co axes, and 6at% in its Ta axis,[75] The AlCo₂Ta_L2₁ phase is also in equilibrium with many other phases in this system at 1000°C as shown in Figures 3.19 and 3.20.

The Laves_C15 phase has a solubility range of approximately 29at% Ta to 33.5at% Ta in the Co-Ta binary at 1000°C.[72], [76], [100] This phase extends up to around 3.5at% into the Ta-Al-Co ternary along the phase boundary points measured in samples 26, 28, 29, & 30, which are plotted on Figures 3.19 & 3.20. The results from samples 26 & 28 are plotted in pink and royal blue respectively, and show tie lines between the Laves_C15 and BCC_B2 phases. And the results from samples 29 & 30 are plotted in turquoise and red respectively and show 3 phase tie triangles between the Laves_C15, BCC_B2, and FCC_A1 Co phases. The results from samples 25 and 27 plotted in grey and light blue, were not in good agreement with those from samples 26, 28, 29, & 30, and so were given less weight when deciding on the Laves_C15, and Laves_C36 phase equilibria for Figures 3.19 and 3.20. The reasoning for this decision will be discussed in further detail in Section 3.4.

The Laves_C36 phase has a narrow solubility range of approximately 25at% Ta to 26at% Ta at 1000°C, and is only stable within the temperature range of 960°C to 1448°C in the Co-Ta binary.[76] Initially there was some uncertainty as to whether the red tie triangle measured from sample 30 in Figures 3.19 & 3.20 was connected to the Laves_C15, or Laves_C36 phases. However, since the turquoise tie triangle measured in the same region of the phase diagram from sample 29, in the same figures, appears to completely bypass the Laves_C36 phase, to connect to the Laves_C15 phase, it was concluded that the red tie triangle from sample 30 was also likely to be connected to the Laves_C15 phase. If the Laves_C36 phase is indeed outside of this tie triangle measured from samples 29 & 30, then this phase must have a maximum ternary solubility of 2-3at%Al.

The Co_7Ta_2 phase is a peritectic compound that is present at 22at% Ta in the Co-Ta binary at 1000°C.[72], [76], [100] This phase appears to exhibit negligible solubility for other elements, outside of its stoichiometric composition in the Co-Ta binary or the Ta-Al-Co ternary, where it is in equilibrium with the Laves_C15, and FCC_A1 Co phases.

FCC_A1 Co is a terminal solid solution phase, that has solubilities of 12at% for Al in the Al-Ta binary,[16], [17], [31], [96] and 1.5at% for Co in the Co-Ta binary,[76] at 1000°C. In the Ta-Al-Co system, this phase extends in to the ternary to an average composition of 12.85%Al-83%Co-4.15%Ta, as measured in samples 29 and 30, and averaged from the values listed in Table 3.2b and plotted in turquoise and red in Figures 3.19 & 3.20. As can be seen from the figures, at 1000°C the FCC_A1 Co phase is in equilibrium with the BCC_B2, Laves_C15, Laves_C36, and Co_7Ta_2 phases.

The average phase boundary compositions measured via SEM EDX for all phases in all Ta-Al-Co alloy samples equilibrated at 1150°C are listed in Tables 3.3a, and 3.3b. These phase boundary compositions are plotted as tie lines and tie triangles, along with the bulk alloy compositions, on a ternary isothermal section for the system at this temperature. This ternary phase boundary data was also combined with the temperature matched binary phase boundary data for the Al-Co,[96] Al-Ta,[48]–[50], [97] and Co-Ta,[72], [76], [100] systems to produce an experimentally determined ternary isothermal section for the Ta-Al-Co system at 1150°C, which is shown in Figures 3.21 & 3.22.

A comparison of Figures 3.20 & 3.22 shows that the ternary isothermal sections for this system at 1000°C and 1150°C, look fairly similar. They share most of the same phases, which are generally in the same positions, however as expected, most phases generally have slightly increased binary and ternary solubility ranges at the higher of the two temperatures. The BCC_A2 Ta and CoTa₂_C16 phases look quite similar at both temperatures. However, the Mu_D8₅ phase is clearly wider and extends further into the ternary Co-Al-Ta system at 1150°C. It also curves upwards to higher Ta compositions slightly more, which appears to have correspondingly skewed the ternary boundaries of the Sigma phase upwards to marginally higher Ta compositions as well. The Laves_C15 phase looks quite similar at both temperatures, but it is also slightly wider, and extends a few at% further towards the Al-Ta binary edge of the ternary isothermal section.

Table 3.3a: Average phase boundary compositions measured via SEM EDX for all phases in alloy samples 1-16 that were exposed to an isothermal hold at for 500Hrs at 1150°C, followed by water quench. Each composition listed is the average of at least 5 measurements. (Continued overleaf in Table 3.3b for samples 18-30)

Alloy Sample No	Phase	Measured composition		
		At% Al	At% Co	At% Ta
1	BCC_A2 Ta	0.00 ± 0.00	3.78 ± 4.12	96.22 ± 4.12
	CoTa ₂ _C16	0.00 ± 0.00	36.47 ± 1.39	63.53 ± 1.39
2	BCC_A2 Ta	4.61 ± 1.36	8.20 ± 1.37	87.19 ± 2.50
	Mu_D8 ₅	14.03 ± 1.26	24.62 ± 3.67	61.35 ± 2.61
3
4
5	BCC_A2 Ta	0.90 ± 0.26	5.44 ± 0.65	93.66 ± 0.39
	Sigma_D8 _b	11.12 ± 1.50	10.88 ± 3.67	78.00 ± 5.07
	Mu_D8 ₅	15.23 ± 0.68	26.96 ± 2.63	57.81 ± 2.13
6	Sigma_D8 _b	11.97 ± 0.72	9.85 ± 1.66	78.18 ± 1.18
	Mu_D8 ₅	16.88 ± 0.90	26.30 ± 3.39	56.82 ± 2.76
7	Sigma_D8 _b	16.44 ± 1.14	6.94 ± 1.65	76.61 ± 1.35
	Mu_D8 ₅	23.46 ± 1.18	21.21 ± 3.83	55.32 ± 3.06
8	Sigma_D8 _b	20.76 ± 1.10	3.95 ± 0.79	75.29 ± 0.96
	Mu_D8 ₅	25.96 ± 1.35	18.36 ± 2.14	55.69 ± 1.10
9	BCC_A2 Ta	0.92 ± 0.37	8.09 ± 0.86	90.99 ± 0.99
	Mu_D8 ₅	10.89 ± 0.92	31.07 ± 3.61	58.04 ± 3.72
10	Sigma_D8 _b	11.59 ± 0.62	11.78 ± 0.60	76.63 ± 0.68
	Mu_D8 ₅	16.78 ± 0.88	32.18 ± 0.84	51.04 ± 0.28
11
12
13	Sigma_D8 _b	26.62 ± 1.77	0.98 ± 0.61	72.40 ± 2.09
	Laves_C14	46.23 ± 0.94	13.46 ± 2.00	40.31 ± 1.53
14
15	Mu_D8 ₅	32.46 ± 0.53	18.75 ± 0.41	48.78 ± 0.11
	Laves_C14	40.90 ± 0.40	20.29 ± 0.29	38.80 ± 0.11
16	Sigma_D8 _b	37.51 ± 0.21	1.77 ± 0.35	60.72 ± 0.31
	Laves_C14	47.58 ± 0.87	12.08 ± 2.19	40.34 ± 1.70
17

Table 3.3b: Average phase boundary compositions measured via SEM EDX for all phases in alloy samples 18-30 that were exposed to an isothermal hold at for 500Hrs at 1150°C, followed by water quench. Each composition listed is the average of at least 5 measurements. (Continued from Table 3.3a for samples 1-17)

Alloy Sample No	Phase	Measured composition		
		At% Al	At% Co	At% Ta
18
19
20
21	L2 ₁	33.09 ± 1.80	48.93 ± 2.29	17.98 ± 0.50
	BCC_B2	40.87 ± 1.05	43.04 ± 1.39	16.09 ± 0.34
22	Laves_C14	37.83 ± 0.26	28.02 ± 0.67	34.14 ± 0.41
	BCC_B2	42.33 ± 0.08	57.32 ± 0.10	0.35 ± 0.02
23	L2 ₁	29.32 ± 1.54	49.63 ± 1.47	21.05 ± 2.26
	BCC_B2	37.55 ± 0.17	51.62 ± 0.55	10.84 ± 0.38
24	Laves_C14	28.68 ± 0.63	39.40 ± 0.94	31.92 ± 1.02
	BCC_B2	34.49 ± 0.77	60.02 ± 0.29	5.49 ± 0.64
25	Laves_C36	1.79 ± 0.14	75.12 ± 0.40	23.09 ± 0.44
	BCC_B2	21.20 ± 0.14	66.37 ± 0.18	12.44 ± 0.14
26	Laves_C15	2.70 ± 0.62	67.95 ± 4.26	29.35 ± 4.08
	BCC_B2	27.40 ± 1.77	54.69 ± 3.77	17.91 ± 1.99
27	Laves_C36	1.62 ± 0.34	77.23 ± 0.63	21.15 ± 0.48
	BCC_B2	21.32 ± 0.84	71.34 ± 1.05	7.34 ± 0.43
28
29
30	Laves_C15	0.60 ± 0.12	72.56 ± 0.59	26.84 ± 0.47
	BCC_B2	18.17 ± 0.21	76.54 ± 0.22	5.29 ± 0.04
	FCC_A1 Co	12.21 ± 1.41	83.19 ± 1.93	4.61 ± 0.52

Sample Number (Starting from Ta corner, moving to Al, then Co)

- ◆ 1 BCC_A2 Ta - CoTa₂C₁₆ Tie Line
- ◆ 2 BCC_A2 Ta - Mu_D85 Tie Line
- 3 Not analysed at 1150°C
- 4 Not analysed at 1150°C
- ◆ 5 BCC_A2 Ta - Sigma_D8b - Mu_D85 Tie Triangle
- ◆ 6 Sigma_D8b - Mu_D85 Tie Line
- ◆ 7 Sigma_D8b - Mu_D85 Tie Line
- ◆ 8 Sigma_D8b - Mu_D85 Tie Line
- ◆ 9 BCC_A2 Ta - Mu_D85 Tie Line
- ◆ 10 Sigma_D8b - Mu_D85 Tie Line
- 11 Not analysed at 1150°C
- 12 Not analysed at 1150°C
- ◆ 13 Sigma_D8b - Laves_C14 Tie Line
- 14 Not analysed at 1150°C
- ◆ 15 Mu_D85 - Laves_C14 Tie Line
- ◆ 16 Sigma_D8b - Laves_C14 Tie Line
- 17 Not analysed at 1150°C
- 18 Not analysed at 1150°C
- 19 Not analysed at 1150°C
- 20 Not analysed at 1150°C
- ◆ 21 L21 - BCC_B2 Tie Line
- ◆ 22 Laves_C14 - BCC_B2 Tie Line
- ◆ 23 L21 - BCC_B2 Tie Line
- ◆ 24 Laves_C14, BCC_B2
- ◆ 25 Laves_C36 - BCC_B2 Tie Line
- ◆ 26 Laves_C15 - L21 Tie Line
- ◆ 27 Laves_C36 - BCC_B2 Tie Line
- 28 Not analysed at 1150°C
- 29 Not analysed at 1150°C
- ◆ 30 FCC_A1 Co - BCC_B2 - Laves_C15 Tie Triangle

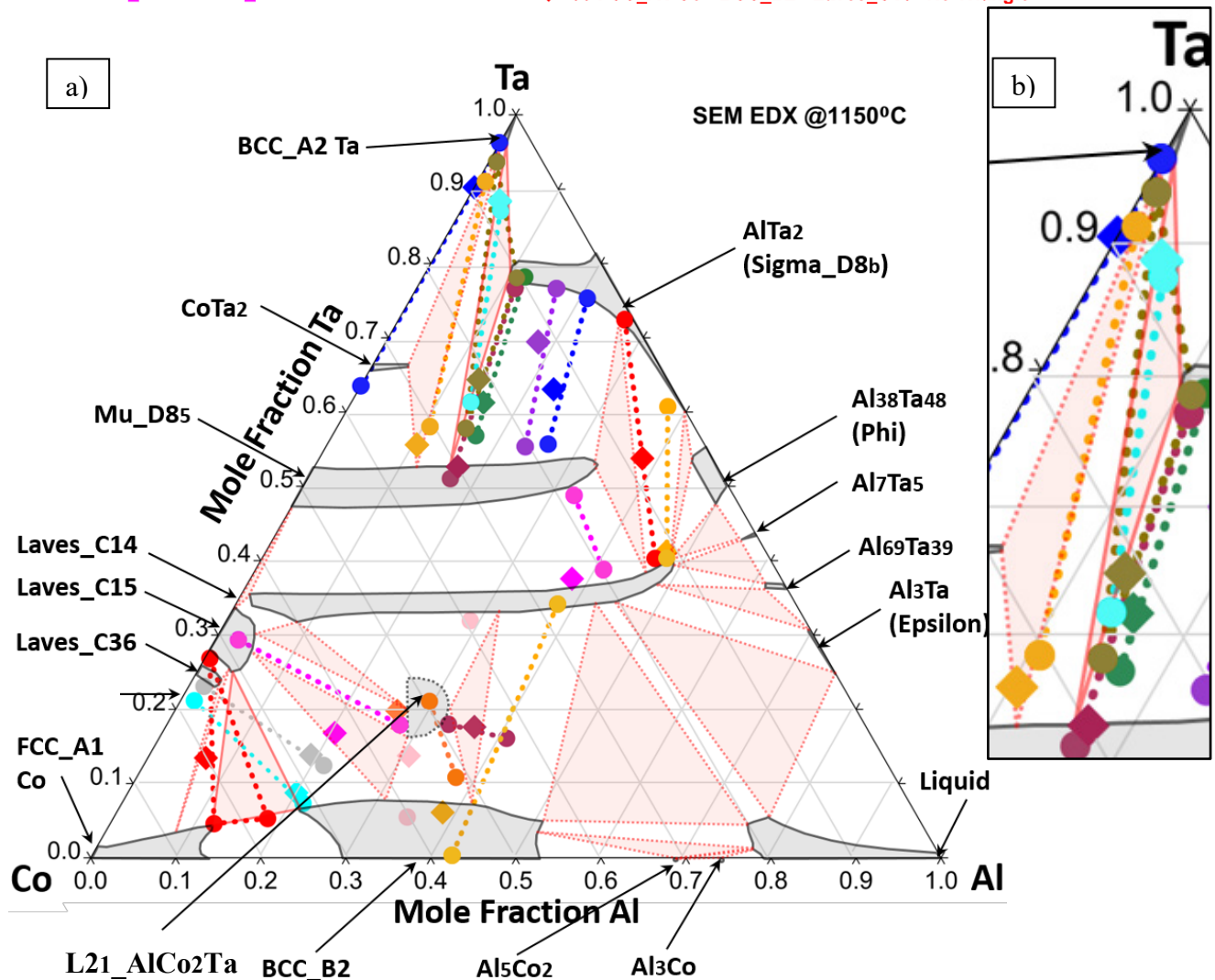


Figure 3.21: b) A ternary isothermal section for the Ta-Al-Co system at 1150°C, determined using SEM EDX analysis of 23 of the 30 different alloy samples after they were exposed to an isothermal hold for 500Hrs at 1150°C, followed by a water quench. Average bulk alloy compositions are marked as solid diamonds, and average phase boundary compositions from Tables 3.3a & 3.3b are marked as solid circles. Tie lines and tie triangles are marked using thick dotted lines. b) A magnified image of the tie triangles in the Ta corner of the system.

Sample Number (Starting from Ta corner, moving to Al, then Co)

- ◆ 1 BCC_A2 Ta - CoTa2_C16 Tie Line
- ◆ 2 BCC_A2 Ta - Mu_D85 Tie Line
- 3 Not analysed at 1150°C
- 4 Not analysed at 1150°C
- ◆ 5 BCC_A2 Ta - Sigma_D8b - Mu_D85 Tie Triangle
- ◆ 6 Sigma_D8b - Mu_D85 Tie Line
- ◆ 7 Sigma_D8b - Mu_D85 Tie Line
- ◆ 8 Sigma_D8b - Mu_D85 Tie Line
- ◆ 9 BCC_A2 Ta - Mu_D85 Tie Line
- ◆ 10 Sigma_D8b - Mu_D85 Tie Line
- 11 Not analysed at 1150°C
- 12 Not analysed at 1150°C
- ◆ 13 Sigma_D8b - Laves_C14 Tie Line
- 14 Not analysed at 1150°C
- ◆ 15 Mu_D85 - Laves_C14 Tie Line
- ◆ 16 Sigma_D8b - Laves_C14 Tie Line
- 17 Not analysed at 1150°C
- 18 Not analysed at 1150°C
- 19 Not analysed at 1150°C
- 20 Not analysed at 1150°C
- ◆ 21 L21 - BCC_B2 Tie Line
- ◆ 22 Laves_C14 - BCC_B2 Tie Line
- ◆ 23 L21 - BCC_B2 Tie Line
- ◆ 24 Laves_C14 , BCC_B2
- ◆ 25 Laves_C36 - BCC_B2 Tie Line
- ◆ 26 Laves_C15 - L21 Tie Line
- ◆ 27 Laves_C36 - BCC_B2 Tie Line
- 28 Not analysed at 1150°C
- 29 Not analysed at 1150°C
- ◆ 30 FCC_A1 Co - BCC_B2 - Laves_C15 Tie Triangle

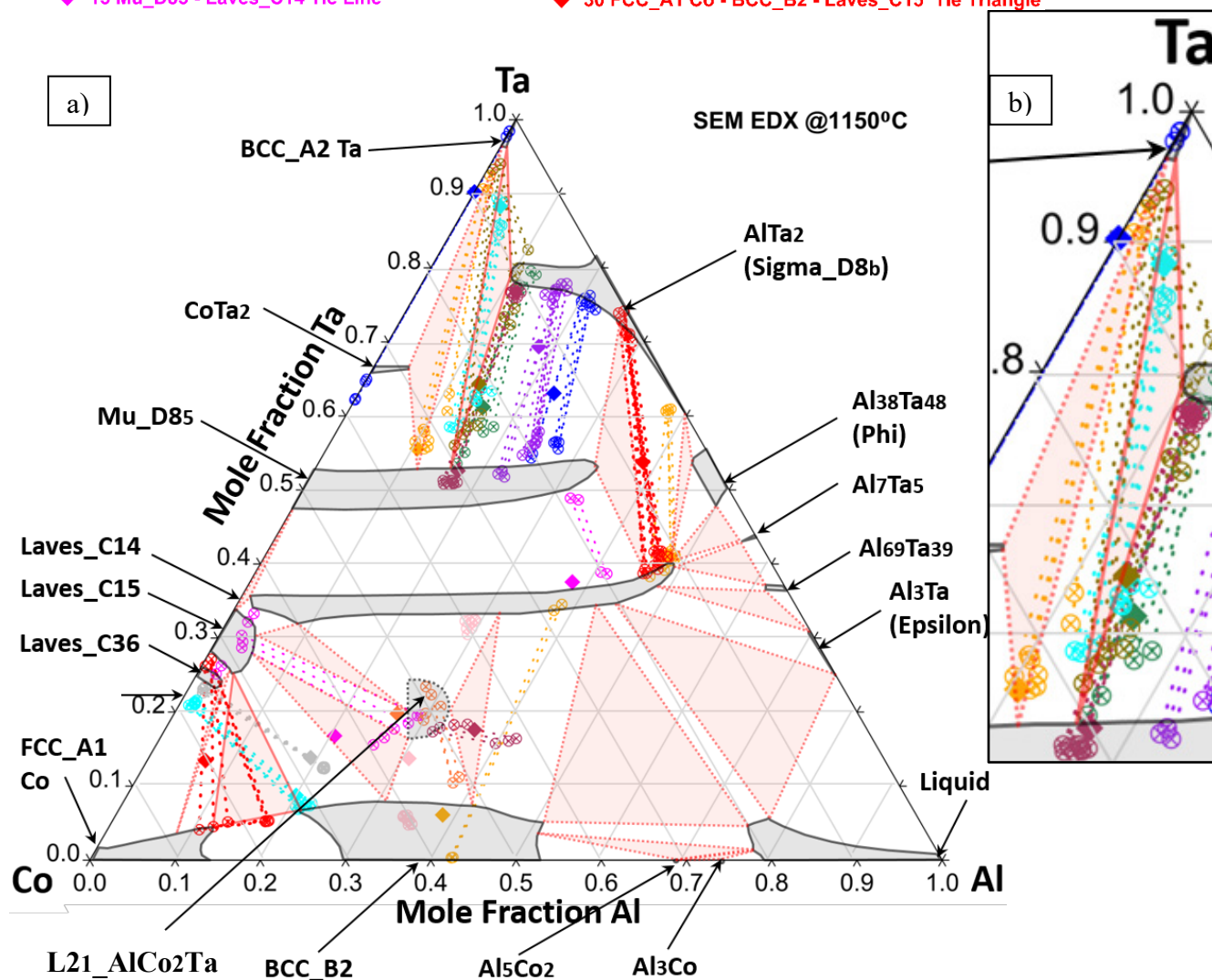


Figure 3.22: a) A ternary isothermal section for the Ta-Al-Co system at 1150°C, determined using SEM EDX analysis of 23 of the 30 different alloy samples after they were exposed to an isothermal hold for 500Hrs at 1150°C, followed by a water quench. Average bulk alloy compositions are marked as solid diamonds, and all measured phase boundary compositions are marked as circles containing a cross. Tie lines and tie triangles are marked using dotted lines. b) A magnified image of the tie triangles in the Ta corner of the system.

When comparing the composition measurements for the upper ternary boundary of the Mu_D8₅ phase in Figure 3.22, the BCC_A2 Ta to Mu_D8₅ tie lines generally put this boundary at a higher Ta content of around 55-63at% Ta compared to the Sigma_D8_b to Mu_D8₅ tie lines, which put the boundary at 50-55at%. The latter grouping of tie lines were given a higher weighting in determining the Mu_D8₅ phase boundary for the diagram than the former, since it was reasoned that latter phase pairing was likely to have gotten closer to equilibrium due to the lower melting point of the Sigma_D8_b phase (ca. 2000°C[97]) compared to the BCC_A2 Ta phase (ca. 3000°C[97]).

The boundaries for the Phi_Al₃₈Ta₄₈, Al₇Ta₅, Al₆₉Ta₃₉, Epsilon_Al₃Ta_D0₂₂, Liquid, Al₃Co and Al₅Co₂_D8₁₁ phases at 1150°C in Figures 3.21 & 3.22 were estimated based on literature data from the binary systems,[34], [48]–[50], [96], [97] and on the ternary data from this work at 1000°C, since samples 17-19 from this area of the phase diagram were analysed at 1000°C, but not 1150°C. The Phi_Al₃₈Ta₄₈, Al₇Ta₅, Al₆₉Ta₃₉ phases generally extend into the ternary by a maximum of 2-3at%. The Epsilon_Al₃Ta_D0₂₂, Al₃Co and Al₅Co₂_D8₁₁ phases do not appear to exhibit any ternary solubility. And the liquid phase field at 1150°C is significantly larger than at 1000°C. At the former temperature it extends from the Al corner along the Al-Co binary edge to 21at% Co, whereas at the latter it only extends to approximately 9-10at% Co.[34], [96]

The BCC_B2 phase also exhibits an increased solubility range of 30at% Al to 53at% Al in the Al-Co binary at 1150°C,[34], [96] and extends into the Ta-Al-Co ternary as shown in Figure 3.22. Its maximum ternary solubility is again reached at around 8at% Ta. Not all of the ternary boundary measurements for this phase were in agreement with each other, so the boundary was drawn based on the best compromise between the results of samples 22-27, & 30. Generally alloy samples 23, 24, 27 and 30 all put this ternary boundary

somewhere in the 6-11 at % Ta range, which was also in good agreement with the results from most of the same alloys at 1000°C. The results from samples 21-23, were quite different from each other, and will be discussed in more detail in Section 3.4.

The $\text{AlCo}_2\text{Ta}_{L2_1}$ ternary Heusler phase is still centred at a composition of around 29%Al-50%Co-21%Ta, in the Ta-Al-Co system at 1150°C, however its solubility range of approximately 6at% in its Al and Co axes, and 8at% in its Ta axis, is larger than it was at 1000°C. The increase in the size of this phase field, with increasing temperature, has also caused a corresponding increase in the size of the Laves_C15 to $\text{AlCo}_2\text{Ta}_{L2_1}$ two phase field, such that sample 26 plotted in dark pink in Figures 3.21 & 3.22 is now situated in this two phase field at 1150°C, when this sample was measured as being predominantly Laves_C15 and BCC_B2 at 1000°C. The Laves_C15 phase has a solubility range of approximately 27.5at% Ta to 33.5at% Ta in the Co-Ta binary at 1150°C, [72], [76], [100] and it extends up to 3.5 to 4at% into the Ta-Al-Co ternary along the phase boundary points measured in sample 26. The Laves_C36 phase has a narrow solubility range of approximately 25at% Ta to 26at% Ta at 1150°C.[76] This phase must have a maximum ternary solubility of 2-3at%Al at 1150°C, to remain outside the Laves_C15, BCC_B2, and FCC_A1 Co tie triangle measured from sample 30, plotted in red in Figures 3.21 & 3.22. The FCC_A1 Co phase has solubilities of 14at% for Al in the Al-Ta binary,[16], [17], [31], [96] and 3.5at% for Co in the Co-Ta binary,[76] at 1150°C. In the Ta-Al-Co system, this phase extends in to the ternary to an average composition of 12.21%Al-83.19%Co-4.61%Ta, as measured in sample 30.

The results at 1150°C from samples 25 and 27 plotted in grey and light blue, were again not in good agreement with those from sample 30, which was also the case at 1000°C. At both temperatures SEM EDX measurements the former samples yielded Laves_C36 – BCC_B2 tie lines, yet measurements from samples 26, 28, 29, & 30 at 1000°C,

and samples 30 at 1150°C, all produced Laves_C15 - BCC_B2 phase tie lines. In the end the phase diagram at 1150°C in Figures 3.21 & 3.22 was plotted based on the majority grouping of samples 26, 28, 29, & 30, giving less weight to samples 25 and 27. Possible reasons for the disagreement between these samples will be discussed in further detail in Section 3.4.

3.4: Discussion

As previously mentioned in Section 3.3.4, the phase boundary lines in the ternary isothermal sections shown in Figures 3.19, 3.20, 3.21, & 3.22 were drawn based on the EDX measured phase boundary compositions from alloys 1-30, after they were equilibrated at 1000°C, and 1150°C. It can be seen from these figures that although the results from most of the samples were generally in good agreement with each other and enabled the boundaries of all phases in the system to be mapped with reasonable accuracy, certain decisions had to be made regarding how best to fit the phase boundary lines to the measured data points. It is normal to see some degree of statistical scatter in such measurements, and in most cases the measured boundary positions for specific phases varied by only a few atomic percent from sample to sample. However, there were a few cases where certain samples disagreed by more significant margins, therefore it was decided that the best course of action would be to critically evaluate the results from each sample based on certain criteria, and give the samples that were judged to yield the most accurate results a higher weighting in determining the phase boundaries, rather than simply plotting average lines of best fit through all of the measured data points.

These criteria will be outlined briefly below, and then explained with reference to certain samples shortly afterwards. Firstly, in cases where numerous samples were in good agreement with each other as to the position of a certain phase boundary, or tie line, but one or two other samples diverged significantly from the majority of the group, a higher weighting was usually given to the majority grouping of samples that agreed with each other, and a lower weighting was given to the outlying samples, unless there was a relevant explanation for their differing position. Secondly, in cases where one or more samples in the same phase field

disagreed with each other with regards to a phase boundary composition, a higher weighting was generally given to the sample with the bulk alloy composition closest to the phase boundary of interest, and a lower weighting was given to the sample with the bulk alloy composition furthest from the phase boundary of interest. So essentially, phase boundary compositions that were measured in samples with bulk alloy compositions closer to the phase being measured, were considered likely to be more accurate than phase boundary compositions that were measured in samples where the bulk alloy composition was much further away from the phase being measured. Thirdly, in cases where samples in different two or three phase fields disagreed with regards to the same phase boundary, a higher weighting was generally given to the samples with the lowest melting points. This is because samples that contain lower melting point phases would be likely to reach equilibrium more quickly during heat treatments than samples that contain higher melting point phases, and would therefore also be more likely to be in an equilibrium state post heat treatment. And finally, some consideration was given as to how well the measured phase boundaries agreed with established literature data. However, since the available data on the Ta-Al-Co system is somewhat limited, most of the literature data used for this comparison came from investigations into the binary subsystems of this ternary. On occasion some of these criteria may clash with one another, so a certain degree of individual judgement as to the dominant factors behind certain results was required.

If we take the phase boundary of the BCC_A2 phase in Figures 3.19 to 3.22 as an example, the ternary phase boundaries of this phase were plotted giving more weight to the results from alloy samples 1 & 3 (both plotted in royal blue), rather than those of samples 2, 4, 5, & 9 (plotted in light blue, turquoise, gold, and light orange). This decision was based on the fact that the ternary extensions of 3-4at% for this phase measured in samples 1 & 3,

were more in line with the 2-4at% solubility for Co reported in this phase in the Co-Ta binary at these temperatures in the literature.[76], [100] The weight of the majority was with samples 2, 4, 5, & 9, however the 7-12 at% ternary extensions for this phase measured in these samples are at least two times larger than the values reported in the literature for the Co-Ta binary. It is possible that the 1000hrs at 1000°C, and 500hrs at 1150°C heat treatments were not sufficient times and temperatures to allow certain alloys to fully reach equilibrium conditions, given that the BCC_A2 phase has a melting point in the region of 3000°C. Therefore due to the support from literature data, the more conservative ternary boundaries for this phase measured in samples 1 & 3 were preferred over the larger majority consensus boundaries measured in samples 2, 4, 5, & 9.

The boundaries of the Sigma_D8_b and Mu_D8₅ phases have been plotted based on the SEM EDX results from samples 2, & 3-16. Looking at the Sigma_D8_b phase boundaries in in Figures 3.19 to 3.22, virtually all of the samples that contain this phase are in fairly good agreement as to where its boundaries are situated. When it comes to the upper boundary of the Mu_D8₅ phase there is slightly more scatter in the results from different samples. However, these samples can essentially be split into two camps. Generally speaking the samples that contain BCC_A2 - Mu_D8₅ equilibria, or have bulk compositions that are further from the Mu_D8₅ phase, such as samples 2 & 4, put the Mu_D8₅ phase upper boundary at around 60 at% Ta. Whereas, samples that contain Sigma_D8_b - Mu_D8₅ equilibria, or have bulk compositions that are closer to the Mu_D8₅ phase, such as samples 5-14, put the Mu_D8₅ phase upper boundary closer to around 52-55 at% Ta. The latter grouping of samples 5-14 were given a much greater weighting when plotting the Mu_D8₅ phase boundary, since they fit much better with the aforementioned selection criteria. Firstly they were the majority grouping, secondly they had bulk compositions closer to the phase of interest, thirdly they

generally had lower melting points, and finally, they agreed better with the available literature data.[75], [77] In addition, when you compare the average Mu_D8_5 phase boundary given for the minority grouping of samples 2 & 4, plotted in light blue and turquoise in Figure 3.19, with the raw data from these samples plotted in Figure 3.20, it seems that the extreme outer edge of the range for these raw data points is actually in good agreement with those of the majority grouping of samples 5-14 anyway. It's just that the larger range of scatter observed in the raw measurements for samples 2 & 4 simply pulled their average values slightly upwards to higher Ta compositions. This is an example of samples that have bulk alloy compositions that are further away from the phase of interest generally exhibiting significantly more scatter in the EDX measurements of the boundaries of that phase in comparison to samples that have bulk compositions that are closer to the phase of interest. These results highlight the importance of looking closely at the raw individual tie line measurements, and not just completely relying on averaged data. Since certain raw data points may be more accurate than others, especially in cases where the bulk alloy composition is in a two or three phase field, but is much closer to the boundary of one specific phase, and therefore also much further away from that of the other phase(s).

The Sigma_D8_b - Mu_D8_5 tie lines from samples 7 and 11, plotted in purple and light green respectively in Figures 3.19 & 3.20 provide perfect case study examples to explain the reasoning behind this phenomenon in more detail. From these figures it can be seen that the bulk alloy composition of sample 7, plotted in purple, is closer to the Sigma_D8_b phase than it is to the Mu_D8_5 phase. Consequently in Figure 3.20, the raw individual phase boundary composition measurements for the Sigma_D8_b phase in this sample are tightly clustered with very little scatter, and the average boundary composition for this phase in this sample is in perfect agreement with that of the majority of other samples. Conversely, since

the bulk alloy composition of sample 7 is further from the Mu_D8₅ phase, the raw individual phase boundary composition measurements for this phase in this sample exhibit significantly more scatter. And in Figure 3.19, the average boundary composition for this phase in this sample is pulled upwards into the two phase region, slightly away from that of the other surrounding samples. The same phenomenon also occurs in sample 11, plotted in light green in Figures 3.19 & 3.20, but the effect is reversed compared to sample 7, plotted in purple. Since sample 11 has a bulk alloy composition that is closer to the Mu_D8₅ phase and further from the Sigma_D8_b phase, Figure 3.20 shows that in this sample the raw individual measurements are more tightly clustered at the Mu_D8₅ phase boundary and exhibit significantly more scatter at the Sigma_D8_b boundary. This again results in average phase boundary compositions that are in good agreement with the surrounding samples for the phase closest to the bulk alloy composition, and worse agreement with the surrounding samples for the phase furthest away from it.

Generally it can be said that phase boundary measurements made via EDX in samples with bulk alloy compositions closer to the boundary of the phase of interest can be considered to be more accurate than measurements made in samples with bulk alloy compositions that are further away from that phase. In such cases, the alloy would contain more of the phase that is closest to the bulk alloy composition, and less of the phases that are further away from it. When measuring the boundary composition of a low volume fraction phase, or a phase that consists of very small or thin precipitates (i.e. 1-3 μ m), in a multi-phase microstructure, the probability of also accidentally sampling some of the more abundant phase(s) increases. Therefore, boundary composition measurements of phases that are closer in composition to the overall bulk alloy composition are usually more accurate. And boundary composition measurements of phases that are further away from the bulk alloy composition generally

exhibit significantly more scatter, since some of these measurements could end up being slightly in the multi-phase region, rather than being exactly on the phase boundary of interest. In the latter case it makes sense to select the data points out of the scatter that extend the furthest towards the phase as being the most accurate, as they are more likely to be closer to the actual phase boundary compositions. And the data points that do not extend so far, are more likely to be in the multiphase region rather than at the exact phase boundaries. So, if you simply take the average of a set of scattered phase boundary composition measurements, the less accurate data points can actually pull this average away from the more accurate points, and therefore result in an average phase boundary composition that is slightly away from the actual phase boundary composition. This is one of the reasons why the above mentioned criteria were applied when plotting the phase boundaries for the isothermal sections in the present work, which were based on the raw measured tie lines in Figures 3.20 & 3.22, rather than simply plotting lines of best fit through the averaged data in Figures 3.19 & 3.21.

Figure 3.23 shows that the Ta-Al-Co isothermal section at 1000°C produced in the present work shares some similarities with that produced by Hunt and Raman.[77] However, there are also a few significant differences between the two diagrams. The key difference is that the results of this work indicate that the Mu_{D85} phase actually appears to curve upwards slightly towards the Sigma_{D8b} phase and higher Ta compositions as it extends into the ternary, rather than downwards and towards the Laves_{C14} phase, as proposed by Hunt and Raman.[77] Tie line measurements from samples 7, 8, & 11 plotted in purple, royal blue, and light green in Figures 3.19 - 3.23 are situated in the area where the Mu prime phase was reported to be present, however they do not appear to support the existence of this phase. Instead these results, in combination with those of the surrounding samples, actually indicate that the Mu_{D85} phase itself curves upwards to occupy the space close to where the

Mu prime ternary phase was reported to be, and that what was thought to be the Mu prime phase is actually just the upper boundary of the ternary extension of the Mu_D8₅ phase.

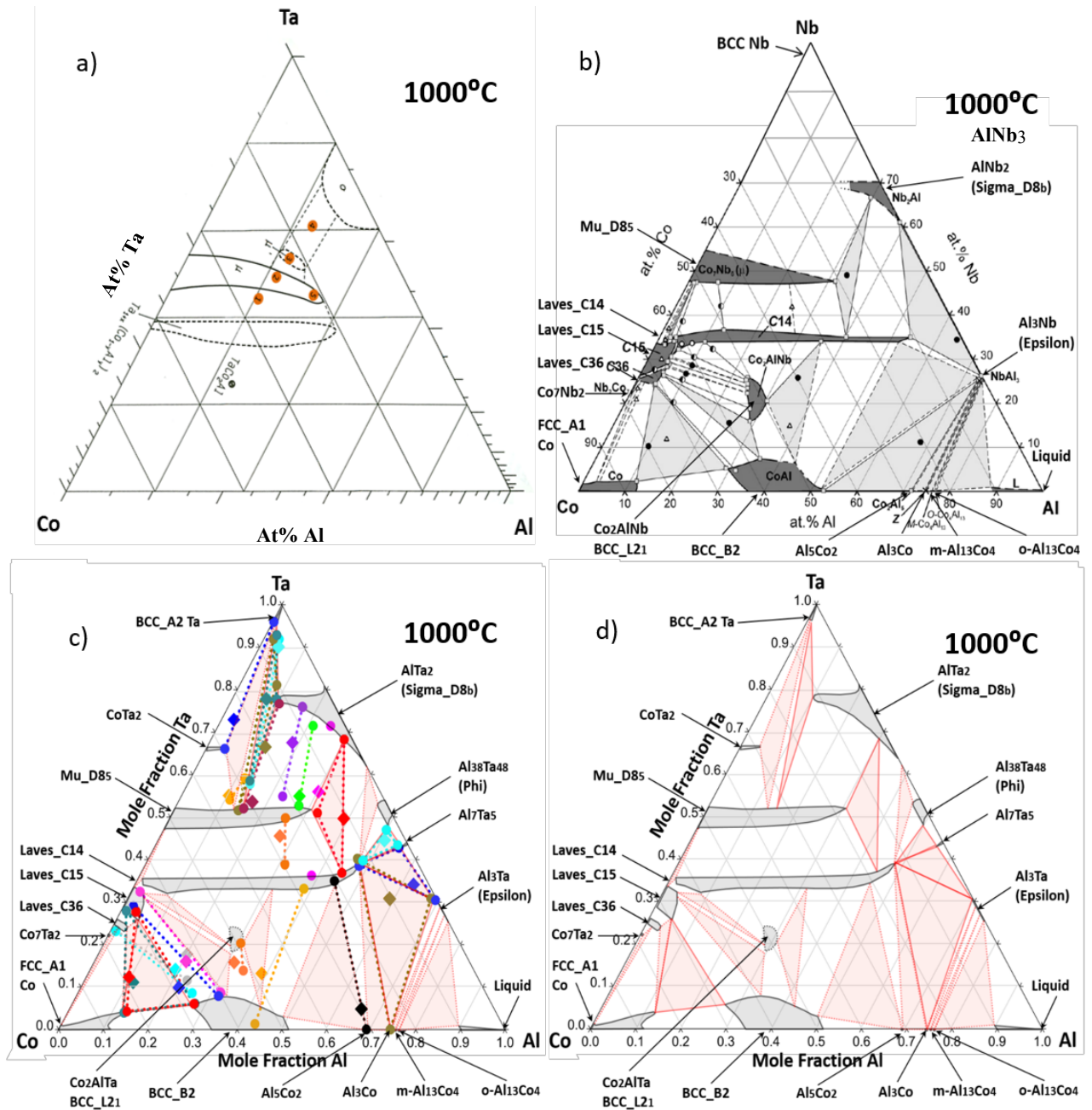


Figure 3.23: A comparison between (a) Hunt and Raman's partial ternary isothermal section for the Ta-Al-Co system at 1000°C,[77] (b) Dovbenko et al.'s temperature matched isothermal section for the Nb-Al-Co system,[75] and (c) & (d) the temperature matched isothermal section produced for the Ta-Al-Co system in this work, with and without averaged SEM EDX data respectively.

This conclusion is also supported by the results of Dovbenko et al.[75] who investigated this region of the Nb-Al-Co system at 1150°C via SEM EDX, electron probe micro-analysis (EPMA), and XRD, and did not find any sign of the ternary Mu prime phase reported at 1000°C in both the Nb-Al-Co and Ta-Al-Co systems by Hunt and Raman.[77] In fact, all of the tie lines measured from samples in in this area of the phase diagram, both in the present work (samples 7, 8, & 11), and also in the study by Dovbenko et al.[75] all show the same thing, which is that the Sigma_D8_b phase is directly in equilibrium with the Mu_D8₅ phase. And that there are no signs of the Mu prime phase or any other ternary phase in this region of the phase diagram. When comparing these results, it is also important to note that the alloys studied by Hunt and Raman.[77] were only heat treated for 168 hours at 1000°C, whereas the alloys studied in this work, and the work of Dovbenko et al.[75] were heat treated for 1000 hours at 1000°C. Moreover, based on observations from this work, I find it likely that 168 hours is probably not long enough to reach a practical equilibrium at 1000°C.

So, unfortunately the Ta-Al-Co system does not appear to contain a disordered BCC_A2 Ta to ordered BCC intermetallic two phase field, which rules out the possibility that this ternary could be used as a base system for a two phase precipitate strengthened Ta alloy. However, this system is still an important ternary subsystem of both Ni, and Co based superalloys, so the experimental data and phase diagrams produced by the present work may still be useful for future alloy design purposes. In any case, the production of complete ternary isothermal sections for the Ta-Al-Co system at 1000°C and 1150°C, shown in Figures 3.19 - 3.22, represents a significant step forward in terms of our knowledge on this system compared to the previously available data, which consisted of the single partial ternary isothermal section at 1000°C produced by Hunt and Raman in 1968.[77]

When comparing the Nb-Al-Co isothermal section at 1000°C produced by Dovbenko et al.,[75] shown in Figure 3.23b, to the temperature matched Ta-Al-Co isothermal section produced in the present work, shown in Figure 3.23c&d it is apparent that the Ta-Al-Co system basically contains almost all of the phases that are present in the Nb-Al-Co system, excluding the AlNb_3 phase only. Moreover, many of these phases also exhibit fairly similar binary and ternary composition ranges in both systems. However, once again despite these similarities, there are also a number differences between the two systems as well.

In the Nb-Al-Co system, the presence of AlNb_3 phase at around 80at% Nb, means that the Sigma_D8_b AlNb_2 phase is limited to a composition of around 60-70at% Nb in the Al-Nb binary, and extends into the ternary at around 66-70at% Ta. This also has a knock on effect on the Mu_D8_5 phase, making its ternary extension thinner and more triangular shaped in the Nb-Al-Co system compared to its Ta-Al-Co counterpart. In the Ta-Al-Co system, the absence of an equivalent to AlNb_3 , has resulted in a much wider binary solubility for the Sigma_D8_b phase, which stretches from around 62-82at% Ta in the Al-Ta binary, and extends significantly into the ternary at around 76-80at% Ta. Since the Sigma_D8_b phase is skewed upward to much higher Ta compositions in the Ta-Al-Co system, this gives more space for the ternary extension of the Mu_D8_5 phase, which is thicker than its Nb-Al-Co counterpart, and it also curves upwards slightly more, towards the Sigma_D8_b phase and higher Ta compositions.

The Ta-Al-Co system also contains four extra phases that are not present in the Nb-Al-Co ternary. These are: CoTa_2 _C16, $\text{Phi_Al}_{38}\text{Ta}_{48}$, Al_7Ta_5 , & $\text{Al}_{69}\text{Ta}_{39}$. All of these extra phases only extend a few atomic percent into the ternary, but the combination of these phases with the differences to the Sigma_D8_b phase, and the highly stable, and slightly upward curving Laves_C14 phase results in some major differences to the two and three phase regions in the Ta and Al corners of the Ta-Al-Co phase diagram, as shown by the tie lines and tie

triangles in Figure 3.23c, compared to those in Figure 3.23b. The Co corner of both ternary systems are generally fairly similar, but there are a few differences that will be discussed in further detail below.

The BCC_B2 phase boundary in Figures 3.19 – 3.23, was plotted based on the results from samples 21 to 30. This phase has a large solubility range in the Al-Co binary, and extends into the ternary up to a maximum of 8at% Ta at 1000°C and 1150°C, and so it forms equilibria with many other phases in the Ta-Al-Co system, as shown in the aforementioned figures. The ternary boundary of this phase appears to be pretty similar in both the Ta-Al-Co, and Nb-Al-Co systems. Samples 26-30 are generally all in good agreement as to the position of the ternary BCC_B2 phase boundary, however, samples 21-25 do not agree quite so well. Therefore this boundary was mostly plotted based on the results from samples 26-30, with an attempted line of best fit extending through the scatter that was yielded by samples 21-25.

The SEM EDX results from samples 21, 22 and 24 in Figure 3.15 and 3.16 show that the BCC_B2 phase forms a two phase ternary eutectic region with the ternary extension of the Laves_C14 phase. Moving leftwards from there to higher Co concentrations yields a Laves_C14 – Ternary L2₁ – BCC_B2 three phase tie triangle. The results from samples 21 and 23 in Figure 3.15 show that moving further leftwards again yields a ternary L2₁ - BCC_B2 two phase region, where the BCC_B2 phase is surrounded by an interconnected network of the ternary L2₁ phase. Figures 3.19 – 3.23 show that the results from these samples are generally in good agreement with regards to the ternary boundary of the Laves_C14 and ternary L2₁ phase, however they don't agree so well on the boundary for the BCC_B2 phase. In Samples 21 and 23, the phase boundaries of the ternary L2₁ phase could be measured with reasonable consistency, but this interconnected network of ternary L2₁ phase made it difficult to measure the boundary of the BCC_B2 phase without also inadvertently sampling some of

the ternary L2₁ phase. This resulted in the measurements for the boundary compositions of the BCC_B2 phase in these samples yielding higher Ta compositions, which placed the measured boundary position in two or three phase regions that were above the actual BCC_B2 phase boundary as shown in Figures 3.19 – 3.22. In samples 22 and 24, both the Laves_C14 and BCC_B2 phase compositions could be measured with no problems. However, the BCC_B2 phase boundary measurement appears to be too low in Ta, and it does not fit well with the measurements from the surrounding samples. The reason for this discrepancy is unclear, although one possible explanation may be that the initial formation of the as cast Laves_C14 – BCC_B2 phase eutectic structure, created a Ta depleted region in the surrounding BCC_B2 phase. And that the subsequent heat treatments were not sufficient to facilitate diffusion to an equilibrium state in these samples due to the stability of the intermetallic Laves_C14 phase. As a result of the discrepancies between the results from samples 21-25, the BCC_B2 phase boundary was mostly plotted based on the results from samples 26-30, with an attempted line of best fit extending through the scatter that was yielded by samples 21-25.

Figure 3.23 shows that the Co corner of the Ta-Al-Co, and Nb-Al-Co ternary isothermal sections are very similar at 1000°C. They contain the same phases, and these phases all have fairly similar ternary solubilities. The key differences between the phase equilibria of these two systems at this temperature appears to be connected to the size of the ternary L2₁ phase field, and how this phase and the BCC_B2 phase interact with the three laves phases that originate from the Co-Ta binary.

Figures 3.19, 3.20 & 3.23c show that the SEM EDX phase boundary measurements from samples 26 & 28-30, plotted in pink, royal blue, turquoise and red have all yielded that at 1000°C, the BCC_B2 and FCC_A1 Co phases both appear to be in equilibrium with the

Laves_C15 phase. Samples 29 & 30, plotted in red and turquoise mark out the Laves_C15 - BCC_B2 - FCC_A1 Co tie triangle, and samples 26 & 28, plotted in pink and royal blue show tie lines that mark out a significant Laves_C15 - BCC_B2 two phase region. The ternary L2₁ phase is relatively small, and it only has a very thin two phase region with the Laves_C15 phase. In contrast, samples 25 & 27, plotted in light blue and grey in Figures 3.19, 3.20 & 3.23c, disagree with samples 29-30, and indicate that the BCC_B2 phase should also be in equilibrium with the Laves_C36 phase and that the tie triangle in this region should actually be between the Laves_C36 - BCC_B2 - FCC_A1 Co phases rather than the Laves_C15 - BCC_B2 - FCC_A1 Co phases. The results from samples 25 & 27 fit better with Dovbenko et al.'s temperature matched isothermal section for the Nb-Al-Co system in which the BCC_B2 and FCC_A1 Co phases are both in equilibrium with the Laves_C36 phase, and not the Laves_C15 phase, and the ternary L2₁ phase is larger, so this phase takes over the equilibrium with the Laves_C15 phase in this region. However, despite the results of samples 25 & 27 matching better with Dovbenko et al.'s Nb-Al-Co phase diagram, the phase boundaries for the diagrams produced in this work were plotted based on the results from samples 26 & 28-30, rather than those from samples 25 & 27, based on the results selection criteria outlined at the start of Section 3.4.

Firstly, Figures 3.19 & 3.20 show that the results from samples 26 & 28-30, plotted in pink, royal blue, turquoise and red, are all in very good agreement with each other with regards to the BCC_B2, and Laves_C15 phase boundaries, making them the majority grouping, and samples 25 & 27, plotted in light blue and grey, the minority grouping. And secondly, despite having bulk alloy compositions that are closer to the BCC_B2 phase than they are to the laves phases, samples 25 & 27 put the BCC_B2 phase boundary at least 2-6at% further into the ternary than any of the other samples do. The increased ternary solubility for the BCC_B2

phase in these two samples raises the possibility that they may not have been fully equilibrated at the selected heat treatment temperature. And that the increased ternary solubility for the BCC_B2 phase in these samples is actually representative of the boundary for this phase at a higher temperature condition left over from the initial arc melting procedure.

Support for the theory that alloys 25 and 27 may be in a higher temperature condition comes from a comparison of Figures 3.19 & 3.20 to Figures 3.21, 3.22 & 3.23b, which show that the size of the BCC_B2 – Laves_C15 two phase region in these systems is somewhat dependent upon the presence and size of the ternary L2₁ phase. At lower temperatures the ternary L2₁ phase and therefore also L2₁ – Laves_C15 two phase region is smaller and consequently the BCC_B2 – Laves_C15 two phase region is larger. However, as the ternary L2₁ phase gets larger with increasing temperature, so does the size of the two phase region that it forms with the Laves_C15 phase, which in turn reduces the size of the BCC_B2 - Laves_C15 two phase region, and pushes it more towards the Laves_C36 phase. This change in phase equilibria with increasing temperature is illustrated nicely by sample 26, plotted in pink, on the isothermal sections in Figures 3.19-3.22, which yields BCC_B2 – Laves_C15 tie lines at 1000°C, but yields L2₁ – Laves_C15 tie lines at 1150°C. So it is not inconceivable that if the temperature was to be increased even further, then the L2₁ – Laves_C15 two phase region would become even larger, and could eventually push the BCC_B2 phase equilibria off of the Laves_C15 phase, and onto the Laves_C36 phase. At this point the diagram would match the results shown in samples 25 and 27, plotted in light blue and grey in Figures 3.19 - 3.23. Therefore, the results from samples 26 & 28-30, plotted in pink, royal blue, turquoise and red, on these figures, were given a higher weighting when charting these phase diagrams in comparison to the results from samples 25 & 27, plotted in light blue and grey.

Figures 3.19 to 3.21 also show that generally the average bulk alloy compositions of most samples match up reasonably well with their respective tie lines and tie triangles. However, there are a number of samples whose bulk alloy compositions lie between 2-6at% off of their respective tie lines and tie triangles. At 1000°C, this mismatch occurs in samples 5, 10, 14, 22, 23, 25, 26, and 28. And at 1150°C, this mismatch occurs in samples 9, 15, 22, 23, and 26.

It is thought that this mismatch between large area average bulk alloy composition measurements and much smaller area local phase composition measurements in these samples is the result of macrosegregation that occurred during solidification of the original alloy ingots. Due to alloy production issues relating to the high melting point of Ta (3017°C) and much lower melting (660°C), and boiling (2470°C) points of Al, not all alloy samples were completely homogeneous. Therefore in certain samples, local compositions/local equilibria did not always completely match up with the larger area bulk measurements.

During alloy production, there was a trade-off between 1) the amount of time that each alloy could be kept above its melting point, and 2) ensuring that each alloy was as close as possible to its target composition. This was because the longer each alloy was kept at temperatures above its melting point, the more Al was lost, due to boiling this element off of the ingot. So the more time spent re-melting and homogenising the alloys, the further they would get away from their target compositions. This is why some alloys ended up not quite matching their target compositions, and others ended up with a small amount of macrosegregation across the ingot.

Initially it was intended that X-ray diffraction (XRD) would also be carried out on the 30 Ta-Al-Co alloys in addition to SEM EDX, however this was not possible due to time constraints. XRD data may have provided additional confirmation of certain conclusions, such as the finding that the Mu prime phase is not present in the system, and that what was reported to be the Mu prime phase by Hunt and Raman,[77] is actually the upper boundary of the ternary extension of the Mu_D8₅ phase. However, due to the number of alloys created and analysed, the volume of self-consistent results produced via SEM & EDX, and their agreement with the existing data on the binary subsystems of the Ta-Al-Co ternary, it can be concluded that the ternary isothermal sections produced in this work are based on generally robust and repeatable results that can stand independently on their own merits.

3.5: Conclusions

An experimental investigation into the phase equilibria of the Ta-Al-Co system has been performed using SEM & EDX analysis of 30 compositionally distinct alloys that were sectioned and then equilibrated at temperatures of 1000°C and 1150°C.

This is the first study to investigate the entire composition range of the Ta-Al-Co system, and has produced the first complete ternary isothermal sections for the system at temperatures of 1000°C and 1150°C. These results are a significant step forward from the limited partial isothermal section at 1000°C produced by Hunt and Raman,[77] which was the best experimental phase diagram information available on this system until now.

Unfortunately, these isothermal sections show that the Ta-Al-Co system does not appear to contain a disordered BCC_A2 Ta to ordered BCC intermetallic two phase field, which rules out the possibility that this ternary could be used as a base system for a two phase precipitation strengthened Ta alloy. However, the Ta-Al-Co system is still an important ternary subsystem of both Ni, and Co based superalloys, so the experimental data and phase diagrams produced by this study could still be useful for the purposes of alloy design in the future.

The results of this study also indicate that the existing thermodynamic assessments for this system are not particularly accurate, due to the lack of available phase diagram data prior to this work. One way to mould the results of this study into a useful format for alloy design purposes would be to produce a new thermodynamic assessment for the Ta-Al-Co system. The resulting ternary database could then be adapted and incorporated into existing superalloy design databases, in order to improve the accuracy of alloy modelling predictions.

3.6: Future Work

The present work focussed on determining the phase equilibria in the Ta-Al-Co system at 1000°C and 1150°C. These temperatures were chosen in order to get data that would be comparable to other literature studies on similar systems. However, they were also chosen for practical purposes, since at temperatures below 1000°C it would take significantly longer than 1000 hours for alloys with a high Ta content to reach equilibrium. In addition, heat treatment temperatures above 1150°C were not carried out in order to avoid the potential problems relating to oxidation and impurity stabilised phases that were encountered by Dovbenko et al.[75]

An attempt was made to perform an investigation that was as comprehensive as possible given the practical difficulties of producing and studying alloys containing both Ta and Al and also considering the time constraints of the project. However, in order to get a more complete picture of the phase equilibria in this system it would also be good to carry out similar investigations at temperatures outside of the 1000°C - 1150°C range. In addition to the temperatures studied in the present work, investigations of the phase equilibria at 800°C and 1300°C, would also be good, along with differential thermal analysis (DTA) to determine phase transition temperatures, and information on the positions of the solidus and liquidus boundaries.

In addition it would be ideal to have also carried out XRD measurements on some of the alloys to get measured crystal structure information on the phases present. And also to provide confirmation that all phases that were recognised by comparing their SEM EDX measured boundary compositions to those found in the literature were definitely identified correctly. As it stands only SEM EDX analysis of the alloys was carried out, and any gaps in

the required information was filled in by combining the results of the present work with data from the literature.

Finally, there is still some disagreement in the literature with regards to the presence of certain intermetallic phases, such as the Al_7Ta_5 phase, and the boundaries of others, such as the $\text{Al}_{69}\text{Ta}_{39}$ & Sigma_D8_b phases in the Al-Ta system, so further investigation into the phase equilibria of this binary is also required to ensure that we have an accurate phase diagram for the system.

Chapter 4: Thermodynamic Assessment of the Ta-Al-Co System

4.1: Introduction

The only existing thermodynamic assessment for the Ta-Al-Co system appears to be the description from the TCNI8, Thermo-Calc Ni alloy database.[99] However, the experimental results on the Ta-Al-Co system produced by this work, shown in Chapter 3, indicate that the TCNI8 description for this system is not particularly accurate with regards to the ternary phase boundaries. This is thought to be due the lack of available ternary phase diagram data on this system prior to this work. Therefore the aim of this chapter of the current work is to perform a new thermodynamic assessment of the Ta-Al-Co system using the CALPHAD method, based on the experimental results on this ternary shown in Chapter 3. This will produce a new thermodynamic description for the Ta-Al-Co system that could be adapted and incorporated into existing multicomponent superalloy databases, in order to improve the accuracy of modelling predictions for alloy design and processing simulations.

4.2: Method

4.2.1: The CALPHAD Method

Detailed instructions on how to perform a thermodynamic assessment via the CALPHAD method are given by Lukas et al. [5], therefore only a brief description of the process followed by a discussion of the specific actions carried out in this work will be given here. The first step of this method is to gather and critically review all available phase diagram and thermodynamic data on the system of interest and its constituent subsystems. The second is to select appropriate models and coefficients to describe the Gibbs energy of each phase in the system based on their crystal structures and physical behaviour. The coefficients of these models should then be fitted to the selected phase diagram and thermodynamic data to produce a thermodynamic description of the system that accurately represents its real life behaviour.

Descriptions of higher order systems are built from the ground up, starting with the production of unary descriptions for the phases that exist in the pure elements. These unary descriptions can be thought of as the initial building blocks that are used as the foundations upon which to build the binary descriptions. Then once completed, these binary descriptions are combined, and used as the foundations upon which to build the ternary descriptions. If accurate and compatible descriptions are created for the necessary unary, binary and ternary systems, based on good experimental data, these descriptions can then be combined to produce credible extrapolated descriptions for higher order systems. Therefore, in order to produce a thermodynamic description for the Ta-Al-Co system it is necessary to first obtain and combine suitable descriptions for the unary and binary subsystems of this ternary. This process is illustrated in Figure 4.1, below.

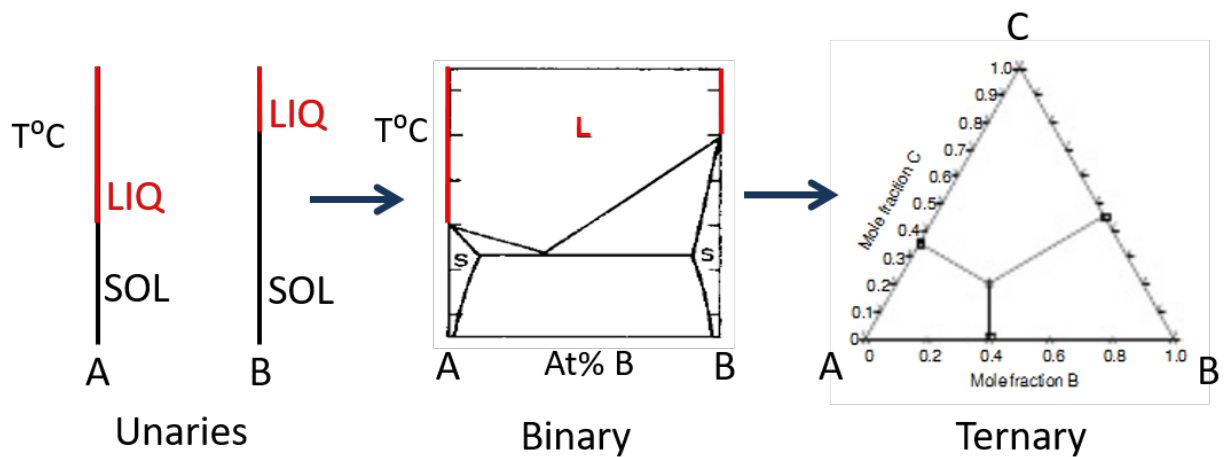


Figure 4.1: A schematic illustration of the process of building a thermodynamic description for a ternary system, starting from the unary descriptions for the pure elements.

At present most modern CALPHAD assessments use the unary descriptions developed by Dinsdale et al. from the Scientific Group Thermodata Europe (SGTE) [105], and so these unary descriptions were also used in the present work. In addition, a review of the published thermodynamic assessments of the required binaries was carried out, since compatible binary descriptions of sufficient accuracy can also be incorporated into the ternary assessment. Fortunately, this review yielded that reasonably accurate and compatible thermodynamic descriptions were available for all three required binaries, thus saving the time and effort that would be required to create these descriptions from scratch. The complete list of binary assessments that were reviewed are discussed in more detail in Chapter 2, therefore for the sake of brevity, only the binary descriptions that were selected to be used for this ternary assessment will be discussed in this Chapter. These were: The Al-Co description of Wang et al.[96] the Al-Ta description of Witusiewicz et al.[97] and the Co-Ta description of Cacciamani et al.[100]

These three binary descriptions were selected for use in the present work, out of the descriptions available in the literature, on the basis that they were the best matching descriptions available that fit all of the following required criteria:

- 1) They were based on the most accurate experimental data currently available.
- 2) They used suitable CALPHAD models to accurately describe the crystal structures and Gibbs energies of all of the required phases.
- 3) The models that the descriptions used were compatible with each other, so that they could be combined together to form a functioning extrapolated ternary description.

The binary descriptions from these papers were transcribed into Thermo-Calc[106] database files, and the binary phase diagrams were recalculated from these databases to ensure that they were accurate reproductions of the original descriptions. Once this was confirmed, the binary databases were then combined to produce an initial extrapolated description of the Ta-Al-Co ternary, which contained the models required to describe the Gibbs energies as a function of composition and temperature for all of the phases present in the unary, and binary systems. The models in this extrapolated ternary description were then edited, based on the experimental data on the Ta-Al-Co ternary, and related systems from this work and from the literature,[75], [77], [107], [108] in order to produce the final Thermo-Calc[106] model set up file that contained the set of phases, models, parameters and coefficients required for the assessment of this ternary. This model set up file will be discussed further in Section 4.2.2.

A literature review was performed to gather experimental phase diagram and thermodynamic data on the Ta-Al-Co ternary to be used for the assessment. However, since very little data was available on this system, the assessment was heavily based on the SEM EDX results on the equilibrated Ta-Al-Co alloys presented in Chapter 3 of this work.

These results were entered into a Thermo-Calc[106] experimental data file in the required format so that they could be used for the assessment.

The Gibbs energy models for all of the phases in the Ta-Al-Co ternary contained in the Thermo-Calc[106] model set up file were then fitted to the data contained in the Thermo Calc[106] experimental data file to create a thermodynamic description of the system that accurately matched the selected experimental data. This fitting process is also known as optimisation, and is an iterative process whereby the coefficients of the Gibbs energy models for all of the phases in the system are altered step by step, until these models fit well with the selected experimental data.

The Thermo Calc[106] PARROT module was designed to facilitate this optimisation process. It works by firstly minimising the Gibbs energy values calculated from the models for each phase utilising the Newton-Raphson method. Then secondly minimising the sum of squared errors between the value of each data point calculated using the current coefficient values in the Gibbs energy models and the experimental value of that data point listed in the experimental data file.[90], [106], [109] These coefficient values are then automatically changed by the PARROT module, and the calculation is repeated until the minimum is found. Numerous re-runs of the PARROT optimisation cycle, are usually required to find the true global minimum.

The optimisation procedure is a purely statistical process, and to reach the best possible result the experimental data should be evenly distributed throughout the phase diagram and the individual data points should exhibit a Gaussian distribution around their true values.[90] Often the experimental data set used for the optimisation of real systems is far from this ideal state. Therefore, a degree of judgement is required on the part of the assessor with regards to

what constitutes an acceptable outcome for the optimisation.[109] Moreover, the PARROT module is simply a tool designed to assist the assessor by automating parts of the process of fitting the model coefficients to the experimental data, and it will not do everything for the assessor. If any of the models, parameters, or coefficients chosen are unsuitable to describe any of the phases, or if any of the initial starting values chosen for the parameter coefficients are not close enough to their ideal values, then the PARROT optimisation will not converge. Therefore the assessor needs to have a good understanding of the system being assessed, the Gibbs energy models chosen to describe each phase, and the experimental data at their disposal. Often, a significant amount of manual editing of models parameters and coefficients, and iterative manual optimisation of coefficients via estimation, calculation and trial and error methods is required before a PARROT optimisation will converge.

4.2.2: Thermodynamic Modelling and the Model Set Up File

As discussed in Section 4.2.1 the models for the assessment of the Ta-Al-Co ternary were built up from the models for the unary and binary subsystems of this ternary, and then edited to ensure that they could describe the Gibbs energy of every phase in the system as a function of composition and temperature. The Gibbs energy is the preferred variable to model since most other thermodynamic variables can be calculated from this value. And the specific model for each type of phase was selected based on its crystal structure and physical behaviour, as will be explained below.

As first introduced in Section 2.5.2, and shown in Equation 4.1 below, the Gibbs energy of a phase, G^ϕ , can be modelled as the sum of three main terms. These are; the Gibbs energy reference term for the unmixed pure elemental phase constituents, $G^{0,\phi}$, an ideal entropy of mixing term, $G^{ideal,\phi}$, and an excess energy term, $G^{xs,\phi}$, to describe any non-ideal atomic interactions. In certain cases they can also be followed by further terms in case of magnetic, $G^{mag,\phi}$, or other interactions.[5], [88], [90]

$$G^\phi = G^{0,\phi} + G^{ideal,\phi} + G^{xs,\phi} + G^{mag,\phi} \quad (4.1)$$

The Gibbs energy models for many different types of phase are generally based on this primary equation, which will be discussed further when these models are introduced.

4.2.2.1: Unary Models for the Gibbs Energy of the Pure Elements

For phases, φ , composed of only a single pure element, A, there is no mixing, nor are there any interactions between different types of atoms, so the second and third terms in Equation 4.1, can be removed, and the Gibbs energy of the phase, G_A^φ , becomes:

$$G_A^\varphi = G_A^{0,\varphi} + G_A^{mag,\varphi} \quad (4.2)$$

The reference term, $G_A^{0,\varphi}$, is temperature dependant and is usually described by the power series given in equation 4.3, below: [5], [88], [90]

$$G_A^{0,\varphi} - H_A^{SER} = a + bT + cT \ln T + dT^2 + eT^{-1} + fT^3 + \dots \quad (4.3)$$

Where, H_A^{SER} is the standard molar enthalpy of element A (i.e., the enthalpy per mole at Temperature = 298.15 K and Pressure = 1 atm/ 101325 Pa), and a, b, c, d, e, f, &... are empirical coefficients that were determined experimentally by Dinsdale et al. of the SGTE.[105] Thus, the unary reference terms for the Gibbs energies as a function of temperature for all the phases that exist in the pure elements in the Ta-Al-Co system; $G_{Ta}^{0,\varphi}$, $G_{Al}^{0,\varphi}$, $G_{Co}^{0,\varphi}$ used in this work were taken from the SGTE database produced by Dinsdale et al.[105]

The magnetic term, $G_A^{mag,\varphi}$, is only necessary for magnetic elements, and is described by Equation 4.4:

$$G_A^{mag,\varphi} = RT \ln (\beta_0^\varphi + 1) f(\tau^\varphi) \quad (4.4)$$

Where, β_0^φ is the average Bohr magneton number per atom in the phase, $f(\tau^\varphi)$ is the integral of a function fitted to the magnetic contribution to the heat capacity, and

$$\tau^\varphi = \frac{T}{T_C^\varphi} \quad (4.5)$$

with T_C^φ , being the Curie temperature of the phase, which is also the critical temperature for magnetic ordering. [5], [88], [90] This magnetic term, $G^{mag,\varphi}$, and the rest of the terms from Equation 4.4 have been discussed in detail in Equations 2.9 to 2.15 in Section 2.5.2, and so will not be covered again here.

4.2.2.2: Gibbs Energy Models for the Disordered Solution Phases

The disordered solution phases, where the atoms mix randomly either in the liquid, or on a lattice, are the: Liquid, BCC_A2 Ta, FCC_A1 Al, FCC_A1 Co, and HCP_A3 Co phases. For the Liquid phase, a substitutional Redlich-Kister subregular solution model[92] was used, with a single sublattice occupancy of: (Al,Co,Ta)₁. From Equation 4.1 the contributions to the Gibbs energy for the Liquid phase model are:

$$G^\varphi = G^{0,\varphi} + G^{ideal,\varphi} + G^{xs,\varphi} \quad (4.6)$$

Where:

$$G^{0,\varphi} = \sum_i x_i G_i^{0,\varphi} \quad (4.7)$$

$$G^{ideal,\varphi} = RT \sum_i x_i \ln x_i \quad (4.8)$$

$$G^{xs,\varphi} = \sum_i \sum_{j>i} x_i x_j \sum_v^n (x_i - x_j)^v L_{ij}^v + \sum_i \sum_{j>i} \sum_{K>j} x_i x_j x_k L_{ijk} \quad (4.9)$$

In this model, x_i are the mole fractions of the elements i ($i = \text{Al, Co, Ta}$), and $G_i^{0,\varphi}$ are the Gibbs energies as a function of temperature for the pure elements in liquid phase form; $G_{Ta}^{0,\varphi}$, $G_{Al}^{0,\varphi}$, $G_{Co}^{0,\varphi}$ taken from Dinsdale et al.[105] and described by Equation 4.3. R is the ideal gas constant, and T is the absolute temperature in degrees Kelvin. And the L terms are the

v -th order interaction parameters between elements i and j or i , j and k , where $(i,j,k = \text{Al, Co, or Ta})$, which describe the Gibbs energy contribution resulting from any non-ideal interactions between these atoms. These L terms are empirical parameters whose temperature dependence is similar to those of the $G_i^{0,\varphi}$ terms in equation 4.3:

$$L = a + bT + cT \ln T + dT^2 + \dots \quad (4.10)$$

Only in this case the L parameters will be optimised in this work by fitting the coefficients, a, b, c, d, \dots to the available experimental data on the system. [5], [88], [90], [92]

Equations 4.6 to 4.9 can be combined and expanded to show the full version of the Gibbs energy model for the Liquid phase in one equation:

$$\begin{aligned} G^\varphi = & x_{Al} G_{Al}^{0,\varphi} + x_{Co} G_{Co}^{0,\varphi} + x_{Ta} G_{Ta}^{0,\varphi} + RT(x_{Al} \ln x_{Al} + x_{Co} \ln x_{Co} + x_{Ta} \ln x_{Ta}) \\ & + x_{Al} x_{Co} \sum_{v=0}^{v=n} (x_{Al} - x_{Co})^v L_{Al,Co}^v \\ & + x_{Al} x_{Ta} \sum_{v=0}^{v=n} (x_{Al} - x_{Ta})^v L_{Al,Ta}^v \\ & + x_{Co} x_{Ta} \sum_{i=0}^{i=n} (x_{Co} - x_{Ta})^i L_{Co,Ta}^i \\ & + x_{Al} x_{Co} x_{Ta} (u_{Al}^{Al} L_{Al,Co,Ta} + u_{Co}^{Co} L_{Al,Co,Ta} + u_{Ta}^{Ta} L_{Al,Co,Ta}) \end{aligned} \quad (4.11)$$

Most of these terms have been defined above, when introducing Equations 4.6 to 4.9, except for the u_i terms, which are related to the mole fractions, x_i , as shown in Equations 4.12 to 4.14, overleaf. These u_i terms describe the composition dependence of the ternary interaction parameters, ${}^iL_{i,j,k}$, which also have the temperature dependence shown in Equation 4.10.[5], [90]

$$u_{Al} = x_{Al} + \frac{1 - x_{Al} - x_{Co} - x_{Ta}}{3} \quad (4.12)$$

$$u_{Co} = x_{Co} + \frac{1 - x_{Al} - x_{Co} - x_{Ta}}{3} \quad (4.13)$$

$$u_{Ta} = x_{Ta} + \frac{1 - x_{Al} - x_{Co} - x_{Ta}}{3} \quad (4.14)$$

To model the BCC_A2 Ta, FCC_A1 Al, FCC_A1 Co, and HCP_A3 Co phases, the more complex compound energy formalism[110] was used. This model is an extension of the substitutional Redlich-Kister subregular solution model, where a sublattice is assigned to each distinct site in the crystal structure, in order to model the energy contributions that arise from specific atoms occupying specific sites on the crystal lattice. Current CALPHAD software can handle up to a maximum of five sublattices, although many phases can often be modelled with less. The following two sublattice models were used for the solid disordered solution phases, with elements highlighted in bold being the major constituents on the sublattice: BCC_A2 Ta: (Al,Co,**Ta**,Va)₁(Va)₃, FCC_A1 Al and Co: (Al,Co,**Ta**)₁(Va)₁, and HCP_A3 Co: (Al,**Co**,**Ta**)₁(Va)_{0.5}. In these models Va stands for vacancy, and the subscript number denotes the site fraction of each sublattice. So in the BCC_A2 Ta model, the crystal lattice is divided into two sublattices, with the first sublattice containing a disordered mix of the species; Al, Co, **Ta**, & Va, on the substitutional lattice sites, which represent 1/4 of the total number of sites on the overall lattice. And the second sublattice contains only vacancies, which corresponds to empty interstitial lattice sites, which represent 3/4 of the total number of sites on the overall lattice. The FCC_A1 Al and FCC_A1 Co phases were both modelled using the same single Gibbs energy model, as any phases with the same crystal structure can all be described by the same model.

The two sublattice compound energy formalism[110] used to model these phases is also derived from the basic model for the Gibbs energy of a phase given in Equation 4.1:

$$G^\varphi = G^{0,\varphi} + G^{ideal,\varphi} + G^{xs,\varphi} + G^{mag,\varphi} \quad (4.15)$$

Where:

$$G^{0,\varphi} = \sum_i \sum_j y_i^1 y_j^2 G_{i,j}^{0\varphi} \quad (4.16)$$

$$G^{ideal,\varphi} = RT \left(a_1 \sum_i y_i^1 \ln y_i^1 + a_2 \sum_j y_j^2 \ln y_j^2 \right) \quad (4.17)$$

$$\begin{aligned} G^{xs,\varphi} = & \sum_i \sum_{j>i} \sum_{k>j} y_i^1 y_j^1 y_k^2 L_{i,j:k} + \sum_i \sum_{j>i} \sum_{k>j} y_k^1 y_i^2 y_j^2 L_{k:i,j} \\ & + \sum_i y_i^1 y_j^1 y_k^1 y_i^2 L_{i,j,k:i} + \sum_i y_i^1 y_i^2 y_j^2 y_k^2 L_{i:i,j,k} \end{aligned} \quad (4.18)$$

$$G^{mag,\varphi} = RT \ln (\beta_0^\varphi + 1) f(\tau^\varphi) \quad (4.19)$$

In this model, $G_{i,j}^{0\varphi}$, are the molar Gibbs energies of hypothetical end-member compounds $i;j$, a_1 & a_2 are the site fractions of sublattices 1 & 2, and y^1 & y^2 are the constituent fractions of species i, j, k on sublattices 1 and 2, where $i,j,k = \text{Al, Co, Ta, or Va}$. R is the ideal gas constant, and T is the absolute temperature in degrees Kelvin. And the L terms are interaction parameters that are optimised in the present work. These L parameters are based on Redlich Kister polynomials, which describe the Gibbs energy contribution resulting from any interactions between the atoms on each sublattice. In addition, the model notation uses a colon to separate the different sublattices, and a comma to separate the species that are interacting on a specific sublattice. The terms for the magnetic contribution to the Gibbs energy, $G^{mag,\varphi}$, in Equation 4.19 are described above in Equations 4.4 and 4.5. [5], [90], [110]

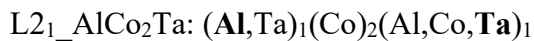
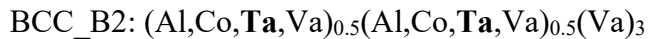
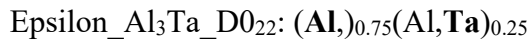
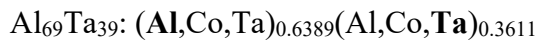
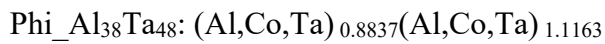
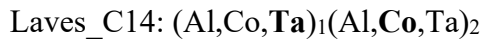
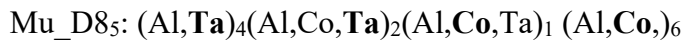
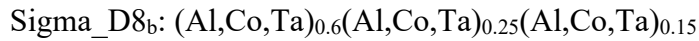
Entering the sublattice models for a specific phase into the compound energy formalism described by Equations 4.15 to 4.19, yields the full expanded model for the Gibbs energy that phase. For example the expansion of the model for the BCC_A2 Ta: (Al,Co,Ta,Va)₁(Va)₃ phase is:

$$\begin{aligned}
G^\varphi = & y_{Al}^1 y_{Va}^2 G_{Al:Va}^{O\varphi} + y_{Co}^1 y_{Va}^2 G_{Co:Va}^{O\varphi} + y_{Ta}^1 y_{Va}^2 G_{Ta:Va}^{O\varphi} + y_{Va}^1 y_{Va}^2 G_{Va:Va}^{O\varphi} \\
& + RT\{1(y_{Al}^1 \ln y_{Al}^1 + y_{Co}^1 \ln y_{Co}^1 + y_{Ta}^1 \ln y_{Ta}^1 + y_{Va}^1 \ln y_{Va}^1) + 3(y_{Va}^2 \ln y_{Va}^2)\} \\
& + y_{Al}^1 y_{Co}^1 y_{Va}^2 \sum_{i=0}^n {}^i L_{Al,Co:Va} (y_{Al}^1 - y_{Co}^1)^i + y_{Al}^1 y_{Ta}^1 y_{Va}^2 \sum_{i=0}^n {}^i L_{Al,Ta:Va} (y_{Al}^1 - y_{Ta}^1)^i \\
& + y_{Al}^1 y_{Va}^1 y_{Va}^2 \sum_{i=0}^n {}^i L_{Al,Va:Va} (y_{Al}^1 - y_{Va}^1)^i + y_{Co}^1 y_{Ta}^1 y_{Va}^2 \sum_{i=0}^n {}^i L_{Co,Ta:Va} (y_{Co}^1 - y_{Ta}^1)^i \\
& + y_{Co}^1 y_{Va}^1 y_{Va}^2 \sum_{i=0}^n {}^i L_{Co,Va:Va} (y_{Co}^1 - y_{Va}^1)^i + y_{Ta}^1 y_{Va}^1 y_{Va}^2 \sum_{i=0}^n {}^i L_{Ta,Va:Va} (y_{Ta}^1 - y_{Va}^1)^i \\
& + \sum_i y_{Al}^1 y_{Co}^1 y_{Ta}^1 y_{Va}^2 L_{Al,Co,Ta:Va} + \sum_i y_{Al}^1 y_{Co}^1 y_{Va}^1 y_{Va}^2 L_{Al,Co,Va:Va} \\
& + \sum_i y_{Al}^1 y_{Ta}^1 y_{Va}^1 y_{Va}^2 L_{Al,Ta,Va:Va} + \sum_i y_{Co}^1 y_{Ta}^1 y_{Va}^1 y_{Va}^2 L_{Co,Ta,Va:Va} \\
G^{mag,\varphi} = & RT \ln (\beta_0^\varphi + 1) f(\tau^\varphi) \tag{4.20}
\end{aligned}$$

Since Equation 4.20 is the combination and expansion of Equations 4.15 to 4.20, the terms in all of these equations are the same as those described above on the previous page.

4.2.2.3: Gibbs Energy Models for the Ordered Intermetallic Phases

Ordered intermetallics have a reference stoichiometry, but also still often exhibit either increased or decreased solubility ranges. In this assessment of the Ta-Al-Co ternary, all of the ordered intermetallic phases in the system were also modelled using the compound energy formalism[110] described above in Equations 4.15 to 4.19. In cases where more than 2 sublattices were required, the model was simply expanded by adding extra terms to represent the additional required sublattices. The sublattice models used for these phases are:



The Al_7Ta_5 phase was not modelled in this Ta-Al-Co assessment, since it was not detected by the EPMA and XRD investigation of Witusiewicz et al.[97] and was therefore not included in their Al-Ta binary description, which was used in this assessment. This will be discussed in more detail in Section 4.4.

As an example, the sublattice model for the Laves phases: $(\text{Al}, \text{Co}, \text{Ta})_1(\text{Al}, \text{Co}, \text{Ta})_2$ has been entered into the general form of the compound energy formalism [110] described by Equations 4.15 to 4.19, to give the expansion of this formalism that was used to model the Gibbs energy for those phases. This expanded model for the Laves phases is shown in Equation 4.21, overleaf. Where, as before, $G_{i;j}^{0\phi}$, are the molar Gibbs energies of hypothetical end-member compounds $i;j$. 1 & 2 are the site fractions of sublattices 1 and 2, & y^1 and y^2 are the constituent fractions of species i, j, k on sublattices 1 and 2, where $i, j, k = \text{Al}, \text{Co}, \text{or Ta}$. R is the ideal gas constant, and T is the absolute temperature in degrees Kelvin. Again the L terms are the interaction parameters that are optimised in the present work. These L parameters describe the Gibbs energy contribution resulting from any interactions between the atoms on each sublattice. In addition, the model notation uses a colon to separate the different sublattices, and a comma to separate the species that are interacting on a specific sublattice.

$$\begin{aligned}
G^\varphi &= y_{Al}^1 y_{Al}^2 G_{Al:Al}^{O\varphi} + y_{Al}^1 y_{Co}^2 G_{Al:Co}^{O\varphi} + y_{Al}^1 y_{Ta}^2 G_{Al:Ta}^{O\varphi} + y_{Co}^1 y_{Al}^2 G_{Co:Al}^{O\varphi} + y_{Co}^1 y_{Co}^2 G_{Co:Co}^{O\varphi} \\
&\quad + y_{Co}^1 y_{Ta}^2 G_{Co:Ta}^{O\varphi} + y_{Ta}^1 y_{Al}^2 G_{Ta:Al}^{O\varphi} + y_{Ta}^1 y_{Co}^2 G_{Ta:Co}^{O\varphi} + y_{Ta}^1 y_{Ta}^2 G_{Ta:Ta}^{O\varphi} \\
&+ RT\{1(y_{Al}^1 \ln y_{Al}^1 + y_{Co}^1 \ln y_{Co}^1 + y_{Ta}^1 \ln y_{Ta}^1) + 2(y_{Al}^2 \ln y_{Al}^2 + y_{Co}^2 \ln y_{Co}^2 + y_{Ta}^2 \ln y_{Ta}^2)\} \\
&\quad + y_{Al}^1 y_{Co}^1 y_{Al}^2 \sum_{i=0}^n {}^i L_{Al,Co:Al} (y_{Al}^1 - y_{Co}^1)^i + y_{Al}^1 y_{Co}^1 y_{Co}^2 \sum_{i=0}^n {}^i L_{Al,Co:Co} (y_{Al}^1 - y_{Co}^1)^i \\
&\quad + y_{Al}^1 y_{Co}^1 y_{Ta}^2 \sum_{i=0}^n {}^i L_{Al,Co:Ta} (y_{Al}^1 - y_{Co}^1)^i + y_{Al}^1 y_{Ta}^1 y_{Al}^2 \sum_{i=0}^n {}^i L_{Al,Ta:Al} (y_{Al}^1 - y_{Ta}^1)^i \\
&\quad + y_{Al}^1 y_{Ta}^1 y_{Co}^2 \sum_{i=0}^n {}^i L_{Al,Ta:Co} (y_{Al}^1 - y_{Ta}^1)^i + y_{Al}^1 y_{Ta}^1 y_{Ta}^2 \sum_{i=0}^n {}^i L_{Al,Ta:Ta} (y_{Al}^1 - y_{Ta}^1)^i \\
&\quad + y_{Co}^1 y_{Ta}^1 y_{Co}^2 \sum_{i=0}^n {}^i L_{Co,Ta:Co} (y_{Co}^1 - y_{Ta}^1)^i + y_{Co}^1 y_{Ta}^1 y_{Al}^2 \sum_{i=0}^n {}^i L_{Co,Ta:Al} (y_{Co}^1 - y_{Ta}^1)^i \\
&\quad + y_{Co}^1 y_{Ta}^1 y_{Ta}^2 \sum_{i=0}^n {}^i L_{Co,Ta:Ta} (y_{Co}^1 - y_{Ta}^1)^i + y_{Al}^1 y_{Al}^2 y_{Co}^2 \sum_{i=0}^n {}^i L_{Al:Al,Co} (y_{Al}^2 - y_{Co}^2)^i \\
&\quad + y_{Co}^1 y_{Al}^2 y_{Co}^2 \sum_{i=0}^n {}^i L_{Co:Al,Co} (y_{Al}^2 - y_{Co}^2)^i + y_{Ta}^1 y_{Al}^2 y_{Co}^2 \sum_{i=0}^n {}^i L_{Ta:Al,Co} (y_{Al}^2 - y_{Co}^2)^i \\
&\quad + y_{Al}^1 y_{Al}^2 y_{Ta}^2 \sum_{i=0}^n {}^i L_{Al:Al,Ta} (y_{Al}^2 - y_{Ta}^2)^i + y_{Co}^1 y_{Al}^2 y_{Ta}^2 \sum_{i=0}^n {}^i L_{Co:Al,Ta} (y_{Al}^2 - y_{Ta}^2)^i \\
&\quad + y_{Ta}^1 y_{Al}^2 y_{Ta}^2 \sum_{i=0}^n {}^i L_{Ta:Al,Ta} (y_{Al}^2 - y_{Ta}^2)^i + y_{Co}^1 y_{Co}^2 y_{Ta}^2 \sum_{i=0}^n {}^i L_{Co:Co,Ta} (y_{Co}^2 - y_{Ta}^2)^i \\
&\quad + y_{Ta}^1 y_{Co}^2 y_{Ta}^2 \sum_{i=0}^n {}^i L_{Ta:Co,Ta} (y_{Co}^2 - y_{Ta}^2)^i + y_{Al}^1 y_{Co}^2 y_{Ta}^2 \sum_{i=0}^n {}^i L_{Al:Co,Ta} (y_{Co}^2 - y_{Ta}^2)^i \\
&\quad + \sum_i y_{Al}^1 y_{Co}^1 y_{Ta}^1 y_{Al}^2 L_{Al,Co,Ta:Al} + \sum_i y_{Al}^1 y_{Co}^1 y_{Ta}^1 y_{Co}^2 L_{Al,Co,Ta:Co} \\
&\quad + \sum_i y_{Al}^1 y_{Co}^1 y_{Ta}^1 y_{Ta}^2 L_{Al,Co,Ta:Ta} + \sum_i y_{Al}^1 y_{Al}^2 y_{Co}^2 y_{Ta}^2 L_{Al:Al,Co,Ta} \\
&\quad + \sum_i y_{Co}^1 y_{Al}^2 y_{Co}^2 y_{Ta}^2 L_{Co:Al,Co,Ta} + \sum_i y_{Ta}^1 y_{Al}^2 y_{Co}^2 y_{Ta}^2 L_{Ta:Al,Co,Ta} \tag{4.21}
\end{aligned}$$

All of the other ordered intermetallic phases in the Ta-Al-Co system listed above were modelled in the same way; using the compound energy formalism,[110] given in Equations 4.15 to 4.19, except for the BCC_B2 phase, which is a slightly special case. This phase was also modelled using the compound energy formalism, but it was modelled as an ordering reaction from disordered BCC_A2 to ordered BCC_B2, using a method developed by Dupin & Ansara.[111] In this model, the Gibbs energy of the ordered BCC_B2 phase, G^{BCC_B2} , is obtained by first calculating the Gibbs energy of the disordered BCC_A2 phase, G^{BCC_A2} , using the compound energy formalism,[110] then adding the energy contribution of the ordering reaction, ΔG^{Ord} , to yield the total Gibbs energy for the ordered BCC_B2 phase as shown in Equations 4.22 and 4.23.

$$G^{BCC} = G^{BCC_A2} + \Delta G^{Ord} \quad (4.22)$$

$$\Delta G^{Ord} = G^{BCC_B2_Ord}(y_i^1, y_i^2, y_{Va}^3) - G^{BCC_B2_Disord}(y_i^1, y_{Va}^3) \quad (4.23)$$

This ordering contribution, ΔG^{Ord} , is also calculated using the compound energy formalism,[110] and is equal to the difference between the Gibbs energy of the BCC_B2 lattice, $G^{BCC_B2_Ord}(y_i^1, y_i^2, y_{Va}^3)$, and the hypothetical Gibbs energy for the BCC_B2 lattice in the disordered state, $G^{BCC_B2_Disord}(y_i^1, y_{Va}^3)$. Therefore, when the BCC lattice is in the disordered state, $\Delta G^{Ord} = 0$, and the Gibbs energy for the lattice = G^{BCC_A2} . And when the BCC lattice is in the ordered BCC_B2 state, $\Delta G^{Ord} < 0$, and the Gibbs energy for the lattice = G^{BCC_B2} . This ordering model enables the disorder/order transformation, to be described using a single Gibbs energy expression for both ordered and disordered phases. And the partitioning between these two states ensures that descriptions of systems that contain phases which undergo disorder/order transformations can be easily combined with descriptions of systems where these phases are always disordered.[111]

4.2.2.4: Gibbs Energy Models for the Stoichiometric Compound Phases

The stoichiometric compound phases were modelled using an n-sublattice model, with each sublattice occupied by only one element. Since the atoms in a stoichiometric compound are fixed in place, the mixing terms of the Gibbs energy are equal to zero. From Equation 4.1 the contributions to the Gibbs energy for a stoichiometric compound phase are:

$$G^\varphi = G^{0,\varphi} + G^{ideal,\varphi} + G^{xs,\varphi} \quad (4.24)$$

Where:

$$G^{0,\varphi} = \sum_i x_i G_i^{O\varphi} \quad (4.25)$$

$$G^{ideal,\varphi} = 0 \quad (4.26)$$

$$G^{xs,\varphi} = \Delta G^{Formation,\varphi} \quad (4.27)$$

In this model, x_i are the mole fractions of the elements i ($i = \text{Al, Co, Ta}$), $G_i^{O,\varphi}$ are the Gibbs energies as a function of temperature for the pure elements in liquid phase form; $G_{Ta}^{O,\varphi}$, $G_{Al}^{O,\varphi}$, $G_{Co}^{O,\varphi}$ taken from Dinsdale et al.[105] and $\Delta G^{formation,\varphi}$, is the molar Gibbs energy of formation of the phase. [5], [88], [90]

The sublattice models used for the stoichiometric compound phases in the system are:

Al₉Co₂: (Al)₉(Co)₂

o-Al₁₃Co₄: (Al)₁₃(Co)₄

y-Al₁₃Co₄: (Al)₁₃(Co)₄

m-Al₁₃Co₄: (Al)₁₃(Co)₄

Al₃Co: (Al)₃(Co)₁

Al₅Co₂: (Al)₅(Co)₂

Co₇Ta₂: (Co)₇(Ta)₂

As an example, the Gibbs energy model for the Al₉Co₂: (Al)₉(Co)₂ phase from equations 4.24 to 4.27 would be:

$$G^\varphi = x_{Al}G_{Al}^{0,\varphi} + x_{Co}G_{Co}^{0,\varphi} + \Delta G^{Formation,Al_9Co_2} \quad (4.28)$$

And the other stoichiometric compound phases were all be modelled in the same way.

4.2.2.5: Summary of the Phases in the Ta-Al-Co system, and the models used to describe them

A summary of the known phases in the Ta-Al-Co system, their crystal structures, and the models used to describe them in this assessment are given in Table 4.1. The phases highlighted in green in this table, namely; Liquid, BCC_A2 Ta, FCC_A1 Al, FCC_A1 Co, and HCP_A3 Co are all disordered solution phases. Out of these phases, the Liquid phase was modelled using the substitutional Redlich-Kister subregular solution model,[92] described by Equations 4.6 to 4.9. [5], [88], [90], [92] And the BCC_A2 Ta, FCC_A1 Al, FCC_A1 Co, and HCP_A3 Co phases were modelled using the compound energy formalism[110] described by Equations 4.15 to 4.19. [5], [90], [110] The phases highlighted in pink in this table are the ordered intermetallic phases. These are: CoTa₂_C16, Sigma_D8b, Mu_D85, Laves_C14, Laves_C15, Laves_C36, Phi_Al₃₈Ta₄₈, Al₆₉Ta₃₉, Epsilon_Al₃Ta_D022, BCC_B2, & L21_AlCo₂Ta. These phases were also modelled using the compound energy formalism[110] described by Equations 4.15 to 4.19. [5], [90], [110] And finally the phases highlighted in blue in this table, namely: Al₉Co₂, o-Al₁₃Co₄, y-Al₁₃Co₄, m-Al₁₃Co₄, Al₃Co, Al₅Co₂, Co₇Ta₂, are the stoichiometric compound phases. These phases were modelled as such using Equations 4.24 to 4.27.[5], [88], [90]

Table 4.1: A summary of the known phases, their crystal structures, and the models currently used to describe them in the extrapolated Ta-Al-Co database produced during this work

N	Phase & Strukturbericht designation	Pearson symbol	Space group	Prototype	Number of Sublattices & Sublattice Model	
1	Liquid	N/A	N/A	N/A	1	(Al,Co,Ta)
2	FCC_A1 Al	cF4	$Fm\bar{3}m$	Cu	2	(Al,Co,Ta) ₁ (Va) ₁
3	FCC_A1 Co	cF4	$Fm\bar{3}m$	Cu	2	(Al,Co,Ta) ₁ (Va) ₁
4	HCP_A3 Co	hP2	$P6_3/mmc$	Mg	2	(Al,Co,Ta) ₁ (Va) _{0.5}
5	BCC_A2 Ta	cI2	$Im\bar{3}m$	W	2	(Al,Co,Ta,Va) ₁ (Va) ₃
6	CoTa ₂ _C16	tI12	$I4/mcm$	Al ₂ Cu	2	(Al,Co,Ta) ₂ (Al,Co,Ta) ₁
7	Sigma_D8 _b	tP30	$P4_2/mmm$	CrFe	3	(Al,Co,Ta) _{0.6} (Al,Co,Ta) _{0.25} (Al,Co,Ta) _{0.15}
8	Mu_D8 ₅	hR13	$R\bar{3}m$	Fe ₇ W ₆	4	(Al,Ta) ₄ (Al,Co,Ta) ₂ (Al,Co,Ta) ₁ (Al,Co) ₆
9	Laves_C14	hP12	$P6_3/mmc$	MgZn ₂	2	(Al,Co,Ta) ₁ (Al,Co,Ta) ₂
10	Laves_C15	cF24	$Fd\bar{3}m$	Cu ₂ Mg	2	(Al,Co,Ta) ₁ (Al,Co,Ta) ₂
11	Laves_C36	hP24	$P6_3/mmc$	MgNi ₂	2	(Al,Co,Ta) ₁ (Al,Co,Ta) ₂
12	Phi_Al ₃₈ Ta ₄₈	mP86	$P2_1/c$...	2	(Al,Ta) _{0.8837} (Al,Ta) _{1.1163}
13	Al ₆₉ Ta ₃₉	cF432	$F4\bar{3}m$	Al ₆₉ Ta ₃₉	2	(Al,Co,Ta) _{0.6389} (Al,Co,Ta) _{0.3611}
14	Epsilon_Al ₃ Ta_D0 ₂₂	tI8	$I4/mmm$	TiAl ₃	2	(Al) _{0.75} (Al,Ta) _{0.25}
15	BCC_B2 AlCo	cP2	$Pm\bar{3}m$	CsCl	3	(Al,Co,Ta,Va) _{0.5} (Al,Co,Ta,Va) _{0.5} ,(Va) ₃
16	L2 ₁ _AlCo ₂ Ta	cF16	...	MnCu ₂ Al	3	(Al,Ta) ₁ (Co) ₂ (Al,Co,Ta) ₁
17	Al ₉ Co ₂	mP22	$P2_1/a$...	2	(Al) ₉ (Co) ₂
18	o-Al ₁₃ Co ₄	mC93	Cm	...	2	(Al) ₁₃ (Co) ₄
19	y-Al ₁₃ Co ₄	mC93	Cm	...	2	(Al) ₁₃ (Co) ₄
20	m-Al ₁₃ Co ₄	mC93	Cm	...	2	(Al) ₁₃ (Co) ₄
21	Al ₃ Co	2	(Al) ₃ (Co) ₁
22	Al ₅ Co ₂ _D8 ₁₁	hP28	$P6_3/mmc$	Co ₂ Al ₅	2	(Al) ₅ (Co) ₂
23	Co ₇ Ta ₂	2	(Co) ₇ (Ta) ₂

Table 4.1 Model Colour Code

Green1: Liquid modelled using the Redlich-Kister subregular solution model
Green2: Disordered solution phases modelled using the compound energy formalism
Orange: Ordered intermetallics modelled using the compound energy formalism
Blue: Modelled as stoichiometric compound phases

4.3: Results

After optimising the coefficients of all required model parameters, a complete, self-consistent thermodynamic description for the Ta-Al-Co system was obtained. This optimised description is listed in full, in Thermo-Calc .tdb format in Appendix 1.

Figure 4.2 shows the Al-Co, Al-Ta, and Co-Ta binary phase diagrams that have been re-calculated from the final optimised ternary description. It is important to check these calculated binary diagrams against those produced from the original binary descriptions to ensure that the model alterations made to describe the ternary system have not produced any unwanted changes to the original binaries. From Figure 4.2 it can be seen that the Al-Co, and Co-Ta binary phase diagrams calculated from the Ta-Al-Co description produced in the present work are exactly the same as the diagrams calculated from the original descriptions by Wang et al.[96] and Cacciamani et al.[100] respectively. However, the the Al-Ta description of Witusiewicz et al.[97] was purposely edited slightly, so that it would better match with the experimental data produced in Chapter 3 of this work relating to the phases in this binary. Specifically, the Sigma_D8_b phase model was edited to enable it to be shifted upwards slightly to higher Ta compositions of 80at% Ta, and the temperature stability of the Al₆₉Ta₃₉ phase was increased slightly so that the phase would be stable at temperature of 1000°C. These changes were made to improve the degree of fit for the descriptions of the Al-Ta and Ta-Al-Co systems to the available experimental data, and will be discussed in more detail in Section 4.4, with reference to the ternary phase diagram.

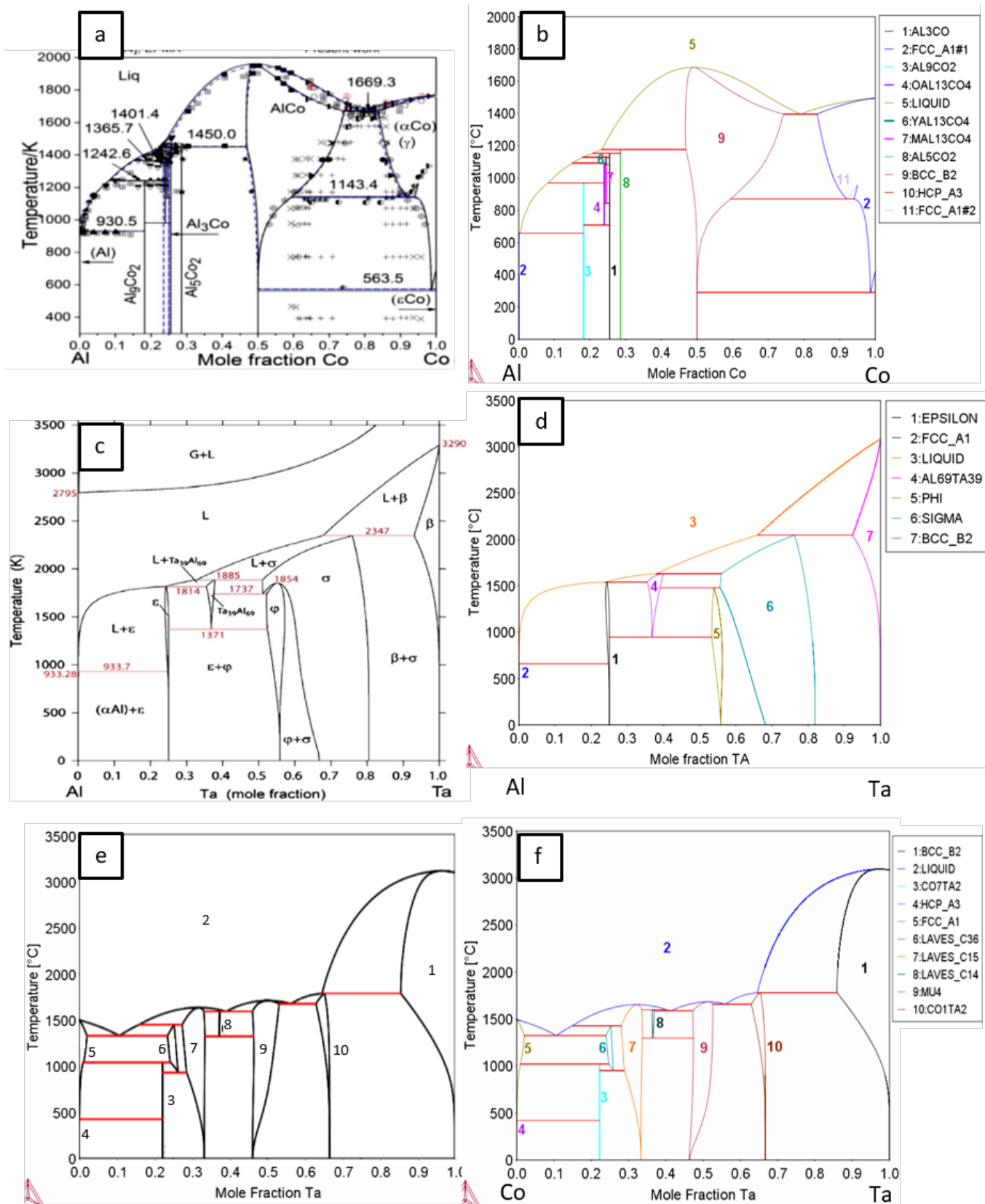


Figure 4.2: The calculated Al-Co, Al-Ta, and Co-Ta binary phase diagrams of Wang et al. (a), [96] Witusiewicz et al. (c), [97] and Cacciamani et al. (e), [100] respectively compared with the recalculated versions from the final optimised Ta-Al-Co description produced in this work, (b), (d) & (f).

Figures 4.3 and 4.4 show a comparison between the experimentally determined isothermal sections for the Ta-Al-Co system at 1000°C and 1150°C, and the temperature matched isothermal sections calculated from the optimised Ta-Al-Co description that were all produced in this work. Generally speaking the calculated isothermal sections match fairly well with the experimentally determined versions. This is to be expected, given that they are both based on the same experimental data. However, it is still important to demonstrate that the Gibbs energy models have been properly fitted to the data and that the thermodynamic description for the ternary system accurately represents its real life behaviour.

The calculated phase boundaries fit well with the experimental data in most cases and it appears that the thermodynamic description for the Ta-Al-Co system is reasonably accurate at these temperatures. However, the calculated boundaries for a few of the phases that originate in the Al-Ta binary, specifically the $\text{Phi_Al}_{38}\text{Ta}_{48}$, and $\text{Epsilon_Al}_3\text{Ta_D0}_{22}$ phases are approximately 4-5at% away from their experimentally measured positions. In addition, the $\text{Al}_{69}\text{Ta}_{39}$ phase is stable at 1000°C in the calculated, but not experimental diagram, and the Al_7Ta_5 peritectic compound phase is not present in the calculated diagrams. All of these discrepancies are due to slight mismatches between the experimental data produced in this work, and the thermodynamic description for the Al-Ta binary produced by Witusiewicz et al.[97] that was selected to be used for the thermodynamic assessment of the Ta-Al-Co system. The selection of this binary description, and its effects on the ternary description produced in this work will be discussed in more detail in Section 4.4

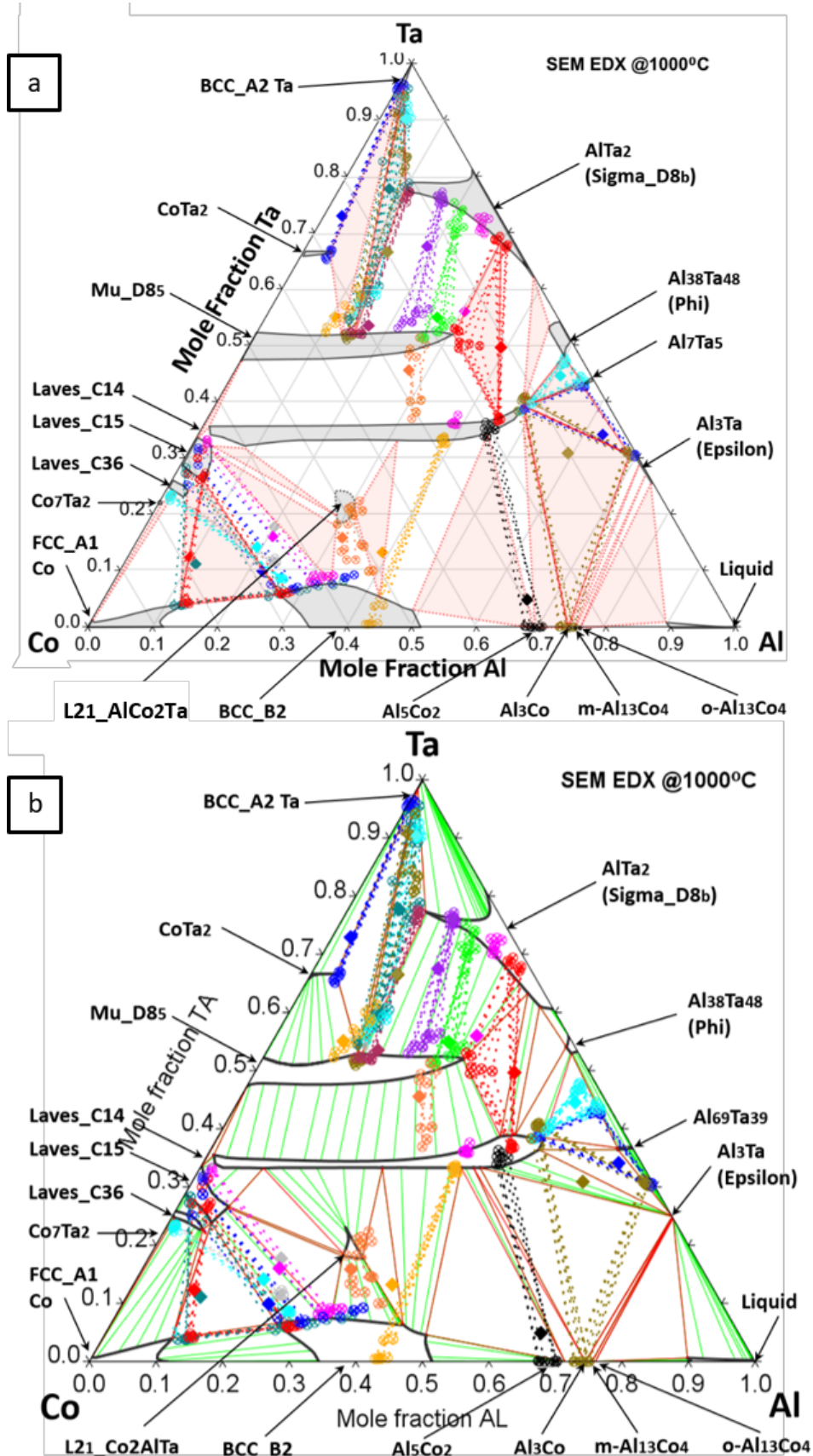


Figure 4.3: The experimentally determined Ta-Al-Co isothermal section at 1000°C produced in this work, (a), compared to the temperature matched isothermal section calculated from the optimised Ta-Al-Co description, also produced in this work, (b). All of the experimentally measured bulk alloy and tie line composition data is overlaid on both isothermal sections.

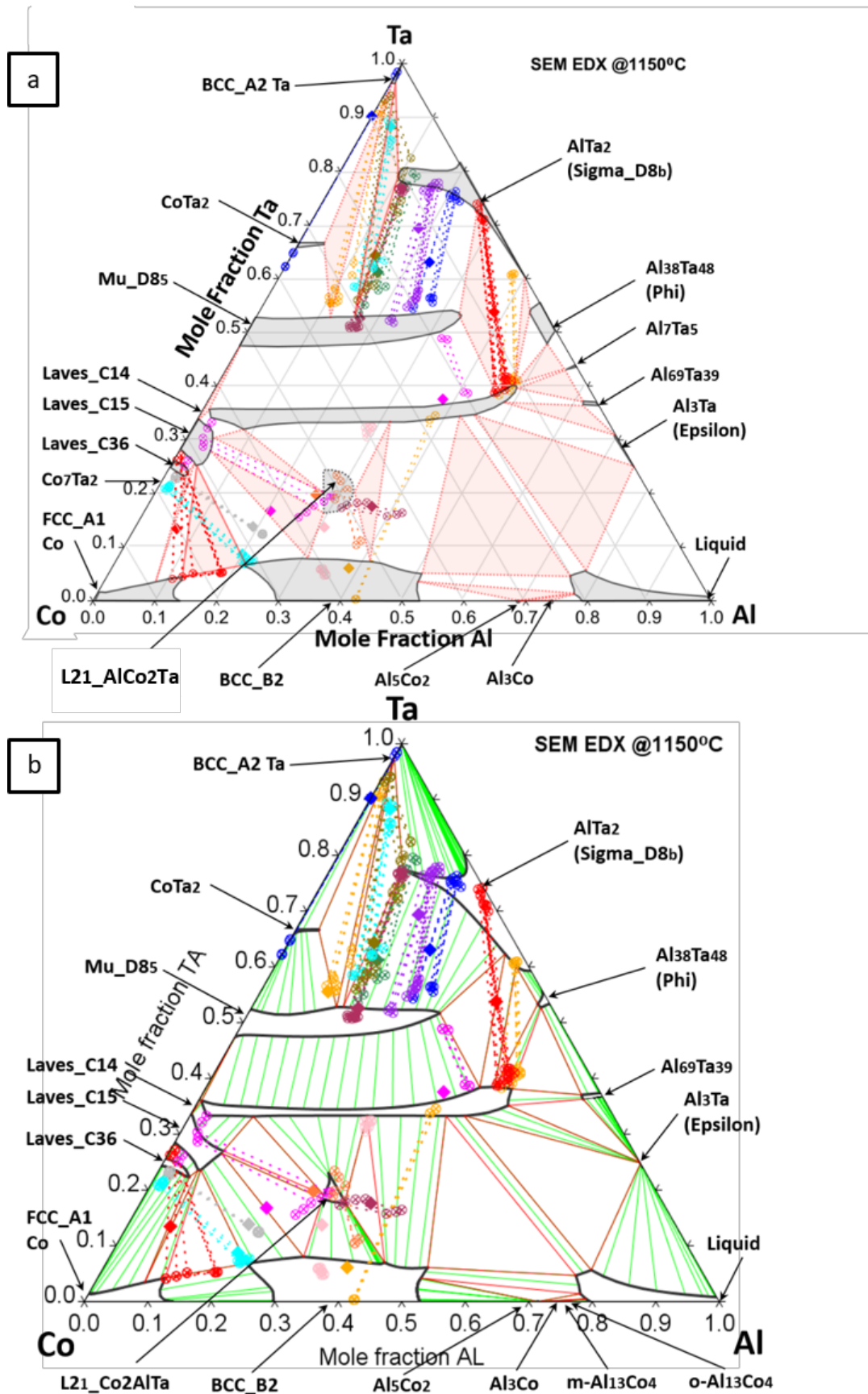


Figure 4.4: The experimentally determined Ta-Al-Co isothermal section at 1150°C produced in this work, (a), compared to the temperature matched isothermal section calculated from the optimised Ta-Al-Co description, also produced in this work, (b). All of the experimentally measured bulk alloy and tie line composition data is overlaid on both isothermal sections

The calculated liquidus projection from the optimised Ta-Al-Co description produced in this work is shown in Figure 4.5. Since there is no data currently available on the ternary liquidus for this system, this calculated liquidus is predominantly the result of the models in the description interpolating the ternary liquidus from the binary liquidus edges and also from the ternary phase stability information at 1000°C and 1150°C. However, in the absence of data on the Ta-Al-Co liquidus, the high temperature ternary stability of certain phases close to the Al-Co binary edge, such as the L2₁_AlCo₂Ta, Laves_C15, and Laves_C14 phases were modelled using experimental data on the Nb-Al-Co liquidus displayed in Figure 4.6 as a guide. Although since most Ta containing phases have higher melting points than their respective Nb containing equivalents, only the relative shapes of the ternary liquidus surfaces of the L2₁_AlCo₂Ta, Laves_C15, and Laves_C14 phases were used in the models and not the absolute values for the melting points of these Nb-Al-Co phases. Based on what we know about these two ternary systems it is expected that their liquidus surfaces would look roughly similar in regions closer to the Al-Co binary edge that they both share, however more significant differences are to be expected in regions further away from this shared binary edge.

Comparing the two liquidus projections shown in Figures 4.5 and 4.6 one significant difference is that the liquidus surface of the Mu_D8₅ phase is much more prominent in the Ta-Al-Co system than it is in the Nb-Al-Co system, where the liquidus surface of the Laves_C14 phase dominates the centre of the diagram. This is to be expected since in the Co-Ta binary the Mu_D8₅ phase has a much higher melting point of approximately 1700°C compared to the Laves_C14 phase, which melts at around 1600°C.[76] Whereas, in the Co-Nb binary, the Laves_C14 phase has the higher melting point of 1423°C, compared to the Mu_D8₅ phase, which melts at 1399°C.[108] Thus the high temperature stability, and liquidus surface of the Mu_D8₅ phase, and all of the other phases with higher Ta contents in the Ta-Al-Co description

are based solely on the models interpolating the ternary liquidus from the binary liquidus edges and also on the experimental ternary phase stability information at 1000°C and 1150°C, and have not been altered based on the Nb-Al-Co liquidus.

The calculated Ta-Al-Co liquidus projection from the TCNi8 Thermocalc database shown in Figure 4.7, appears to look topologically similar to that of the Nb-Al-Co system presented in Figure 4.6, except for the fact that the Sigma_D8_b phase liquidus does not extend so much into the ternary in the TCNi8 liquidus. Therefore just like the Nb-Al-Co liquidus, the calculated Ta-Al-Co liquidus from the TCNi8 database is similar to the liquidus projection calculated from the optimised ternary description produced in this work, in the region close to the Co-Al binary, but it differs in the centre of the diagram in the region close to the Mu_D8₅ phase. Since TCNi8 is a proprietary database, its owners have not made it publicly available as to whether this liquidus is simply an interpolation from the binary descriptions, or if they have fitted their models to some data on the ternary system. In any case, in the present work the parameters of a few key end members in the model for the Mu_D8₅ phase were fitted to the ternary experimental data on this phase from Chapter 3. And the remaining end members from this model were assigned values based on a linear interpolation of Sluiter's calculated ab-initio lattice stabilities for the Mu_D8₅ phase in the pure elements, Al, Co, and Ta.[112]

Moreover, since the Mu_D8₅ phase has a melting point that is approximately 100°C higher than the Laves_C14 phase in the Co-Ta binary,[76] it seems reasonable to conclude that the liquidus surface of the Mu_D8₅ phase would also extend into the ternary at a higher temperature than that of the Laves_C14 phase, as it does in the calculated liquidus projection of the present work, rather than the way it does in the liquidus projection calculated from the TCNi8 database.

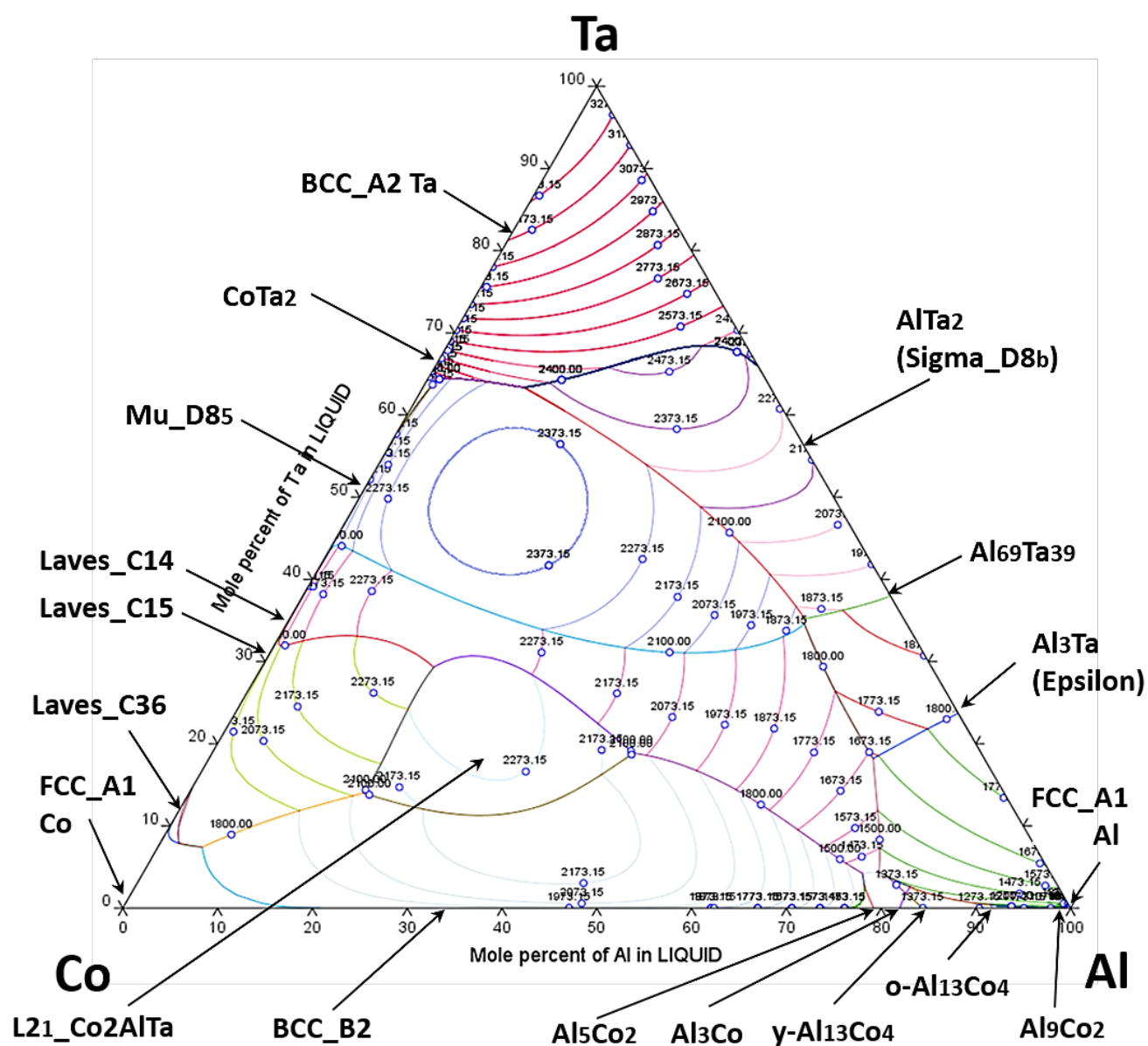


Figure 4.5: The liquidus projection calculated from the optimised Ta-Al-Co description produced in this work. Isotherm temperatures are given in degrees Kelvin.

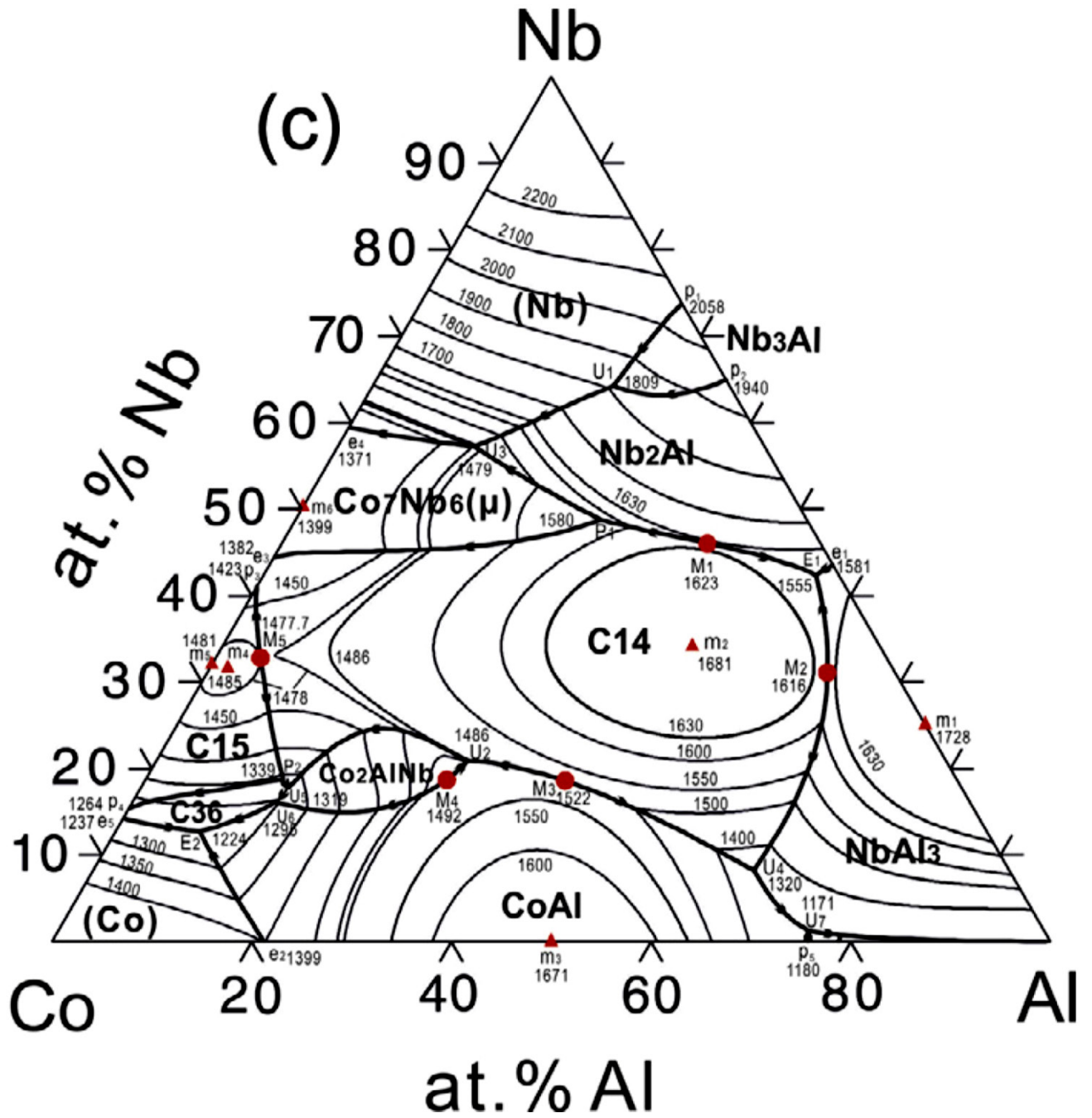


Figure 4.6: Palm et al.'s [107], [108] experimentally determined liquidus projection for the Nb-Al-Co system. Isotherm temperatures are given in degrees Celsius.

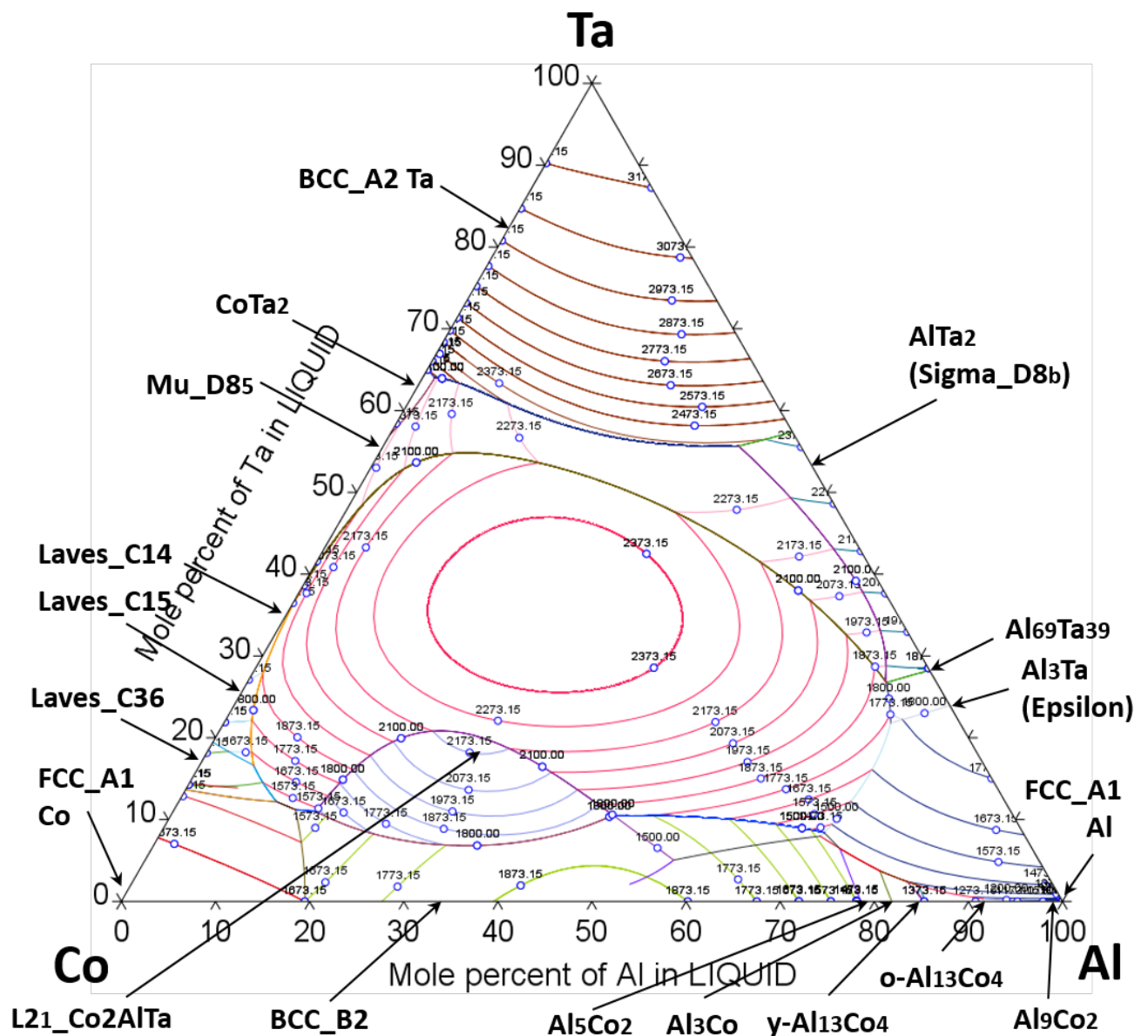


Figure 4.7: The liquidus projection calculated from the Thermo-Calc TCNi8 database.[99] Isotherm temperatures are given in degrees Kelvin.

At present, there are no openly published thermodynamic assessments on the Ta-Al-Co system. So the only assessments that can be reasonably compared to the present work are the proprietary Ta-Al-Co assessment in the TCNi8 database, and the recent assessment of the Nb-Al-Co system by He et al.[108] that is heavily based on the previous experimental work on that system by Dovbenko et al.[75] and Palm et al.[107]

Figures 4.8 and 4.9 show a comparison between He et al.'s[108] calculated isothermal sections for the Nb-Al-Co system at 1000°C and 1150°C, and the temperature matched isothermal sections calculated from the optimised Ta-Al-Co description produced in the present work. Generally speaking the calculated isothermal sections match fairly well for most of the phases that originate in the Al-Co, and Co-Ta/Nb-Ta binaries, but there are a number of differences that arise as a result of the differences between the Al-Ta, and Al-Nb binaries. Essentially, the presence of the Al_3Nb phase, reduces the size of the Σ_{D8b} Al_2Nb phase, and there is no $CoNb_2$ phase in the Nb-Al-Co system. This significantly alters the phase equilibria in the Nb corner of this system and also slightly reduces the ternary solubility of the μ_{D85} phase compared to the phase equilibria in the equivalent region of the Ta-Al-Co ternary. Also, the presence of extra intermetallic phases around the centre of the Al-Ta binary in comparison to the Al-Nb binary alters the tie triangles that are present in the Al corner of the Ta-Al-Co system in comparison to the Nb-Al-Co system.

Most of these differences have already been discussed in detail in Chapter 3 when comparing the experimentally determined isothermal sections for the Ta-Al-Co system with the Dovbenko et al.'s[75] temperature matched isothermal sections for the Nb-Al-Co system. And since the thermodynamic assessments of these two systems are based on the data from these two experimental studies, the differences in the experimentally determined isothermal sections have also carried over into the calculated isothermal sections.

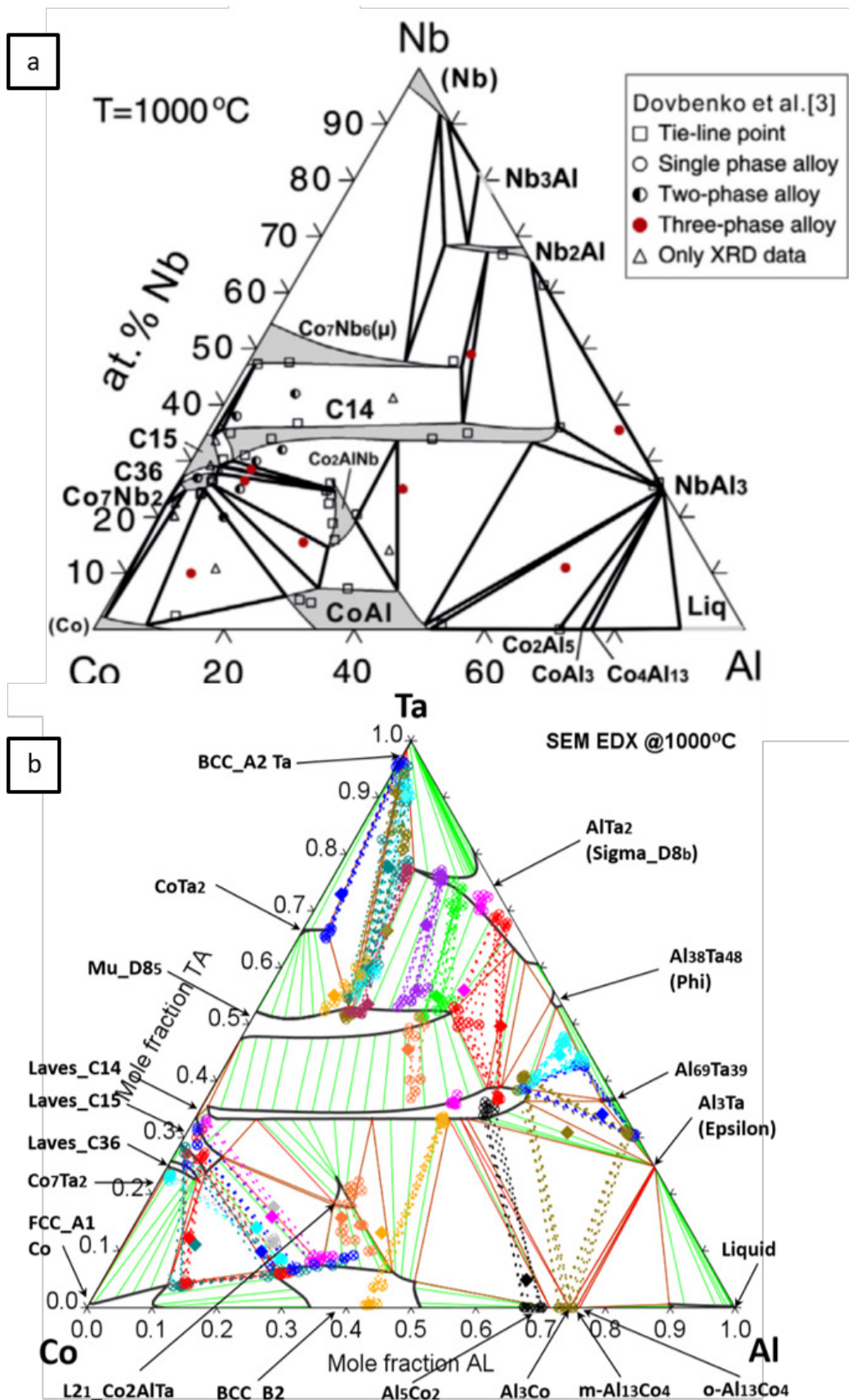


Figure 4.8: The calculated Nb-Al-Co isothermal section at 1000°C produced by He et al, (a),[108] compared to the temperature matched isothermal section calculated from the optimised Ta-Al-Co description produced in this work, (b).

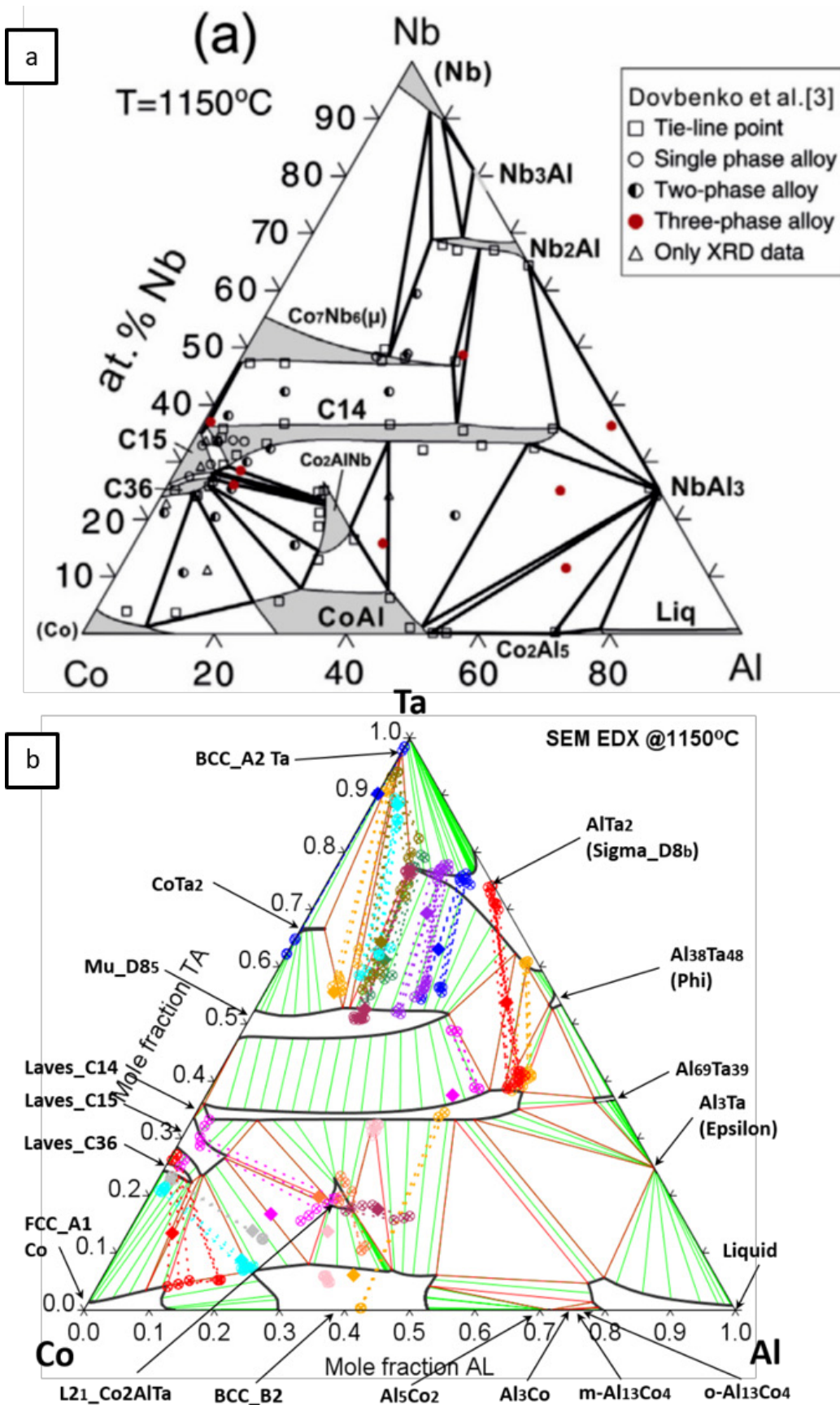


Figure 4.9: The calculated Nb-Al-Co isothermal section at 1150°C produced by He et al, (a), [108] compared to the temperature matched isothermal section calculated from the optimised Ta-Al-Co description produced in this work, (b).

Figures 4.10 and 4.11 show a comparison between the calculated isothermal sections for the Ta-Al-Co system at 1000°C and 1250°C from the TCNi8 database,[99] and the temperature matched isothermal sections calculated from the optimised Ta-Al-Co description produced in this work. The diagrams from both databases contain the same phases along the binary edges, except for the $\text{Phi_Al}_{38}\text{Ta}_{48}$ phase, which is missing in the TCNi8 [99] diagrams. Apart from that, the TCNi8 [99] diagrams do look like fairly reasonable approximations, considering that they are likely to be based on limited experimental data. However, these TCNi8 [99] isothermal sections only show reasonable ternary solubility ranges for a few of the phases in the diagram, namely the Sigma_D8_b , Mu_D8_5 , Laves_C14 , FCC_A1 Co , and Liquid phases, and the boundaries of these phases do not completely match with the experimental data produced in the present work. Moreover, the TCNi8 [99] diagrams also show little to no ternary solubility for the CoTa_2_C16 , $\text{Al}_{69}\text{Ta}_{39}$, BCC_B2 , $\text{L21_AlCo}_2\text{Ta}$, Laves_C15 , and Laves_C36 phases, in contrast with the calculated and experimental diagrams produced in this work. In addition, since TCNi8 [99] is a Ni alloy database, it prioritises Ni alloy phase equilibria above all else, and as a result a ternary $\gamma'_FCC_L1_2$ phase field has stabilised in the Co corner of its calculated isothermal section at 1250°C, when there is no evidence that this phase should be present in the Ta-Al-Co system.

The Ta-Al-Co ternary in the TCNi8 database[99] appears to be built upon the Al-Co, Al-Ta, and Co-Ta binary descriptions of Dupin,[30] Du & Schmid-Fetzer,[53] and Liu et al.,[68] which have been re-calculated from the database, and are shown in Figure 4.12. These re-calculated diagrams are exact matches with their published equivalents, and so it is clear that the TCNi8 [99] description for this ternary is built upon these binary descriptions. Although it is possible that the creators of this database may have also modified these

descriptions slightly to ensure that they were compatible with those of the other systems included in the database.

The binaries used to build the Ta-Al-Co ternary description in the TCNi8 database[99] are compared to those used to build this ternary description in the present work in Figure 4.12. From this figure, it can be seen that the Al-Co descriptions from both databases are quite similar, however, there are some fairly significant differences between the Al-Ta, and Co-Ta descriptions used in the different ternary descriptions. The TCNi8 [99] Al-Ta,[53] and Co-Ta[68] descriptions are older, and use stoichiometric line compound models for the Epsilon_Al₃Ta_D0₂₂, Al₆₉Ta₃₉, Phi_Al₃₈Ta₄₈, and CoTa₂ phases, when later studies have indicated that these phases all exhibit compositional solubility ranges.[76], [97] The composition ranges for these phases are all described by the sublattice models used in the later descriptions of Witusiewicz et al,[97] and Cacciamani et al.[100] that were utilised for the Ta-Al-Co assessment in the present work.

Figure 4.13 indicates that the ternary solubility of the phases in the Ta-Al-Co description of the TCNi8 database[99] are likely to be based on the limited partial isothermal section of Hunt & Raman,[77] since the Mu_D8₅ phase shape and extension seems to match up reasonably well in the two diagrams. Moreover, this appears to have been the only publically available phase diagram data on this ternary system at the time when the TCNi8 database[99] was created. The TCNi8 creators do not include the ternary Mu prime phase in their models either, and it can be speculated that this could potentially be because the existence of this phase has been disputed by other work on similar systems.[75]

All things considered, the optimised description of the Ta-Al-Co system produced by the present work appears to represent, a significant improvement when compared

to the previous best available description for this ternary, which is the version contained in the TCNi8 database. [99]

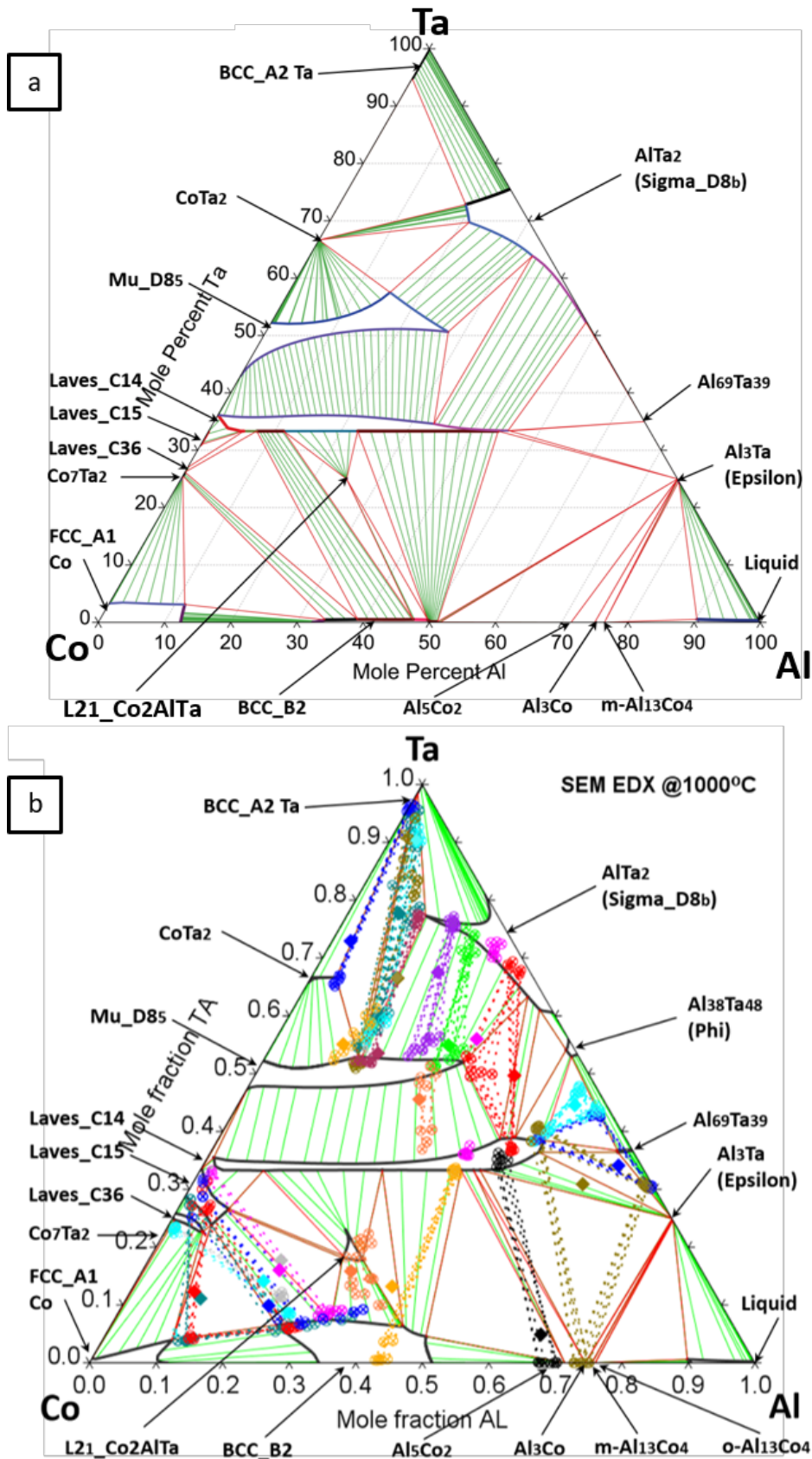


Figure 4.10: The Ta-Al-Co isothermal section at 1000°C calculated from the Thermo-Calc TCNi8 database, (a).[99] compared to the temperature matched isothermal section calculated from the optimised Ta-Al-Co description produced in this work, (b).

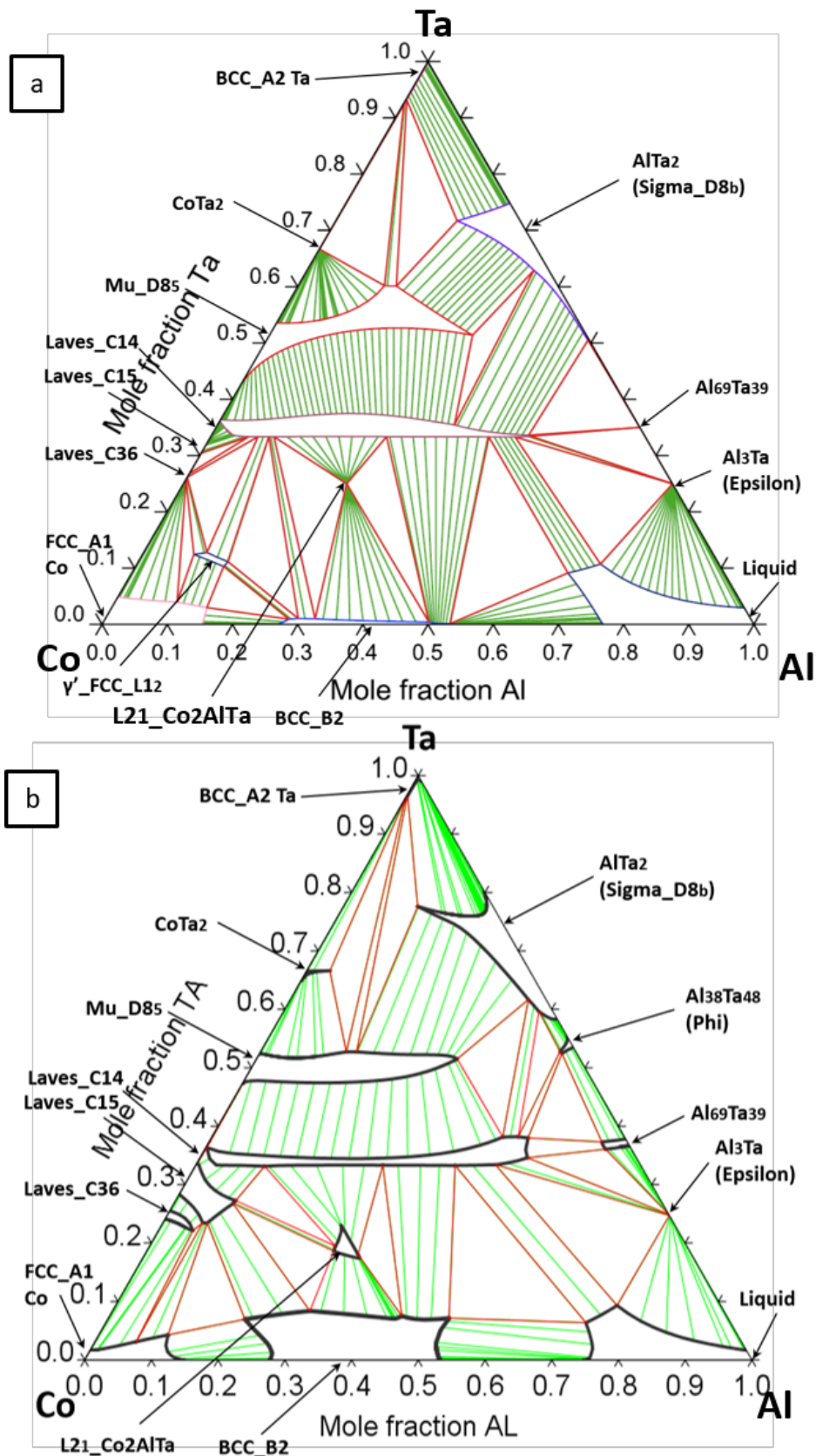


Figure 4.11: The Ta-Al-Co isothermal section at 1250°C calculated from the Thermo-Calc TCNi8 database, (a).[99] compared to the temperature matched isothermal section calculated from the optimised Ta-Al-Co description produced in this work, (b).

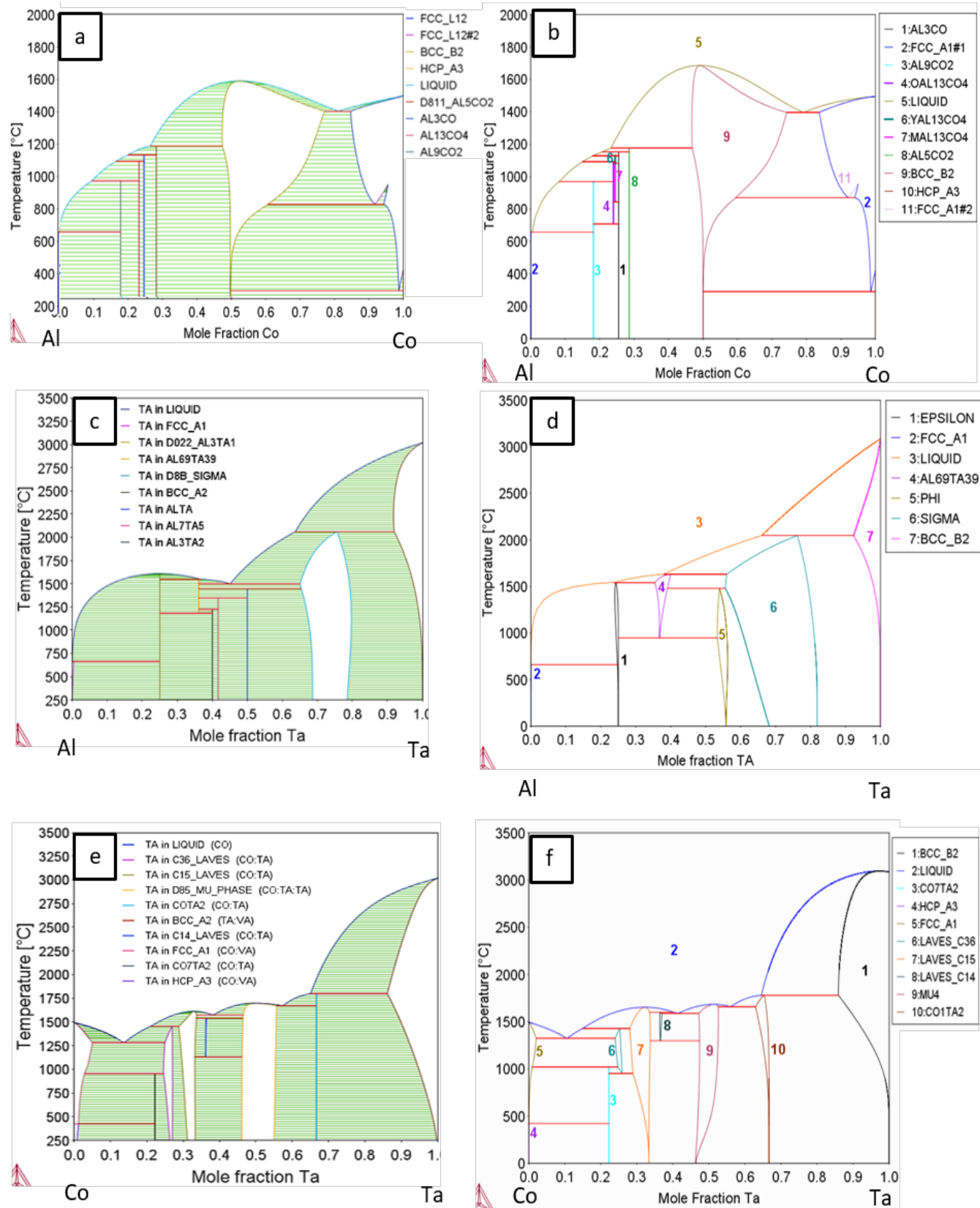


Figure 4.12: The Al-Co, Al-Ta, and Co-Ta binary phase diagrams of Dupin, (a),[30] Du & Schmid-Fetzer, (c), [53] and Liu et al., (e),[68] which were calculated from the TCNi8 database,[99] compared to the calculated diagrams of Wang et al. (b), [96] Witusiewicz et al. (d),[97] and Cacciamani et al. (f),[100] that were used for the Ta-Al-Co assessment in the present work.

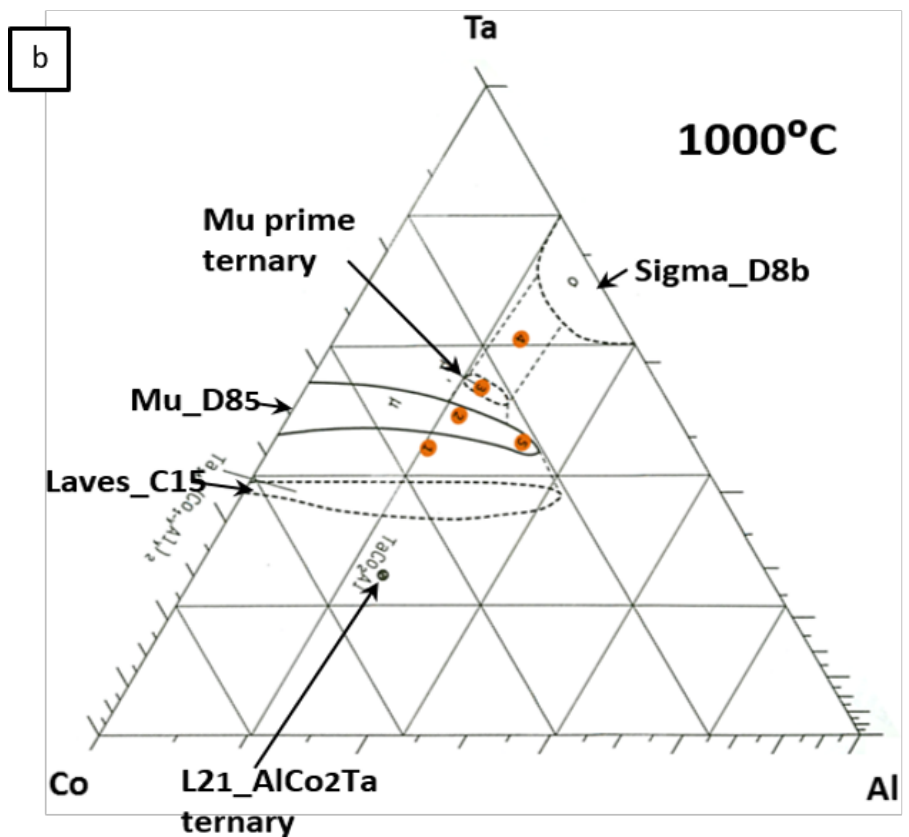
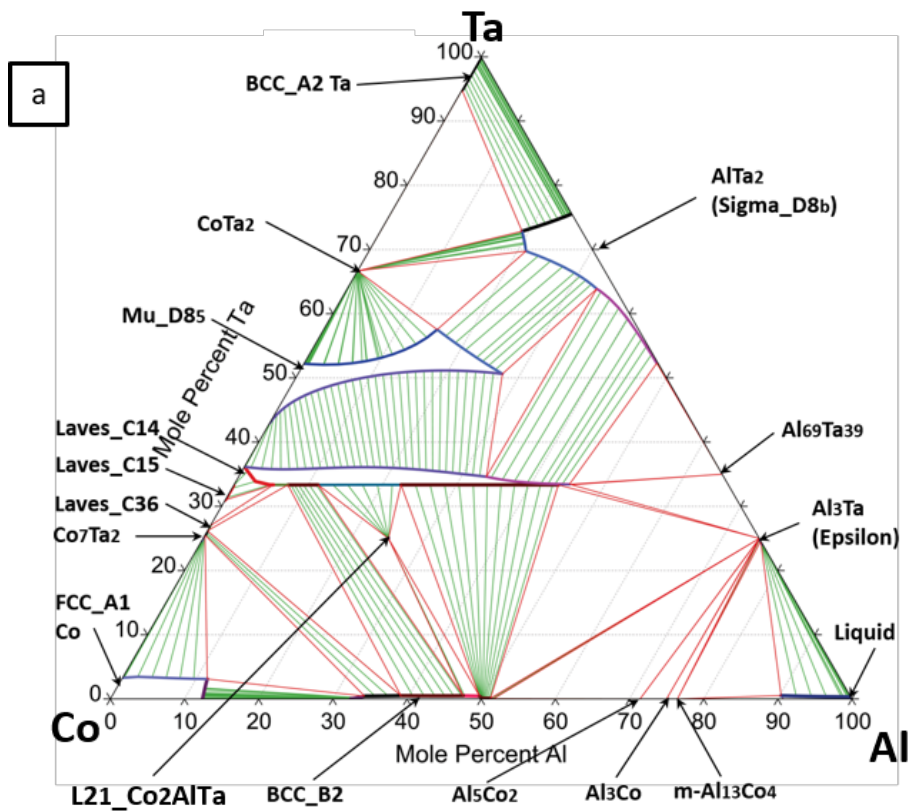


Figure 4.13: The Ta-Al-Co isothermal section at 1000°C calculated from the Thermo-Calc TCNi8 database, (a).[99] compared to the temperature matched experimentally determined partial isothermal section of Hunt & Raman (b).[77]

4.4: Discussion

The isothermal sections at 1000°C and 1150°C calculated from the optimised Ta-Al-Co description shown in Figures 4.3 & 4.4 match up well with the experimentally determined versions. The general criteria used in selecting how to weight the data when fitting the models during the optimisation were the same as those used when producing the experimental diagrams, and are discussed in detail in Section 3.4. The calculated phase boundaries fit well with the experimental data in most cases and it appears that the optimised thermodynamic description for the Ta-Al-Co system is reasonably accurate at these temperatures. Moreover, the liquidus projection calculated from this description, shown in Figure 4.5 also seems reasonable based on the comparison to the liquidi of the binary subsystems displayed in Figure 4.2, and also to the experimental and calculated ternary liquidi shown in Figures 4.6 & 4.7.

However, the calculated boundaries for a few of the intermetallic phases that originate in the Al-Ta binary are a few atomic percent away from their experimentally measured positions in some places, due to slight mismatches between the experimental data produced in this work, and the thermodynamic description for the Al-Ta binary produced by Witusiewicz et al.[97] that was selected to be used for the assessment of the Ta-Al-Co ternary. This selection was made out of three possible options: 1) was to use the Al-Ta description of Witusiewicz et al. shown in Figure 4.2(c), 2) was to use the Al-Ta description of Du & Schmid-Fetzer shown in Figure 4.12(c), and 3) was to perform a re-assessment of the Al-Ta system so that it better matched with the experimental data produced in this work. Looking back, the ideal choice would probably have been to perform a re-assessment of this binary. However, when this Ta-Al-Co assessment was started, not all of the ternary

experimental data from Chapter 3 was available, and the Al-Ta assessment of Witusiewicz et al.[97] is based on a significant amount of binary experimental data, and seemed to be the best choice at the time. Moreover, as discussed in Section 2.2 there are a number of conflicting studies on the Al-Ta system, [40], [48]–[50], [53], [97] and performing a re-assessment of this binary would require a significant amount of time. Therefore due to time constraints, it was decided to press on with the ternary assessment using the Al-Ta description of Witusiewicz et al.,[97] which is still the best description currently available for this system.

However, during the assessment, it became apparent that the $(\text{Al,Co,Ta})_{0.533}(\text{Al,Co,Ta})_{0.333}(\text{Al,Co,Ta})_{0.134}$ sublattice model used by Witusiewicz et al.[97] to model the Sigma_D8_b phase is not ideal to describe the ternary extension of this phase in the Ta-Al-Co system, so the sublattice site fractions were altered to $(\text{Al,Co,Ta})_{0.6}(\text{Al,Co,Ta})_{0.25}(\text{Al,Co,Ta})_{0.15}$. This altered model is closer to the $(\text{A,B})_{18}(\text{B})_8(\text{A})_4$ site occupancy proposed by Andersson & Sundman[113] to describe the Sigma_D8_b phase in the Cr-Fe system, which would translate to $(\text{Al,Co,Ta})_{0.6}(\text{Al,Co,Ta})_{0.266}(\text{Al,Co,Ta})_{0.134}$ in the format used in the current system. This enabled the Sigma_D8_b phase boundary to be shifted upwards slightly to higher Ta compositions of 80at% Ta. In addition, the temperature stability range of the Al₆₉Ta₃₉ phase was increased slightly so that the phase would be stable at 1000°C. These changes were made to improve the degree of fit for the descriptions of the Al-Ta and Ta-Al-Co systems to the ternary experimental data produced in this work.

The Ta-Al-Co phase diagrams calculated from the TCNi8 database[99] shown in Figures 4.7, 4.10 and 4.11 indicate that their thermodynamic description for this ternary is a fairly reasonable approximation of the system, considering that it is likely to be based on limited ternary experimental data. However, as discussed in Section 4.3, these TCNi8 [99]

diagrams only show reasonable ternary solubilities for a few of the phases in the diagram, and the boundaries of these phases do not match that well with the experimental data produced in the present work. In addition, since TCNi8 [99] is a Ni alloy database, it prioritises Ni alloy phase equilibria above all else, and as a result, a ternary γ' _FCC_L1₂ phase field has stabilised in the Co corner of its calculated isothermal section at 1250°C, as shown in Figure 4.11(a), when there is no evidence that this phase should be present in this system. So, it appears that in the TCNi8 database, the accuracy of the γ _FCC_A1 and γ' _FCC_L1₂ phase fields in the region of compositional space required for Ni-based superalloys have been optimised. Yet it seems to have been overlooked that the γ' _FCC_L1₂ phase is stabilising in places where it shouldn't exist, in regions of compositional space outside of the databases' main region of focus. All things considered, the optimised thermodynamic description of the Ta-Al-Co system produced in the present work, seems to be a significant improvement in comparison to the version contained in the TCNi8 database,[99] which until now was the only other available description for this ternary.

Since the ternary phase boundaries in the Ta-Al-Co description of the TCNi8 database[99] are not particularly accurate, due to the lack of available phase diagram data prior to this investigation, it may be worth considering whether the updated thermodynamic description of the Ta-Al-Co system produced by this work could be adapted and incorporated into existing superalloy design databases. This could potentially improve the accuracy of multicomponent alloy modelling predictions in the compositional space close to the Ta-Al-Co ternary. However, in order for any two thermodynamic descriptions to be compatible with each other they must use the same sublattice models for the same phases. So if any existing databases use different models for any of the phases present in the Ta-Al-Co system, then the

description produced in the present work would have to be altered in order to make it compatible with the database in question.

4.5: Conclusions

A thermodynamic assessment of the Ta-Al-Co system has been performed using the CALPHAD method. In this method, the Thermo-Calc software system was used to optimise, or fit the parameters of the Gibbs energy models for all of the phases in this ternary to the experimental data presented in Chapter 3 of this work. The optimisation produced a complete, self-consistent thermodynamic description for the Ta-Al-Co system.

The isothermal sections at 1000°C and 1150°C calculated from this description match up well with the experimentally determined versions produced in Chapter 3, and the interpolated liquidus projection seems reasonable based on the currently available information. Overall the thermodynamic description of the Ta-Al-Co system produced in the present work, seems to be a significant improvement when compared to the only other available description for this ternary, which is the version contained in the TCNi8 database.

Since the only other existing thermodynamic assessment for this system is not particularly accurate, due to the lack of available phase diagram data prior to this investigation, it may be worth considering whether the updated thermodynamic description of the Ta-Al-Co system produced by this work could be adapted and incorporated into existing superalloy design databases. This could potentially improve the accuracy of multicomponent alloy modelling predictions in the compositional space close to the Ta-Al-Co ternary.

4.6: Future work

As mentioned in Section 3.6 an attempt was made to perform an investigation that was as comprehensive as possible given the practical difficulties of producing and studying alloys containing both Ta and Al and also considering the time constraints of the project. However, in order to get a more complete picture of the phase equilibria in this system it would also be good to carry out (DTA) investigations, to determine phase transition temperatures, and information on the positions of the ternary solidus and liquidus boundaries. This information could then be used to refine the models and improve the accuracy of the interpolated solidus and liquidus boundaries that can be calculated from the current optimised ternary description of the Ta-Al-Co system.

It was initially planned that the calculation of all of the invariant points in the ternary would be performed, and a table of all of the invariant reactions for the system would be produced. This would provide more detailed insight into the phase equilibria of the system, particularly on the reactions to form all of the specific phases in the ternary as it cools from the liquid. Unfortunately this plan was not executed due to time constraints.

Finally, as discussed in Sections 4.3 & 4.4, there were some discrepancies between the Al-Ta binary description of Witusiewicz et al.[97] used for this thermodynamic assessment of the Ta-Al-Co ternary and the experimental data produced in the present work. Re-assessing the Al-Ta binary system to take this new experimental data into account, and then using this new reassessed binary in the ternary assessment would result in descriptions for both the Al-Ta and Ta-Al-Co system that are in better agreement with the data from this work. Although, the changes to the ternary description would likely be relatively minor. However, since there are a number of conflicting studies on the intermetallic phases that exist in the Al-Ta system,[40],

[48]–[50], [53], [97] this binary would seem to merit further study, in order to produce a definitive phase diagram and thermodynamic description for the system.

Chapter 5: Thermodynamic Assessment of the Ti-Fe-Mo System

5.1: Introduction

The Ti-Fe-Mo ternary was originally of interest as a subsystem of multicomponent high strength steel alloys, particularly tool steels, which sometimes contain up to 10% Mo.[114] In recent years, interest in the system has grown as it can also be used to create high strength titanium alloys with excellent corrosion resistance and mechanical properties for aerospace and automotive applications.[114] Until recently, data on this system was fairly scarce, and consisted of a partial isothermal section at 900°C produced by Sokolovskaya et al.,[115] a partial isothermal study at 1000°C, and thermodynamic assessment by Jin et al.,[116] and an investigation of the Ti rich compositions at 600°C and 750°C by Shurin et al.[117] However, a comprehensive investigation of this ternary has recently been carried out by Knowles et al.[1]–[3] who produced complete isothermal sections for the system at 750°C, 900°C, and 1000°C. This study established that an extensive BCC_A2 - BCC_B2 (β - β') two-phase field exists in the system and extends all the way to the Mo rich compositions. It also demonstrated that it was possible to form BCC_B2_TiFe precipitates, within a Mo rich BCC_A2 (Ti, Mo) matrix in the Ti-Fe-Mo system. All of which indicates that this ternary is likely to be an attractive base system for the creation of high strength β/β' precipitate strengthened Ti and Mo based alloys for structural applications within the aerospace industry.

Comparing Jin et al.'s[116] calculated isothermal section for the Ti-Fe-Mo system at 1000°C to the temperature matched experimentally determined version of Knowles et al.,[3] in Figure 5.1, shows that there are a few differences between the two diagrams. Specifically that

Jin et al.[116] modelled the Laves_C14 and BCC_B2_TiFe phases as stoichiometric, whereas the data of Knowles et al.[3] indicates that these phases exhibit both binary and ternary solubility ranges. Moreover in the diagram of Jin et al.[116] the Mu_D8₅ phase extends into the ternary to an approximate Ti composition of only 14at%, whereas in that of Knowles et al.,[3] this phase extends much further to around 22at%. This indicates that it would be worthwhile to perform a new thermodynamic assessment on the Ti-Fe-Mo ternary that takes into account the more recent comprehensive data on this system produced by Knowles et al.[1]–[3]

However, during the course of this work, another more recent thermodynamic assessment of the Ti-Fe-Mo system was also performed,[114] which addressed some of the issues with Jin et al.'s[116] earlier assessment. Although this assessment still used the same Fe-Mo binary description as Jin et al.[116] and also kept the same Mu_D8₅ phase model and description. Moreover, this assessment also did not take into account the data of Knowles et al.,[1]–[3] and so as shown in Figure 5.2, the calculated phase diagram from Watson & Markus[114] does not completely match the experimental version of Knowles et al.[3] particularly with regards to the ternary extension of the Mu_D8₅ phase. Therefore there is still the need to perform a new thermodynamic assessment that accurately describes the current data on the Ti-Fe-Mo system.

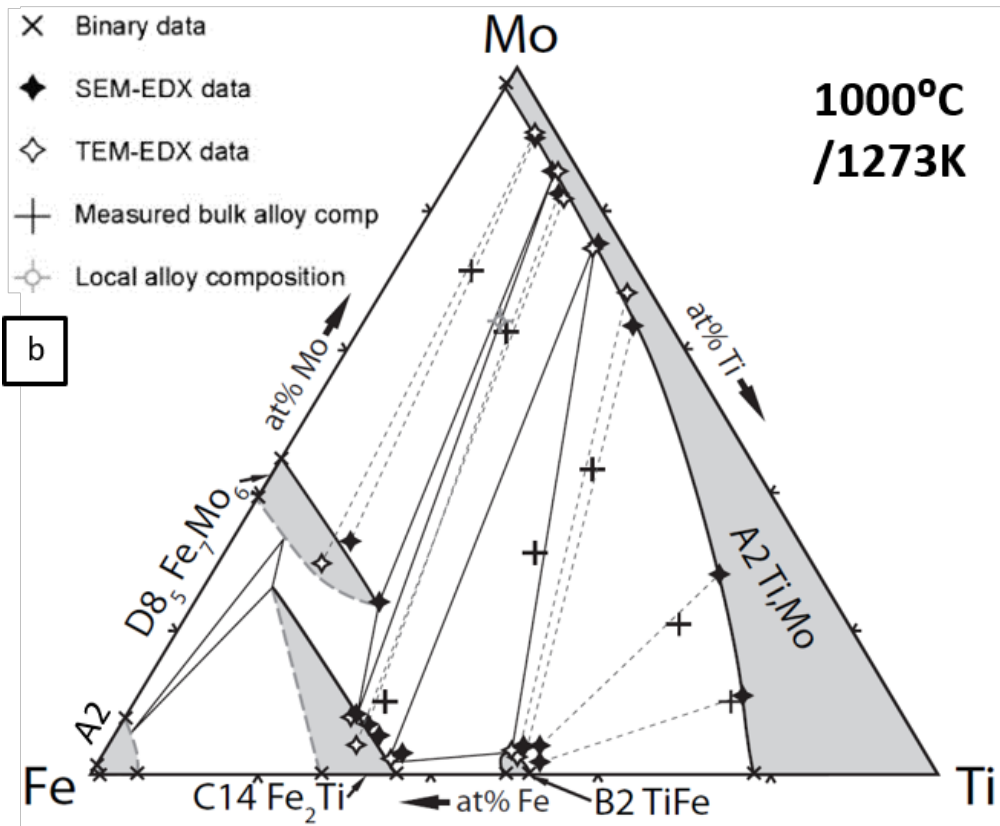
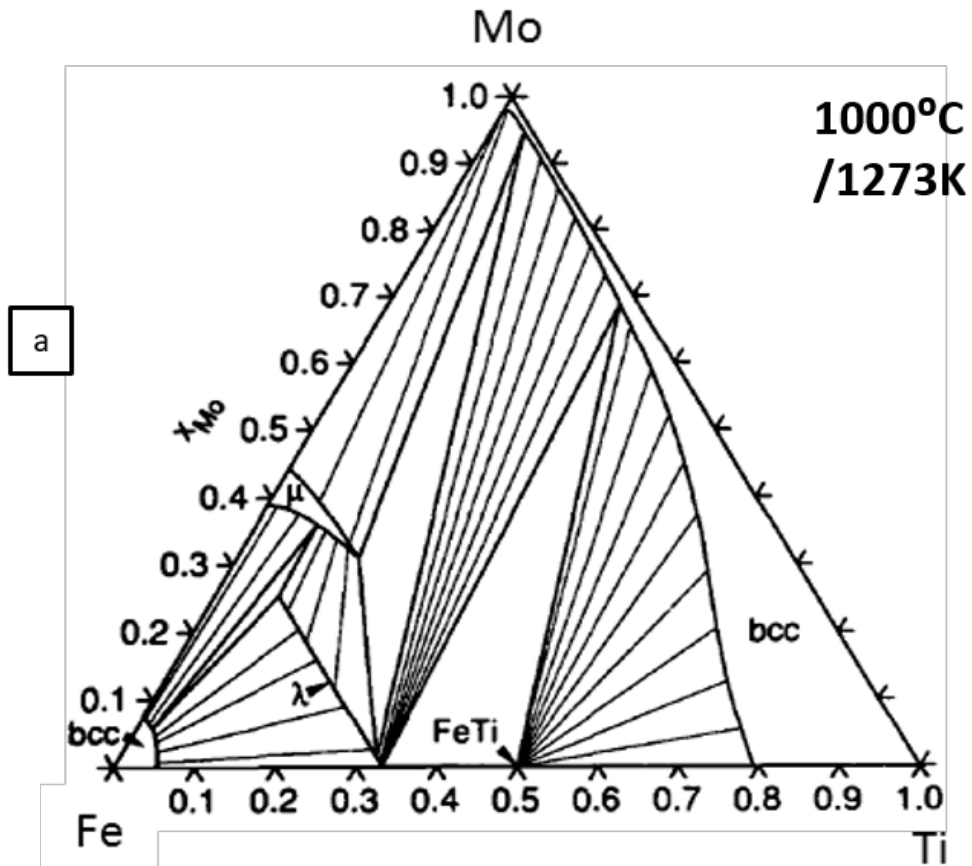


Figure 5.1: The Ti-Fe-Mo isothermal section at 1000°C calculated from the description of Jin et al., (a),[116] compared to the temperature matched experimentally determined isothermal section of Knowles et al. (b).[3]

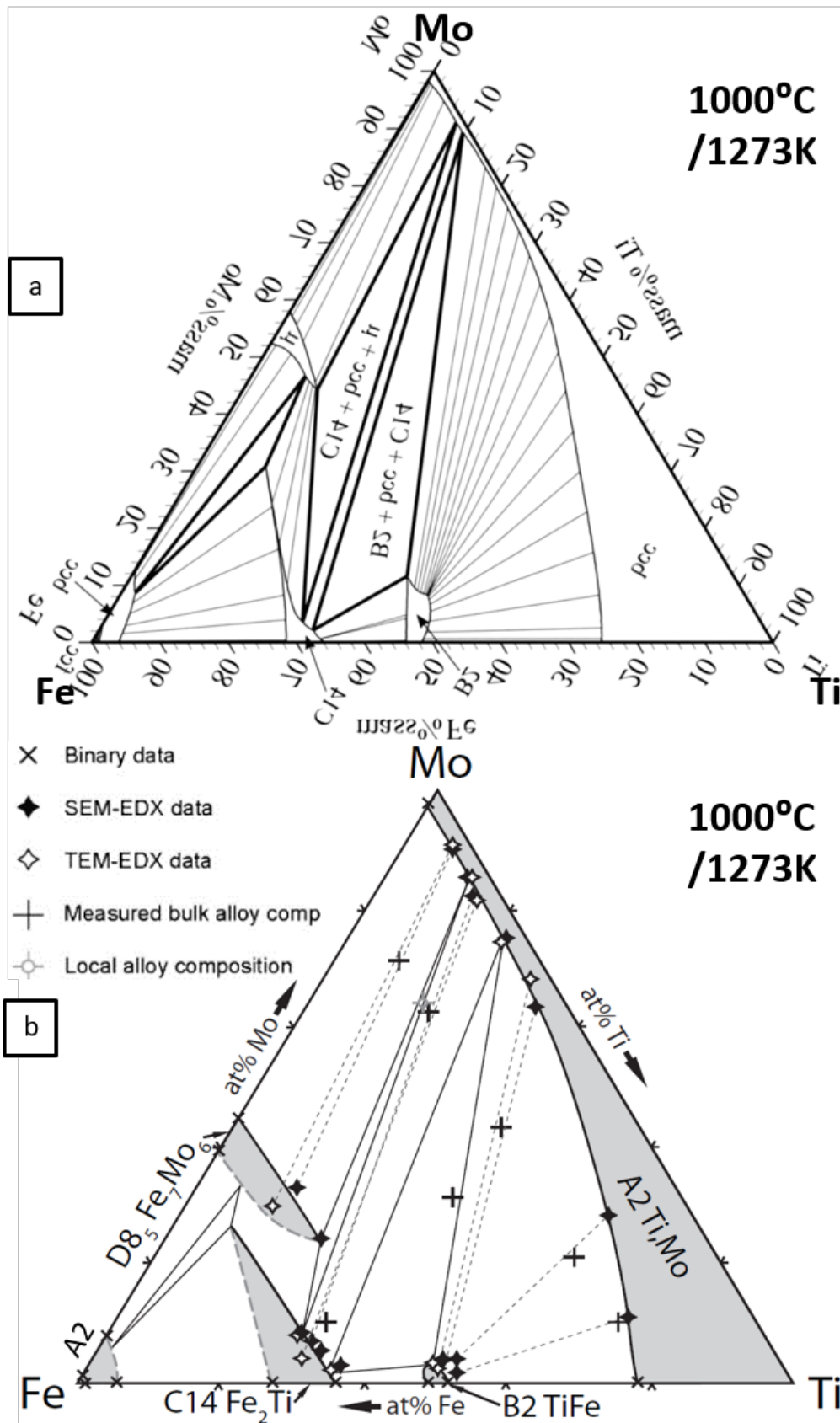


Figure 5.2: The Ti-Fe-Mo isothermal section at 1000°C calculated from the description of Watson & Markus., (a),[114] compared to the temperature matched experimentally determined isothermal section of Knowles et al. (b).[3] It should be noted that the axes of diagram (a) are in mass %, and the axes of diagram (b) are in at%.

5.2: Method

5.2.1: Introduction to the Method

Since the CALPHAD method was used for both the assessment of the Ta-Al-Co, and Ti-Fe-Mo systems, the general method used was the same as that described in Section 4.2.1. Therefore only a very brief summary will be given here, since a more detailed description has already been given in Section 4.2.1. Essentially this method consists of, selecting Gibbs energy models for the phases that exist in the pure elements and then fitting these to the available experimental data to produce the optimised unary descriptions. These unary descriptions are then incorporated into the selected Gibbs energy models for the phases in the binary systems, which are again fitted to the available binary experimental data to produce the optimised binary descriptions. Then finally the binary descriptions are incorporated into the selected Gibbs energy models for the phases in the ternary systems, which are again fitted to the available ternary experimental data to produce the optimised ternary descriptions. Therefore, in order to produce a thermodynamic description for the Ti-Fe-Mo system it is necessary to first obtain and combine suitable descriptions for the unary and binary subsystems of this ternary.

At present most modern CALPHAD assessments use the unary descriptions developed by Dinsdale et al. from the Scientific Group Thermodata Europe (SGTE) [105], and so these unary descriptions were also used in the present work. In addition, a review of the published thermodynamic assessments of the required binaries was carried out, since compatible binary descriptions of sufficient accuracy can also be incorporated into the ternary assessment, thus saving the time and effort that would be required to create these descriptions from scratch. The binary descriptions selected from the literature for this assessment were the Fe-Mo

description of Rajkumar et al.,[118] the Fe-Ti description of Santhy et al.,[119] and the Mo-Ti description of Chung et al.[120] Again, these three descriptions were selected on the basis that they were the best matching descriptions available that fit all of the required criteria:

- 1) They were based on the most accurate experimental data currently available.
- 2) They used suitable CALPHAD models to accurately describe the crystal structures and Gibbs energies of all of the required phases.
- 3) The models that the descriptions used were compatible with each other, so that they could be combined together to form a functioning extrapolated ternary description.

The binary descriptions from these papers were transcribed into Thermo-Calc[106] database files, and the binary phase diagrams were recalculated from these databases to ensure that they were accurate reproductions of the original descriptions. Once this was confirmed, the binary databases were then combined to produce an initial extrapolated description of the Ti-Fe-Mo ternary, which contained the models required to describe the Gibbs energies as a function of composition and temperature for all of the phases present in the unary, and binary systems. The models in this extrapolated ternary description were then edited, based on the experimental data on the Ti-Fe-Mo ternary, and related systems from the literature,[1]–[3], [115]–[117] in order to produce the final Thermo-Calc[106] model set up file that contained the set of phases, models, parameters and coefficients required for the assessment of this ternary. This model set up file will be discussed further in Section 5.2.2.

A literature review was performed to gather experimental phase diagram and thermodynamic data on the Ti-Fe-Mo ternary to be used for the assessment. And these results were entered into a .pop Thermo-Calc[106] experimental data file in the required format so that they could be used for the assessment. Since the bulk of the experimental data came from

the work of Knowles et al, [1]–[3] the optimisation was quite heavily based on this data, with the next highest contribution coming from the work of Jin et al.[116]

The Gibbs energy models for all of the phases in the Ti-Fe-Mo ternary contained in the Thermo-Calc[106] model set up file were then fitted to the data contained in the Thermo Calc[106] experimental data file to create a thermodynamic description of the system that accurately matched the selected experimental data. This fitting process is also known as optimisation, and is an iterative process whereby the coefficients of the Gibbs energy models for all of the phases in the system are altered step by step, until the models fit well with the selected experimental data. The Thermo Calc[106] PARROT module was used to facilitate the optimisation process as described in Section 4.2.1.

5.2.2: Thermodynamic Modelling and the Model Set Up File

As discussed in Section 5.2.1 the models for the assessment of the Ti-Fe-Mo ternary were built up from the models for the unary and binary subsystems of this ternary, and then edited to ensure that they could describe the Gibbs energy of every phase in the system as a function of composition and temperature. The specific model for each type of phase was selected based on its crystal structure and physical behaviour, as will be explained below.

5.2.2.1: Gibbs Energy Models for the Disordered Solution Phases

The disordered solution phases in the Ti-Fe-Mo system, where the atoms mix randomly either in the liquid, or on a lattice, are the: Liquid, FCC_A1 Fe, BCC_A2 Fe, BCC_A2 Mo, BCC_A2 Ti, and HCP_A3 Ti phases. The substitutional Redlich-Kister subregular solution model[92] was used, to model each of these phases with a single sublattice occupancy of: (Fe,Mo,Ti)₁. The contributions to the Gibbs energy for these disordered solution phases are:

$$G^\varphi = G^{0,\varphi} + G^{ideal,\varphi} + G^{xs,\varphi} + G^{mag,\varphi} \quad (5.1)$$

Where:

$$G^{0,\varphi} = \sum_i x_i G_i^{0\varphi} \quad (5.2)$$

$$G^{ideal,\varphi} = RT \sum_i x_i \ln x_i \quad (5.3)$$

$$G^{xs,\varphi} = \sum_i \sum_{j>i} x_i x_j \sum_v^n (x_i - x_j)^v L_{ij}^v + \sum_i \sum_{j>i} \sum_{k>j} x_i x_j x_k L_{ijk} \quad (5.4)$$

$$G_A^{mag,\varphi} = RT \ln (\beta_0^\varphi + 1) f(\tau^\varphi) \quad (5.5)$$

In this model, x_i are the mole fractions of the elements i ($i = \text{Fe}, \text{Mo}, \text{Ti}$), and $G_i^{O,\varphi}$ are the Gibbs energies as a function of temperature for the pure elements in liquid phase form; $G_{Fe}^{O,\varphi}, G_{Mo}^{O,\varphi}, G_{Ti}^{O,\varphi}$ taken from Dinsdale et al.[105] and described by Equation 4.3. R is the ideal gas constant, and T is the absolute temperature in degrees Kelvin. And the L terms are the ν -th order interaction parameters between elements i and j or i, j and k , where ($i, j, k = \text{Fe}, \text{Mo}, \text{or Ti}$), which describe the Gibbs energy contribution resulting from any non-ideal interactions between these atoms. These L terms are empirical parameters whose temperature dependence is similar to those of the $G_i^{O,\varphi}$ terms in equation 4.3:

$$L = a + bT + cT \ln T + dT^2 + \dots \quad (5.6)$$

Only in this case the L parameters will be optimised in this work by fitting the coefficients, a, b, c, d, \dots to the available experimental data on the system. [5], [88], [90], [92]

The magnetic term, $G_A^{mag,\varphi}$, in Equation 5.5 is only necessary if the phase is magnetic. In this equation, β_0^φ is the average Bohr magneton number per atom in the phase, $f(\tau^\varphi)$ is the integral of a function fitted to the magnetic contribution to the heat capacity, and

$$\tau^\varphi = \frac{T}{T_C^\varphi} \quad (5.7)$$

with T_C^φ , being the Curie temperature of the phase, which is also the critical temperature for magnetic ordering. [5], [88], [90]

5.2.2.2: Gibbs Energy Models for the Ordered Intermetallic Phases

Ordered intermetallics have a reference stoichiometry, but also still often exhibit either increased or decreased solubility ranges. In this assessment of the Ti-Fe-Mo ternary, all of the ordered intermetallic phases in the system were modelled using the compound energy formalism.[110] The 2 sublattice form of this model is described below in Equations 5.8 to 5.12. In cases where more than 2 sublattices were required, the model was simply expanded by adding extra terms to represent the additional required sublattices.

$$G^\varphi = G^{0,\varphi} + G^{ideal,\varphi} + G^{xs,\varphi} + G^{mag,\varphi} \quad (5.8)$$

Where:

$$G^{0,\varphi} = \sum_i \sum_j y_i^1 y_j^2 G_{i,j}^{0\varphi} \quad (5.9)$$

$$G^{ideal,\varphi} = RT \left(a_1 \sum_i y_i^1 \ln y_i^1 + a_2 \sum_j y_j^2 \ln y_j^2 \right) \quad (5.10)$$

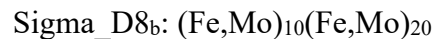
$$\begin{aligned} G^{xs,\varphi} = & \sum_i \sum_{j>i} \sum_{K>j} y_i^1 y_j^1 y_k^2 L_{i,j:k} + \sum_i \sum_{j>i} \sum_{K>j} y_k^1 y_i^2 y_j^2 L_{k:i,j} \\ & + \sum_i y_i^1 y_j^1 y_k^1 y_i^2 L_{i,j,k:i} + \sum_i y_i^1 y_i^2 y_j^2 y_k^2 L_{i:i,j,k} \end{aligned} \quad (5.11)$$

$$G^{mag,\varphi} = RT \ln (\beta_0^\varphi + 1) f(\tau^\varphi) \quad (5.12)$$

In this model, $G_{i,j}^{0\varphi}$, are the molar Gibbs energies of hypothetical end-member compounds $i:j$, a_1 & a_2 are the site fractions of sublattices 1 & 2, and y^1 & y^2 are the constituent fractions of species i, j, k on sublattices 1 and 2, where $i,j,k = \text{Fe, Mo, or Ti}$. R is the ideal gas constant, and T is the absolute temperature in degrees Kelvin. And again the L terms are the interaction parameters that are optimised in the present work. These L parameters are based

on Redlich-Kister polynomials, which describe the Gibbs energy contribution resulting from any non-ideal interactions between the atoms on each sublattice. In addition, the model notation uses a colon to separate the different sublattices, and a comma to separate the species that are interacting on a specific sublattice. The magnetic term, $G_A^{mag,\varphi}$, in Equation 5.12 is only necessary if the phase is magnetic, and the terms for this contribution are described above when discussing Equation 5.5. [5], [90], [110]

The sublattice models used for the ordered intermetallic phases in the Ti-Fe-Mo system are:



All of the other ordered intermetallic phases in the system listed above were modelled in the same way; using the compound energy formalism,[110] given in Equations 5.8 to 5.12, except for the BCC_B2 phase, which is a slightly special case. This phase was also modelled using the compound energy formalism, but it was modelled as an ordering reaction from disordered BCC_A2 to ordered BCC_B2, using the method developed by Dupin & Ansara.[111] In this model, the Gibbs energy of the ordered BCC_B2 phase, G^{BCC_B2} , is obtained by first calculating the Gibbs energy of the disordered BCC_A2 phase, G^{BCC_A2} , using the compound energy formalism,[110] then adding the energy contribution of the ordering reaction, ΔG^{Ord} , to yield the total Gibbs energy for the ordered BCC_B2 phase as shown in Equations 5.13 and 5.14.

$$G^{BCC} = G^{BCC_A2} + \Delta G^{Ord} \quad (5.13)$$

$$\Delta G^{Ord} = G^{BCC_B2_Ord}(y_i^1, y_i^2, y_{Va}^3) - G^{BCC_B2_Disord}(y_i^1, y_{Va}^3) \quad (5.14)$$

This ordering contribution, ΔG^{Ord} , is also calculated using the compound energy formalism,[110] and is equal to the difference between the Gibbs energy of the BCC_B2 lattice, $G^{BCC_B2_Ord}(y_i^1, y_i^2, y_{Va}^3)$, and the hypothetical Gibbs energy for the BCC_B2 lattice in the disordered state, $G^{BCC_B2_Disord}(y_i^1, y_{Va}^3)$. Therefore, when the BCC lattice is in the disordered state, $\Delta G^{Ord} = 0$, and the Gibbs energy for the lattice = G^{BCC_A2} . And when the BCC lattice is in the ordered BCC_B2 state, $\Delta G^{Ord} < 0$, and the Gibbs energy for the lattice = G^{BCC_B2} . This ordering model enables the disorder/order transformation, to be described using a single Gibbs energy expression for both ordered and disordered phases. And the partitioning between these two states ensures that descriptions of systems that contain phases which undergo disorder/order transformations can be easily combined with descriptions of systems where these phases are always disordered.[111]

5.2.2.3: Summary of the Phases in the Ti-Fe-Mo system, and the models used to describe them

A summary of the known phases in the Ti-Fe-Mo system, their crystal structures, and the models used to describe them in this assessment are given in Table 5.1. The phases highlighted in green in this table, namely; Liquid, FCC_A1 Fe, BCC_A2 Fe, BCC_A2 Mo, BCC_A2 Ti, and HCP_A3 Ti are all disordered solution phases, and are modelled using the substitutional Redlich-Kister subregular solution model,[92] described by Equations 5.1 to 5.7. [5], [88], [90], [92] And the phases highlighted in orange in this table are the ordered intermetallic phases, namely: Mu_D8₅, Laves_C14, Sigma_D8_b, R, & BCC_B2_TiFe. These phases were modelled using the compound energy formalism[110] described by Equations 5.8 to 5.14. [5], [90], [110]

Table 5.1: A summary of the known phases, their crystal structures, and the models currently used to describe them in the optimised Ti-Fe-Mo description produced during this work

N	Phase	Pearson symbol	Space group	Prototype	Number of Sublattices & Sublattice Model	
1	Liquid	N/A	N/A	N/A	1	(Fe,Mo,Ti)
2	HCP_A3 Ti	hP2	P6 ₃ /mmc	Mg	1	(Fe,Mo,Ti)
3	BCC_A2 Ti	cI2	<i>Im</i> $\bar{3}$ <i>m</i>	W	1	(Fe,Mo,Ti)
4	BCC_A2 Fe	cI2	<i>Im</i> $\bar{3}$ <i>m</i>	W	1	(Fe,Mo,Ti)
5	FCC_A1 Fe	cF4	<i>Fm</i> $\bar{3}$ <i>m</i>	Cu	1	(Fe,Mo,Ti)
6	BCC_A2 Mo	cI2	<i>Im</i> $\bar{3}$ <i>m</i>	W	1	(Fe,Mo,Ti)
7	BCC_B2 _TiFe	cP2	<i>Pm</i> $\bar{3}$ <i>m</i>	CsCl	2	(Fe,Mo,Ti) _{0.5} (Fe,Mo,Ti) _{0.5}
8	Laves_C14	hP12	P6 ₃ /mmc	MgZn ₂	2	(Fe,Mo,Ti) ₂ (Fe,Mo,Ti) ₁
9	Mu_D8 ₅	hR13	<i>R</i> $\bar{3}$ <i>m</i>	Fe ₇ W ₆	4	(Fe,Mo,Ti) ₆ (Fe,Mo,Ti) ₂ (Mo,Ti) ₄ (Fe,Mo,Ti) ₁
10	Sigma_D8 _b	tP30	P4 ₂ /mmm	CrFe	2	(Fe,Mo) ₁₀ (Fe,Mo) ₂₀
11	R	hR159	R-3	Co ₅ Cr ₂ Mo ₃	3	(Fe) ₃₂ (Mo) ₁₈ (Fe,Mo) ₃
Table 4.1 Model Colour Code						
Green1: Disordered solution phases modelled using the Redlich-Kister subregular solution model						
Orange: Ordered intermetallics modelled using the compound energy formalism						

5.3: Results

After optimising the coefficients of all required model parameters, a complete, self-consistent thermodynamic description for the Ti-Fe-Mo system was obtained. This optimised description is listed in full, in Thermo-Calc .tdb format in Appendix 2.

Figure 5.3 shows the Fe-Mo, Fe-Ti, and Mo-Ti binary phase diagrams that have been re-calculated from the final optimised ternary description. It is important to check these calculated binary diagrams against those produced from the original binary descriptions to ensure that the model alterations made to describe the ternary system have not produced any unwanted changes to the original binaries. From Figure 5.3 it can be seen that the Fe-Mo, Fe-Ti, and Mo-Ti binary phase diagrams that have been re-calculated from the optimised Ti-Fe-Mo description produced in the present work are exactly the same as the diagrams calculated from the original descriptions by Rajkumar et al.,[118] Santhy et al.,[119] and Chung et al.[120] respectively.

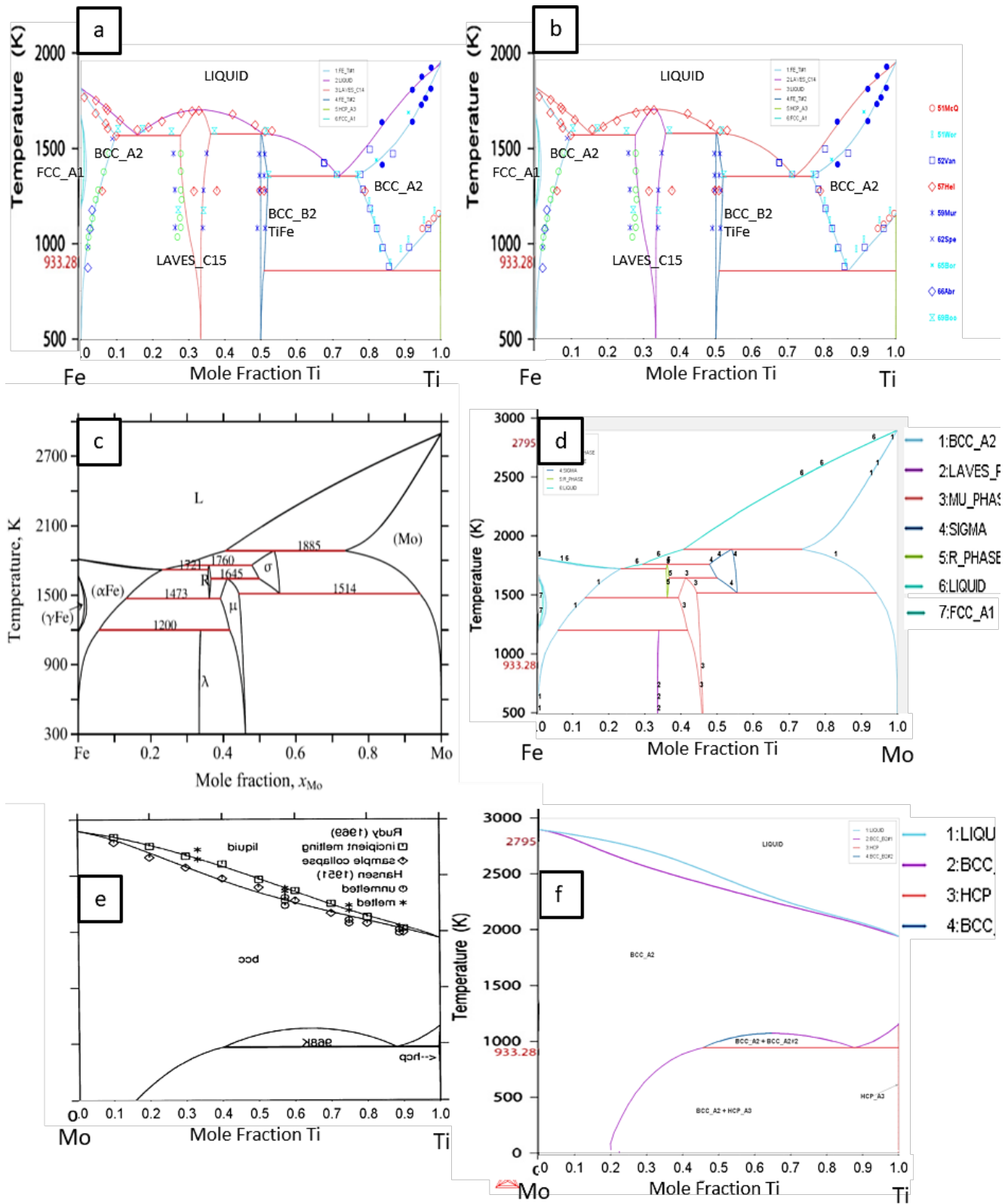


Figure 5.3: The calculated Fe-Ti, Fe-Mo and Mo-Ti binary phase diagrams of Santhy et al.[119] (a), Rajkumar et al.[118] (c) and Chung et al.[120] (e) respectively compared with the recalculated versions from the final optimised Ti-Fe-Mo description produced in this work, (b), (d) & (f).

Figures 5.4 to 5.6 show comparisons between the experimentally determined isothermal sections of the Ti-Fe-Mo system at 750°C, 900°C, and 1000°C of Knowles et al.[2], [3] compared to the temperature matched calculated isothermal sections from the optimised Ti-Fe-Mo description produced by the present work. The calculated isothermal section at 1000°C, matches very well with the experimental version of Knowles et al.[3] in terms of the ternary phase boundaries of virtually all of the phases in the diagrams. However, the calculated diagrams at 750°C, & 900°C match well in terms of the boundaries of the BCC_A2 Fe, BCC_A2 Ti, BCC_B2 TiFe, and Laves_C14 phases, but do not match up so well with the boundaries of the BCC_A2 Mo, and Mu_D8₅ phases.

Initially, considerable effort was expended to fit the models for the BCC_A2 Mo, and Mu_D8₅ phases accurately to the data of Knowles et al.[2], [3] at all temperatures, with little success. After a while it became clear that the reason the boundaries of these two phases would not fit well to the data at temperatures below 1000°C, was that the data on these phases was likely to be incorrect at the lower temperatures. In Figure 5.7, the ternary experimental data on the position of the BCC_A2 Mo solvus boundary from Knowles et al. [2], [3] at 750°C, 900°C, & 1000°C, is compared to the calculated version of this boundary from the Fe-Mo binary description of Rajkumar et al.[118] that was used in ternary Fe-Mo-Ti description produced in the present work. This figure demonstrates that the data matches the calculated boundary at 1000°C, but not at 750°C, 900°C. And that if you were to fit the solvus boundary to this data, at the lower temperatures, you would end up with a very unrealistic looking boundary. Moreover, you can also see from Figures 5.4(a) and 5.5(a), that the binary boundary data points marked with an X in the Mo corners of the diagrams do not match the BCC_A2 Mo solvus boundary from Knowles et al.[2] at 750°C & 900°C. Therefore, it can be concluded that the phase boundary compositions measured in the Mo rich region of the ternary diagrams

at 750°C & 900°C by Knowles et al.[1]–[3] are not accurate equilibrium condition phase boundaries, but those measured in this region of the diagrams at temperatures of 1000°C or more are likely to be accurate equilibrium condition phase boundaries.

Moreover, comparing Figure 5.4(a) to Figure 5.8(a), we can see that the phase boundary data of Knowles et al.[2] for the equilibria between the BCC_A2 Mo & Mu_D8₅ phases, and the BCC_A2 Mo & BCC_B2 TiFe phases at 750°C fits better with the boundaries for these phases at around 1200°C, rather than 750°C. And since the boundaries for these phases have likely been measured under non equilibrium conditions in the alloys that were heat treated at 750°C & 900°C, it is also likely that the ternary solubilities for these phases at these temperatures have been overestimated. Therefore the boundaries of the BCC_A2 Mo, and Mu_D8₅ phases were fitted to the data from Knowles et al. [2], [3] at temperatures of 1000°C or higher, but the data on the boundaries of these phases at temperatures lower than 1000°C was excluded from the optimisation.

This example illustrates the importance of the assessor's judgement in critically assessing the data to be used in the optimisation of a thermodynamic description. It also demonstrates that a calculated ternary phase boundary that is interpolated from accurate binary descriptions may in some cases be more accurate than an experimentally measured dataset. In addition, it highlights how performing a thermodynamic assessment of an alloy system can complement an experimental investigation, and help researchers to identify which measured data points are likely to be accurate, and which measured data points are likely to be less so.

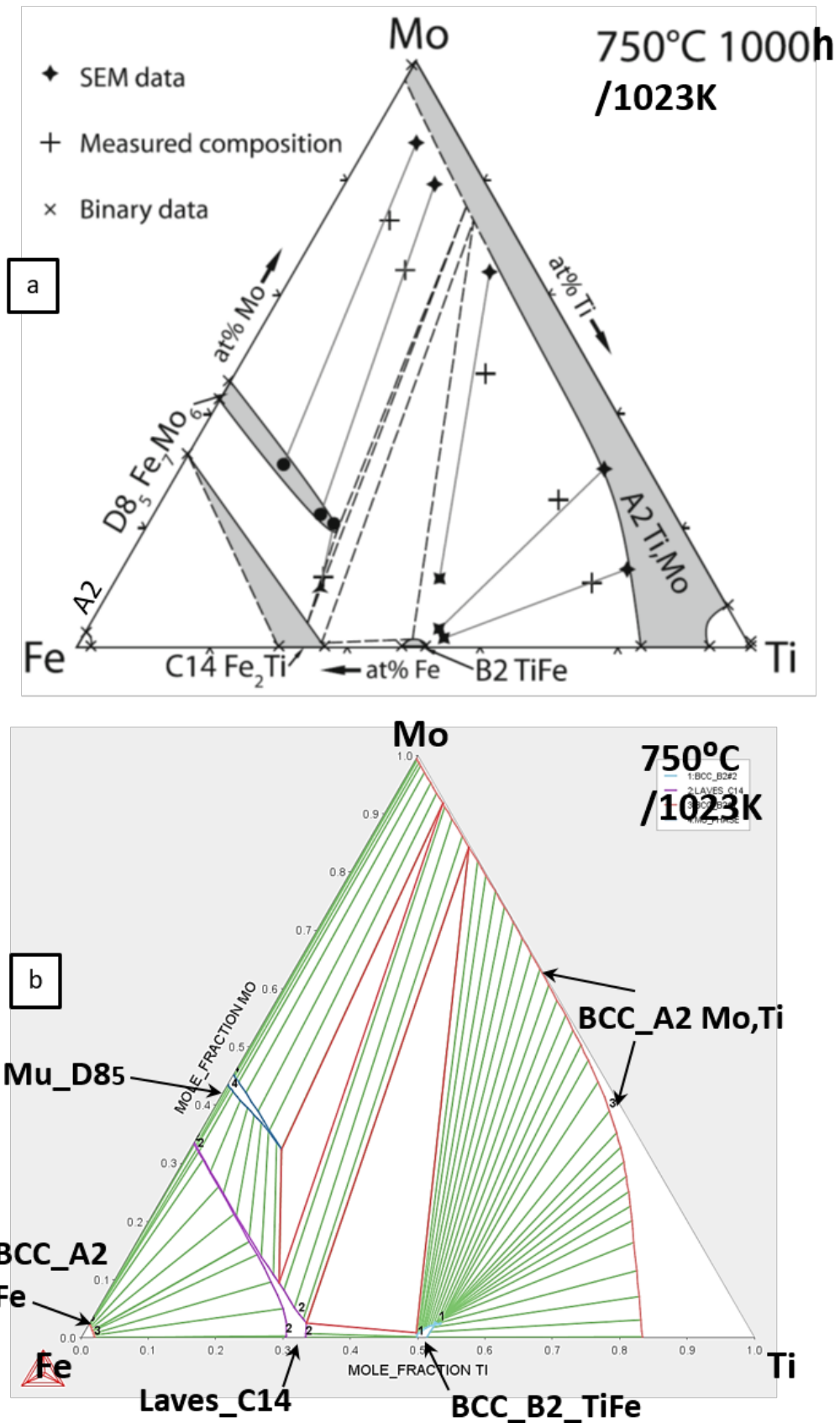


Figure 5.4: The experimentally determined isothermal section of the Ti-Fe-Mo system at 750°C of Knowles et al. (a),[2] compared to the temperature matched calculated isothermal section from the optimised Ti-Fe-Mo description produced by the present work (b).

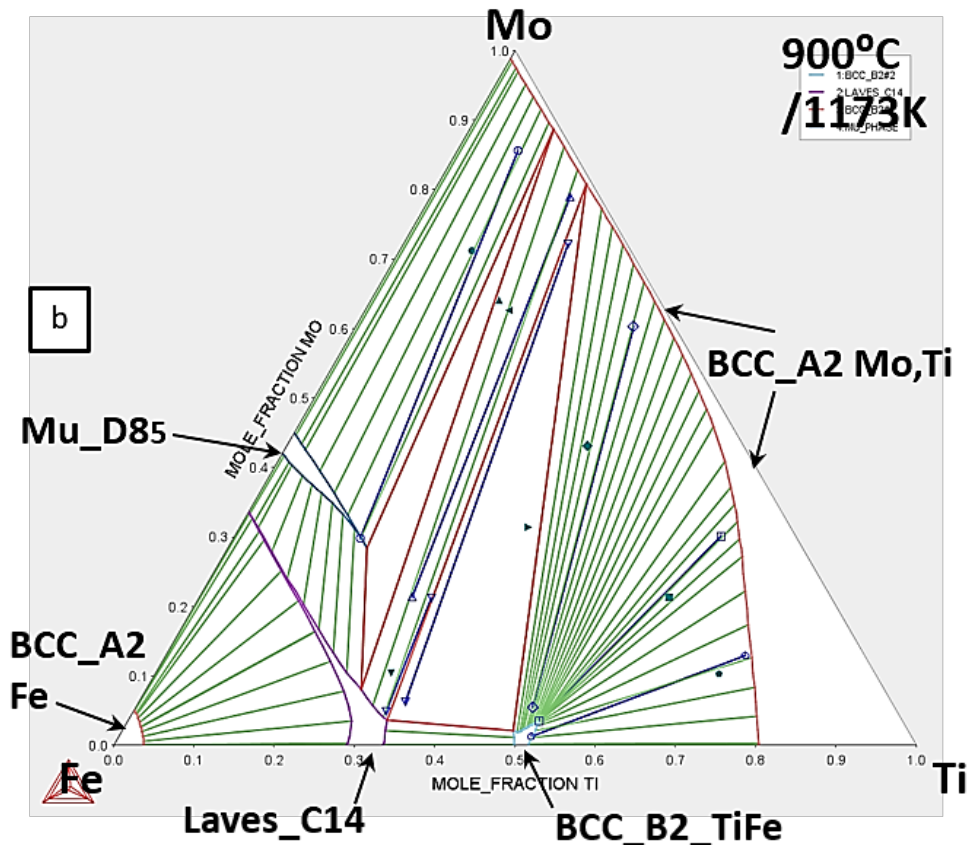
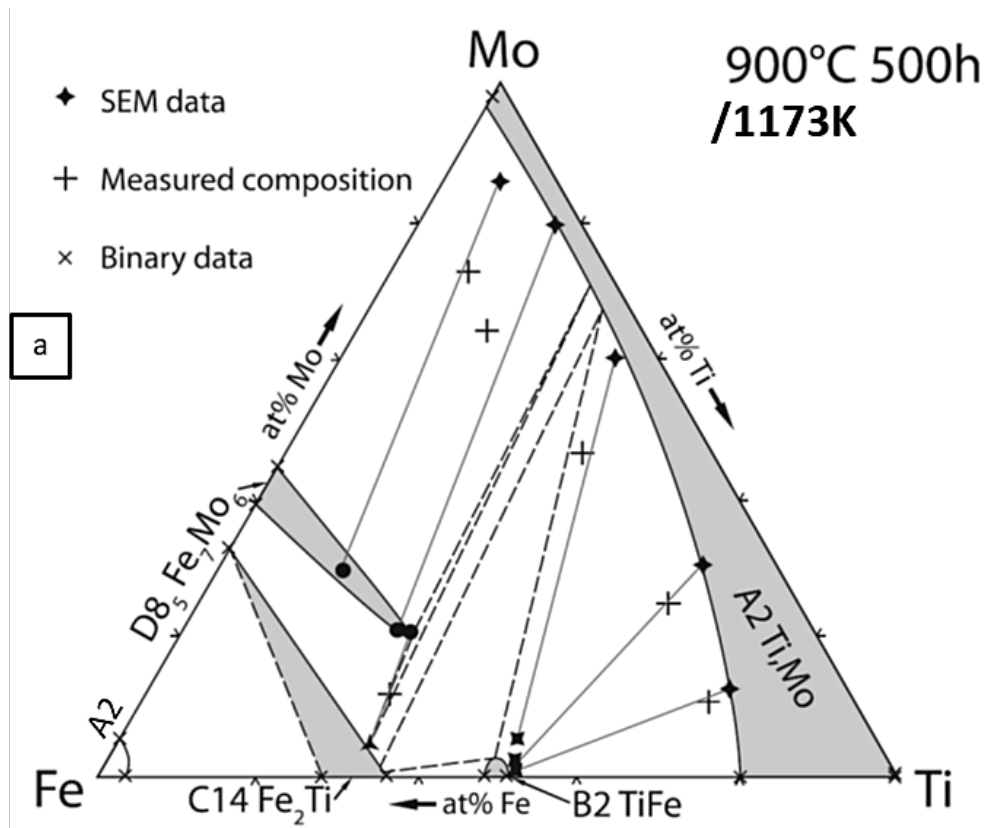


Figure 5.5: The experimentally determined isothermal section of the Ti-Fe-Mo system at 900°C of Knowles et al. (a),[2] compared to the temperature matched calculated isothermal section from the optimised Ti-Fe-Mo description produced by the present work (b). Alloy composition and tie line data overlaid on both diagrams is from Knowles et al.[2]

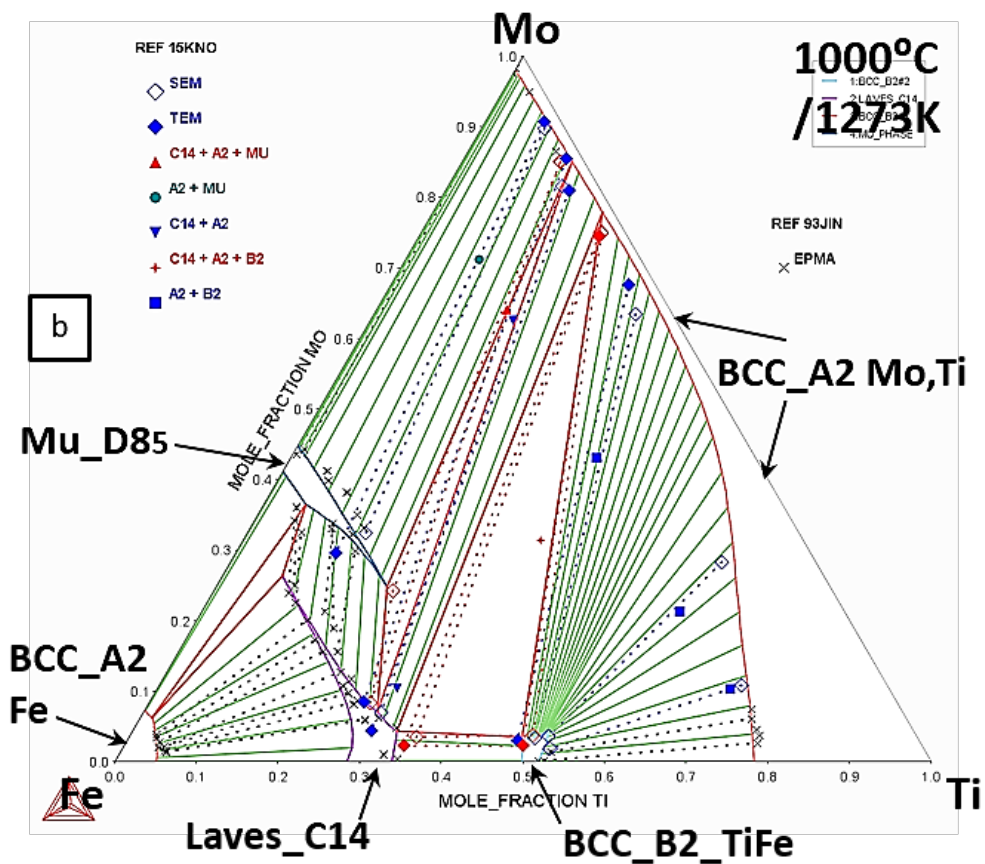
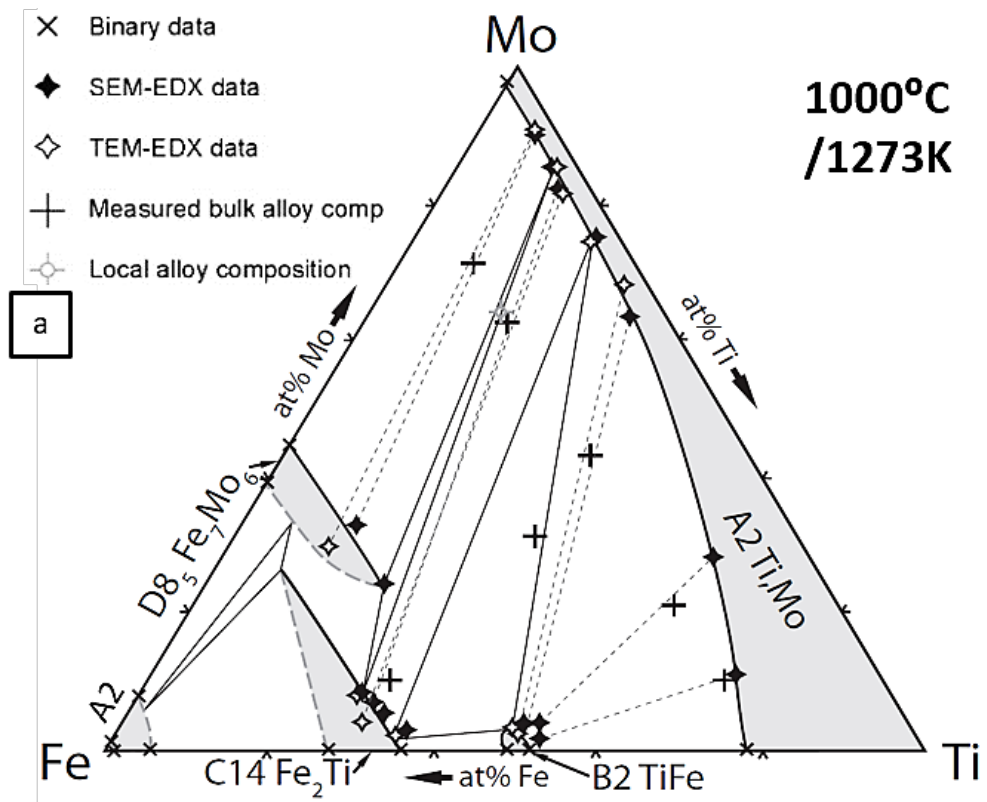


Figure 5.6: The experimentally determined isothermal section of the Ti-Fe-Mo system at 1000°C of Knowles et al. (a),[3] compared to the temperature matched calculated isothermal section from the optimised Ti-Fe-Mo description produced by the present work, (b). Alloy composition and tie line data overlaid on diagram (b) is from Knowles et al.[3] & Jin et al.[116]

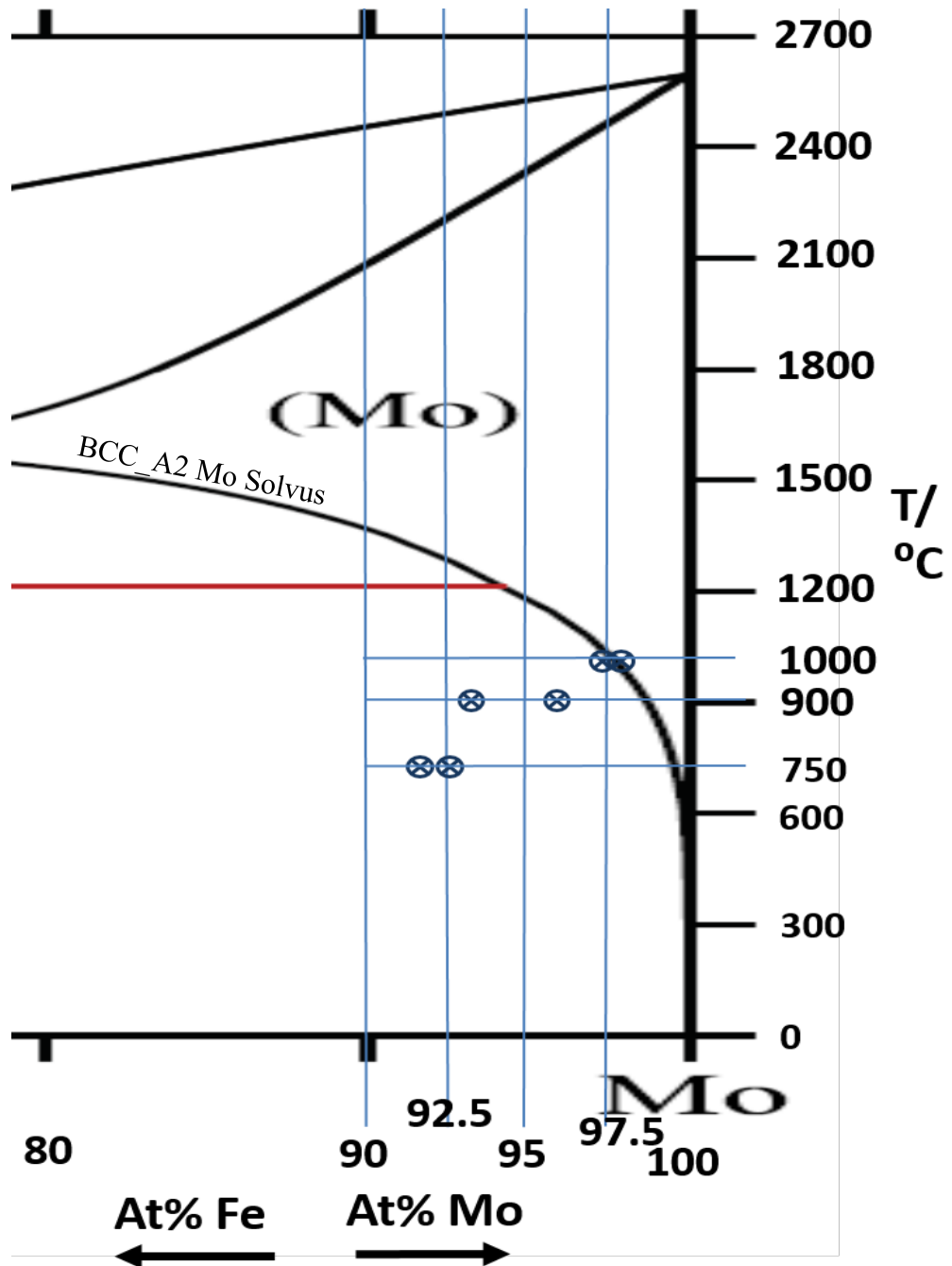


Figure 5.7: The Mo rich end of the calculated Fe-Mo binary from Rajkumar et al.[118] that was used to produce the optimised Ti-Fe-Mo description produced by the present work, with selected ternary experimental data points from Knowles et al.[2], [3] overlaid on the diagram. This figure shows the comparison of the calculated BCC_A2 Mo solvus boundary to the experimental data points on the position of that boundary in the ternary system from Knowles et al. (b).[2], [3]

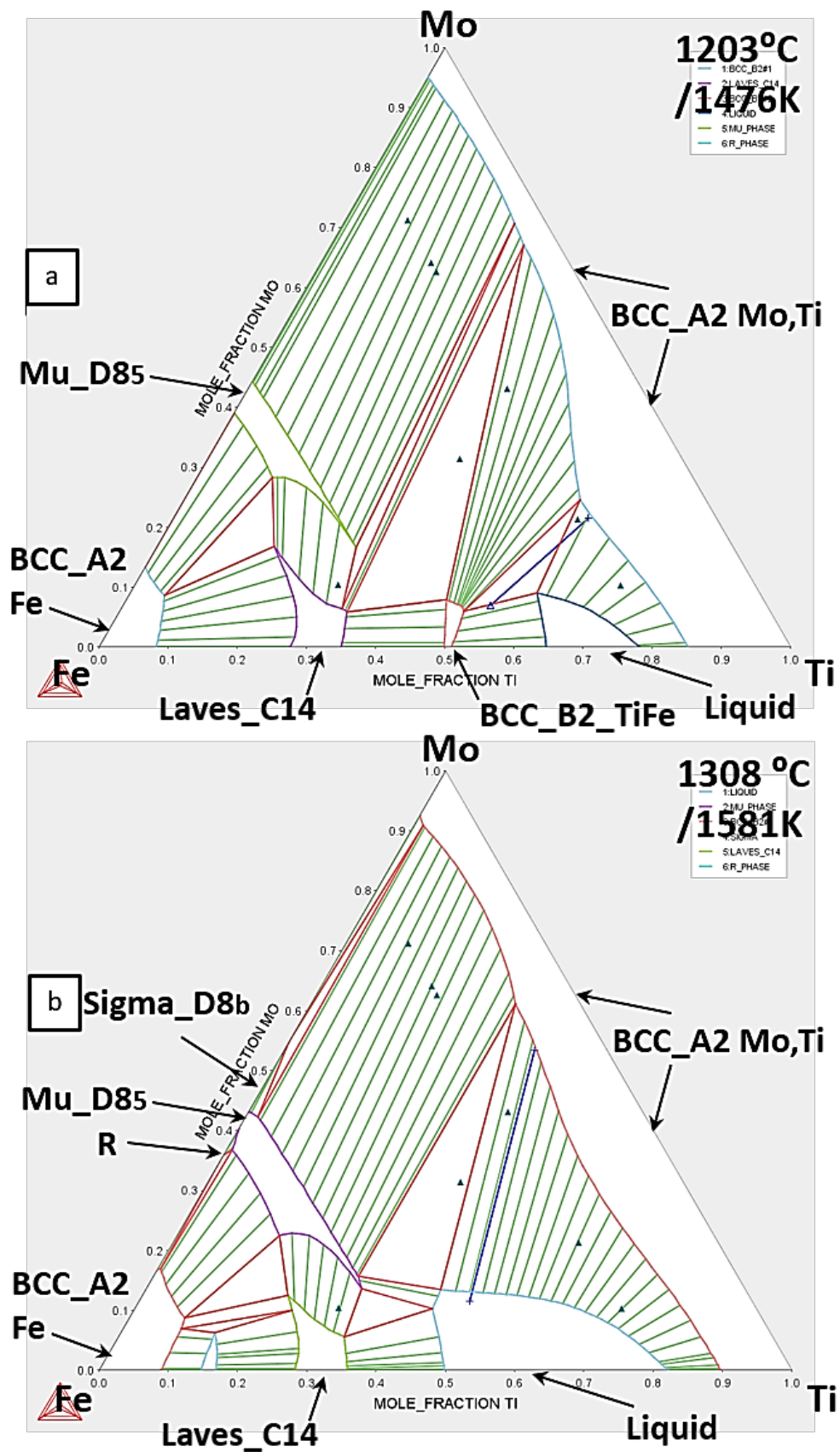


Figure 5.8: The calculated isothermal sections at 1203°C, (a), & 1308°C, (b), from the optimised Ti-Fe-Mo description produced by the present work. The blue overlaid tieline data is from the experimental work of Knowles.[1]

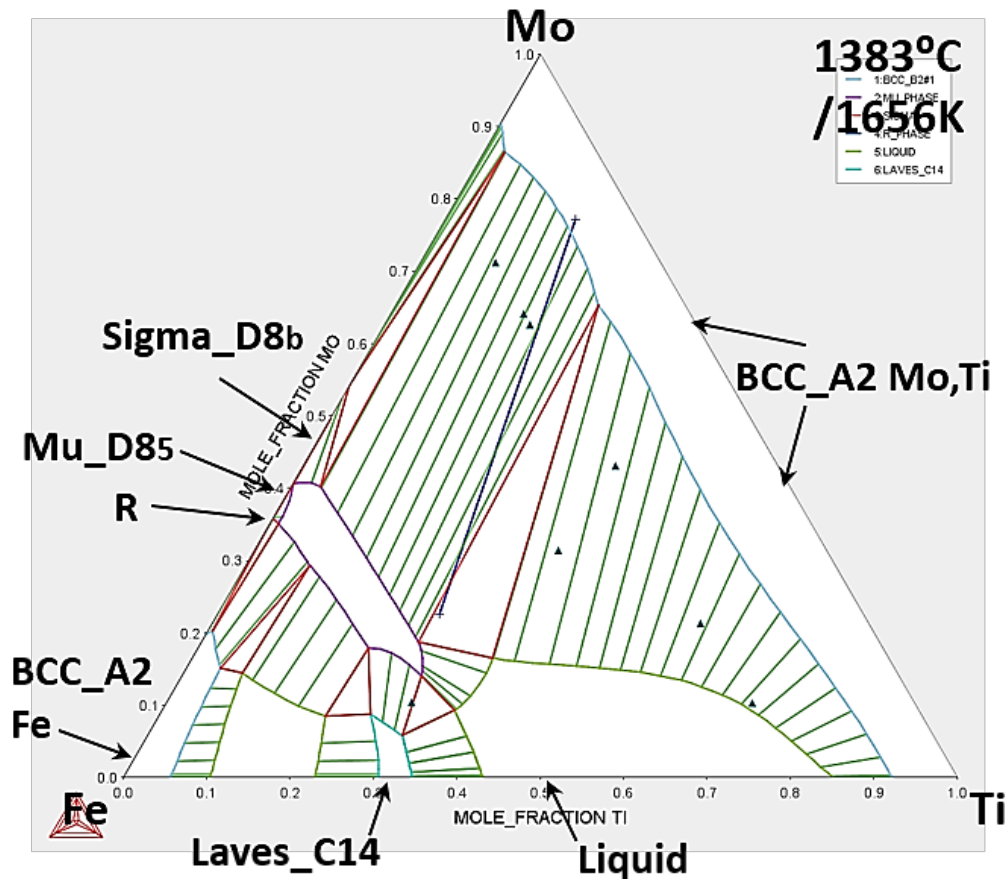


Figure 5.9: The calculated isothermal section at 1383°C from the optimised Ti-Fe-Mo description produced by the present work. The single overlaid tieline is from the experimental work of Knowles.[1]

Figures 5.8 to 5.9 illustrate that the calculated phase boundaries of the BCC_A2, BCC_B2, Mu_D85, and Liquid phases from the optimised Ti-Fe-Mo description produced in this work match up reasonably well with the ternary experimental data of Knowles[1] at these temperatures. And Figure 5.10 shows that the calculated Ti-Fe-Mo liquidus projection from this work also, appears to look topologically similar to that calculated from the description of Watson & Markus. [114] Most of the discrepancies between these liquidus projections arise from the fact that the axes of the diagram from the present work, (a), are in mole fraction, and the axes of Watson & Markus.'s [114] diagram (b) are in mass %.

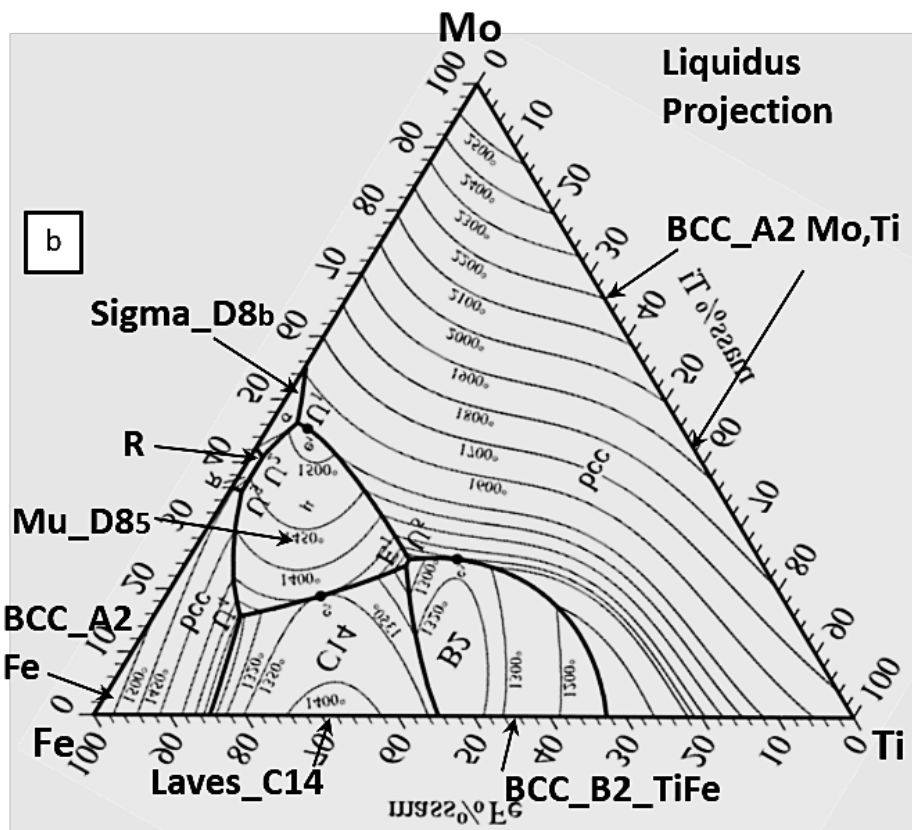
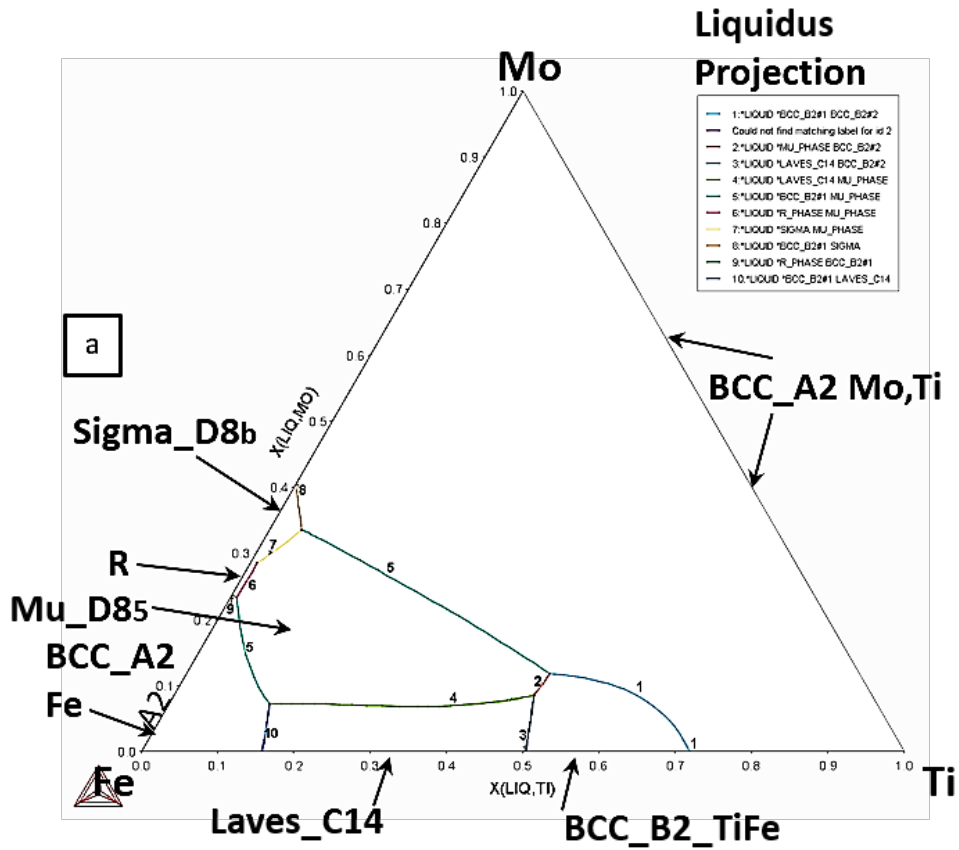


Figure 5.10: The Ti-Fe-Mo liquidus projection calculated from the optimised description produced by the present work, (a) compared to the calculated liquidus projection description of Watson & Markus., (b), [114]. It should be noted that the axes of diagram (a) are in mole fraction, and the axes of diagram (b) are in mass %.

However the most significant difference between these two liquidus projections is that the Mu_D8₅ phase extends much further into the diagram in the liquidus calculated using the optimised Fe-Mo-Ti description from the present work, than it does in the liquidus projection of Watson & Markus.[114] This is due to the fact that the description from the present work is heavily based on the data from Knowles et al.[1]–[3] (at or above 1000°C), and the description of Watson & Markus.[114] uses both the data and the exact same thermodynamic model for the Mu_D8₅ phase as that of Jin et al. [116] And as can be seen from Figures 5.1 & 5.2 this phase extends much further into the ternary in the phase diagram of Knowles et al.[3] than it does in the diagrams of Jin et al.[116] and Watson & Markus.[114] However, apart from the differences relating to the Mu_D8₅ phase, these two liquidus projections match up pretty well with each other.

5.4: Discussion

Figure 5.6 shows that the calculated isothermal section at 1000°C from the optimised Ti-Fe-Mo description produced in the present work fits well with the data from Knowles et al.[3]. However, the calculated boundaries for the Mu_D8₅ phase and Laves_C14 phase are narrower than those in the experimental diagram of Knowles et al.[3] displayed in Figure 5.6(a). This is due to the influence of the data from Jin et al.[116], marked with an X on the diagram in Figure 5.6(b), on the optimisation. Jin et al.[116] produced a reasonable amount of data on the ternary phase boundaries in the Fe corner of the Fe-Mo-Ti system. They did not correctly determine the ternary extension of the Mu_D8₅ phase, because they did not investigate the central regions of the diagram in detail, however, their data in the Fe corner of the diagram seems to be fairly comprehensive, and was therefore included in the optimisation. Consequently, the calculated boundaries for the Mu_D8₅ phase and Laves_C14 phases are the result of the combination of the data on these phases from Jin et al.[116] and Knowles et al.[1]–[3].

Overall, the isothermal sections at 1000°C and above calculated from the optimised Ti-Fe-Mo description shown in Figures 5.6-5.9 match up very well with the available experimental data. The isothermal sections calculated at temperatures below 1000°C also match up well with most of the experimental data, excluding the non-equilibrium data points on the BCC_A2 Mo, and Mu_D8₅ phase boundaries, which were already discussed in Section 5.3. Moreover, the liquidus projection calculated from this description, shown in Figure 5.10 also seems reasonable based on the comparison to the liquidus of the binary subsystems displayed in Figure 5.3, and also to the calculated ternary liquidus of Watson & Markus[114] shown in Figures 5.10.

Figure 5.11 shows that the isothermal section at 1000°C calculated from the optimised thermodynamic description for the Ti-Fe-Mo system produced in the present work appears to be a significant improvement over the version calculated from the description of Jin et al.[116]. The description from the present work models both the binary and ternary solubility ranges of the Laves_C14 and BCC_B2_TiFe phases, which were modelled as stoichiometric by Jin et al.[116]. Moreover, the ternary boundaries for all of the phase fields in the diagram match up much better with the data produced by Knowles et al.[1]–[3] whose recent investigation into the Ti-Fe-Mo ternary is the most comprehensive experimental investigation available on this system at present.

Figure 5.12 compares the isothermal section at 1000°C calculated from the description for the Ti-Fe-Mo system produced in the present work to the version calculated from the description of Watson & Markus.[114]. Both diagrams appear to be pretty similar, except for the aforementioned differences with regards to the Mu_D8₅ phase. The description of Watson & Markus.[114] appears to address most of the problems that were present in the earlier description of Jin et al.[116]. However, neither of these two descriptions match up well with the most recent data on the system produced by Knowles et al.[1]–[3].

Since the description of Ti-Fe-Mo system produced in the present work appears to be the most accurate description currently available, it may be worth considering if it could be adapted and incorporated into any current multicomponent alloy design databases. This could potentially improve the accuracy of alloy modelling predictions in the compositional space close to the Ti-Fe-Mo ternary, which could be useful for a range of practical steel and titanium alloys. Moreover, the work of Knowles et al. [1]–[3] has shown that BCC_A2 Mo,Ti - BCC_B2_TiFe alloys show a lot of promise as for structural applications in the aerospace industry, therefore the ability to accurately model the phase equilibria in the

Ti-Fe-Mo system could prove to be very useful in the future. However, in order for any two thermodynamic descriptions to be compatible with each other they must use the same sublattice models for the same phases. So if any existing databases use different models for any of the phases present in the Ti-Fe-Mo system, then the description produced in the present work would have to be altered in order to make it compatible with the database in question.

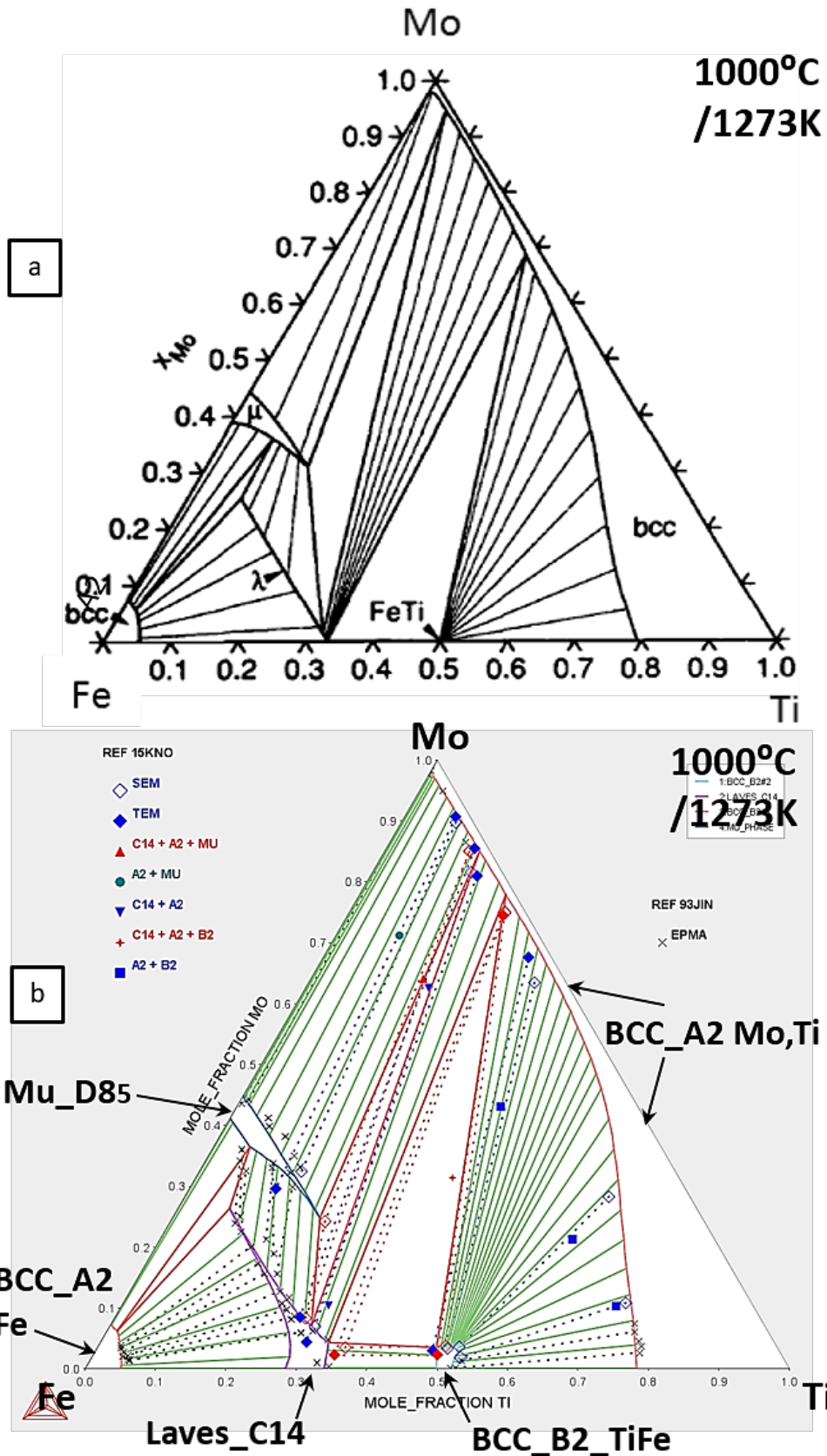


Figure 5.11: The calculated isothermal section for the Ti-Fe-Mo system at 1000°C of Jin et al.[116], (a), compared to the temperature matched calculated isothermal section from the optimised Ti-Fe-Mo description produced by the present work, (b). Alloy composition and tie line data overlaid on diagram (b) is from Knowles et al.[3] & Jin et al.[116]

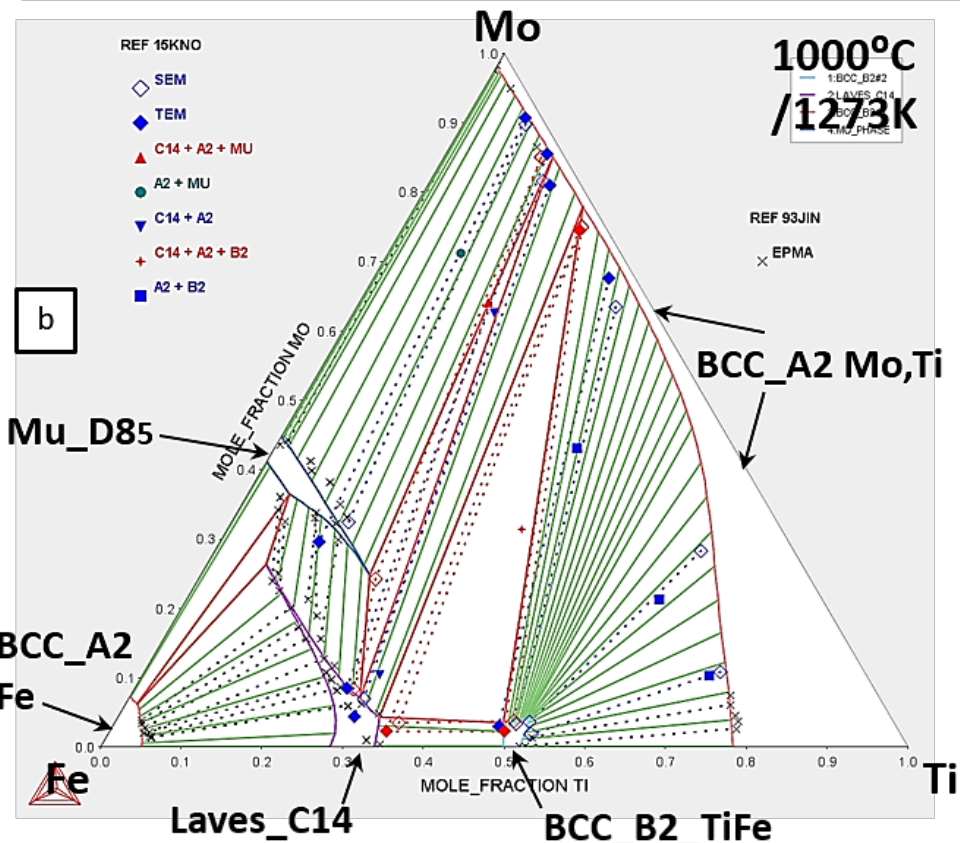
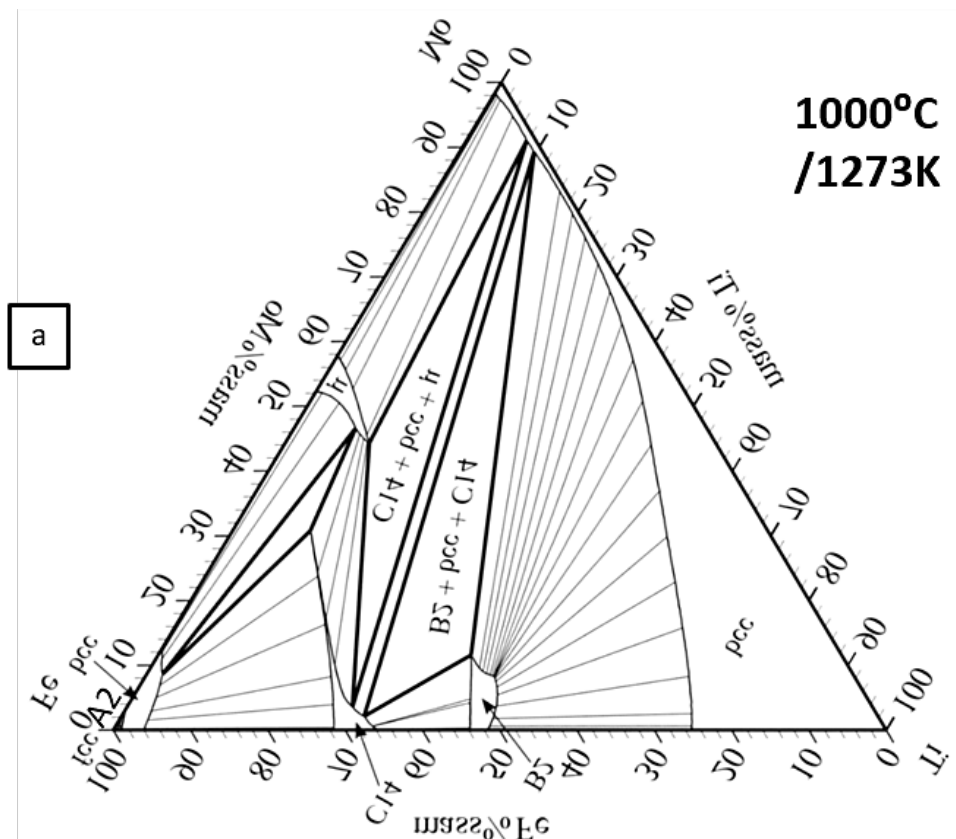


Figure 5.12: The calculated isothermal section for the Ti-Fe-Mo system at 1000°C of Watson & Markus,[114], (a), compared to the temperature matched calculated isothermal section from the optimised Ti-Fe-Mo description produced by the present work, (b). Alloy composition and tie line data overlaid on diagram (b) is from Knowles et al.[3] & Jin et al.[116]. It should also be noted that the axes of diagram (a) are in mass %, and the axes of diagram (b) are in mole fraction.

5.5: Conclusions

A thermodynamic assessment of the Ti-Fe-Mo system has been performed using the CALPHAD method. In this method, the Thermo-Calc software system was used to optimise, or fit the parameters of the Gibbs energy models for all of the phases in this ternary to the experimental data of Jin et al.[116] and Knowles et al.[1]–[3]. The optimisation produced a complete, self-consistent thermodynamic description for the Ti-Fe-Mo system.

The isothermal sections calculated from this description match up well with the available experimental data, and the calculated liquidus projection also seems reasonable based on the currently available information. Overall the thermodynamic description of the Ti-Fe-Mo system produced in the present work, seems to be a significant improvement when compared to the other available descriptions for this ternary by Jin et al.[116] and Watson & Markus.[114]

Since the existing thermodynamic assessments for this system do not completely match up with the recent data of Knowles et al.[1]–[3], due to the lack of phase diagram data prior to this investigation, it may be worth considering whether the updated thermodynamic description of the Ti-Fe-Mo system produced by this work could be adapted and incorporated into existing alloy design databases. This could potentially improve the accuracy of multicomponent alloy modelling predictions in the compositional space close to the Ti-Fe-Mo ternary.

5.6: Future Work

It was initially planned that the calculation of all of the invariant points in the Ti-Fe-Mo ternary would be performed, and a table of all of the invariant reactions for the system would be produced. This would provide more detailed insight into the phase equilibria of the system, particularly on the reactions to form all of the specific phases in the ternary as it cools from the liquid. Unfortunately this plan was not executed due to time constraints.

Also, the models for the disordered solution phases in the optimised description for the Ti-Fe-Mo system produced in the present work use a single sublattice model with a sublattice occupancy of $(Al,Co,Va)_1$. This description would be improved by using a 2 sublattice model for most of the terminal solid solution phases; FCC_A1 Fe, BCC_A2 Fe, BCC_A2 Mo, BCC_A2 Ti, and HCP_A3 Ti, to enable the interstitial vacancy sites in these lattices to be included in the Gibbs energy models. This would enable the ternary description to be combined with other descriptions containing interstitial alloying elements such as carbon. The system was not modelled in this way initially as it would have required modification to the models for these phases in some of the binary systems, which were not performed due to time constraints.

Chapter 6: Conclusions

6.1: Conclusions on the Experimental Determination of the Ta-Al-Co System

An experimental investigation into the phase equilibria of the Ta-Al-Co system has been performed using SEM & EDX analysis of 30 compositionally distinct alloys that were sectioned and then equilibrated at temperatures of 1000°C and 1150°C.

This is the first study to investigate the entire composition range of the Ta-Al-Co system, and has produced the first complete ternary isothermal sections for the system at temperatures of 1000°C and 1150°C. These results are a significant step forward from the limited partial isothermal section at 1000°C produced by Hunt and Raman,[77] which was the best experimental phase diagram information available on this system until now.

Unfortunately, these isothermal sections show that the Ta-Al-Co system does not appear to contain a disordered BCC_A2 Ta to ordered BCC intermetallic two phase field, which rules out the possibility that this ternary could be used as a base system for a two phase precipitation strengthened Ta alloy. However, the Ta-Al-Co system is still an important ternary subsystem of both Ni, and Co based superalloys, so the experimental data and phase diagrams produced by this study could still be useful for the purposes of alloy design in the future.

The results of this study also indicate that the existing thermodynamic assessments for this system are not particularly accurate, due to the lack of available phase diagram data prior to this work. One way to mould the results of this study into a useful format for alloy design purposes would be to produce a new thermodynamic assessment for the Ta-Al-Co

system. The resulting ternary database could then be adapted and incorporated into existing superalloy design databases, in order to improve the accuracy of alloy modelling predictions.

6.2: Conclusions on the Thermodynamic Assessment of the Ta-Al-Co System

A thermodynamic assessment of the Ta-Al-Co system has been performed using the CALPHAD method. In this method, the Thermo-Calc software system was used to optimise, or fit the parameters of the Gibbs energy models for all of the phases in this ternary to the experimental data presented in Chapter 3 of this work. The optimisation produced a complete, self-consistent thermodynamic description for the Ta-Al-Co system.

The isothermal sections at 1000°C and 1150°C calculated from this description match up well with the experimentally determined versions produced in Chapter 3, and the interpolated liquidus projection seems reasonable based on the currently available information. Overall the thermodynamic description of the Ta-Al-Co system produced in the present work, seems to be a significant improvement when compared to the only other available description for this ternary, which is the version contained in the TCNi8 database.

Since the only other existing thermodynamic assessment for this system is not particularly accurate, due to the lack of available phase diagram data prior to this investigation, it may be worth considering whether the updated thermodynamic description of the Ta-Al-Co system produced by this work could be adapted and incorporated into existing superalloy design databases. This could potentially improve the accuracy of multicomponent alloy modelling predictions in the compositional space close to the Ta-Al-Co ternary.

6.3: Conclusions on the Thermodynamic Assessment of the Ti-Fe-Mo System

A thermodynamic assessment of the Ti-Fe-Mo system has been performed using the CALPHAD method. In this method, the Thermo-Calc software system was used to optimise, or fit the parameters of the Gibbs energy models for all of the phases in this ternary to the experimental data of Jin et al.[116] and Knowles et al.[1]–[3]. The optimisation produced a complete, self-consistent thermodynamic description for the Ti-Fe-Mo system.

The isothermal sections calculated from this description match up well with the available experimental data, and the calculated liquidus projection also seems reasonable based on the currently available information. Overall the thermodynamic description of the Ti-Fe-Mo system produced in the present work, seems to be a significant improvement when compared to the other available descriptions for this ternary by Jin et al.[116] and Watson & Markus.[114]

Since the existing thermodynamic assessments for this system do not completely match up with the recent data of Knowles et al.[1]–[3], due to the lack of phase diagram data prior to this investigation, it may be worth considering whether the updated thermodynamic description of the Ti-Fe-Mo system produced by this work could also be adapted and incorporated into existing alloy design databases. This could potentially improve the accuracy of multicomponent alloy modelling predictions in the compositional space close to the Ti-Fe-Mo ternary.

References

- [1] A. J. Knowles, “Novel refractory metal alloys for high temperature service, PhD thesis, University of Cambridge, Department of Materials Science and Metallurgy.,” University of Cambridge, 2016.
- [2] A. J. Knowles, N. G. Jones, C. N. Jones, and H. J. Stone, “Phase Equilibria in the Fe-Mo-Ti Ternary System at 1173 K (900°C) and 1023 K (750°C),” *Metall. Mater. Trans. A*, vol. 48A, pp. 4334–4331, 2017.
- [3] A. J. Knowles, N. G. Jones, O. M. D. M. Messe, J. S. Barnard, C. N. Jones, and H. J. Stone, “Phase equilibria in the Fe-Mo-Ti ternary system at 1000°C,” *Int. J. Refract. Met. Hard Mater.*, vol. 60, pp. 160–168, 2016.
- [4] B. Sundman, B. Jansson, and J. Ågren, “Thermocalc 2018.” 2018.
- [5] H. Lukas, S. G. Fries, and B. Sundman, *Computational Thermodynamics - The CALPHAD Method*, Cambridge University Press. 2007.
- [6] L. Guillet, “La constitution des alliages (The constitution of alloys),” *Le Génie Civ.*, vol. 41, pp. 169–172, 1902.
- [7] L. Guillet, “Contributions a l’étude des alliages d’aluminium (Contribution to the study of Al alloys),” *Bull Soc D’Encour Ind Natl*, vol. 104, pp. 221–273, 1902.
- [8] A. G. C. Gwyer, “Über die legierungen des aluminiums mit kupfer, eisen, nickel, kobalt, blei und cadmium,” *Z. Anorg. Chem.*, vol. 57, pp. 113–153, 1908.
- [9] W. L. Fink and H. R. Freche, “Equilibrium relations in Al–Co alloys of high purity,” *Trans AIME*, vol. 99, pp. 141–148, 1932.
- [10] T. Gödecke, “Zahl und Lage der intermetallische Phasen im System Aluminium-Kobalt zwischen 10 und 40 At.-% Co (Number and position of the intermetallic phases in the system Al-Co between 10 and 40 at.% Co),” *Zeitschrift für Met.*, vol. 62, pp. 842–843, 1971.
- [11] W. Köster, “Das System Eisen-Kobalt-Aluminium [The system Fe–Co–Al],” *Arch Eisenhüttenwes*, vol. 7, pp. 263–264, 1933.
- [12] J. Schramm, “Das Teilsystem Kobalt-CoAl,” *Zeitschrift für Met. Res. Adv. Tech.*, vol. 33, pp. 381–387, 1941.
- [13] A. J. McAlister, “The Al-Co (Aluminum-Cobalt) system,” *Bull. Alloy Phase Diagrams*, vol. 10, no. 6, pp. 646–650, Dec. 1989.
- [14] P. Villars, H. Okamoto, and K. Cenzual, Eds., *ASM handbook. Vol.3, Alloy phase diagrams*. ASM International, Materials Park, Ohio, USA, 1992.
- [15] W. Köster, “The system Co-Mn-Al,” *Zeitschrift für Met. Res. Adv. Tech.*, vol. 30, pp. 281–286, 1938.
- [16] H. E. Cline, “The Mechanical Properties of the CoAl-Co Eutectic,” *Trans Met. Soc. AIME*, vol. 239, pp. 1906–1916, 1967.

- [17] T. Takayama, M. Y. Wey, and T. Nishizawa, "Effect of Magnetic Transition on the Solubility of Alloying Elements in BCC Iron and FCC Cobalt.pdf," *Mater. Trans. Japan Inst. Met.*, vol. 22, no. 5, pp. 315–325, 1981.
- [18] H. J. Schaller and T. Bretschneider, "Thermodynamics of Co-Al Alloys," *Zeitschrift für Met. Res. Adv. Tech.*, vol. 76, pp. 143–149, 1985.
- [19] A. M. B. Parker, "Unit Cell and Space-Group of Co₂Al₉," *Nature*, vol. 156, pp. 783–783, 1945.
- [20] A. M. B. Douglas, "The structure of Co₂Al₉," *Acta Crystallogr.*, vol. 3, pp. 19–24, 1950.
- [21] A. J. Bradley and G. C. Seager, "An X-Ray Investigation of Co-Al Alloys," *J. Inst. Met.*, vol. 64, pp. 81–88, 1939.
- [22] R. C. Hudd and W. H. Taylor, "Structure of Co₄Al₁₃," *Acta Crystallogr.*, vol. 15, pp. 441–442, 1962.
- [23] A. J. Bradley, "Crystal Structure of Co₂Al₅," *Z. Krist.*, vol. 99, pp. 480–487, 1938.
- [24] J. B. Newkirk, P. J. Black, and A. Damjanovic, "Refinement of the Co₂Al₅ Structure," *Acta Crystallogr.*, vol. 14, pp. 532–533, 1961.
- [25] Y. I. Dutchak and V. G. Chekh, "High Temperature X-Ray Diffraction Study of the Lattice Dynamics of the Compounds AlCo and AlNi," *Zh. Fiz. Khim./Russ. J. Phys. Chem.*, vol. 55, pp. 2342–2345, 1981.
- [26] L. A. Panteleimonov, E. B. Badtiev, and L. V. Aleshina, "A study of alloys in the aluminium–cobalt System," *Moscow Univ Chem Bull.*, vol. 29, pp. 91–92, 1974.
- [27] M. Ettenberg, K. L. Komarek, and E. Miller, "Thermodynamic Properties and Ordering in CoAl," *Trans. Met. Soc. AIME*, vol. 242, pp. 1801–1807, 1968.
- [28] A. A. Vecher, V. M. Es'kov, and V.V. Samokhval, "Thermodynamic Properties of Al-Co Alloys," *Izv. Akad Nauk. SSSR Met./TRRuss. Met.*, vol. 4, pp. 67–69, 1975.
- [29] P. Villars and K. Cenzual, Eds., *Pearson's Crystal Data*. ASM International, Materials Park, Ohio, USA.
- [30] N. Dupin and I. Ansara, "Évaluation thermodynamique du système Al-Co (Thermodynamic assesement of the system Al–Co)," *La Rev. Metall.*, vol. 95, pp. 1121–1129, 1998.
- [31] K. Yoshisato, K. Haruyoshi, S. Tomoo, and M. Yoshinao, "Microstructure Control and Mechanical Properties of Binary Co-Al Alloys Based on B2 Intermetallic Compound CoAl," *Mater. Trans. Japan Inst. Met. Vol.35 No.03*, pp. 182–188, 1994.
- [32] T. Gödecke and M. Ellner, "Phase equilibria in the aluminium-rich portion of the binary system Co–Al and in the cobalt/aluminium-rich portion of the ternary system Co–Ni–Al," *Zeitschrift für Met.*, vol. 87, pp. 854–864, 1996.
- [33] B. Grushko, R. Wittenberg, K. Bickmann, and C. Freiburg, "The constitution of aluminum-cobalt alloys between Al₅Co₂ and Al₉Co₂," *J. Alloys Compd.*, vol. 233, no. 1–2, pp. 279–287, Jan. 1996.

- [34] F. Stein, C. He, and N. Dupin, "Melting behaviour and homogeneity range of B2 CoAl and updated thermodynamic description of the Al-Co system," *Intermetallics*, vol. 39, pp. 58–68, Aug. 2013.
- [35] V. M. Glazov, M. V. Mal'tsev, and Y. D. Chistyakov, "The solubility of some transition metals in Aluminium," *Izv Akad Nauk SSSR, Otd Tekh Nauk*, vol. 4, p. 131, 1956.
- [36] V. M. Glazov, G. P. Lazarev, and G. Korolkov, "The solubility of some transition metals in Aluminium," *Met. Term. Obrab. Met.*, vol. 10, pp. 48–50, 1959.
- [37] V. . Yeremenko, Y. . Natanzon, and V. I. Dybkov, "Interaction of the refractory metals with liquid aluminum," *J Less-Common Met*, vol. 50, no. 16, pp. 29–48, 1976.
- [38] H. Kimura, O. Nakano, and T. Ohkoshi, "On the aluminum-tantalum system," *Keikhzzoku*, vol. 23, p. 106, 1973.
- [39] J. C. Schuster, "Phases and Phase Relations in the System Ta-Al.," *Zeitschrift fuer Met. Res. Adv. Tech.*, vol. 76, no. 11, pp. 724–727, 1985.
- [40] P. R. Subramanian, D. B. Miracle, and S. Mazdiyasn, "Phase relationships in the Al-Ta system," *Metall. Trans. A*, vol. 21, no. 2, pp. 539–545, Feb. 1990.
- [41] H. A. Wilhelm and J. H. Witte, "Aluminum-tantalum alloy studies, Report No. IS-500, M48 U.S. Atomic Energy Commission," 1962.
- [42] H. Nowotny, C. Brukl, and F. Benesovsky, "Untersuchungen in den Systemen Tantal-Aluminium-Silicium und Wolfram-Aluminium-Silicium," *Monatshefte für Chemie*, vol. 92, no. 1, pp. 116–127, 1961.
- [43] P. Kofstad, "Technical Report AFML-TR-66-60 (AD 485023), Air Force Materials Laboratory, Wright-Patterson Air Force Base, Dayton, OH, USA," 1966.
- [44] K. Girgis and A. B. Harnik, "A new phase Ta₂Al₃," *Naturwissenschaften*, vol. 57, no. 5, pp. 242–242, May 1970.
- [45] A. Raman, *Aluminum*, 1965, vol. 41, 5, pp. 318–19. .
- [46] K. Schubert, H. G. Meissner, A. Raman, and W. Rossteutscher, "Einige Strukturdaten metallischer Phasen (9)," *Naturwissenschaften*, vol. 51, no. 12, pp. 287–287, 1964.
- [47] L.-E. Edshammar and B. Holmberg, "The Sigma-Phase Ta₂Al," *Acta Chem. Scand.*, vol. 14, no. 5, pp. 1219–1220, 1960.
- [48] S. Mahne and F. Krumeich, "Phase relations in the Al-Ta system : on the translational symmetries of Al₁₃Ta₂ and AlTa," vol. 201, pp. 167–174, 1993.
- [49] S. Mahne and B. Harbrecht, "Al₆₉Ta₃₉ - a new variant of a face-centred cubic giant cell structure," *J. Alloys Compd.*, vol. 203, pp. 271–279, Jan. 1994.
- [50] S. Mahne, B. Harbrecht, and F. Krumeich, "Phase relations in the Al□Ta system: on the translational symmetries of a triclinic structure and a new hexagonal giant cell structure," *J. Alloys Compd.*, vol. 218, no. 2, pp. 177–182, Mar. 1995.
- [51] A. Boulineau, J.-M. Joubert, and R. Černý, "Structural characterization of the Ta-rich

- part of the Ta–Al system,” *J. Solid State Chem.*, vol. 179, no. 11, pp. 3385–3393, Nov. 2006.
- [52] L. Kaufman, “Coupled thermochemical and phase diagram data for tantalum based binary alloys,” *Calphad*, vol. 15, no. 3, pp. 243–259, Jul. 1991.
- [53] Y. Du and R. Schmid-Fetzer, “Thermodynamic modeling of the Al-Ta system,” *J. Phase Equilibria*, vol. 17, no. 4, pp. 311–324, Aug. 1996.
- [54] V. T. Witusiewicz *et al.*, “Experimental study and thermodynamic re-assessment of the binary Al–Ta system,” *Intermetallics*, vol. 18, no. 1, pp. 92–106, Jan. 2010.
- [55] G. Brauer, “Über die Kristallstruktur von $TiAl_3$, $NbAl_3$, $TaAl_3$, und $ZrAl_3$,” *Zeitschrift für Anorg. und Allg. Chemie*, vol. 242, no. 1, pp. 1–22, Jul. 1939.
- [56] U. Hashimoto, “Relation between the Allotropic Transformation of Cobalt and Some Additional Elements,” *Nippon Kinzoku Gakkaishi*, vol. 1, no. 5, pp. 177–190, 1937.
- [57] W. Köster and W. Mulfinger, “The systems of cobalt with boron, arsenic, zirconium, niobium and tantalum,” *Zeitschrift für Met.*, vol. 39, no. 9, 1938.
- [58] H. J. Wallbaum, “The system of the iron metals,” *Arch Eisenhüttenwes*, vol. 14, p. 521, 1941.
- [59] H. J. Wallbaum, “Results of X-ray structure investigations of alloys with the composition AB_2 of the iron metals with Ti, Zr, Ta and Nb,” *Z. Krist.*, vol. 103, 1941.
- [60] M. Korchynsky and R. W. Fountain, “Precipitated phenomena in cobalt-tantalum alloys,” in *Amer. Inst. Min. Engrs. Annual Meeting*, pp. 562–563.
- [61] R. D. Dragsdorf and W. D. Forgeing, “The intermetallic phases in the cobalt–tantalum system,” *Acta Crystallogr.*, vol. 15, no. 6, pp. 531–536, Jun. 1962.
- [62] A. Raman, “Röntgenographische Untersuchungen im System Tantal-Kobalt,” *Met.*, vol. 21, pp. 900–903, 1967.
- [63] V. V. Petkov, Y. A. Kocherzhinsky, and V. Y. Markiv, *Dopov. Akad. Nauk Ukr., Ser. A*. 1971.
- [64] V. V. Petkov, Y. A. Kocherzhinsky, and V. Y. Markiv, *Metall. Vesp. Mezhved. Sb.* 1972.
- [65] V. B. Bernard, L. A. Yurchenko, O. I. Bodak, and V. V. Kuprina, *Vestn. Mosk. Univ. Khim.*, 17. 1976.
- [66] Y. N. Barabash, O.M., Koval, *Crystal Structure of Metals and Alloys*, Kiev: Naukova Dumka. 1986.
- [67] H. Okamoto, “Co-Ta (Cobalt-Tantalum),” *J. Phase Equilibria Diffus.*, vol. 25, no. 6, pp. 571–572, Dec. 2004.
- [68] Z.-K. Liu and Y. A. Chang, “Thermodynamic assessment of the Co-Ta system,” *Calphad*, vol. 23, no. 3–4, pp. 339–356, Sep. 1999.
- [69] T. . Rezukhina and L. . Kravchenko, “The thermodynamic properties of Laves phases in mixtures of Ta+Co. Solid-electrolyte galvanic cell studies,” *J. Chem. Thermodyn.*,

- vol. 4, no. 5, pp. 655–667, Sep. 1972.
- [70] A. K. Niessen, F. R. de Boer, R. Boom, P. F. de Châtel, W. C. M. Mattens, and A. R. Miedema, “Model predictions for the enthalpy of formation of transition metal alloys II,” *Calphad*, vol. 7, no. 1, pp. 51–70, Jan. 1983.
- [71] C. Colinet, A. Pasturel, and P. Hicter, “Trends in cohesive energy of transition metal alloys,” *Calphad*, vol. 9, no. 1, pp. 71–99, Jan. 1985.
- [72] K. C. Hari Kumar, T. Rompaey, and P. Van-Wollants, “Thermodynamic calculation of the phase diagram of the Co-Nb-Ta system,” *Zeitschrift für Met.*, vol. 93, no. 11, pp. 1146–1153, 2002.
- [73] J. C. Zhao, “fcc/hcp phase equilibria and phase transformation in cobalt-based binary systems,” *Zeitschrift fuer Met. Res. Adv. Tech.*, vol. 90, no. 3, pp. 223–232, 1999.
- [74] F. Stein, D. Jiang, M. Palm, G. Sauthoff, D. Grüner, and G. Kreiner, “Experimental reinvestigation of the Co–Nb phase diagram,” *Intermetallics*, vol. 16, no. 6, pp. 785–792, 2008.
- [75] O. Dovbenko, F. Stein, M. Palm, and O. Prymak, “Experimental determination of the ternary Co–Al–Nb phase diagram,” *Intermetallics*, vol. 18, no. 11, pp. 2191–2207, Nov. 2010.
- [76] K. Shinagawa *et al.*, “Phase equilibria and thermodynamic calculation of the Co–Ta binary system,” *Intermetallics*, vol. 49, pp. 87–97, Jun. 2014.
- [77] C. R. J. Hunt and A. Raman, “Alloy Chemistry of $\sigma(\beta\text{U})$ -Related Phases. I. Extension of μ - and occurrences of μ' -Phases in the Ternary Systems Nb(Ta)-X-Al (X=Fe, Co, Ni, Cu, Cr, Mo),” *Zeitschrift für Met. Res. Adv. Tech.*, vol. 59, pp. 701–707, 1968.
- [78] V. Y. Markiv, “New compound of the MgCu₂Al and MgZn₂ types containing Aluminium and Gallium,” *Sov. Phys. Crystallogr.*, vol. 9, pp. 619–620, 1965.
- [79] K. H. J. Buschow and P. G. van Engen, “Magnetic and magneto-optical properties of heusler alloys based on aluminium and gallium,” *J. Magn. Magn. Mater.*, vol. 25, no. 1, pp. 90–96, Nov. 1981.
- [80] R. Ferro, A. Saccone, and S. Delfino, *Aluminium-Cobalt-Tantalum, in Ternary Alloys: A comprehensive compendium of evaluated constitutional data and phase diagrams, Vol 4 Al-Cd-Ce to Al-Cu-Ru, ed. Petzow, G., VCH. 1991.*
- [81] J. W. Gibbs, “On the Equilibrium of Heterogeneous Substances,” *Am. J. Sci. Arts*, pp. 285–302, 1878.
- [82] J. Hertz, “Josiah willard gibbs and teaching thermodynamics of materials (history),” *J. Phase Equilibria*, vol. 13, no. 5, pp. 450–458, Oct. 1992.
- [83] J. J. Van Laar, “Die Scmeltz - oder erstarrungskurven bei binaren systemen, wenn die feste phase ein gemisch (amorphe feste losung oder mishkristalle) der beiden komponentern ist,” *Z. Phys. Chem.*, vol. 63, pp. 216–253, 1908.
- [84] J. J. Van Laar, “Die Scmeltz - oder erstarrungskurven bei binaren systemen, wenn die feste phase ein gemisch (amorphe feste losung oder mishkristalle) der beiden

- komponentern ist.," *Z. Phys. Chem.*, vol. 64, no. 257–297, 1908.
- [85] J. . Meijering and H. . Hardy, "Closed miscibility gaps in ternary and quaternary regular alloy solutions," *Acta Metall.*, vol. 4, no. 3, pp. 249–256, May 1956.
- [86] J. . Meijering, "Calculation of the nickel-chromium-copper phase diagram from binary data," *Acta Metall.*, vol. 5, no. 5, pp. 257–264, May 1957.
- [87] L. Kaufman and H. Bernstein, *Computer Calculation of Phase Diagrams with Special Reference to Refractory Metals (New York: Academic Press, 1970)*. .
- [88] U. R. Kattner, "The thermodynamic modeling of multicomponent phase equilibria," *JOM*, vol. 49, no. 12, pp. 14–19, Dec. 1997.
- [89] Y. A. Chang *et al.*, "Phase diagram calculation: past, present and future," *Prog. Mater. Sci.*, vol. 49, no. 3–4, pp. 313–345, Jan. 2004.
- [90] N. Saunders and A. P. Miodownik, *CALPHAD - Calculation of Phase Diagrams - A Comprehensive Guide, Pergamon Press*. 1998.
- [91] D. A. Porter, K. E. Easterling, and M. Sherif, *Phase Transformations in Metals and Alloys, Third Edition, CRC Press, FL, USA*. 2009.
- [92] O. Redlich and A. T. Kister, "Algebraic Representation of Thermodynamic Properties and the Classification of Solutions," *Ind. Eng. Chem.*, vol. 40, pp. 345–348, 1948.
- [93] B. D. Cullity, *Elements of X-Ray Diffraction, Addison-Wesley*. 1956.
- [94] V. T. Witusiewicz, A. A. Bondar, U. Hecht, and T. Y. Velikanova, "Phase Equilibria in Binary and Ternary Systems with Chemical and Magnetic Ordering," *J. Phase Equilibria Diffus.*, vol. 32, no. 4, pp. 329–349, May 2011.
- [95] M. Hillert and M. Jarl, "A model for alloying in ferromagnetic metals," *Calphad*, vol. 2, no. 3, pp. 227–238, Jan. 1978.
- [96] P. Wang *et al.*, "Thermodynamic re-assessment of the Al-Co-W system," *Calphad Comput. Coupling Phase Diagrams Thermochem.*, 2017.
- [97] V. T. Witusiewicz *et al.*, "Experimental study and thermodynamic re-assessment of the binary Al–Ta system," *Intermetallics*, vol. 18, no. 1, pp. 92–106, Jan. 2010.
- [98] ThermoTech, "TTNi8, Thermotech Ni-based Superalloys Database for Thermocalc." .
- [99] Thermo-CalcSoftwareAB, "TCNi8: TCS Ni-based Superalloys Database for Thermocalc." .
- [100] G. Cacciamani, G. Roncallo, Y. Wang, E. Vacchieri, and A. Costa, "Thermodynamic modelling of a six component (C-Co-Cr-Ni-Ta-W) system for the simulation of Cobalt based alloys," *J. Alloys Compd.*, vol. 730, pp. 291–310, Jan. 2018.
- [101] Y. Z. Zhan, Y. Du, and Y. H. Zhuang, "Chapter 4: Determination of Phase Diagrams Using Equilibrated Alloys," in *Methods of Phase Diagram Determination, J.-C. Zhao (Ed.)*, 2007, pp. 108–150.
- [102] V. T. Witusiewicz *et al.*, "Experimental study and thermodynamic modelling of the ternary Al–Ta–Ti system," *Intermetallics*, vol. 19, no. 3, pp. 234–259, Mar. 2011.

- [103] R. Castaing, "Electron Probe Microanalysis," *Adv. Electron. Electron Phys.*, vol. 13, no. C, pp. 317–386, Jan. 1960.
- [104] "Oxford INCA Energy Software, Version 18B, Oxford Instruments." .
- [105] A. T. Dinsdale, "SGTE data for pure elements," *Calphad*, vol. 15, no. 4, pp. 317–425, Oct. 1991.
- [106] B. Sundman, B. Jansson, and J. Ågren, "Thermocalc 3.01." 2013.
- [107] M. Palm, C. He, O. Dovbenko, F. Stein, and J. C. Schuster, "Liquidus Projection and Reaction Scheme of the Co-Al-Nb System," *J. Phase Equilibria Diffus.*, vol. 33, no. 3, pp. 210–221, May 2012.
- [108] C. He, F. Stein, and M. Palm, "Thermodynamic description of the systems Co–Nb, Al–Nb and Co–Al–Nb," *J. Alloys Compd.*, vol. 637, pp. 361–375, Jul. 2015.
- [109] F. Tang and H. Bengt, "Using the PARROT module of Thermo-Calc with the Cr–Ni system as example," *Calphad*, vol. 55, pp. 260–269, Dec. 2016.
- [110] M. Hillert, "The compound energy formalism," *J. Alloys Compd.*, vol. 320, no. 2, pp. 161–176, May 2001.
- [111] N. Dupin and I. Ansara, "On the sublattice formalism applied to the B2 phase," *Zeitschrift fuer Met. Res. Adv. Tech.*, vol. 90, pp. 76–85, 1999.
- [112] Sluiter and M.H.F., "Ab initio lattice stabilities of some elemental complex structures," *CALPHAD*, vol. 30, pp. 357–366, 2006.
- [113] J.-O. Andersson and B. Sundman, "Thermodynamic properties of the Cr-Fe system," *CALPHAD*, vol. 11, no. 1, pp. 83–92, 1987.
- [114] A. Watson and T. Markus, "Fe-Mo-Ti (Iron-Molybdenum-Titanium)," in *Thermodynamic Properties of Inorganic Materials, Landolt-Börnstein. New series. Group 4 Physical Chemistry ; IV/19-C2, Compiled by SGTE, Subvolume C: Ternary Steel Systems, Phase Diagrams and Phase Transition Data: part 2 : ternary systems from Cr-Mn-N to*, 2015.
- [115] E. F. Sokolovskaya, E.M. Kazakova, B. I. Gryzunov, M. Duidebaev, and B. K. Konysova, "Interactions and Properties of Intermediate Phases in the Fe-Ti-Mo System at 900°C," *Vestn. Mosk. Univ. Ser. Khim.*, vol. 43, pp. 404–405, 1988.
- [116] Z.-P. Jin and C. Qiu, "An experimental study and thermodynamic evaluation of the Fe-Mo-Ti system at 1000 °C," *Metall. Trans. A*, vol. 24, no. 10, pp. 2137–2144, Oct. 1993.
- [117] A. K. Shurin, G. P. Dmitrieva, and T. S. Cherepova, "Phase equilibria in titanium-rich alloys of the Fe-Mo-Ti system," *Powder Metall. Met. Ceram.*, vol. 42, no. 9–10, pp. 513–516, 2003.
- [118] V. B. Rajkumar and K. C. Hari Kumar, "Thermodynamic modeling of the Fe–Mo system coupled with experiments and ab initio calculations," *J. Alloys Compd.*, vol. 611, pp. 303–312, Oct. 2014.
- [119] K. Santhy, "Phase Diagram Calculation of Certain Titanium Containing Alloy

- Systems by Coupling Calphad and First-Principle Methods, PhD thesis, IIT Madras.,” 2010.
- [120] H.-J. Chung, J.-H. Shim, and D. Nyung Lee, “Thermodynamic evaluation and calculation of phase equilibria of the Ti–Mo–C–N quaternary system,” *J. Alloys Compd.*, vol. 282, no. 1–2, pp. 142–148, Jan. 1999.
- [121] H. Bethe, “Zur Theorie des Durchgangs schneller Korpuskularstrahlen durch Materie,” *Ann. Phys.*, vol. 397, no. 3, pp. 325–400, Jan. 1930.
- [122] T. Matsukawa, R. Shimizu, K. Harada, and T. Kato, “Investigation of kilovolt electron energy dissipation in solids,” *J. Appl. Phys.*, vol. 45, no. 2, pp. 733–740, 1974.
- [123] H.-J. Fitting and J. Reinhardt, “Monte-Carlo simulation of keV-electron scattering in solid targets,” *Phys. status solidi*, vol. 88, no. 1, pp. 245–259, Mar. 1985.
- [124] V. Afonin, V. Lebed’, and N. Losev, “Metod Monte-Karlo v rentgenospektral’nom mikroanalize (Monte Carlo Method in X-ray Spectral Micro Analysis),” *Nauk. Sib. otd-nie*, 1989.
- [125] M. El Azzouzi, L. Khouchaf, and A. Achahbar, “Monte Carlo Study of the Interaction Volume Changes by the Beam Skirt in VP-SEM,” vol. 132, 2017.
- [126] V. E. Cosslett and R. N. Thomas, “Multiple scattering of 5-30 keV electrons in evaporated metal films II: Range-energy relations,” *Br. J. Appl. Phys.*, vol. 15, no. 11, p. 1283, 1964.
- [127] K. Kanaya and S. Okayama, “Penetration and energy-loss theory of electrons in solid targets,” *J. Phys. D. Appl. Phys.*, vol. 5, no. 1, pp. 43–58, 1972.
- [128] D. B. Wittry and D. F. Kyser, “Measurement of diffusion lengths in direct-gap semiconductors by electron-beam excitation,” *J. Appl. Phys.*, vol. 38, no. 1, pp. 375–382, 1967.
- [129] W. Williamson, A. J. Antolak, and R. J. Meredith, “An energy-dependent electron backscattering coefficient,” *J. Appl. Phys.*, vol. 61, no. 9, pp. 4612–4618, 1987.
- [130] P. J. Potts, *A Handbook of Silicate Rock Analysis*. Dordrecht: Springer, 1987.
- [131] F. A. Lukiyarov, E. I. Rau, and R. A. Sennov, “Depth range of primary electrons, electron beam broadening, and spatial resolution in electron-beam studies,” *Bull. Russ. Acad. Sci. Phys.*, vol. 73, no. 4, pp. 441–449, May 2009.
- [132] Joseph I. Goldstein et al., *Scanning electron microscopy and x-ray microanalysis*, 4th Edition. New York, USA: Springer, 2018.
- [133] C. A. Anderson and M. F. Hasler, “4th Intl. Conf. On X-ray Optics and Microanalysis (R. Castaing, P. Deschamps and J. Philibert, eds.) Hermann: Paris,” 1966, p. 310.
- [134] “Hydrocarbon contamination control for electron microscopes, such as TEM, SEM and FIB.” [Online]. Available: https://www.piescientific.com/Application_pages/Applications_Analytical_SEM. [Accessed: 26-Apr-2020].

Appendix 1: SEM EDX Sampling Volume Dimensions and Quantification Procedure

Appendix 1.1: SEM EDX Point Analysis Sampling Volume Dimensions

The sampling volume dimensions for the EDX point analysis measurements taken in the present work were dependent upon the electron beam/specimen interaction volume, which is a function of a number of different variables, particularly the electron beam accelerating voltage, and the density of the target phase. There are a number of different methods of calculating the effective vertical and lateral electron ranges, and the broadening of a focussed electron beam as it penetrates into a solid material. These methods include theoretical physics based models,[121] Monte-Carlo simulations,[122]–[125] experimental studies,[122], [126]–[128] and semi-empirical models which have been fitted to experimental data.[122], [126]–[130]

In most theoretical models of interactions between electron beams and solid materials, electrons penetrate into the material to a diffusion depth, x_d , lose energy according to the Bethe Law, and undergo angular scattering according to the Rutherford cross section.[121] Due to multiple scattering events, electron paths at depth, x_d , become circuitous and the electrons begin to move in various different directions, until they run out of energy, E . The maximum range of primary electron path lengths through the material is taken as the Bethe range, S_B , and the distance from the surface to this point is known as the depth range, R . This depth range, R , is defined differently by different methods, as illustrated in Figure A1.1, which will be explained in more detail below.

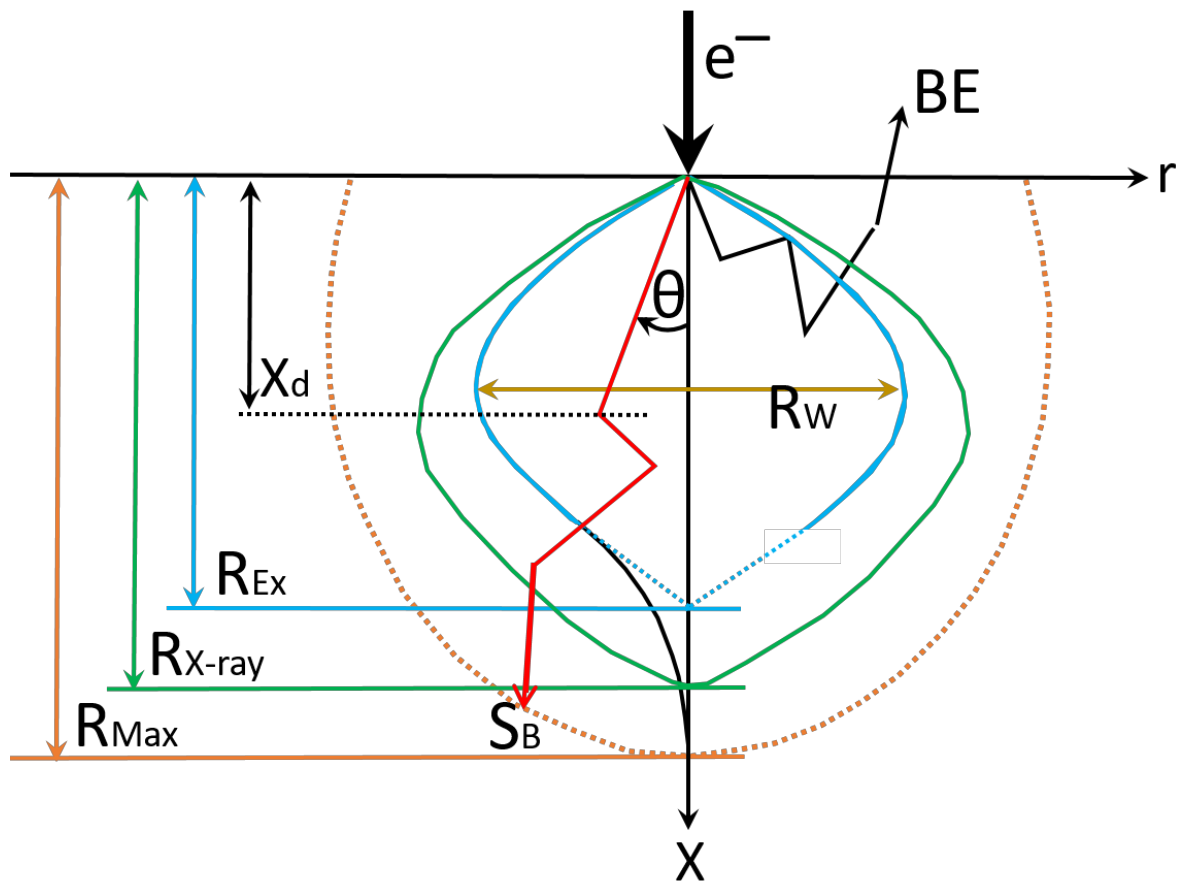


Figure A1.1: Diagram showing the external boundary of the electron scattering sphere, or Bethe range (dotted orange line) and the primary electron penetration ranges as defined by the various models used to calculate the sampling depth and width of the SEM EDX techniques used to investigate the Ta-Al-Co alloys studied in the present work. Modified from Lukiyarov et al.[131]

The first method for calculating the maximum penetration depth, R_{Max} , of electrons into the different samples analysed in this work was the approximation model for calculating the Bethe range, S_B , developed by Williamson et al,[129] shown in Equation A1.4 overleaf. The Bethe range, S_B , of an electron can be defined as the integral of energy loss, dE , per unit of path travelled, ds :[121]

$$S_B = \int_E^0 \frac{1}{dE/ds} dE \quad \text{Equation A1.1}$$

Where dE/ds describes the energy loss according to the Bethe law:[121]

$$-\frac{dE}{ds} (KeV cm^{-1}) = 7.85 * 10^4 \frac{\rho Z}{AE} \ln \left(1.65 \frac{E}{J} \right) \quad \text{Equation A1.2}$$

In this equation, ρ is the density of the target material in g/cm^3 ; Z and A are the atomic number and atomic mass respectively; E is the energy of the electron, and J is the average ionization potential of the target atoms.

The Bethe range, S_B , can only be calculated numerically from these equations because the integral in Equation A1.1 with substitution of Equation A1.2 cannot be expressed in terms of elementary functions.[129], [131] Therefore, for convenience, Williamson et al.,[129] developed the following approximation for S_B :

$$S_B = \left(\frac{0.058A}{\rho Z} \right) \left(\frac{E_0^{1.7}}{J^{-0.3}} \right) \quad \text{Equation A1.3}$$

And since J can be replaced with its approximate value: $J \approx 0.0115 Z$, Williamson et al's[129] model can be further simplified as:

$$S_B = \frac{0.0152 A E_0^{1.7}}{\rho Z^{0.7}} \quad \text{Equation A1.4}$$

Where S_B is in μm , and E_0 is in KeV.

Since the exact Bethe range, S_B , cannot be directly measured experimentally, Williamson et al.[129], compared the values calculated from their model to the results of Monte Carlo simulations from the literature,[124] and concluded that their model was an accurate approximation for, S_B . One possible example of a complete electron path from the surface of the specimen to the Bethe range, S_B , is marked in red on Figure A1.1 above.

The penetration depth range, R , of electrons into the samples analysed in this work was also calculated using a number of empirically based approximation models, which were developed by fitting the coefficients of these models to experimentally measured values.[122], [126]–[128], [130] Typically in these works, R , was found by measuring the flux, or energy of electrons transmitted through a range of thin films of different thicknesses. The film thickness at which these values tended to zero was then taken to be the penetration depth of electrons of specified energy for the material studied.[131] One of the most popular empirical models from the literature is that of Kanaya and Okayama,[127] which is based on the a similar expression to that of the model of Williamson: [129]

$$R = \frac{CAE_0^n}{\rho Z^d} \quad \text{Equation A1.5}$$

Where, C and d are coefficients based on the target material, and n is a coefficient based on the accepted scattering model, ρ is the density of the target material in g/cm^3 ; Z and A are the atomic number and atomic mass respectively, and, E_0 is the beam accelerating voltage in KeV.

Kanaya and Okayama[127] fitted this expression to their experimentally measured electron penetration depth data to produce the following model for maximum penetration depth range of electrons into a material, R_{Max} in μm , which is marked in orange in Figure A1.1:

$$R_{\text{Max}} = \frac{0.0276AE_0^{1.67}}{\rho Z^{0.89}} \quad \text{Equation A1.6}$$

However, in practice it is difficult to accurately experimentally determine the maximum penetration depth range, R_{Max} , due to the statistical nature, and small magnitude of the energy of primary electrons nearing the end of their path through a film of critical thickness, $d = R_{\text{Max}}$.[131] Therefore, many researchers prefer to extrapolate the curves of energy losses or transmitted electron beam intensity from a given point near the end of the

primary electron paths to the zero energy point. This results in an extrapolated, penetration depth range, R_{Ex} , which is shown in blue in Figure A1.1. To date, a number of independent researchers have developed empirical models for, R_{Ex} based on the following expression:[122], [126], [128], [130]

$$R_{Ex} = \frac{CE_0^n}{\rho^d} \quad \text{Equation A1.7}$$

However, there is no unified universal expression for R_{Ex} because it is obtained empirically, by fitting the coefficients C, d and n to the data from different experiments. In many cases the d coefficient is simply set as 1, and only the C and n coefficients are used. Again, ρ is the density of the target material in g/cm^3 , and E_0 is the beam accelerating voltage in KeV.

The extrapolated penetration depth range, R_{Ex} in μm , of electrons into the specimens used in this work was also calculated using the models of Cosslett and Thomas,[126] Matsukawa et al.,[122] Potts,[130] and Wittry and Kyser.[128] These models are shown below in Equations A1.8-A1.11, respectively.

$$R_{Ex} = \frac{0.074E_0^{1.55}}{\rho} \quad \text{Equation A1.8}$$

$$R_{Ex} = \frac{0.074E_0^{1.7}}{\rho} \quad \text{Equation A1.9}$$

$$R_{Ex} = \frac{0.1E_0^{1.5}}{\rho} \quad \text{Equation A1.10}$$

$$R_{Ex} = \frac{0.0789E_0^{1.7}}{\rho} \quad \text{Equation A1.11}$$

Beam broadening, or penetration width, R_w in μm , shown in gold in Figure A1.1, was also calculated using the empirical models of Potts,[130] and Goldstein,[132] which are shown in Equations A1.12 and A1.13, respectively:

$$R_w = \frac{0.077E_0^{1.5}}{\rho} \quad \text{Equation A1.12}$$

$$R_w = 0.625 \left(\frac{Z}{E_0}\right) \left(\frac{\rho}{A}\right)^{0.5} x_0^{1.5} \quad \text{Equation A1.13}$$

In these models, ρ is the density of the target material in g/cm^3 , E_0 is the beam accelerating voltage in KeV, and x_0 is the penetration depth in μm .

In addition to the electron penetration depth and width values calculated from the models discussed above, the X-Ray generation depth, $R_{X\text{-ray}}$, for EDX was also calculated for the materials analysed in this work using the models of Castaing,[103] and Anderson and Hassler[133] shown below in Equations A1.14, and A1.15, respectively.

$$R_{X\text{-ray}} = 0.033(E_0^{1.7} - E_C^{1.7}) \left(\frac{A}{\rho Z}\right) \quad \text{Equation A1.14}$$

$$R_{X\text{-ray}} = 0.064(E_0^{1.68} - E_C^{1.68}) \left(\frac{1}{\rho}\right) \quad \text{Equation A1.15}$$

In these models, E_0 is the beam accelerating voltage in KeV, E_C is the critical X-ray emission voltage, Z and A are the atomic number and atomic mass respectively, and ρ is the density of the target material in g/cm^3 ,

The results of all electron penetration depth and width calculations, and X-Ray generation depth calculations for Al, Co, and Ta, and also for the Ta-Al-Co alloys studied in this work are shown in Table A1.1, overleaf.

Table A1.1 - The results of all electron penetration depth and width calculations, in μm , and X-Ray generation depth and width calculations, also in μm , for Al, Co, and Ta, and also for the range of densities of the Ta-Al-Co alloys studied in this work.

Element	E ₀ , K	ρ , g/cm ³	S _B	R _{Max}	R _{Ex}	R _{Ex}	R _{Ex}	R _{Ex}	R _W	R _w	Rx-ray in μm			Rx-ray, μm			R _{EDXD}	R _{EDXW}
			μm Williamson et al [129]	μm Kanaoya & Okayama [127]	μm Cosslett [126]	μm Matsukawa et al [122]	μm Potts [130]	μm Wittry & Kyser [128]	μm Potts [130]	μm Goldstein [132]	K α	L α	M	K α	L α	M	μm	μm
Ta	20	16.65	1.33	0.98	0.46	0.51	0.54	0.77	0.41	0.47		0.63	0.79		0.46	0.58	0.71	0.54
Co	20	8.9	1.63	1.45	0.86	0.95	1.00	1.44	0.77	0.57	1.10	1.31		0.92	1.10		1.32	1.02
Al	20	2.69	4.12	4.21	2.86	3.15	3.33	4.78	2.56	1.34	4.10			3.60			4.36	3.36
Ta	20	16.65	1.33	0.98	0.46	0.51	0.54	0.77	0.41	0.47		0.63	0.79		0.46	0.58	0.71	0.54
Alloy	20	16			0.48	0.53	0.56	0.80	0.43								0.73	0.56
Alloy	20	15			0.51	0.56	0.60	0.86	0.46								0.78	0.60
Alloy	20	14			0.55	0.60	0.64	0.92	0.49								0.84	0.65
Alloy	20	13			0.59	0.65	0.69	0.99	0.53								0.90	0.70
Alloy	20	12			0.64	0.71	0.75	1.07	0.57								0.98	0.75
Alloy	20	11			0.70	0.77	0.81	1.17	0.63								1.07	0.82
Alloy	20	10			0.77	0.85	0.89	1.28	0.69								1.17	0.90
Alloy	20	9			0.85	0.94	0.99	1.43	0.77								1.30	1.00
Co	20	8.9	1.63	1.45	0.86	0.95	1.00	1.44	0.77	0.57	1.10	1.31		0.92	1.10		1.32	1.02
Alloy	20	8			0.96	1.06	1.12	1.61	0.86								1.47	1.13
Alloy	20	7			1.10	1.21	1.28	1.84	0.98								1.68	1.29
Alloy	20	6			1.28	1.41	1.49	2.14	1.15								1.96	1.51
Alloy	20	5			1.54	1.69	1.79	2.57	1.38								2.35	1.81
Alloy	20	4			1.92	2.12	2.24	3.21	1.72								2.93	2.26
Alloy	20	3			2.56	2.82	2.98	4.28	2.30								3.91	3.01
Al	20	2.69	4.12	4.21	2.86	3.15	3.33	4.78	2.56	1.34	4.10			3.60			4.36	3.36

As expected, the calculated electron penetration depth, and width values for the element with the highest density, Ta, are the smallest, and the values for the element with the lowest density, Al, are the largest. The values calculated for the maximum penetration depth range, R_{Max} , using the models of Williamson et al.,[129] and Kanaya and Okayama,[127] are in reasonably good agreement with each other for the lightest element Al, but as we move to the heavier elements, Co, and Ta the differences between the calculated values for, R_{Max} , start to diverge. The values of the extrapolated penetration depth range, R_{Ex} , calculated using the models of Cosslett and Thomas,[126] Matsukawa et al.,[122] and Potts[130] are generally in good agreement with each other for the heavier elements, Co, and Ta, but start to diverge for the lighter element, Al. However, the R_{Ex} values calculated using the model of Wittry and Kyser[128] are closer to the R_{Max} values calculated using Kanaya and Okayama's[127] model than they are to the values calculated using the other models for R_{Ex} .

The values calculated using the models for electron penetration width, R_w , of Potts,[130] and Goldstein[132] were in fairly good agreement with each other for the heavier elements, Co and Ta, but diverged significantly for the lightest element, Al. In this case the values calculated using the model of Potts[130] were considered to be more accurate, since both Lukiyanov,[131] and Azzouzi et al.,[125] found that their models for beam broadening fit reasonably well with the model of Potts[130] for beam interactions with Al, but that Goldstein's[132] model appears to underestimate beam broadening in lighter elements such as Al.

The X-Ray generation depth, R_{X-ray} , for EDX was also calculated for the materials analysed in this work using the models of Castaing,[103] and Anderson and Hassler,[133] and the values yielded from these models for R_{X-ray} were generally in between the values from the

models for maximum penetration depth range, R_{Max} and those from the models for extrapolated penetration depth range, R_{Ex} .

In order to determine the approximate sampling depth of the EDX point analysis measurements made in the present work, it was decided that X-ray generation depth values calculated from the model for $R_{\text{X-ray}}$ of Castaing[103] would be used. The reasoning for this is outlined briefly below. Firstly, it seems likely that the models for the maximum penetration depth range, R_{Max} , may slightly overestimate the effective sampling volume for the heavier elements, Co and Ta. Since the primary electron penetration depth, R , can exhibit a significant statistical range, particularly in denser materials, it is likely that the majority of characteristic X-rays emitted from the samples analysed in this work were produced from a sampling volume that is slightly smaller than the maximum possible interaction volume range, and that the proportion of primary electrons that reach this maximum range, R_{Max} , will be very small indeed, as will the amount of energy that they have at this point. Therefore the very few electrons at the outer edges of this max range are unlikely to excite a noticeable amount of characteristic X-rays from the sample. Secondly, although they are in reasonable agreement with each other, the models for the extrapolated penetration depth range, R_{Ex} , generally produced values that were lower than the models for the X-ray generation depth range, $R_{\text{X-ray}}$, so it could be risky to simply assume that the sampling volumes of the EDX point analysis measurements in this work were in line with those calculated from the R_{Ex} models.

It was a relatively simple task to calculate the approximate EDX point analysis sampling depths for the elements used in this work, using the X-Ray generation depth, $R_{\text{X-ray}}$, model of Castaing.[103] However, since this model requires values to be entered for the atomic mass, Z , and atomic number, A , of the target material, it would require composition dependant averages for these values to be calculated for numerous unknown Ta-Al-Co phase

compositions in order to use this model to calculate EDX sampling depth values for the phases analysed in this work. Moreover, since this model also requires you to input the energies of the X-ray emission lines for specific elements, the calculation becomes even more complicated when you are dealing with alloys instead of pure elements. Such calculations would not be very practical, therefore a simpler model where the only required material input parameter was density, was created to approximate Castaing's[103] model for X-Ray generation depth, $R_{X\text{-ray}}$ for the materials studied in the present work. This model was produced by simply modifying the coefficients from the standard empirical models for extrapolated electron penetration depth range, R_{EX} , so that the values produced by the resulting model were in satisfactory agreement with those produced by Castaing's[103] model for $R_{X\text{-ray}}$. This new model for EDX point analysis sampling depth, R_{EDXD} , is shown below in Equation A1.16, and the values calculated using this model for the elements studied in the present work are listed in Table A1.1. From this table it can be seen that the calculated values for R_{EDXD} produced from this model are in reasonably good agreement with those produced using Castaing's[103] model for $R_{X\text{-ray}}$.

$$R_{EDXD} = \frac{0.13125E_0^{1.5}}{\rho} \quad \text{Equation A1.16}$$

A model for EDX point analysis sampling width, R_{EDXW} , was also created by adding a numerical constant coefficient, W to the model for R_{EDXD} . This constant, $W=0.77$, was found by comparing Potts'[130] empirical models for extrapolated electron penetration depth and width ranges, R_{EX} , and R_w respectively, to yield that for these models, $R_w = 0.77R_{EX}$. Therefore it was assumed that the same relationship should also be reasonable for the models produced in the present work, i.e. $R_{EDXW} = 0.77 R_{EDXD}$. Thus:

$$R_{EDXW} = \frac{0.77 * 0.13125E_0^{1.5}}{\rho} \quad \text{Equation A1.17}$$

The values for approximate EDX point analysis sampling depth, R_{EDXD} , and width, R_{EDXW} , for Ta-Al-Co alloys spanning the range of densities studied in the present work, were calculated using the models given in Equations A1.16, and A1.17 respectively, and are also listed in Table A1.1. These density based interaction volume dimensions were then used to aid decision making with regards to where to position EDX point analysis measurements of phase boundary compositions depending on the density of the phase being measured. Eg. In phases with densities of 11g/cm^3 or more, EDX point analysis measurements could be positioned much closer to the physical boundaries of said phases, as seen on SEM BSE images. Since EDX point analysis measurements on phases with densities $>11\text{g/cm}^3$ are likely to have a sampling volume of $1\mu\text{m}^3$ or less. Conversely, EDX point analysis measurements on phases with densities between 11g/cm^3 - 3g/cm^3 are likely to have sampling volumes in the range of 1 - $4\mu\text{m}^3$, depending on the density of the phase in question. The EDX point analysis sampling volume dimensions shown in Table A1.1 were combined with the calculated density guide for the Ta-Al-Co system shown in Figure A1.2, to provide reasonable estimates of the EDX sampling volume dimensions for point analysis measurements taken on phases of various densities/compositions across the Ta-Co-Al phase diagram.

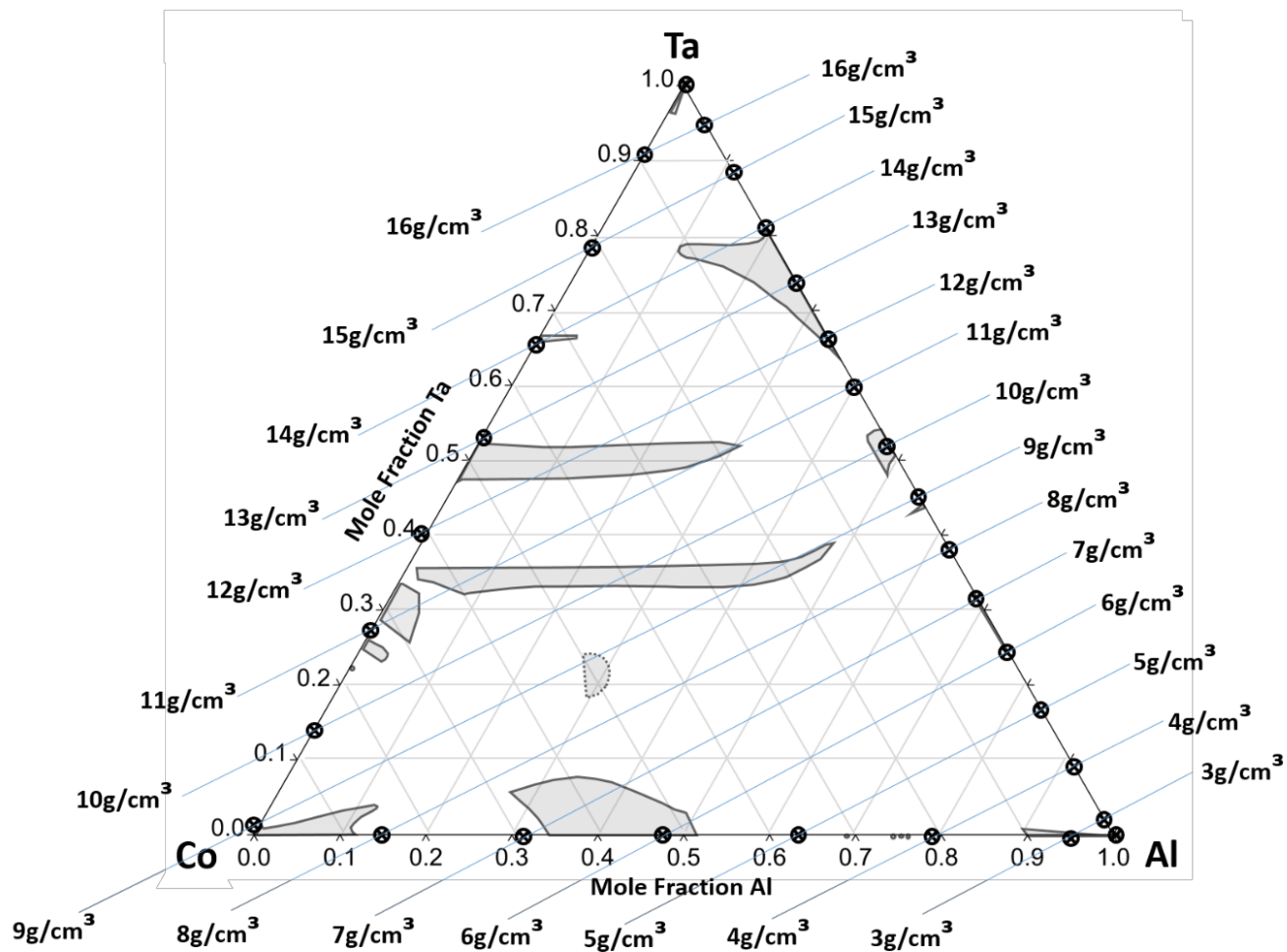
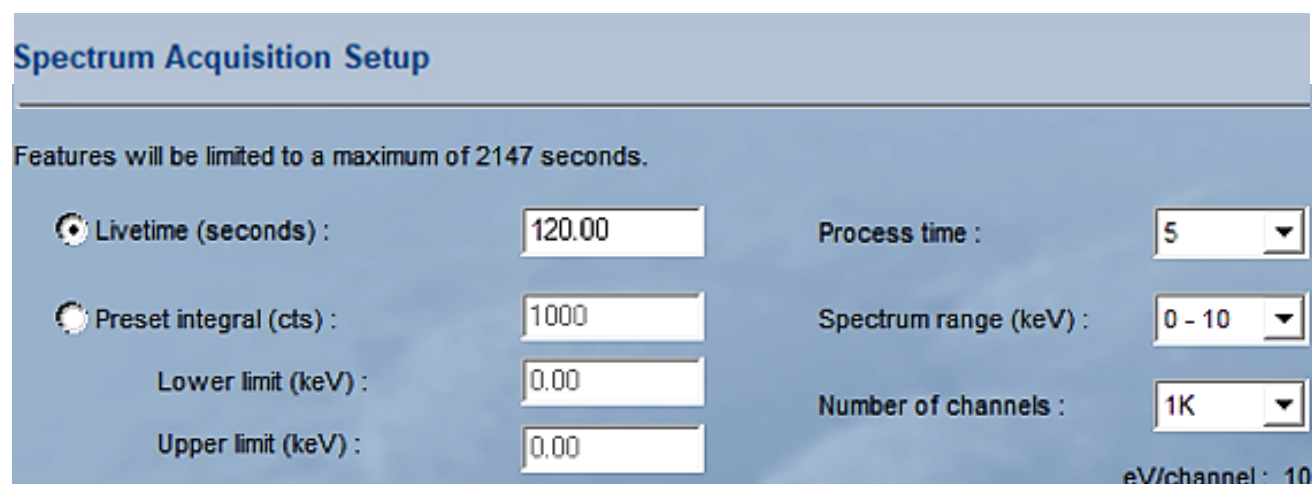


Figure A1.2: The calculated density guide for the Ta-Al-Co system produced in the present work, showing density as a function of composition for all alloy/phase compositions across the ternary system.

Appendix 1.2: SEM EDX Acquisition and Quantification

All of the EDX measurements in the present work were performed using Oxford INCA 300 EDX systems on either a JEOL 6060 or JEOL 7000 SEM. The results of these measurements were then analysed and quantified to yield bulk alloy compositions and phase compositions using the Oxford INCA Energy EDX analysis software.[104]

The typical spectrum acquisition setup is shown in Figure A1.3, and the quantitative analysis setup for all scans is shown in Figure A1.4. Area scans to measure bulk alloy compositions typically collected around 20,000 emitted X-ray counts, and point analysis measurements to measure phase boundary compositions typically collected around 10,000 emitted X-ray counts. EDX spectra were collected in the energy range of 0-10 KeV, and the processing options selected for the quantification were to quantify all selected elements, and to normalise the quantitative results.



The screenshot shows the 'Spectrum Acquisition Setup' window. At the top, it states 'Features will be limited to a maximum of 2147 seconds.' Below this, there are several configuration options:

- Lifetime (seconds):** 120.00 (selected with a radio button)
- Process time:** 5 (dropdown menu)
- Preset integral (cts):** 1000
- Spectrum range (keV):** 0 - 10 (dropdown menu)
- Lower limit (keV):** 0.00
- Number of channels:** 1K (dropdown menu)
- Upper limit (keV):** 0.00

At the bottom right, it indicates 'eV/channel : 10'.

Figure A1.3: The typical spectrum acquisition setup for the EDX scans performed during the present work. Area scans had a livetime of 120 seconds, whereas point analysis measurements had a livetime of 60 seconds.

The screenshot displays the INCA software interface. On the left, a 'Navigator' pane shows a workflow diagram with the following steps: Project, Sample, Microscope Setup, Site of Interest, Image Setup, Acquire Spectra, Acquisition Setup, Confirm Elements, Quant, Quant Setup, and Report. The 'Quant Setup' box is highlighted with a dashed border. Below the workflow is a 'Point & ID' button. At the bottom of the Navigator are icons for 'analyzer', 'Point & ID', 'Mapping', 'QuantMap', and 'Energy'. The main window is titled 'Quantitative Analysis Setup' and contains two sections: 'Processing option' with radio buttons for 'All elements' (selected), 'Element by difference', and 'Element by stoichiometry', and a checked checkbox for 'Normalize Quantitative Results'; and 'Element list' with radio buttons for 'Current spectrum' (selected), 'Combined', and 'Fixed list'. At the bottom of the main window are 'Save' and 'Delete' buttons, and a dropdown menu currently set to 'Existing'.

Figure A1.4: The quantitative analysis setup for all EDX scans performed during the present work.

The quantification was non-standardised, in that it compared the measured EDX spectra to the Oxford INCA Energy software's default virtual standards for X-ray emission lines[104] in order to identify and quantify the various X-ray emission peaks in the spectra. A typical measured EDX spectrum for one of the alloy samples studied in the current work is shown in Figure A1.5, with the positions of the characteristic X-ray emission lines for the various elements in the sample according to the Oxford INCA Energy software's default virtual standards[104] overlaid on top of the spectrum. From this figure, it is clear that the positions of the emission lines according to INCA's default standard are well matched with the positions of the measured X-ray emission peaks for the various elements. Moreover, the characteristic X-ray peaks for each individual element in the sample are sufficiently different that there is little chance of confusing them with each other in the analysis, since there are no overly close/overlapping emission lines/peaks in the EDX spectra of Ta-Al-Co ternary alloys.

In addition to the peaks for the expected elements of Al, Co, and Ta, the EDX spectra for all alloy samples also contained a small carbon (C) peak, as illustrated in Figure A1.6. If this peak was included in the quantification it typically corresponded to between 0.4 and 2wt% C, with the expected metallic elements making up the remaining measured composition. Since this peak was so small in magnitude, and was in line with the typical expected peak for surface C contamination, it was removed from the list of selected elements prior to quantification. This kind of surface C contamination is very common during SEM EDX analysis, and although steps can be taken to minimise its magnitude, in practice it is difficult to eliminate completely, especially when using older microscopes that experience a heavy volume of different student users. Moreover, Pie Scientific claim that XPS data shows that surface of a clean sample will be contaminated by airborne hydrocarbons after exposure to air for just one hour.[134]

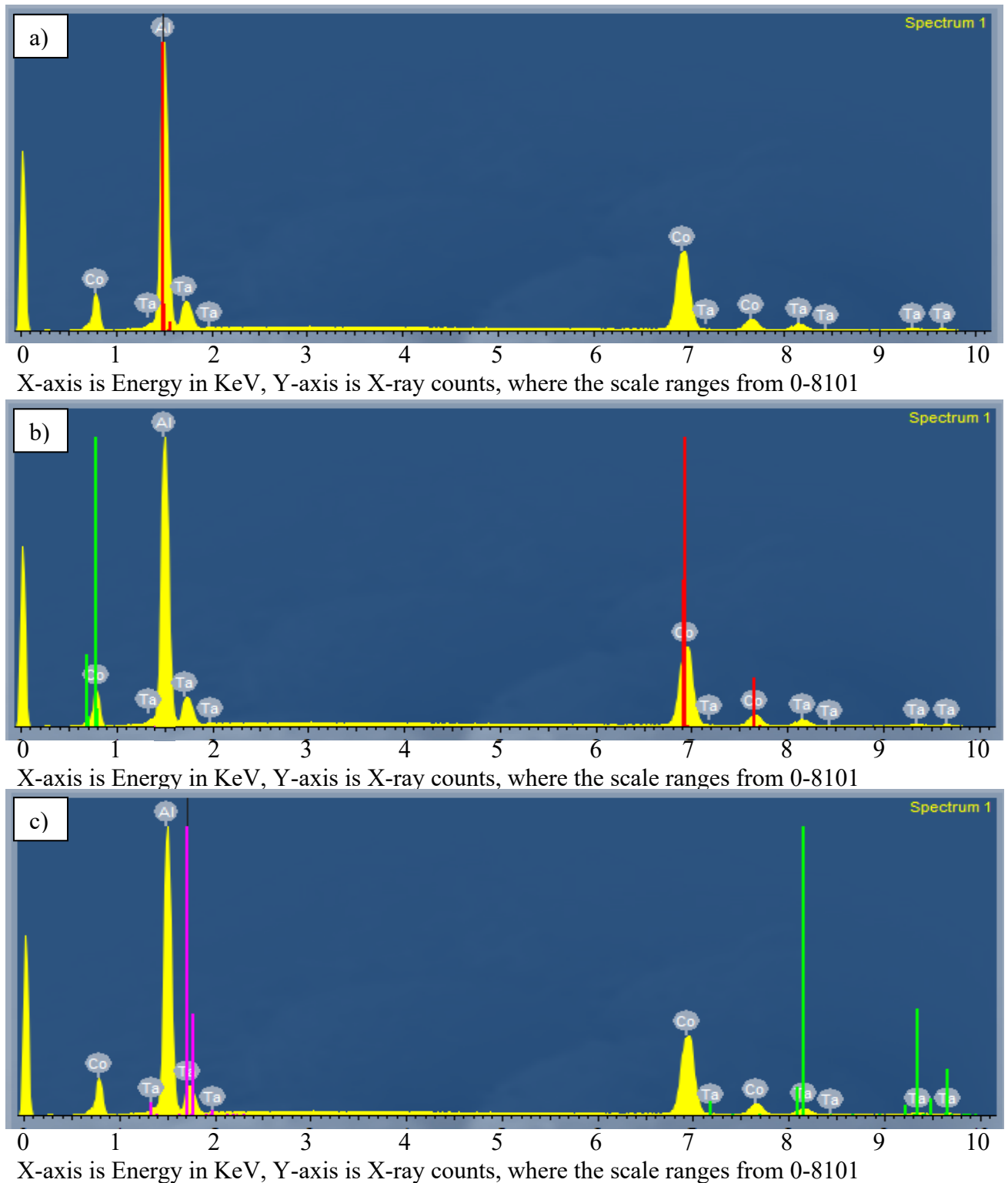


Figure A1.5: A typical measured EDX spectrum for one of the alloy samples studied, with the positions of the characteristic X-ray emission lines for a) Al, b) Co, and c) Ta according to the Oxford INCA Energy software's default virtual standards, marked as coloured lines on top of the spectrum. On spectrum a) $K\alpha$ for Al is marked in red at 1.486 KeV. On spectrum b) $L\alpha$ and $K\alpha$ for Co are marked in green at 0.776 KeV and red at 6.924 KeV respectively. On spectrum c) M and $K\alpha$ for Ta are marked in purple at 1.709 KeV and green at 8.145 KeV respectively. Moreover, INCA's virtual standards also contain a number of more minor emission lines, which are also highlighted on the spectra.

Once this C peak was removed from the selection, only the expected elements of Al, Co, and Ta remained. So when the processing options ‘all elements’, and ‘normalise quantitative results’ were selected for the quantification, this only included the three expected metallic elements, and the surface C contamination peak was excluded from the quantification for all spectra. An example of the quantitative results from a typical EDX scan from the present work are shown overleaf in Figure A1.7. These results also correspond to the EDX spectrum shown in Figures A1.5 and A1.6.

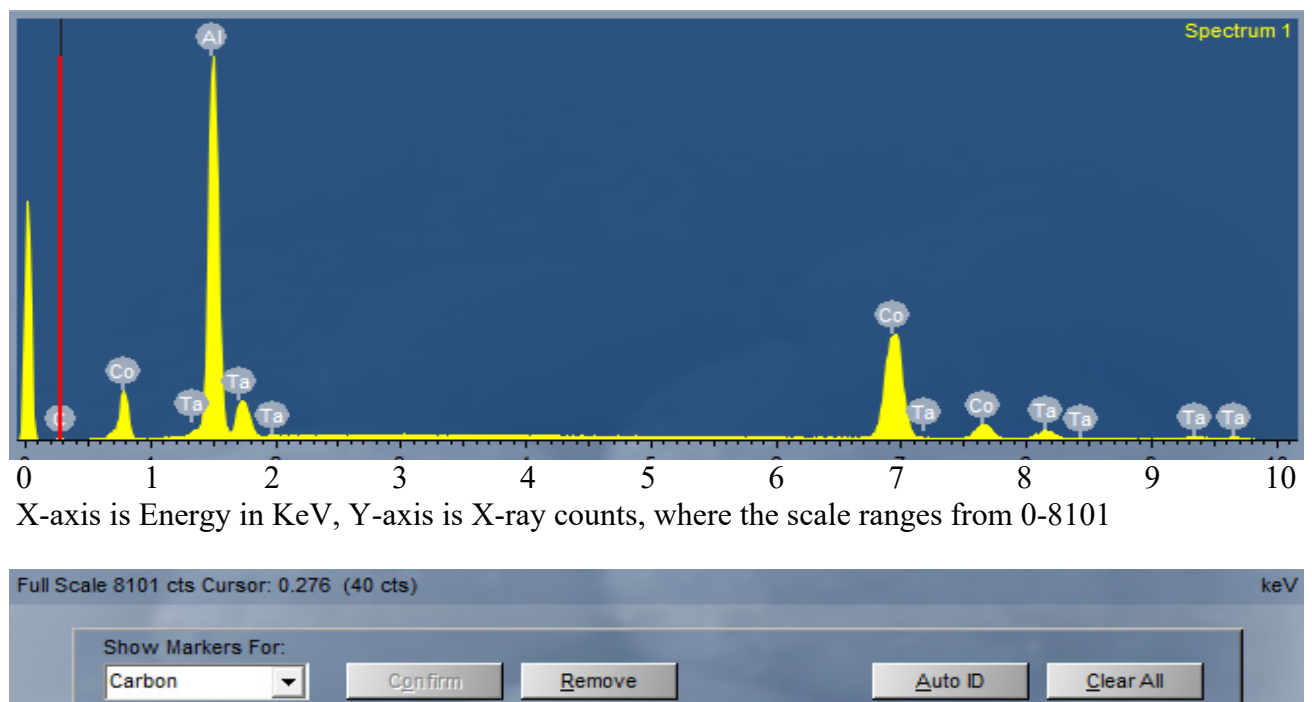


Figure A1.6: A typical measured EDX spectrum for one of the alloy samples studied, with the position of the characteristic X-ray emission line for C according to the Oxford INCA software’s default virtual standards, marked in red on top of the spectrum.

Quantitative Analysis

Spectrum 1

Full results :

Processing option : All elements analyzed (Normalised) Number of iterations : 4

Element	Line	App. Conc	k ratio	Intensity corr.	Weight%	Weight% sigma	Atomic%	Standard
Al	K_SERIES	33.19	0.2445	0.7214	37.38	0.30	60.93	Al2O3 1
Co	K_SERIES	55.87	0.55869	0.9578	47.38	0.35	35.37	Co 1-Jur
Ta	M_SERIES	8.95	0.08954	0.4773	15.24	0.41	3.70	Ta 1-Jur
Totals					100.00			

Figure A1.7: An example of the quantitative results from a typical EDX scan from the present work. These results also correspond to the EDX spectrum shown in Figures A1.5 and A1.6.

For bulk alloy composition measurements, EDX area scans were carried out on five different 962x725 μ m areas of the sample at 130x magnification. The mean of these 5 measurements was then taken as the bulk alloy composition for the sample. For phase composition measurements, 5-10 EDX point analysis measurements were carried out on specific phases at a magnification of 5000X, at a number of different areas of the sample. Again, the mean of these measurements was then taken as the composition for that phase.

Appendix 2: Thermodynamic Parameters for the Optimised Ta-Al-Co Description Produced in ‘this Work’ (TW)

Table A2.1: Thermodynamic Parameters for the optimised Ta-Al-Co description.

Phase and Model	Thermodynamic Parameters	Parameter Values	Ref
Functions that are used for multiple phases	GHSERAL	SGTE Unary Fuction taken from Dinsdale	[105]
	GHSERCO	SGTE Unary Fuction taken from Dinsdale	[105]
	GHSERTA	SGTE Unary Fuction taken from Dinsdale	[105]
	GLIQAL	SGTE Unary Fuction taken from Dinsdale	[105]
	GLIQCO	SGTE Unary Fuction taken from Dinsdale	[105]
	GLIQTA	SGTE Unary Fuction taken from Dinsdale	[105]
	GBCCAL	SGTE Unary Fuction taken from Dinsdale	[105]
	GBCCCO	SGTE Unary Fuction taken from Dinsdale	[105]
	GFCCCO	SGTE Unary Fuction taken from Dinsdale	[105]
	GFCCTA	SGTE Unary Fuction taken from Dinsdale	[105]
	GHCPAL	SGTE Unary Fuction taken from Dinsdale	[105]
	GHCPA	SGTE Unary Fuction taken from Dinsdale	[105]
Liquid (Al,Co,Ta)	G(LIQUID,AL;0)	+GLIQAL#	[105]
	G(LIQUID,CO;0)	+GLIQCO#	[105]
	G(LIQUID,TA;0)	+GLIQTA#	[105]
	L(LIQUID,AL,CO;0)	-140962.8+27.1374*T	[96]
	L(LIQUID,AL,CO;1)	-32294.9+12.6454*T	[96]
	L(LIQUID,AL,CO;2)	+33074.5-3.40903*T	[96]
	L(LIQUID,AL,TA;0)	-55024.576+9.489*T	[97]
	L(LIQUID,AL,TA;1)	-32750.134+19.689*T	[97]
	L(LIQUID,AL,TA;2)	+26570-4.667*T	[97]
	L(LIQUID,CO,TA;0)	-171992+35*T	[100]
	L(LIQUID,CO,TA;1)	-2958	[100]
	L(LIQUID,CO,TA;2)	+24975	[100]
FCC_A1 (Al,Co,Ta) ₁ (Va) ₁	G(FCC_A1,AL:VA;0)	+GHSERAL#	[105]
	G(FCC_A1,CO:VA;0)	+GFCCCO#	[105]
	G(FCC_A1,TA:VA;0)	+GFCCTA#	[105]
	TC(FCC_A1,CO:VA;0)	+1396	[105]
	BMAGN(FCC_A1,CO:VA;0)	+1.35	[105]
	L(FCC_A1,AL,CO:VA;0)	-124200+17.24*T	[96]
	L(FCC_A1,AL,CO:VA;2)	+28740	[96]
	TC(FCC_A1,AL,CO:VA;0)	-1500	[96]
	TC(FCC_A1,AL,CO:VA;1)	+650	[96]
	BMAGN(FCC_A1,AL,CO:VA;0)	+10	[96]
	L(FCC_A1,AL,TA:VA;0)	-125394.75+78.85*T	[97]
	TC(FCC_A1,CO,TA:VA;0)	-2200	[100]

Table A2.1: Thermodynamic Parameters for the optimised Ta-Al-Co description, continued.

Phase and Model	Thermodynamic Parameters	Parameter Values	Ref
FCC_A1 (Al,Co,Ta) ₁ (Va) ₁	TC(FCC_A1,CO,TA:VA;1)	-804	[100]
	L(FCC_A1,CO,TA:VA;0)	-80000+38*T	[100]
	L(FCC_A1,CO,TA:VA;1)	-60000	[100]
	L(FCC_A1,AL,CO,TA:VA;0)	-515000+17.3*T	TW
HCP_A3 (Al,Co,Ta) ₁ (Va) _{0.5}	G(HCP_A3,AL:VA;0)	+GHCPAL#	[105]
	G(HCP_A3,CO:VA;0)	+GHSERCO#	[105]
	G(HCP_A3,TA:VA;0)	+GHCPA#	[105]
	TC(HCP_A3,CO:VA;0)	+1396	[105]
	BMAGN(HCP_A3,CO:VA;0)	+1.35	[105]
	L(HCP_A3,AL,TA:VA;0)	-111000+36.6*T	[97]
	L(HCP_A3,CO,TA:VA;0)	-102000+15*T	[100]
BCC_A2 (Al,Co,Ta,Va) ₁ (Va) ₃	G(BCC_A2,AL:VA;0)	+GBCCAL#	[105]
	G(BCC_A2,CO:VA;0)	+GBCCCO#	[105]
	G(BCC_A2,TA:VA;0)	+GHSERTA#	[105]
	G(BCC_A2,VA:VA;0)	+30*T	[96]
	TC(BCC_A2,CO:VA;0)	+1450	[105]
	BMAGN(BCC_A2,CO:VA;0)	+1.35	[105]
	L(BCC_A2,AL,VA:VA;0)	+46912	[96]
	B2ALCO	-136736.6+28.25753*T	[96]
	LB2ALCO	+40492.9-24.9834*T	[96]
	L(BCC_A2,AL,CO:VA;0)	+B2ALCO#+LB2ALCO#	[96]
	L(BCC_A2,AL,TA:VA;0)	-6000+2*T	[97]
	L(BCC_A2,CO,VA:VA;0)	+126184	[100]
	L(BCC_A2,CO,TA:VA;0)	-59084+5.334*T	[97]
	L(BCC_A2,CO,TA:VA;1)	-20000+10*T	[100]
BCC_B2 AlCo (Al,Co,Ta,Va) _{0.5} (Al,Co,Ta,Va) _{0.5} (Va) ₃	G(BCC_B2,AL:AL:VA;0)	0 (Disordered contribution comes from BCC_A2)	[105]
	G(BCC_B2,CO:CO:VA;0)	0 (Disordered contribution comes from BCC_A2)	[105]
	G(BCC_B2,TA:TA:VA;0)	0 (Disordered contribution comes from BCC_A2)	[105]
	B2ALCO	-136736.6+28.25753*T	[96]
	LB2ALCO	+40492.9-24.9834*T	[96]
	UBALCO	+0.125*B2ALCO# - 0.125*LB2ALCO#	[96]
	G(BCC_B2,AL:CO:VA;0)	+4*UBALCO#	[96]
	G(BCC_B2,CO:AL:VA;0)	+4*UBALCO#	[96]
	TC(BCC_B2,AL:CO:VA;0)	-1400	[96]
	TC(BCC_B2,CO:AL:VA;0)	-1400	[96]
	G(BCC_B2,TA:CO:VA;0)	0 (Disordered contribution comes from BCC_A2)	[100]
	G(BCC_B2,VA:CO:VA;0)	0 (Disordered contribution comes from BCC_A2)	[96]
	G(BCC_B2,AL:TA:VA;0)	0 (Disordered contribution comes from BCC_A2)	[97]
	G(BCC_B2,CO:TA:VA;0)	0 (Disordered contribution comes from BCC_A2)	[100]

Table A2.1: Thermodynamic Parameters for the optimised Ta-Al-Co description, continued.

Phase and Model	Thermodynamic Parameters	Parameter Values	Ref
BCC_B2 AlCo (Al,Co,Ta,Va) _{0.5} (Al,Co,Ta,Va) _{0.5} (Va) ₃	G(BCC_B2,VA:TA:VA;0)	0 (Disordered contribution comes from BCC_A2)	[97]
	G(BCC_B2,AL:VA:VA;0)	0 (Disordered contribution comes from BCC_A2)	[96]
	G(BCC_B2,CO:VA:VA;0)	0 (Disordered contribution comes from BCC_A2)	[96]
	G(BCC_B2,TA:VA:VA;0)	0 (Disordered contribution comes from BCC_A2)	[97]
	G(BCC_B2,VA:VA:VA;0)	0 (Disordered contribution comes from BCC_A2)	[96]
	L(BCC_B2,CO,VA:AL:VA;0)	-28079-38.4534*T	[96]
	L(BCC_B2,AL:CO,VA:VA;0)	-28079-38.4534*T	[96]
	L(BCC_B2,CO:AL,TA:VA;0)	-161000-18*T	TW
	L(BCC_B2,AL,TA:CO:VA;0)	-161000-18*T	TW
	L(BCC_B2,CO:CO,TA:VA;0)	-266770-18*T	TW
	L(BCC_B2,CO,TA:CO:VA;0)	-266770-18*T	TW
	L(BCC_B2,CO:CO,TA:VA;1)	+12000	TW
	L(BCC_B2,CO,TA:CO:VA;1)	+12000	TW
	L(BCC_B2,AL:CO,TA:VA;0)	+80000	TW
	L(BCC_B2,CO,TA:AL:VA;0)	+80000	TW
	L(BCC_B2,AL:AL,TA:VA;0)	-110000	TW
L(BCC_B2,AL,TA:AL:VA;0)	-110000	TW	
L2 ₁ _AlCo ₂ Ta (Al,Ta) ₁ (Co) ₂ (Al,Co,Ta) ₁	G(L21,AL:CO:AL;0)	+2*GHSERAL#+2*GHSERCO#-225260+38.5*T	[108]
	G(L21,TA:CO:AL;0)	+GHSERTA#+2*GHSERCO#+GHSERAL#	TW
	G(L21,AL:CO:CO;0)	+GHSERAL#+3*GHSERCO#-97150	[108]
	G(L21,TA:CO:CO;0)	+GHSERTA#+3*GHSERCO#+146000	[108]
	G(L21,AL:CO:TA;0)	+GHSERAL#+2*GHSERCO#+GHSERTA# -244781+26.58*T	TW
	G(L21,TA:CO:TA;0)	+2*GHSERTA#+2*GHSERCO#+150000	[108]
	L(L21,AL,TA:CO:TA;0)	-162000-73*T	TW
	L(L21,AL:CO:Al,TA;0)	-20000	TW
CoTa ₂ _C16 (Al,Co,Ta) ₂ (Al,Co,Ta) ₁	G(CO1TA2,AL:AL;0)	+3*GHSERAL#	[105]
	G(CO1TA2,CO:CO;0)	+3*GHSERCO#+30000	[100]
	G(CO1TA2,TA:TA;0)	+3*GHSERTA#+152640	[100]
	G(CO1TA2,CO:AL;0)	+2*GHSERCO# +GHSERAL#	TW
	G(CO1TA2,TA:AL;0)	+2*GHSERTA#+GHSERAL#	TW
	G(CO1TA2,AL:TA;0)	+2*GHSERAL#+GHSERTA#	TW
	G(CO1TA2,AL:CO;0)	+2*GHSERAL#+GHSERCO#	TW
	G(CO1TA2,TA:CO;0)	+2*GHSERTA#+GHSERCO#-94343+10*T	[100]
	G(CO1TA2,CO:TA;0)	+2*GHSERCO#+GHSERTA#+90000+9*T	[100]
	L(CO1TA2,CO,TA:CO;0)	-100000	[100]
	L(CO1TA2,TA:CO,TA;0)	+20000	[100]
	L(CO1TA2,TA:AL,CO;0)	-110343+10*T	TW
	L(CO1TA2,TA:AL,TA;0)	-150000	TW

Table A2.1: Thermodynamic Parameters for the optimised Ta-Al-Co description, continued.

Phase and Model	Thermodynamic Parameters	Parameter Values	Ref
Sigma_D8b (Al,Co,Ta) _{0.6} (Al,Co,Ta) _{0.25} (Al,Co,Ta) _{0.15}	G(SIGMA,AL:AL:AL;0)	+GHSERAL	[105]
	G(SIGMA,CO:CO:CO;0)	+GHSERCO	[105]
	G(SIGMA,TA:TA:TA;0)	+GHSERTA+2.4499*T	[97]
	G(SIGMA,AL:AL:TA;0)	+ .85*GHSERAL#+.15*GHSERTA# -13500+7.0992*T	TW
	G(SIGMA,TA:AL:TA;0)	+ .75*GHSERTA#+.25*GHSERAL# -18800+3.0651*T	TW
	G(SIGMA,AL:TA:TA;0)	+ .6*GHSERAL#+.4*GHSERTA#	[97]
	G(SIGMA,AL:AL:CO;0)	+ .85*GHSERAL#+.15*GHSERCO#	TW
	G(SIGMA,CO:AL:CO;0)	+ .25*GHSERAL#+.75*GHSERCO#	TW
	G(SIGMA,TA:AL:CO;0)	+ .6*GHSERTA#+.25*GHSERAL# +.15*GHSERCO#	TW
	G(SIGMA,AL:CO:CO;0)	+ .6*GHSERAL#+.4*GHSERCO#	TW
	G(SIGMA,TA:CO:CO;0)	+ .6*GHSERTA#+.4*GHSERCO#	TW
	G(SIGMA,AL:TA:CO;0)	+ .6*GHSERAL#+.25*GHSERTA# +.15*GHSERCO#	TW
	G(SIGMA,CO:TA:CO;0)	+ .75*GHSERCO#+.25*GHSERTA#	TW
	G(SIGMA,TA:TA:CO;0)	+ .85*GHSERTA#+.15*GHSERCO#-10000	TW
	G(SIGMA,CO:AL:TA;0)	.6*GHSERCO#+.25*GHSERAL# +.15*GHSERTA#	TW
	G(SIGMA,AL:CO:TA;0)	.6*GHSERAL#+.25*GHSERCO# +.15*GHSERTA#	TW
	G(SIGMA,CO:CO:TA;0)	+ .85*GHSERCO#+.15*GHSERTA#+5000	TW
	G(SIGMA,TA:CO:TA;0)	+ .75*GHSERTA#+.25*GHSERCO#-10000	TW
	G(SIGMA,CO:TA:TA;0)	+ .6*GHSERCO#+.4*GHSERTA#+5000	TW
	G(SIGMA,CO:AL:AL;0)	+ .6*GHSERCO#+.4*GHSERAL#	TW
	G(SIGMA,TA:AL:AL;0)	+ .6*GHSERTA#+.4*GHSERAL#	TW
	G(SIGMA,AL:CO:AL;0)	+ .75*GHSERAL#+.25*GHSERCO#	TW
	G(SIGMA,CO:CO:AL;0)	+ .85*GHSERCO#+.15*GHSERAL#	TW
	G(SIGMA,TA:CO:AL;0)	+ .6*GHSERTA#+.25*GHSERCO# +.15*GHSERAL#	TW
	G(SIGMA,AL:TA:AL;0)	+ .75*GHSERAL#+.25*GHSERTA#	TW
	G(SIGMA,CO:TA:AL;0)	+ .6*GHSERCO#+.25*GHSERTA# +.15*GHSERAL#	TW
	G(SIGMA,TA:TA:AL;0)	+ .85*GHSERTA#+.15*GHSERCO#-10000+10*T	TW
	L(SIGMA,AL,TA:AL:TA;0)	-29268.5+4.1*T	TW
L(SIGMA,TA:AL,CO:TA;0)	-32000	TW	
L(SIGMA,TA:AL,CO:TA;1)	-8000	TW	
L(SIGMA,TA:TA,CO:TA;1)	-50000	TW	

Table A2.1: Thermodynamic Parameters for the optimised Ta-Al-Co description, continued.

Phase and Model	Thermodynamic Parameters	Parameter Values	Ref
Mu_D85 (Al,Ta) ₄ (Al,Co,Ta) ₂ (Al,Co,Ta) ₁ (Al,Co) ₆	GMUAL	+GHSERAL#+9700	[112]
	GMUCO	+GHSERCO#+11800	[112]
	GMUTA	+GHSERTA#+11800	[112]
	GMTACO	-525200+60*T	[100]
	GMLCOTA	+532324	TW
	GM2COTA	+133081	[100]
	GM3TACO	-6500	TW
	GM4TACO	+671970	TW
	CO3TA10	+GMTACO+GM2COTA+GM4TACO +3*GHSERCO+10*GHSERTA	TW
	CO5TA8	+GMTACO+GMLCOTA+GM4TACO +5*GHSERCO+8*GHSERTA	TW
	CO6TA7	-467000+38*T+6*GHSERCO+7*GHSERTA	[100]
	CO7TA6	-523319+62*T+7*GHSERCO+6*GHSERTA	[100]
	CO8TA5	+GMTACO+GM2COTA+GM3TACO +8*GHSERCO+5*GHSERTA	[100]
	CO9TA4	+GMTACO+GM2COTA+9*GHSERCO# +4*GHSERTA#	[100]
	CO11TA2	+GMTACO+GMLCOTA+11*GHSERCO +2*GHSERTA	TW
	CO12TA1	+GMTACO+GMLCOTA+GM2COTA +GM3TACO+12*GHSERCO+1*GHSERTA	TW
	AL3TA10	3*GMUAL+10*GMUTA	TW
	AL5TA8	5*GMUAL+8*GMUTA	TW
	AL6TA7	6*GMUAL+7*GMUTA	TW
	AL7TA6	7*GMUAL+6*GMUTA	TW
	AL8TA5	8*GMUAL+5*GMUTA	TW
	AL9TA4	9*GMUAL+4*GMUTA	TW
	AL11TA2	11*GMUAL+2*GMUTA	TW
	AL12TA1	12*GMUAL+1*GMUTA	TW
	THREE	+3	TW
	TRD	+THREE**(-1)	TW
	TWOTRD	+2*TRD	TW
	SIX	+6	TW
	ONESIX	+SIX**(-1)	TW
	TWOSIX	+2*ONESIX	TW
	THRSIX	+3*ONESIX	TW
	FOUSIX	+4*ONESIX	TW
FIVSIX	+5*ONESIX	TW	

Table A2.1: Thermodynamic Parameters for the optimised Ta-Al-Co description, continued.

Phase and Model	Thermodynamic Parameters	Parameter Values	Ref
Mu_D85 (Al,Ta) ₄ (Al,Co,Ta) ₂ (Al,Co,Ta) ₁ (Al,Co) ₆	SEVEN	+7	TW
	ONESEV	+SEVEN**(-1)	TW
	TWOSEV	+2*ONESEV	TW
	THRSEV	+3*ONESEV	TW
	FOUSEV	+4*ONESEV	TW
	FIVSEV	+5*ONESEV	TW
	SIXSEV	+6*ONESEV	TW
	NINE	+9	TW
	ONENIN	+NINE**(-1)	TW
	TWONIN	+2*ONENIN	TW
	THRNIN	+3*ONENIN	TW
	SIXNIN	+6*ONENIN	TW
	SEVNIN	+7*ONENIN	TW
	EIGNIN	+8*ONENIN	TW
	ELEVEN	+11	TW
	ONEELE	+ELEVEN**(-1)	TW
	FOUELE	+4*ONEELE	TW
	FIVELE	+5*ONEELE	TW
	SIXELE	+6*ONEELE	TW
	SEVELE	+7*ONEELE	TW
	TENELE	+10*ONEELE	TW
	G(MU4,TA:TA:CO:CO;0)	-523319+62*T+7*GHSERCO+6*GHSERTA	[100]
	G(MU4,TA:TA:TA:CO;0)	-467000+38*T+6*GHSERCO+7*GHSERTA	[100]
	G(MU4,TA:TA:CO:TA;0)	+GMTACO+GM4TACO+1*GHSERCO +12*GHSERTA	TW
	G(MU4,TA:CO:TA:TA;0)	+GMTACO+GM2COTA+GM3TACO +GM4TACO+2*GHSERCO+11*GHSERTA	TW
	G(MU4,TA:CO:CO:TA;0)	+GMTACO+GM2COTA+GM4TACO +3*GHSERCO+10*GHSERTA	TW
	G(MU4,CO:TA:TA:TA;0)	+GMTACO+GMLCOTA+GM3TACO +GM4TACO+4*GHSERCO+9*GHSERTA	TW
	G(MU4,CO:TA:CO:TA;0)	+GMTACO+GMLCOTA+GM4TACO +5*GHSERCO+8*GHSERTA	TW
	G(MU4,CO:CO:TA:TA;0)	+GMTACO+GMLCOTA+GM2COTA +GM3TACO+GM4TACO+6*GHSERCO +7*GHSERTA	TW
	G(MU4,CO:CO:CO:TA;0)	+GMTACO+GMLCOTA+GM2COTA +GM4TACO+7*GHSERCO+6*GHSERTA	TW
	G(MU4,TA:CO:TA:CO;0)	+GMTACO+GM2COTA+GM3TACO +8*GHSERCO+5*GHSERTA	[100]
	G(MU4,TA:CO:CO:CO;0)	+GMTACO+GM2COTA+9*GHSERCO +4*GHSERTA	[100]
	G(MU4,CO:TA:TA:CO;0)	+GMTACO+GMLCOTA+GM3TACO +10*GHSERCO+3*GHSERTA	TW

Table A2.1: Thermodynamic Parameters for the optimised Ta-Al-Co description, continued.

Phase and Model	Thermodynamic Parameters	Parameter Values	Ref
Mu_D85 (Al,Ta) ₄ (Al,Co,Ta) ₂ (Al,Co,Ta) ₁ (Al,Co) ₆	G(MU4,CO:TA:CO:CO;0)	+GMTACO+GMLCOTA+11*GHSERCO +2*GHSERTA	TW
	G(MU4,CO:CO:TA:CO;0)	+GMTACO+GMLCOTA+GM2COTA +GM3TACO+12*GHSERCO+1*GHSERTA	TW
	G(MU4,AL:AL:AL:AL;0)	+13*GMUAL	TW
	G(MU4,TA:AL:AL:AL;0)	+9*GMUAL+4*GMUTA	TW
	G(MU4,AL:CO:AL:AL;0)	+2*GMUCO+11*GMUAL	TW
	G(MU4,TA:CO:AL:AL;0)	+TWONIN*CO9TA4+SEVNIN*AL9TA4	TW
	G(MU4,AL:TA:AL:AL;0)	+11*GMUAL+2*GMUTA	TW
	G(MU4,TA:TA:AL:AL;0)	+7*GMUAL+6*GMUTA	TW
	G(MU4,AL:AL:CO:AL;0)	+12*GMUAL+1*GMUCO	TW
	G(MU4,TA:AL:CO:AL;0)	+ONENIN*CO9TA4+EIGNIN*AL9TA4	TW
	G(MU4,AL:CO:CO:AL;0)	+10*GMUAL+3*GMUCO	TW
	G(MU4,TA:CO:CO:AL;0)	+THRNNIN*CO9TA4+SIXNIN*AL9TA4	TW
	G(MU4,AL:TA:CO:AL;0)	+ONEELE*CO11TA2+TENELE*AL11TA2	TW
	G(MU4,TA:TA:CO:AL;0)	+6*GMUAL+1*GMUCO+6*GMUTA -510000+72.7*T	TW
	G(MU4,AL:AL:TA:AL;0)	+12*GMUAL+1*GMUTA	TW
	G(MU4,TA:AL:TA:AL;0)	+8*GMUAL+5*GMUTA	TW
	G(MU4,AL:CO:TA:AL;0)	+ONESIX*CO12TA1+FIVSIX*AL12TA1	TW
	G(MU4,TA:CO:TA:AL;0)	+0.25*CO8TA5+0.75*AL8TA5	TW
	G(MU4,AL:TA:TA:AL;0)	+10*GMUAL+3*GMUTA	TW
	G(MU4,TA:TA:TA:AL;0)	+6*GMUAL+7*GMUTA-390000+72.7*T	TW
	G(MU4,AL:AL:AL:CO;0)	+7*GMUAL+6*GMUCO	TW
	G(MU4,TA:AL:AL:CO;0)	+SIXNIN*CO9TA4+THRNNIN*AL9TA4	TW
	G(MU4,AL:CO:AL:CO;0)	+5*GMUAL+8*GMUCO	TW
	G(MU4,TA:CO:AL:CO;0)	+EIGNIN*CO9TA4+ONENIN*AL9TA4	TW
	G(MU4,AL:TA:AL:CO;0)	+SIXELE*CO11TA2+FIVELE*AL11TA2	TW
	G(MU4,TA:TA:AL:CO;0)	+SIXSEV*CO7TA6+ONESEV*AL7TA6	TW
	G(MU4,AL:AL:CO:CO;0)	+6*GMUAL+7*GMUCO	TW
	G(MU4,TA:AL:CO:CO;0)	+SEVNIN*CO9TA4+TWONIN*AL9TA4	TW
	G(MU4,AL:CO:CO:CO;0)	+4*GMUAL+9*GMUCO	TW
	G(MU4,AL:TA:CO:CO;0)	+SEVELE*CO11TA2+FOUELE*AL11TA2	TW
	G(MU4,AL:AL:TA:CO;0)	+THRSIX*CO12TA1+THRSIX*AL12TA1	TW
	G(MU4,TA:AL:TA:CO;0)	+0.75*CO8TA5+0.25*AL8TA5	TW
	G(MU4,AL:CO:TA:CO;0)	+FOUSIX*CO12TA1+TWOSIX*AL12TA1	TW
	L(MU4,TA:TA:CO:CO,AL;0)	-740000	TW
	L(MU4,TA:TA:CO:CO,AL;1)	+40000	TW
	L(MU4,TA:TA:TA:CO,AL;0)	-740000+10*T	TW
	L(MU4,TA:TA:TA:CO,AL;1)	-24000	TW

Table A2.1: Thermodynamic Parameters for the optimised Ta-Al-Co description, continued.

Phase and Model	Thermodynamic Parameters	Parameter Values	Ref
Laves_C14 (Al,Co,Ta) ₁ (Al,Co,Ta) ₂	GC14AL	+GHSERAL#+13900	[112]
	GC14CO	+GHSERCO#+16400	[100]
	GC14TA	+GHSERTA#+9350	[100]
	G(LAVES_C14,AL:AL;0)	+3*GC14AL#	TW
	G(LAVES_C14,CO:CO;0)	+3*GC14CO#	[100]
	G(LAVES_C14,TA:TA;0)	+3*GC14TA#	[100]
	G(LAVES_C14,CO:AL;0)	+2*GC14AL#+GC14CO#	TW
	G(LAVES_C14,TA:AL;0)	+2*GC14AL#+GC14TA#-107500+9.7*T	TW
	G(LAVES_C14,AL:CO;0)	+2*GC14CO#+GC14AL#-40700	TW
	G(LAVES_C14,TA:CO;0)	+2*GC14CO#+GC14TA#-179988+26*T	[100]
	G(LAVES_C14,AL:TA;0)	+2*GC14TA#+GC14AL#+210050+0.112*T	TW
	G(LAVES_C14,CO:TA;0)	+2*GC14TA#+GC14CO#+136700+26.5*T	[100]
	L(LAVES_C14,TA:CO,TA;0)	-54700	[100]
	L(LAVES_C14,AL,TA:CO;0)	-90810+8*T	TW
	L(LAVES_C14,AL,TA:CO;1)	+9130	TW
	L(LAVES_C14,TA:CO,AL;0)	-284000+49*T	TW
	L(LAVES_C14,TA:CO,AL;1)	+110000	TW
L(LAVES_C14,TA:AL,TA;0)	-170000+90*T	TW	
Laves_C15 (Al,Co,Ta) ₁ (Al,Co,Ta) ₂	GC15AL	+GHSERAL#+15100	[112]
	GC15CO	+GHSERCO#+19600	[100]
	GC15TA	+GHSERTA#+10940	[100]
	G(LAVES_C15,AL:AL;0)	+3*GC15AL#+50000	TW
	G(LAVES_C15,CO:CO;0)	+3*GC15CO#	[100]
	G(LAVES_C15,TA:TA;0)	+3*GC15TA#	[100]
	G(LAVES_C15,CO:AL;0)	+2*GC15AL#+GC15CO#	TW
	G(LAVES_C15,TA:AL;0)	+2*GC15AL#+GC15TA#-40000	TW
	G(LAVES_C15,AL:CO;0)	+2*GC15CO#+GC15AL#-15000	TW
	G(LAVES_C15,TA:CO;0)	+2*GC15CO#+GC15TA#-189440+26.15*T	[100]
	G(LAVES_C15,AL:TA;0)	+2*GC15TA#+GC15AL#	TW
	G(LAVES_C15,CO:TA;0)	+GC15CO#+2*GC15TA#+138000+26.15*T	[100]
	L(LAVES_C15,CO,TA:CO;0)	-61500	[100]
	L(LAVES_C15,AL,TA:CO;0)	-205700	TW
	L(LAVES_C15,TA:CO,AL;0)	-260010+6*T	TW
	L(LAVES_C15,TA:CO,AL;1)	+65000	TW
	L(LAVES_C15,AL,CO:CO;0)	-180000	TW

Table A2.1: Thermodynamic Parameters for the optimised Ta-Al-Co description, continued.

Phase and Model	Thermodynamic Parameters	Parameter Values	Ref
Laves_C36 (Al,Co,Ta)1 (Al,Co,Ta)2	GC36AL	+GHSERAL#+13900	[112]
	GC136CO	+GHSERCO#+16400	[100]
	GC36TA	+GHSERTA#+10150	[100]
	G(LAVES_C36,AL:AL;0)	+3*GC36AL#+50000	TW
	G(LAVES_C36,CO:CO;0)	+3*GC36CO#	[100]
	G(LAVES_C36,TA:TA;0)	+3*GC36TA#	[100]
	G(LAVES_C36,CO:AL;0)	+2*GC36AL#+GC36CO#	TW
	G(LAVES_C36,TA:AL;0)	+2*GC36AL#+GC36TA#-55000	TW
	G(LAVES_C36,AL:CO;0)	+2*GC36CO#+GC36AL#	TW
	G(LAVES_C36,TA:CO;0)	+2*GC36CO#+GC36TA#-180090+27.2*T	[100]
	G(LAVES_C36,AL:TA;0)	+2*GC36TA#+GC36AL#	TW
	G(LAVES_C36,CO:TA;0)	+GC36CO#+2*GC36TA#+137000+27.2*T	[100]
	L(LAVES_C36,CO,TA:CO;0)	-69200	[100]
	L(LAVES_C36,TA:CO,AL;0)	-208974+8*T	TW
	L(LAVES_C36,AL,TA:CO;0)	-220000	TW
	L(LAVES_C36,AL,TA:CO;1)	+14000	TW
	L(LAVES_C36,AL,CO:CO;0)	-150000	TW
L(LAVES_C36,AL,CO:TA;0)	+81000	TW	
Phi_Al38Ta48 (Al,Ta)0.8837 (Al,Ta)1.1163	G(PHI,AL:AL;0)	+2*GHSERAL#+500	[97]
	G(PHI,CO:CO;0)	+2*GHSERCO#	TW
	G(PHI,TA:TA;0)	+2*GHSERTA#+22500	[97]
	G(PHI,CO:AL;0)	+ .8837*GHSERCO#+1.1163*GHSERAL#	TW
	G(PHI,TA:AL;0)	+1.1163*GHSERAL#+.8837*GHSERTA#	[97]
	G(PHI,AL:CO;0)	+ .8837*GHSERAL#+1.1163*GHSERCO#	TW
	G(PHI,TA:CO;0)	+ .8837*GHSERTA#+1.1163*GHSERCO	TW
	G(PHI,AL:TA;0)	+ .8837*GHSERAL#+1.1163*GHSERTA# -50500+7*T	TW
	G(PHI,CO:TA;0)	+ .8837*GHSERCO#+1.1163*GHSERTA#	TW
	L(PHI,AL:AL,TA;0)	-52500+32.7892*T	[97]
	L(PHI,AL,TA:TA;0)	-27895.6+8.5005*T	[97]
	L(PHI,AL:CO,TA;0)	-118000	TW

Table A2.1: Thermodynamic Parameters for the optimised Ta-Al-Co description, continued.

Phase and Model	Thermodynamic Parameters	Parameter Values	Ref
Al ₆₉ Ta ₃₉	G(AL69TA39,AL:AL;0)	+GHSERAL#+3000	[97]
(Al,Co,Ta) _{0.6389}	G(AL69TA39,CO:AL;0)	+.6389*GHSERCO#+.3611*GHSERAL#	TW
(Al,Co,Ta) _{0.3611}	G(AL69TA39,TA:AL;0)	+.6389*GHSERTA#+.3611*GHSERAL#	[97]
	G(AL69TA39,AL:CO;0)	+.6389*GHSERAL#+.3611*GHSERCO#	TW
	G(AL69TA39,CO:CO;0)	+GHSERCO#	TW
	G(AL69TA39,TA:CO;0)	+.6389*GHSERTA#+.3611*GHSERCO#	TW
	G(AL69TA39,AL:TA;0)	+.6389*GHSERAL#+.3611*GHSERTA#	[97]
		-25904+3.502*T	
	G(AL69TA39,CO:TA;0)	+.6389*GHSERCO#+.3611*GHSERTA#	TW
	G(AL69TA39,TA:TA;0)	+GHSERTA#+9000	[97]
	L(AL69TA39,AL,CO:TA;0)	-67000	TW
Epsilon_Al ₃ Ta	G(EPSILON,AL:AL;0)	+GHSERAL#+20000;	[97]
_D022	G(EPSILON,AL:TA;0)	+.75*GHSERAL#+.25*GHSERTA#-29950	[97]
(Al) _{0.75}		+6.576*T;	
(Al,Ta) _{0.25}	G(EPSILON,AL:AL,TA;0)	-1494-10.6211*T;	[97]
Al ₉ Co ₂	G(AL9CO2,AL:CO;0)	+9*GHSERAL#+2*GHSERCO#	[96]
(Al) ₉ (Co) ₂		-334995.1+56.7277*T	
o-Al ₁₃ Co ₄	G(OAL13CO4,AL:CO;0)	+.76*GHSERAL#+.24*GHSERCO#	[96]
(Al) ₁₃ (Co) ₄		-39769.2+7.6677*T	
γ-Al ₁₃ Co ₄	G(YAL13CO4,AL:CO;0)	+.755*GHSERAL#+.245*GHSERCO#	[96]
(Al) ₁₃ (Co) ₄		-39956.6+7.4808*T	
m-Al ₁₃ Co ₄	G(MAL13CO4,AL:CO;0)	+.755*GHSERAL#+.245*GHSERCO#	[96]
(Al) ₁₃ (Co) ₄		-40740+8.0589*T	
Al ₃ Co	G(AL3CO,AL:CO;0)	+.745*GHSERAL#+.255*GHSERCO#	[96]
(Al) ₃ (Co) ₁		-42728.3+8.8831*T	
Al ₅ Co ₂ _D811	G(AL5CO2,AL:CO;0)	+5*GHSERAL#+2*GHSERCO#	[96]
(Al) ₅ (Co) ₂		-322674+67.6931*T	
Co ₇ Ta ₂	G(CO7TA2,TA:CO;0)	+7*GHSERCO#+2*GHSERTA#	[100]
(Co) ₇ (Ta) ₂		-309000+66.5*T	

Appendix 3: Thermodynamic Parameters for the Optimised Ti-Fe-Mo Description Produced in ‘this Work’ (TW)

Table A3.1: Thermodynamic Parameters for the optimised Ti-Fe-Mo description.

Phase and Model	Thermodynamic Parameters	Parameter Values	Ref
Functions that are used for multiple phases	GHSEFE	SGTE Unary Fuction taken from Dinsdale	[105]
	GHSEMO	SGTE Unary Fuction taken from Dinsdale	[105]
	GHSETI	SGTE Unary Fuction taken from Dinsdale	[105]
	GLIQFE	SGTE Unary Fuction taken from Dinsdale	[105]
	GLIQMO	SGTE Unary Fuction taken from Dinsdale	[105]
	GLIQTI	SGTE Unary Fuction taken from Dinsdale	[105]
	GBCCTI	SGTE Unary Fuction taken from Dinsdale	[105]
	GFCCFE	SGTE Unary Fuction taken from Dinsdale	[105]
	GFCCMO	SGTE Unary Fuction taken from Dinsdale	[105]
	GFCCTI	SGTE Unary Fuction taken from Dinsdale	[105]
	GHCPFE	SGTE Unary Fuction taken from Dinsdale	[105]
	GHCPMO	SGTE Unary Fuction taken from Dinsdale	[105]
Liquid (Fe,Mo,Ti)	G(LIQUID,FE;0)	+GLIQFE#	[105]
	G(LIQUID,MO;0)	+GLIQMO#	[105]
	G(LIQUID,TI;0)	+GLIQTI#	[105]
	L(LIQUID,FE,TI;0)	-76384+17.884*T	[119]
	L(LIQUID,FE,TI;1)	+7944-6.071*T	[119]
	L(LIQUID,FE,MO;0)	-11712+2.917*T	[118]
	L(LIQUID,MO,TI;0)	-17494.7-3.57111*T	[120]
	L(LIQUID,MO,TI;1)	-463.9+9.0476*T	[120]
	L(LIQUID,FE,MO,TI;0)	+17000	TW
FCC_A1 (Fe,Mo,Ti)	G(FCC_A1,FE;0)	+GFCCFE#	[105]
	G(FCC_A1,MO;0)	+GFCCMO#	[105]
	G(FCC_A1,TI;0)	+GFCCTI#	[105]
	TC(FCC_A1,FE;0)	-201	[105]
	BMAGN(FCC_A1,FE;0)	-2.1	[105]
	L(FCC_A1,FE,TI;0)	-55592+8.644*T	[119]
	L(FCC_A1,FE,TI;1)	+4352-4.014*T	[119]
	L(FCC_A1,FE,TI;2)	+28697-12.022*T	[119]
	L(FCC_A1,FE,MO;0)	+20978-11.843*T	[118]
	L(FCC_A1,MO,TI;0)	-23224.5	[120]

Table A3.1: Thermodynamic Parameters for the optimised Ti-Fe-Mo description, continued.

Phase and Model	Thermodynamic Parameters	Parameter Values	Ref
HCP_A3 (Fe,Mo,Ti)	G(HCP,FE;0)	+GHCPFE#	[105]
	G(HCP,MO;0)	+GHCPMO#	[105]
	G(HCP,TI;0)	+GHSERTI#	[105]
	L(HCP,FE,TI;0)	+16370-13.261*T	[119]
	L(HCP,MO,TI;0)	+14250.8	[120]
BCC_A2 (Fe,Mo,Ti)	G(BCC_A2,FE;0)	+GHSERFE#	[105]
	G(BCC_A2,MO;0)	+GHSERMOMO#	[105]
	G(BCC_A2,TI;0)	+GBCCTI#	[105]
	TC(BCC_A2,FE;0)	+1043	[105]
	BMAGN(BCC_A2,FE;0)	+2.22	[105]
	LFETIB0	-68448+23.825*T	[119]
	LFETIB1	+5467-5.083*T	[119]
	LFETIB2	+25262-15.83*T	[119]
	L(BCC_A2,FE,TI;0)	+LFETIB0#	[119]
	L(BCC_A2,FE,TI;1)	+LFETIB1#	[119]
	L(BCC_A2,FE,TI;2)	+LFETIB2#	[119]
	TC(BCC_A2,FE,TI;0)	+637.79	[119]
	TC(BCC_A2,FE,MO;0)	+334	[118]
	TC(BCC_A2,FE,MO;1)	+531	[118]
	L(BCC_A2,FE,MO;0)	+38849-9.539*T	[118]
	L(BCC_A2,FE,MO;1)	-8988	[118]
	L(BCC_A2,MO,TI;0)	+3383.4-10.0774*T	[120]
	L(BCC_A2,MO,TI;1)	-56704.6+32.12*T	[120]
	L(BCC_A2,MO,TI;2)	-15172.4	[120]
	L(BCC_A2,FE,MO,TI;0)	-20000+17*T	TW
BCC_B2 AlCo (Fe,Mo,Ti) _{0.5} (Fe,Mo,Ti) _{0.5}	G(BCC_B2,FE:FE;0)	0 (Disordered contribution comes from BCC_A2)	[105]
	G(BCC_B2,MO:MO;0)	0 (Disordered contribution comes from BCC_A2)	[105]
	G(BCC_B2,TI:TI;0)	0 (Disordered contribution comes from BCC_A2)	[105]
	GFETI	-76147-46.603*T+8.663*T*LN(T) -.007151*T**2+1.121169E-06*T**3	[119]
	G(BCC_B2,TI:FE;0)	+5*GFETI#	[119]
	G(BCC_B2,FE:TI;0)	+5*GFETI#	[119]
	TC(BCC_B2,TI:FE;0)	-1325	[119]
	TC(BCC_B2,FE:TI;0)	-1325	[119]
	G(BCC_B2,FE:MO;0)	0 (Disordered contribution comes from BCC_A2)	[105]
	G(BCC_B2,MO:FE;0)	0 (Disordered contribution comes from BCC_A2)	[105]
	G(BCC_B2,TI:MO;0)	0 (Disordered contribution comes from BCC_A2)	[105]
	G(BCC_B2,MO:TI;0)	0 (Disordered contribution comes from BCC_A2)	[105]
	L(BCC_B2,FE,TI:FE;0)	-10953	[119]
	L(BCC_B2,FE:FE,TI;0)	-10953	[119]

Table A3.1: Thermodynamic Parameters for the optimised Ti-Fe-Mo description, continued.

Phase and Model	Thermodynamic Parameters	Parameter Values	Ref
BCC_B2 AlCo (Fe,Mo,Ti) _{0.5} (Fe,Mo,Ti) _{0.5}	L(BCC_B2,FE:FE,TI;1)	-13719	[119]
	L(BCC_B2,FE,TI:FE;1)	-13719	[119]
	LBFETIMO	-8000	TW
	L(BCC_B2,MO:FE,TI;0)	+LBFETIMO#	TW
	L(BCC_B2,FE,TI:MO;0)	+LBFETIMO#	TW
	L(BCC_B2,FE,TI:TI;0)	-6097	[119]
	L(BCC_B2,TI:FE,TI;0)	-6097	[119]
	L(BCC_B2,FE,TI:TI;1)	+12256	[119]
	L(BCC_B2,TI:FE,TI;1)	+12256	[119]
	L(BCC_B2,FE:MO,TI;0)	+800	TW
	L(BCC_B2,MO,TI:FE;0)	+800	TW
	L(BCC_B2,FE,MO:TI;0)	+2000	TW
	L(BCC_B2,TI:FE,MO;0)	+2000	TW
Laves_C14 (Fe,Mo,Ti) ₂ (Fe,Mo,Ti) ₁	G(LAVES_C14,FE:FE;0)	+3*GHSERFE#+15000	[119]
	G(LAVES_C14,MO:MO;0)	+3*GHSERMO#+15000	[120]
	G(LAVES_C14,TI:TI;0)	+3*GHSERTI#+15000	[120]
	G(LAVES_C14,FE:MO;0)	+2*GHSERFE#+GHSERMO#-20443+7.289*T	[118]
	G(LAVES_C14,MO:FE;0)	+2*GHSERMO#+GHSERFE#+50443-7.289*T	[118]
	GFE2TI	-78627+326.7*T-60.471*T*LN(T) -.031*T**2+5.715108E-06*T**3+73193*T**(-1)	[119]
	G(LAVES_C14,FE:TI;0)	+GFE2TI#	[119]
	G(LAVES_C14,TI:FE;0)	+GHSERFE#+2*GHSERTI#+30000-GFE2TI#	[119]
	TC(LAVES_C14,FE:TI;0)	+273.88	[119]
	BMAGN(LAVES_C14,FE:TI;0)	+1.417	[119]
	G(LAVES_C14,TI:MO;0)	+2*GHSERTI#+GHSERMO#+60000	[120]
	G(LAVES_C14,MO:TI;0)	+2*GHSERMO#+GHSERTI#+60000	[120]
	G(LAVES_C14,FE:FE,MO;0)	+70000	[118]
	G(LAVES_C14,FE:FE,TI;0)	+3498	[119]
	G(LAVES_C14,FE,MO:MO;0)	+59450	[118]
	G(LAVES_C14,FE:MO,TI;0)	+0.0	TW
	G(LAVES_C14,FE:MO,TI;1)	+3000	TW
	G(LAVES_C14,FE,TI:TI;0)	+11807	TW
G(LAVES_C14,FE,MO:TI;0)	-30000	TW	

Table A3.1: Thermodynamic Parameters for the optimised Ti-Fe-Mo description, continued.

Phase and Model	Thermodynamic Parameters	Parameter Values	Ref
Mu_D85 (Fe,Mo,Ti) ₆ (Fe,Mo,Ti) ₂ (Mo,Ti) ₄ (Fe,Mo,Ti) ₁	THREE	+3	TW
	TRD	+THREE#*(-1)	TW
	TWOTRD	+2*TRD#	TW
	SEVEN	+7	TW
	ONESEV	+SEVEN#*(-1)	TW
	TWOSEV	+2*ONESEV#	TW
	THRSEV	+3*ONESEV#	TW
	FOUSEV	+4*ONESEV#	TW
	FIVSEV	+5*ONESEV#	TW
	SIXSEV	+6*ONESEV#	TW
	FE6MO7	+GHSERFE#+7*GHSERMO##+23550	[118]
	FE6TI7	+GHSERFE#+7*GHSERTI#	TW
	FE7MO6	+7*GHSERFE#+6*GHSERMO##-68875+8.955*T	[118]
	FE7TI6	+7*GHSERFE#+6*GHSERTI##-230000	TW
	FE8MO5	+8*GHSERFE#+5*GHSERMO##+100890	[118]
	FE8TI5	+8*GHSERFE#+5*GHSERTI#	TW
	GMUMO	+GHSERMO##+30380	[112]
	GMUTI	+GBCCTI##+12200	[112]
	G(MU,FE:FE:MO:FE;0)	+9*GHSERFE#+4*GHSERMO##+74090-76.677*T	[118]
	G(MU,MO:FE:MO:FE;0)	+3*GHSERFE#+10*GHSERMO##+445950	[118]
	G(MU,TI:FE:MO:FE;0)	+3*GHSERFE#+6*GHSERTI##+4*GHSERMO##+445950	TW
	G(MU,FE:MO:MO:FE;0)	+FE7MO6#	[118]
	G(MU,MO:MO:MO:FE;0)	+GHSERFE##+12*GHSERMO##+340960	[118]
	G(MU,TI:MO:MO:FE;0)	+GHSERFE##+6*GHSERMO##+6*GHSERTI##+340960	TW
	G(MU,FE:TI:MO:FE;0)	+TWOTRD##FE7MO6#+TRD##FE7TI6#	TW
	G(MU,MO:TI:MO:FE;0)	+GHSERFE##+10*GHSERMO##+2*GHSERTI##+340960	TW
	G(MU,TI:TI:MO:FE;0)	+GHSERFE##+8*GHSERTI##+4*GHSERMO##+340960	TW
	G(MU,FE:FE:TI:FE;0)	+9*GHSERFE##+4*GHSERTI##-215000	TW
	G(MU,MO:FE:TI:FE;0)	+3*GHSERFE##+6*GHSERMO##+4*GHSERTI##+445950	TW
	G(MU,TI:FE:TI:FE;0)	+3*GHSERFE##+10*GHSERTI##+445950	TW
	G(MU,FE:MO:TI:FE;0)	+TRD##FE7MO6##+TWOTRD##FE7TI6#	TW
	G(MU,MO:MO:TI:FE;0)	+GHSERFE##+8*GHSERMO##+4*GHSERTI##+340960	TW
	G(MU,TI:MO:TI:FE;0)	+GHSERFE##+10*GHSERTI##+2*GHSERMO##+340960	TW
G(MU,FE:TI:TI:FE;0)	+FE7TI6#	TW	
G(MU,MO:TI:TI:FE;0)	+GHSERFE##+6*GHSERTI##+6*GHSERMO##+340960	TW	
G(MU,TI:TI:TI:FE;0)	+GHSERFE##+12*GHSERTI##+340960	TW	

Table A3.1: Thermodynamic Parameters for the optimised Ti-Fe-Mo description, continued.

Phase and Model	Thermodynamic Parameters	Parameter Values	Ref
Mu_D85 (Fe,Mo,Ti) ₆ (Fe,Mo,Ti) ₂ (Mo,Ti) ₄ (Fe,Mo,Ti) ₁	G(MU,FE:FE:MO:MO;0)	+FE8MO5#	[118]
	G(MU,MO:FE:MO:MO;0)	+2*GHSERFE#+11*GHSERMO#+484770	[118]
	G(MU,TI:FE:MO:MO;0)	+2*GHSERFE#+6*GHSERTI#+5*GHSERMO#+484770	TW
	G(MU,FE:MO:MO:MO;0)	+FE6MO7#	[118]
	G(MU,MO:MO:MO:MO;0)	+13*GMUMO#	[112]
	G(MU,TI:MO:MO:MO;0)	+7*GMUMO#+6*GMUTI#	TW
	G(MU,FE:TI:MO:MO;0)	+TWOSEV#+FE6MO7#+FIVSEV#+FE6TI7#	TW
	G(MU,MO:TI:MO:MO;0)	+11*GMUMO#+2*GMUTI#	TW
	G(MU,TI:TI:MO:MO;0)	+5*GMUMO#+8*GMUTI#	TW
	G(MU,FE:FE:TI:MO;0)	+.2*FE8MO5#+.8*FE8TI5#	TW
	G(MU,MO:FE:TI:MO;0)	+2*GHSERFE#+4*GHSERTI#+7*GHSERMO#+484770	TW
	G(MU,TI:FE:TI:MO;0)	+2*GHSERFE#+GHSERMO#+10*GHSERTI#+484770	TW
	G(MU,FE:MO:TI:MO;0)	+FOUSEV#+FE6MO7#+THRSEV#+FE6TI7#	TW
	G(MU,MO:MO:TI:MO;0)	+9*GMUMO#+4*GMUTI#	TW
	G(MU,TI:MO:TI:MO;0)	+3*GMUMO#+10*GMUTI#	TW
	G(MU,FE:TI:TI:MO;0)	+SIXSEV#+FE6MO7#+ONESEV#+FE6TI7#	TW
	G(MU,MO:TI:TI:MO;0)	+7*GMUMO#+6*GMUTI#	TW
	G(MU,TI:TI:TI:MO;0)	+GMUMO#+12*GMUTI#	TW
	G(MU,FE:FE:MO:TI;0)	+.2*FE8TI5#+.8*FE8MO5#	TW
	G(MU,MO:FE:MO:TI;0)	+2*GHSERFE#+GHSERTI#+10*GHSERMO#+484770	TW
	G(MU,TI:FE:MO:TI;0)	+2*GHSERFE#+4*GHSERMO#+7*GHSERTI#+484770	TW
	G(MU,FE:MO:MO:TI;0)	+ONESEV#+FE6MO7#+SIXSEV#+FE6TI7#	TW
	G(MU,MO:MO:MO:TI;0)	+12*GMUMO#+GMUTI#	TW
	G(MU,TI:MO:MO:TI;0)	+6*GMUMO#+7*GMUTI#	TW
	G(MU,FE:TI:MO:TI;0)	+FOUSEV#+FE6MO7#+THRSEV#+FE6TI7#	TW
	G(MU,MO:TI:MO:TI;0)	+10*GMUMO#+3*GMUTI#	TW
	G(MU,TI:TI:MO:TI;0)	+4*GMUMO#+9*GMUTI#	TW
	G(MU,FE:FE:TI:TI;0)	+FE8TI5#	TW
	G(MU,MO:FE:TI:TI;0)	+2*GHSERFE#+6*GHSERMO#+5*GHSERTI#+484770	TW
	G(MU,TI:FE:TI:TI;0)	+2*GHSERFE#+11*GHSERTI#+484770	TW
	G(MU,FE:MO:TI:TI;0)	+TWOSEV#+FE6MO7#+FIVSEV#+FE6TI7#	TW
	G(MU,MO:MO:TI:TI;0)	+8*GMUMO#+5*GMUTI#	TW
	G(MU,TI:MO:TI:TI;0)	+2*GMUMO#+11*GMUTI#	TW
	G(MU,FE:TI:TI:TI;0)	+FE6TI7#	TW
	G(MU,MO:TI:TI:TI;0)	+6*GMUMO#+7*GMUTI#	TW
	G(MU,TI:TI:TI:TI;0)	+13*GMUTI#	[112]

Table A3.1: Thermodynamic Parameters for the optimised Ti-Fe-Mo description, continued.

Phase and Model	Thermodynamic Parameters	Parameter Values	Ref
Mu_D85	L(MU,FE:FE,MO:MO:FE;0)	-137510+105.096*T	[118]
(Fe,Mo,Ti) ₆	L(MU,FE:MO,TI:MO:FE;0)	-83000+28*T	[118]
(Fe,Mo,Ti) ₂	L(MU,FE:MO:MO,TI:FE;0)	-166000+56*T	TW
(Mo,Ti) ₄	L(MU,FE:TI:MO,TI:FE;0)	-166000+56*T	TW
(Fe,Mo,Ti) ₁	L(MU,FE:MO,TI:TI:FE;0)	-83000+28*T	TW
Sigma_D8b	G(SIGMA,FE:FE;0)	+226500+30*GHSEFFE#	[118]
(Fe,Mo) ₁₀	G(SIGMA,MO:FE;0)	+20*GHSEFFE#+10*GHSEFMO#+487900	[118]
(Fe,Mo) ₂₀	G(SIGMA,FE:MO;0)	+10*GHSEFFE#+20*GHSEFMO#+31407 -43.882*T	[118]
	G(SIGMA,MO:MO;0)	+486900+30*GHSEFMO#	[118]
	L(SIGMA,FE:FE,MO;0)	-48114	[118]
R	G(R,FE:MO:FE;0)	+35*GHSEFFE#+18*GHSEFMO#+50909 -177.308*T	[118]
(Fe) ₃₂			
(Mo) ₁₈	G(R,FE:MO:MO;0)	+32*GHSEFFE#+21*GHSEFMO#-91498	[118]
(Fe,Mo) ₃		-83.151*T	

Appendix 4: .tdb Thermo-Calc database for the optimised Ta-Al-Co description produced in this work

```

ELEMENT /- ELECTRON_GAS      0.0000E+00 0.0000E+00 0.0000E+00!
ELEMENT VA VACUUM           0.0000E+00 0.0000E+00 0.0000E+00!
ELEMENT AL FCC_A1           2.6982E+01 4.5773E+03 2.8322E+01!
ELEMENT CO HCP_A3           5.8933E+01 4.7656E+03 3.0040E+01!
ELEMENT TA BCC_A2           1.8095E+02 5.6819E+03 4.1472E+01!

FUNCTION GLIQAL 298.14 +11005.029-11.841867*T+7.934E-20*T**7+GHSERAL#;
933.47 Y
+10482.282-11.253974*T+1.231E+28*T**(-9)+GHSERAL#; 6000 N !
FUNCTION GLIQCO 298.15 +15085.037-8.931932*T-2.19801E-
21*T**7+GHSERCO#;
1768 Y
+16351.056-9.683796*T-9.3488E+30*T**(-9)+GHSERCO#; 6000 N !
FUNCTION GLIQTAL 298.15 +21875.086+111.561128*T-23.7592624*T*LN(T)
-.002623033*T**2+1.70109E-07*T**3-3293*T**(-1); 1000 Y
+43884.339-61.981795*T+.0279523*T*LN(T)-.012330066*T**2
+6.14599E-07*T**3-3523338*T**(-1); 3290 Y
-6314.543+258.110873*T-41.84*T*LN(T); 6000 N !
FUNCTION GBCCAL 298.15 +10083-4.813*T+GHSERAL#; 6000 N !
FUNCTION GBCCCO 298.15 +2938-.7138*T+GHSERCO#; 6000 N !
FUNCTION GHSERTA 298.15 -7285.889+119.139857*T-23.7592624*T*LN(T)
-.002623033*T**2+1.70109E-07*T**3-3293*T**(-1); 1300 Y
-22389.955+243.88676*T-41.137088*T*LN(T)+.006167572*T**2
-6.55136E-07*T**3+2429586*T**(-1); 2500 Y
+229382.886-722.59722*T+78.5244752*T*LN(T)-.017983376*T**2

```

$+1.95033E-07*T^{**3}-93813648*T^{**(-1)}$; 3290 Y
 $-1042384.01+2985.49125*T-362.159132*T*LN(T)+.043117795*T^{**2}$
 $-1.055148E-06*T^{**3}+5.54714342E+08*T^{**(-1)}$; 6000 N !
 FUNCTION B2ALCO 298.15 -136736.6+28.25753*T; 6000 N !
 FUNCTION LB2ALCO 298.15 +40492.9-24.9834*T; 6000 N !
 FUNCTION UBALCO 298.15 +.125*B2ALCO#-.125*LB2ALCO#; 6000 N !
 FUNCTION GHSERAL 298.15 -7976.15+137.093038*T-24.3671976*T*LN(T)
 $-.001884662*T^{**2}-8.77664E-07*T^{**3}+74092*T^{**(-1)}$; 700 Y
 $-11276.24+223.048446*T-38.5844296*T*LN(T)+.018531982*T^{**2}$
 $-5.764227E-06*T^{**3}+74092*T^{**(-1)}$; 933.60 Y
 $-11278.378+188.684153*T-31.748192*T*LN(T)-1.231E+28*T^{**(-9)}$; 6000 N !
 FUNCTION GFCCCO 298.15 +427.59-.61525*T+GHSERCO#; 6000 N !
 FUNCTION GFCCTA 298.15 +GHSERTA#+16000+1.7*T; 6000 N !
 FUNCTION GHCPAL 298.15 +5481-1.8*T+GHSERAL#; 6000 N !
 FUNCTION GHSERCO 298.15 +310.241+133.36601*T-25.0861*T*LN(T)
 $-.002654739*T^{**2}-1.7348E-07*T^{**3}+72526.9*T^{**(-1)}$; 1768 Y
 $-17197.666+253.28374*T-40.5*T*LN(T)+9.3488E+30*T^{**(-9)}$; 6000 N !
 FUNCTION GHCPTA 298.15 +GHSERTA#+12000+2.4*T; 6000 N !

 FUNCTION GC14AL 298.15 +13900+GHSERAL#; 6000 N !
 FUNCTION GC14CO 298.15 +16400+GHSERCO#; 6000 N !
 FUNCTION GC14TA 298.15 +9350+GHSERTA#; 6000 N !
 FUNCTION GC15AL 298.15 +15100+GHSERAL#; 6000 N !
 FUNCTION GC15CO 298.15 +19600+GHSERCO#; 6000 N !
 FUNCTION GC15TA 298.15 +10940+GHSERTA#; 6000 N !
 FUNCTION GC36AL 298.15 +13900+GHSERAL#; 6000 N !
 FUNCTION GC36CO 298.15 +16400+GHSERCO#; 6000 N !
 FUNCTION GC36TA 298.15 +10150+GHSERTA#; 6000 N !
 FUNCTION GMTACO 298.15 -525200+60*T; 6000 N !
 FUNCTION GMLCOTA 298.15 +532324; 6000 N !
 FUNCTION GM2COTA 298.15 +133081; 6000 N !

FUNCTION GM3TACO 298.15 -6500; 6000 N !
 FUNCTION GM4TACO 298.15 +671970; 6000 N !
 FUNCTION GMUAL 298.15 +GHSERAL#+9700; 6000 N !
 FUNCTION GMUCO 298.15 +GHSERCO#+11800; 6000 N !
 FUNCTION GMUTA 298.15 +GHSERTA#+11800; 6000 N !
 FUNCTION CO3TA10 298.15
 +GMTACO+GM2COTA+GM4TACO+3*GHSERCO+10*GHSERTA; 6000 N !
 FUNCTION CO5TA8 298.15
 +GMTACO+GMLCOTA+GM4TACO+5*GHSERCO+8*GHSERTA; 6000 N !
 FUNCTION CO6TA7 298.15
 -467000+38*T+6*GHSERCO+7*GHSERTA; 6000 N !
 FUNCTION CO7TA6 298.15
 -523319+62*T+7*GHSERCO+6*GHSERTA; 6000 N !
 FUNCTION CO8TA5 298.15
 +GMTACO+GM2COTA+GM3TACO+8*GHSERCO+5*GHSERTA; 6000 N !
 FUNCTION CO9TA4 298.15
 +GMTACO+GM2COTA +9*GHSERCO+4*GHSERTA; 6000 N !
 FUNCTION CO11TA2 298.15
 +GMTACO+GMLCOTA+11*GHSERCO+2*GHSERTA; 6000 N !
 FUNCTION CO12TA1 298.15
 +GMTACO+GMLCOTA+GM2COTA+GM3TACO+12*GHSERCO+1*GHSERTA; 6000
 N !
 FUNCTION AL3TA10 298.15
 +3*GMUAL+10*GMUTA; 6000 N !
 FUNCTION AL5TA8 298.15
 +5*GMUAL+8*GMUTA; 6000 N !
 FUNCTION AL6TA7 298.15
 +6*GMUAL+7*GMUTA; 6000 N !
 FUNCTION AL7TA6 298.15
 +7*GMUAL+6*GMUTA; 6000 N !
 FUNCTION AL8TA5 298.15

+8*GMUAL+5*GMUTA; 6000 N !

FUNCTION AL9TA4 298.15

+9*GMUAL+4*GMUTA; 6000 N !

FUNCTION AL11TA2 298.15

+11*GMUAL+2*GMUTA; 6000 N !

FUNCTION AL12TA1 298.15

+12*GMUAL+1*GMUTA; 6000 N !

FUNCTION THREE 298.15 +3; 6000 N !

FUNCTION TRD 298.15 +THREE **(-1); 6000 N !

FUNCTION TWOTRD 298.15 +2*TRD ; 6000 N !

FUNCTION SIX 298.15 +6; 6000 N !

FUNCTION ONESIX 298.15 +SIX **(-1); 6000 N !

FUNCTION TWOSIX 298.15 +2*ONESIX ; 6000 N !

FUNCTION THRSIX 298.15 +3*ONESIX ; 6000 N !

FUNCTION FOUSIX 298.15 +4*ONESIX ; 6000 N !

FUNCTION FIVSIX 298.15 +5*ONESIX ; 6000 N !

FUNCTION SEVEN 298.15 +7; 6000 N !

FUNCTION ONESEV 298.15 +SEVEN **(-1); 6000 N !

FUNCTION TWOSEV 298.15 +2*ONESEV ; 6000 N !

FUNCTION THRSEV 298.15 +3*ONESEV ; 6000 N !

FUNCTION FOUSEV 298.15 +4*ONESEV ; 6000 N !

FUNCTION FIVSEV 298.15 +5*ONESEV ; 6000 N !

FUNCTION SIXSEV 298.15 +6*ONESEV ; 6000 N !

FUNCTION NINE 298.15 +9; 6000 N !

FUNCTION ONENIN 298.15 +NINE **(-1); 6000 N !

FUNCTION TWONIN 298.15 +2*ONENIN ; 6000 N !

FUNCTION THRNIN 298.15 +3*ONENIN ; 6000 N !

FUNCTION SIXNIN 298.15 +6*ONENIN ; 6000 N !

FUNCTION SEVNIN 298.15 +7*ONENIN ; 6000 N !

FUNCTION EIGNIN 298.15 +8*ONENIN ; 6000 N !

FUNCTION ELEVEN 298.15 +11; 6000 N !

FUNCTION ONEELE 298.15 +ELEVEN **(-1); 6000 N !

FUNCTION FOU ELE 298.15 +4*ONEELE ; 6000 N !

FUNCTION FIVELE 298.15 +5*ONEELE ; 6000 N !

FUNCTION SIXELE 298.15 +6*ONEELE ; 6000 N !

FUNCTION SEVELE 298.15 +7*ONEELE ; 6000 N !

FUNCTION TENELE 298.15 +10*ONEELE ; 6000 N !

FUNCTION UN_ASS 298.15 +0; 300 N !

TYPE_DEFINITION % SEQ *!

DEFINE_SYSTEM_DEFAULT ELEMENT 2 !

DEFAULT_COMMAND DEF_SYS_ELEMENT VA /- !

PHASE AL3CO % 2 .745 .255 !

CONSTITUENT AL3CO :AL : CO : !

PARAMETER G(AL3CO,AL:CO;0) 298.15 -42728.3+8.8831*T
+.745*GHSERAL#+.255*GHSERCO#; 6000 N REF0 !

PHASE AL5CO2 % 2 5 2 !

CONSTITUENT AL5CO2 :AL : CO : !

PARAMETER G(AL5CO2,AL:CO;0) 298.15 -322674+67.6931*T
+5*GHSERAL#+2*GHSERCO#; 6000 N REF0 !

PHASE AL69TA39 % 2 .6389 .3611 !

CONSTITUENT AL69TA39 :AL%,CO,TA : AL,CO,TA% : !

PARAMETER G(AL69TA39,AL:AL;0) 298.15 +GHSERAL#+3000; 6000 N REF0
!

PARA G(AL69TA39,CO:AL;0) 298.15 +.6389*GHSERCO#
+.3611*GHSERAL#; 6000 N!

PARAMETER G(AL69TA39,TA:AL;0) 298.15 +.6389*GHSERTA#
+.3611*GHSERAL#; 6000 N REF0 !

PARA G(AL69TA39,AL:CO;0) 298.15 +.6389*GHSERAL#
+.3611*GHSERCO#; 6000 N!

PARA G(AL69TA39,CO:CO;0) 298.15 +GHSERCO#; 6000 N!

PARA G(AL69TA39,TA:CO;0) 298.15 +.6389*GHSERTA#
+.3611*GHSERCO#; 6000 N!

PARAMETER G(AL69TA39,AL:TA;0) 298.15 -25904+3.502*T
+.6389*GHSERAL#+.3611*GHSERTA#; 6000 N REF0 !

PARA G(AL69TA39,CO:TA;0) 298.15 +.6389*GHSERCO#
+.3611*GHSERTA#; 6000 N!

PARAMETER G(AL69TA39,TA:TA;0) 298.15 +GHSERTA#+9000; 6000 N REF0
!

PARAMETER L(AL69TA39,AL,CO:TA;0) 298.15 -67000; 6000 N !

PHASE AL9CO2 % 2 9 2 !

CONSTITUENT AL9CO2 :AL : CO : !

PARAMETER G(AL9CO2,AL:CO;0) 298.15 -334995.1+56.7277*T
+9*GHSERAL#+2*GHSERCO#; 6000 N REF0 !

TYPE_DEFINITION & GES A_P_D BCC_A2 MAGNETIC -1.0 4.00000E-01 !
PHASE BCC_A2 %& 2 1 3 !

CONSTITUENT BCC_A2 :AL,CO,TA%,VA : VA : !

PARAMETER G(BCC_A2,AL:VA;0) 298.15 +GBCCAL#; 6000 N REF0 !
PARAMETER G(BCC_A2,CO:VA;0) 298.15 +GBCCCO#; 6000 N REF0 !
PARAMETER TC(BCC_A2,CO:VA;0) 298.15 +1450; 6000 N REF0 !
PARAMETER BMAGN(BCC_A2,CO:VA;0) 298.15 +1.35; 6000 N REF0 !
PARAMETER G(BCC_A2,TA:VA;0) 298.15 +GHSERTA#; 2900 N REF0 !
PARAMETER G(BCC_A2,VA:VA;0) 298.15 +30*T; 6000 N REF0 !
PARAMETER G(BCC_A2,AL,VA:VA;0) 298.15 +46912; 6000 N REF0 !
PARAMETER G(BCC_A2,AL,CO:VA;0) 298.15 +B2ALCO#+LB2ALCO#; 6000 N
REF0 !
PARAMETER G(BCC_A2,AL,TA:VA;0) 298.15 -6000+2*T; 6000 N REF0 !
PARAMETER G(BCC_A2,CO,VA:VA;0) 298.15 +126184; 6000 N REF0 !
PARAMETER G(BCC_A2,CO,TA:VA;0) 298.15 -59084+5.334*T; 6000 N REF0 !
PARAMETER G(BCC_A2,CO,TA:VA;1) 298.15 -20000+10*T; 6000 N REF0 !

\$ THIS PHASE HAS A DISORDERED CONTRIBUTION FROM BCC_A2

TYPE_DEFINITION ' GES AMEND_PHASE_DESCRIPTION BCC_B2 DIS_PART
BCC_A2,,,!

TYPE_DEFINITION (GES A_P_D BCC_B2 MAGNETIC -1.0 4.00000E-01 !

PHASE BCC_B2 %!(3 .5 .5 3 !

CONSTITUENT BCC_B2 :AL,CO,TA%,VA : AL,CO,TA%,VA : VA : !

PARAMETER G(BCC_B2,AL:AL:VA;0) 298.15 +0; 6000 N!
PARAMETER G(BCC_B2,CO:AL:VA;0) 298.15 +4*UBALCO#; 6000 N REF0 !
PARAMETER TC(BCC_B2,CO:AL:VA;0) 298.15 -1400; 6000 N REF0 !
PARAMETER G(BCC_B2,TA:AL:VA;0) 298.15 +0; 6000 N!
PARAMETER G(BCC_B2,VA:AL:VA;0) 298.15 +0; 6000 N!

PARAMETER G(BCC_B2,AL:CO:VA;0) 298.15 +4*UBALCO#; 6000 N REF0 !
 PARAMETER TC(BCC_B2,AL:CO:VA;0) 298.15 -1400; 6000 N REF0 !
 PARA G(BCC_B2,CO:CO:VA;0) 298.15 +0; 6000 N!
 PARA G(BCC_B2,TA:CO:VA;0) 298.15 +0; 6000 N!
 PARA G(BCC_B2,VA:CO:VA;0) 298.15 +0; 6000 N!
 PARA G(BCC_B2,AL:TA:VA;0) 298.15 +0; 6000 N!
 PARA G(BCC_B2,CO:TA:VA;0) 298.15 +0; 6000 N!
 PARA G(BCC_B2,TA:TA:VA;0) 298.15 +0; 6000 N!
 PARA G(BCC_B2,VA:TA:VA;0) 298.15 +0; 6000 N!
 PARA G(BCC_B2,AL:VA:VA;0) 298.15 +0; 6000 N!
 PARA G(BCC_B2,CO:VA:VA;0) 298.15 +0; 6000 N!
 PARA G(BCC_B2,TA:VA:VA;0) 298.15 +0; 6000 N!
 PARA G(BCC_B2,VA:VA:VA;0) 298.15 +0; 6000 N!
 PARAMETER G(BCC_B2,CO,VA:AL:VA;0) 298.15 -28079-38.4534*T; 6000 N
 REF0 !
 PARAMETER G(BCC_B2,AL:CO,VA:VA;0) 298.15 -28079-38.4534*T; 6000 N
 REF0 !
 PARAMETER L(BCC_B2,CO:AL,TA:VA;0) 2.98150E+02 -161000-18*T;
 6.00000E+03 N !
 PARAMETER L(BCC_B2,AL,TA:CO:VA;0) 2.98150E+02 -161000-18*T;
 6.00000E+03 N !
 PARAMETER L(BCC_B2,CO:CO,TA:VA;0) 2.98150E+02 -266770-18*T;
 6.00000E+03 N !
 PARAMETER L(BCC_B2,CO,TA:CO:VA;0) 2.98150E+02 -266770-18*T;
 6.00000E+03 N !
 PARAMETER L(BCC_B2,CO:CO,TA:VA;1) 2.98150E+02 +12000;
 6.00000E+03 N !
 PARAMETER L(BCC_B2,CO,TA:CO:VA;1) 2.98150E+02 +12000;
 6.00000E+03 N !
 PARAMETER L(BCC_B2,AL:CO,TA:VA;0) 2.98150E+02 +80000;
 6.00000E+03 N !

PARAMETER L(BCC_B2,CO,TA:AL:VA;0) 2.98150E+02 +80000;
6.00000E+03 N !

PARAMETER L(BCC_B2,AL:AL,TA:VA;0) 2.98150E+02 -110000;
6.00000E+03 N !

PARAMETER L(BCC_B2,AL,TA:AL:VA;0) 2.98150E+02 -110000;
6.00000E+03 N !

PHASE CO1TA2 % 2 2 1 !

CONSTITUENT CO1TA2 :AL,CO,TA% : AL,CO%,TA : !

PARA G(CO1TA2,AL:AL;0) 298.15 +3*GHSERAL#; 6000 N!

PARA G(CO1TA2,CO:AL;0) 298.15 +2*GHSERCO#
+GHSERAL; 6000 N!

PARA G(CO1TA2,TA:AL;0) 298.15 +2*GHSERTA#
+GHSERAL#; 6000 N!

PARA G(CO1TA2,AL:TA;0) 298.15 +2*GHSERAL#
+GHSERTA#; 6000 N!

PARA G(CO1TA2,AL:CO;0) 298.15 +2*GHSERAL#
+GHSERCO#; 6000 N!

PARAMETER G(CO1TA2,CO:CO;0) 298.15 +30000+3*GHSERCO#; 6000 N
REF0 !

PARAMETER G(CO1TA2,TA:CO;0) 298.15 -94343+10*T+GHSERCO#
+2*GHSERTA#; 6000 N REF0 !

PARAMETER G(CO1TA2,CO:TA;0) 298.15 +90000+9*T+2*GHSERCO#
+GHSERTA#; 6000 N REF0 !

PARAMETER G(CO1TA2,TA:TA;0) 298.15 +152640+3*GHSERTA#; 6000 N
REF0 !

PARAMETER G(CO1TA2,CO,TA:CO;0) 298.15 -100000; 6000 N REF0 !

PARAMETER G(CO1TA2,TA:CO,TA;0) 298.15 +20000; 6000 N REF0 !

PARAMETER L(CO1TA2,TA:AL,CO;0) 298.15 -110343+10*T; 6000 N REF0 !

PARAMETER L(CO1TA2,TA:AL,TA;0) 298.15 -150000; 6000 N REF0 !

PHASE CO7TA2 % 2 2 7 !

CONSTITUENT CO7TA2 :TA : CO : !

PARAMETER G(CO7TA2,TA:CO;0) 298.15 +7*GHSERCO#+2*GHSERTA#
-309000+66.5*T; 6000 N REF0 !

PHASE EPSILON % 2 .75 .25 !

CONSTITUENT EPSILON :AL% : AL,TA% : !

PARAMETER G(EPSILON,AL:AL;0) 298.15 +GHSERAL#+20000; 6000 N
REF0 !

PARAMETER G(EPSILON,AL:TA;0) 298.15 +.75*GHSERAL#+.25*GHSERTA#
-29950+6.576*T; 6000 N REF0 !

PARAMETER G(EPSILON,AL:AL,TA;0) 298.15 -1494-10.6211*T; 6000 N
REF0 !

TYPE_DEFINITION) GES A_P_D FCC_A1 MAGNETIC -3.0 2.80000E-01 !

PHASE FCC_A1 %) 2 1 1 !

CONSTITUENT FCC_A1 :AL,CO,TA : VA% : !

PARAMETER G(FCC_A1,AL:VA;0) 298.15 +GHSERAL#; 6000 N REF0 !

PARAMETER G(FCC_A1,CO:VA;0) 298.15 +GFCCCO#; 6000 N REF0 !

PARAMETER TC(FCC_A1,CO:VA;0) 298.15 +1396; 6000 N REF0 !

PARAMETER BMAGN(FCC_A1,CO:VA;0) 298.15 +1.35; 6000 N REF0 !

PARAMETER G(FCC_A1,TA:VA;0) 298.15 +GFCCTA#; 6000 N REF0 !

PARAMETER G(FCC_A1,AL,CO:VA;0) 298.15 -124200+17.24*T; 6000 N
 REF0 !
 PARAMETER G(FCC_A1,AL,CO:VA;2) 298.15 +28740; 6000 N REF0 !
 PARAMETER TC(FCC_A1,AL,CO:VA;0) 298.15 -1500; 6000 N REF0 !
 PARAMETER TC(FCC_A1,AL,CO:VA;1) 298.15 +650; 6000 N REF0 !
 PARAMETER BMAGN(FCC_A1,AL,CO:VA;0) 298.15 +10; 6000 N REF0 !
 PARAMETER G(FCC_A1,AL,TA:VA;0) 298.15 -125394.75+78.85*T; 6000 N
 REF0 !
 PARAMETER TC(FCC_A1,CO,TA:VA;0) 298.15 -2200; 6000 N REF0 !
 PARAMETER TC(FCC_A1,CO,TA:VA;1) 298.15 -804; 6000 N REF0 !
 PARAMETER G(FCC_A1,CO,TA:VA;0) 298.15 -80000+38*T; 6000 N REF0 !
 PARAMETER G(FCC_A1,CO,TA:VA;1) 298.15 -60000; 6000 N REF0 !
 PARAMETER L(FCC_A1,AL,CO,TA:VA;0) 298.15 -515000+17.3*T; 6000 N REF0 !

TYPE_DEFINITION * GES A_P_D HCP_A3 MAGNETIC -3.0 2.80000E-01 !

PHASE HCP_A3 %* 2 1 .5 !

CONSTITUENT HCP_A3 :AL,CO%,TA : VA% : !

PARAMETER G(HCP_A3,AL:VA;0) 298.15 +GHCPAL#; 6000 N REF0 !
 PARAMETER G(HCP_A3,CO:VA;0) 298.15 +GHSERCO#; 6000 N REF0 !
 PARAMETER TC(HCP_A3,CO:VA;0) 298.15 +1396; 6000 N REF0 !
 PARAMETER BMAGN(HCP_A3,CO:VA;0) 298.15 +1.35; 6000 N REF0 !
 PARAMETER G(HCP_A3,TA:VA;0) 298.15 +GHCPTA#; 6000 N REF0 !
 PARAMETER G(HCP_A3,AL,TA:VA;0) 298.15 -111000+36.6*T; 6000 N REF0 !
 PARAMETER G(HCP_A3,CO,TA:VA;0) 298.15 -102000+15*T; 6000 N REF0 !

PHASE LAVES_C14 % 2 1 2 !

CONSTITUENT LAVES_C14 :AL,CO,TA% : AL,CO%,TA : !

PARA G(LAVES_C14,AL:AL;0) 298.15 +3*GC14AL#; 6000 N!

PARA G(LAVES_C14,CO:AL;0) 298.15 +2*GC14AL#
+GC14CO#; 6000 N!

PARA G(LAVES_C14,TA:AL;0) 298.15 +2*GC14AL#
+GC14TA#-107500+9.7*T; 6000 N!

PARA G(LAVES_C14,AL:CO;0) 298.15 +2*GC14CO#
+GC14AL#-40700; 6000 N!

PARAMETER G(LAVES_C14,CO:CO;0) 298.15 +3*GC14CO#; 6000 N REF0 !

PARAMETER G(LAVES_C14,TA:CO;0) 298.15 -179988+26*T+2*GC14CO#
+GC14TA#; 6000 N REF0 !

PARA G(LAVES_C14,AL:TA;0) 298.15 +2*GC14TA#
+GC14AL#+210050+0.112*T; 6000 N!

PARAMETER G(LAVES_C14,CO:TA;0) 298.15 +136700+26.5*T+2*GC14TA#
+GC14CO#; 6000 N REF0 !

PARAMETER G(LAVES_C14,TA:TA;0) 298.15 +3*GC14TA#; 6000 N REF0 !

PARAMETER L(LAVES_C14,TA:CO,TA;0) 298.15 -54700; 6000 N REF0 !

PARAMETER L(LAVES_C14,AL,TA:CO;0) 298.15 -90810+8*T; 6000 N REF0 !

PARAMETER L(LAVES_C14,AL,TA:CO;1) 298.15 +9130; 6000 N REF0 !

PARAMETER L(LAVES_C14,TA:CO,AL;0) 298.15 -284000+49*T; 6000 N REF0 !

PARAMETER L(LAVES_C14,TA:CO,AL;1) 298.15 +110000; 6000 N REF0 !

PARAMETER L(LAVES_C14,TA:AL,TA;0) 298.15 -170000+90*T; 6000 N REF0 !

PHASE LAVES_C15 % 2 1 2 !

CONSTITUENT LAVES_C15 :AL,CO,TA% : AL,CO%,TA : !

PARA G(LAVES_C15,AL:AL;0) 298.15 +3*GC15AL#+50000; 6000 N!

PARA G(LAVES_C15,CO:AL;0) 298.15 +2*GC15AL#
+GC15CO#; 6000 N!; 6000 N!

PARA G(LAVES_C15,TA:AL;0) 298.15 +2*GC15AL#
+GC15TA#-40000; 6000 N!

PARA G(LAVES_C15,AL:CO;0) 298.15 +2*GC15CO#
+GC15AL#-15000; 6000 N!

PARAMETER G(LAVES_C15,CO:CO;0) 298.15 +3*GC15CO#; 6000 N REF0 !

PARAMETER G(LAVES_C15,TA:CO;0) 298.15 -189440+26.15*T+2*GC15CO#
+GC15TA#; 6000 N REF0 !

PARA G(LAVES_C15,AL:TA;0) 298.15 +2*GC15TA#
+GC15AL#; 6000 N!

PARAMETER G(LAVES_C15,CO:TA;0) 298.15 +138000+26.15*T+GC15CO#
+2*GC15TA#; 6000 N REF0 !

PARAMETER G(LAVES_C15,TA:TA;0) 298.15 +3*GC15TA#; 6000 N REF0 !

PARAMETER L(LAVES_C15,CO,TA:CO;0) 298.15 -61500; 6000 N REF0 !

PARAMETER L(LAVES_C15,AL,TA:CO;0) 298.15 -205700; 6000 N REF0 !

PARAMETER L(LAVES_C15,TA:CO,AL;0) 298.15 -260010+6*T; 6000 N REF0 !

PARAMETER L(LAVES_C15,TA:CO,AL;1) 298.15 +65000; 6000 N REF0 !

PARAMETER L(LAVES_C15,AL,CO:CO;0) 298.15 -180000; 6000 N REF0 !

PHASE LAVES_C36 % 2 1 2 !

CONSTITUENT LAVES_C36 :AL,CO,TA% : AL,CO%,TA : !

PARA G(LAVES_C36,AL:AL;0) 298.15 +3*GC36AL#+50000; 6000 N!

PARA G(LAVES_C36,CO:AL;0) 298.15 +2*GC36AL#
+GC36CO#; 6000 N!

PARA G(LAVES_C36,TA:AL;0) 298.15 +2*GC36AL#
+GC36TA#-55000; 6000 N!

PARA G(LAVES_C36,AL:CO;0) 298.15 +2*GC36CO#
+GC36AL#; 6000 N!

PARAMETER G(LAVES_C36,CO:CO;0) 298.15 +3*GC36CO#; 6000 N REF0 !

PARAMETER G(LAVES_C36,TA:CO;0) 298.15 -180090+27.2*T+2*GC36CO#
+GC36TA#; 6000 N REF0 !

PARA G(LAVES_C36,AL:TA;0) 298.15 +2*GC36TA#
+GC36AL#; 6000 N!

PARAMETER G(LAVES_C36,CO:TA;0) 298.15 +137000+27.2*T+GC36CO#
+2*GC36TA#; 6000 N REF0 !

PARAMETER G(LAVES_C36,TA:TA;0) 298.15 +3*GC36TA#; 6000 N REF0 !

PARAMETER L(LAVES_C36,CO,TA:CO;0) 298.15 -69200; 6000 N REF0 !

PARAMETER L(LAVES_C36,TA:CO,AL;0) 298.15 -208974 + 8*T; 6000 N REF0 !

PARAMETER L(LAVES_C36,AL,TA:CO;0) 298.15 -220000; 6000 N REF0 !

PARAMETER L(LAVES_C36,AL,TA:CO;1) 298.15 +14000; 6000 N REF0 !

PARAMETER L(LAVES_C36,AL,CO:CO;0) 298.15 -150000; 6000 N REF0 !

PARAMETER L(LAVES_C36,AL,CO:TA;0) 298.15 +81000; 6000 N REF0 !

PHASE LIQUID % 1 1.0 !

CONSTITUENT LIQUID :AL,CO,TA : !

PARAMETER G(LIQUID,AL;0)	298.15 +GLIQAL#; 6000 N REF0 !
PARAMETER G(LIQUID,CO;0)	298.15 +GLIQCO#; 6000 N REF0 !
PARAMETER G(LIQUID,TA;0)	298.15 +GLIQTA#; 6000 N REF0 !
PARAMETER G(LIQUID,AL,CO;0)	298.15 -140962.8+27.1374*T; 6000 N REF0 !
PARAMETER G(LIQUID,AL,CO;1)	298.15 -32294.9+12.6454*T; 6000 N REF0 !
PARAMETER G(LIQUID,AL,CO;2)	298.15 +33074.5-3.40903*T; 6000 N REF0 !
PARAMETER G(LIQUID,AL,TA;0)	298.15 -55024.576+9.489*T; 6000 N REF0 !
PARAMETER G(LIQUID,AL,TA;1)	298.15 -32750.134+19.689*T; 6000 N REF0 !
PARAMETER G(LIQUID,AL,TA;2)	298.15 +26570-4.667*T; 6000 N REF0 !
PARAMETER G(LIQUID,CO,TA;0)	298.15 -171992+35*T; 6000 N REF0 !
PARAMETER G(LIQUID,CO,TA;1)	298.15 -2958; 6000 N REF0 !
PARAMETER G(LIQUID,CO,TA;2)	298.15 +24975; 6000 N REF0 !

PHASE MAL13CO4 % 2 .755 .245 !

CONSTITUENT MAL13CO4 :AL : CO : !

PARAMETER G(MAL13CO4,AL:CO;0)	298.15 -40740+8.0589*T +.755*GHSERAL#+.245*GHSERCO#; 6000 N REF0 !
-------------------------------	---

PHASE MU4 % 4 4 2 1 6 !

CONSTITUENT MU4 :AL,TA% : AL,CO,TA% : AL,CO%,TA : AL,CO% : !

PARAMETER G(MU4,TA:TA:CO:CO;0) 298.15

-523319+62*T+7*GHSERCO+6*GHSERTA; 6000 N !

PARAMETER G(MU4,TA:TA:TA:CO;0) 298.15

-467000+38*T+6*GHSERCO+7*GHSERTA; 6000 N !

PARAMETER G(MU4,TA:TA:CO:TA;0) 298.15

+GMTACO+GM4TACO+1*GHSERCO+12*GHSERTA; 6000 N !

PARAMETER G(MU4,TA:CO:TA:TA;0) 298.15

+GMTACO+GM2COTA+GM3TACO+GM4TACO+2*GHSERCO+11*GHSERTA; 6000 N !

PARAMETER G(MU4,TA:CO:CO:TA;0) 298.15

+GMTACO+GM2COTA+GM4TACO+3*GHSERCO+10*GHSERTA; 6000 N !

PARAMETER G(MU4,CO:TA:TA:TA;0) 298.15

+GMTACO+GMLCOTA+GM3TACO+GM4TACO+4*GHSERCO+9*GHSERTA; 6000 N !

PARAMETER G(MU4,CO:TA:CO:TA;0) 298.15

+GMTACO+GMLCOTA+GM4TACO+5*GHSERCO+8*GHSERTA; 6000 N !

PARAMETER G(MU4,CO:CO:TA:TA;0) 298.15

+GMTACO+GMLCOTA+GM2COTA+GM3TACO+GM4TACO+6*GHSERCO+7*GHSERTA; 6000 N !

PARAMETER G(MU4,CO:CO:CO:TA;0) 298.15

+GMTACO+GMLCOTA+GM2COTA+GM4TACO+7*GHSERCO+6*GHSERTA; 6000 N !

PARAMETER G(MU4,TA:CO:TA:CO;0) 298.15

+GMTACO+GM2COTA+GM3TACO+8*GHSERCO+5*GHSERTA; 6000 N !

PARAMETER G(MU4,TA:CO:CO:CO;0) 298.15

+GMTACO+GM2COTA +9*GHSERCO+4*GHSERTA; 6000 N !

PARAMETER G(MU4,CO:TA:TA:CO;0) 298.15

+GMTACO+GMLCOTA+GM3TACO+10*GHSERCO+3*GHSERTA; 6000 N !

PARAMETER G(MU4,CO:TA:CO:CO;0) 298.15

+GMTACO+GMLCOTA+11*GHSERCO+2*GHSERTA; 6000 N !

PARAMETER G(MU4,CO:CO:TA:CO;0) 298.15

+GMTACO+GMLCOTA+GM2COTA+GM3TACO+12*GHSERCO+1*GHSERTA; 6000 N !

PARA G(MU4,AL:AL:AL:AL;0) 298.15 +13*GMUAL; 6000 N!

PARA G(MU4,TA:AL:AL:AL;0) 298.15 +9*GMUAL+4*GMUTA; 6000 N!

PARA G(MU4,AL:CO:AL:AL;0) 298.15 +2*GMUCO+11*GMUAL; 6000 N!

PARA G(MU4,TA:CO:AL:AL;0) 298.15

+TWNIN*CO9TA4+SEVNIN*AL9TA4; 6000 N!

PARA G(MU4,AL:TA:AL:AL;0) 298.15 +11*GMUAL+2*GMUTA; 6000 N!

PARA G(MU4,TA:TA:AL:AL;0) 298.15 +7*GMUAL+6*GMUTA; 6000 N!

PARA G(MU4,AL:AL:CO:AL;0) 298.15 +12*GMUAL+1*GMUCO; 6000 N!

PARA G(MU4,TA:AL:CO:AL;0) 298.15

+ONENIN*CO9TA4+EIGNIN*AL9TA4; 6000 N!

PARA G(MU4,AL:CO:CO:AL;0) 298.15 +10*GMUAL+3*GMUCO; 6000 N!

PARA G(MU4,TA:CO:CO:AL;0) 298.15

+THRNIN*CO9TA4+SIXNIN*AL9TA4; 6000 N!

PARA G(MU4,AL:TA:CO:AL;0) 298.15

+ONEELE*CO11TA2+TENELE*AL11TA2; 6000 N!

PARA G(MU4,TA:TA:CO:AL;0) 298.15

+6*GMUAL+1*GMUCO+6*GMUTA-510000+72.7*T; 6000 N!

PARA G(MU4,AL:AL:TA:AL;0) 298.15 +12*GMUAL+1*GMUTA; 6000 N!

PARA G(MU4,TA:AL:TA:AL;0) 298.15 +8*GMUAL+5*GMUTA; 6000 N!

PARA G(MU4,AL:CO:TA:AL;0) 298.15

+ONESIX*CO12TA1+FIVSIX*AL12TA1; 6000 N!

PARA G(MU4,TA:CO:TA:AL;0) 298.15

+0.25*CO8TA5+0.75*AL8TA5; 6000 N!

PARA G(MU4,AL:TA:TA:AL;0) 298.15 +10*GMUAL+3*GMUTA; 6000 N!

PARA G(MU4,TA:TA:TA:AL;0) 298.15 +6*GMUAL+7*GMUTA-390000+72.7*T;
6000 N!

PARA G(MU4,AL:AL:AL:CO;0) 298.15 +7*GMUAL+6*GMUCO; 6000 N!

PARA G(MU4,TA:AL:AL:CO;0) 298.15

+SIXNIN*CO9TA4+THRNIN*AL9TA4; 6000 N!

PARA G(MU4,AL:CO:AL:CO;0) 298.15 +5*GMUAL+8*GMUCO; 6000 N!

PARA G(MU4,TA:CO:AL:CO;0) 298.15

+EIGNIN*CO9TA4+ONENIN*AL9TA4; 6000 N!

PARA G(MU4,AL:TA:AL:CO;0) 298.15

+SIXELE*CO11TA2+FIVELE*AL11TA2; 6000 N!

PARA G(MU4,TA:TA:AL:CO;0) 298.15

+SIXSEV*CO7TA6+ONESEV*AL7TA6; 6000 N!

PARA G(MU4,AL:AL:CO:CO;0) 298.15 +6*GMUAL+7*GMUCO; 6000 N!

PARA G(MU4,TA:AL:CO:CO;0) 298.15

+SEVNIN*CO9TA4+TWONIN*AL9TA4; 6000 N!

PARA G(MU4,AL:CO:CO:CO;0) 298.15 +4*GMUAL+9*GMUCO; 6000 N!

PARA G(MU4,AL:TA:CO:CO;0) 298.15

+SEVELE*CO11TA2+FOUELE*AL11TA2; 6000 N!

PARA G(MU4,AL:AL:TA:CO;0) 298.15

+THRSIX*CO12TA1+THRSIX*AL12TA1; 6000 N!

PARA G(MU4,TA:AL:TA:CO;0) 298.15

+0.75*CO8TA5+0.25*AL8TA5; 6000 N!

PARA G(MU4,AL:CO:TA:CO;0) 298.15

+FOUSIX*CO12TA1+TWOSIX*AL12TA1; 6000 N!

\$ L:0 1,26 (9,52)

PARA L(MU4,TA:TA:CO:CO,AL;0) 298.15

-740000; 6000 N!

\$ L:0 1,26 (9,52)

PARA L(MU4,TA:TA:CO:CO,AL;1) 298.15

+40000; 6000 N!

\$ L:0 2,32

PARA L(MU4,TA:TA:TA:CO,AL;0) 298.15

-740000+10*T; 6000 N!

PARA L(MU4,TA:TA:TA:CO,AL;1) 298.15

-24000; 6000 N!

PHASE OAL13CO4 % 2.76 .24 !

CONSTITUENT OAL13CO4 :AL : CO : !

PARAMETER G(OAL13CO4,AL:CO;0) 298.15 -39769.2+7.6677*T

+0.76*GHSERAL#+.24*GHSERCO#; 6000 N REF0 !

PHASE PHI % 2.8837 1.1163 !

CONSTITUENT PHI :AL,CO,TA : AL,CO,TA : !

PARAMETER G(PHI,AL:AL;0) 298.15 +2*GHSERAL#+500; 6000 N

REF0 !

PARA G(PHI,CO:AL;0) 298.15 +.8837*GHSERCO#

+1.1163*GHSERAL#; 6000 N!

PARAMETER G(PHI,TA:AL;0) 298.15 +1.1163*GHSERAL#

+0.8837*GHSERTA#; 6000 N REF0 !

PARA G(PHI,AL:CO;0) 298.15 +.8837*GHSERAL#

+1.1163*GHSERCO#; 6000 N!

PARA G(PHI,CO:CO;0) 298.15 +2*GHSERCO#; 6000 N!

PARA G(PHI,TA:CO;0) 298.15 +.8837*GHSERTA#

+1.1163*GHSERCO; 6000 N!

PARAMETER G(PHI,AL:TA;0) 298.15 +.8837*GHSERAL#

+1.1163*GHSERTA#-50500+7*T; 6000 N REF0 !

PARA G(PHI,CO:TA;0) 298.15 +.8837*GHSERCO#
 +1.1163*GHSERTA#; 6000 N!
 PARAMETER G(PHI,TA:TA;0) 298.15 +2*GHSERTA#+22500; 6000 N
 REF0 !
 PARAMETER L(PHI,AL:AL,TA;0) 298.15 -52500+32.7892*T; 6000 N
 REF0 !
 PARAMETER L(PHI,AL,TA:TA;0) 298.15 -27895.6+8.5005*T; 6000 N
 REF0 !
 PARAMETER L(PHI,AL:CO,TA;0) 298.15 -118000; 6000 N REF0 !

PHASE SIGMA % 3 .6 .25 .15 !

CONSTITUENT SIGMA :AL,CO,TA : AL,CO,TA : AL,CO,TA : !

PARAMETER G(SIGMA,AL:AL:TA;0) 298.15 +.85*GHSERAL#
 +.15*GHSERTA#-13500+7.0992*T; 6000 N REF0 !
 PARAMETER G(SIGMA,TA:AL:TA;0) 298.15 +.75*GHSERTA#
 +.25*GHSERAL#-18800+3.0651*T; 6000 N REF0 !
 PARAMETER G(SIGMA,AL:TA:TA;0) 298.15 +.6*GHSERAL#
 +.4*GHSERTA#; 6000 N REF0 !
 PARAMETER G(SIGMA,TA:TA:TA;0) 298.15 +2.4499*T+GHSERTA#; 6000 N
 REF0 !
 PARA G(SIGMA,AL:AL:CO;0) 298.15 +.85*GHSERAL#
 +.15*GHSERCO#; 6000 N!
 PARA G(SIGMA,CO:AL:CO;0) 298.15 +.25*GHSERAL#
 +.75*GHSERCO#; 6000 N!
 PARA G(SIGMA,TA:AL:CO;0) 298.15 +.6*GHSERTA#+.25*GHSERAL#
 +.15*GHSERCO#; 6000 N!
 PARA G(SIGMA,AL:CO:CO;0) 298.15 +.6*GHSERAL#
 +.4*GHSERCO#; 6000 N!
 PARA G(SIGMA,CO:CO:CO;0) 298.15 +GHSERCO#; 6000 N!

PARA G(SIGMA,TA:CO:CO;0) 298.15 +.6*GHSERTA#
 +.4*GHSERCO#; 6000 N!
 PARA G(SIGMA,AL:TA:CO;0) 298.15 +.6*GHSERAL#+.25*GHSERTA#
 +.15*GHSERCO#; 6000 N!
 PARA G(SIGMA,CO:TA:CO;0) 298.15 +.75*GHSERCO#
 +.25*GHSERTA#; 6000 N!
 PARA G(SIGMA,TA:TA:CO;0) 298.15 +.85*GHSERTA#
 +.15*GHSERCO#-10000; 6000 N!
 PARA G(SIGMA,CO:AL:TA;0) 298.15 .6*GHSERCO#+.25*GHSERAL#
 +.15*GHSERTA#; 6000 N!
 PARA G(SIGMA,AL:CO:TA;0) 298.15 .6*GHSERAL#+.25*GHSERCO#
 +.15*GHSERTA#; 6000 N!
 PARA G(SIGMA,CO:CO:TA;0) 298.15 +.85*GHSERCO#
 +.15*GHSERTA#+5000; 6000 N!
 PARA G(SIGMA,TA:CO:TA;0) 298.15 +.75*GHSERTA#
 +.25*GHSERCO#-10000; 6000 N!
 PARA G(SIGMA,CO:TA:TA;0) 298.15 +.6*GHSERCO#
 +.4*GHSERTA#+5000; 6000 N!
 PARA G(SIGMA,AL:AL:AL;0) 298.15 +GHSERAL#; 6000 N!
 PARA G(SIGMA,CO:AL:AL;0) 298.15 +.6*GHSERCO#
 +.4*GHSERAL#; 6000 N!
 PARA G(SIGMA,TA:AL:AL;0) 298.15 +.6*GHSERTA#
 +.4*GHSERAL#; 6000 N!; 6000 N!
 PARA G(SIGMA,AL:CO:AL;0) 298.15 +.75*GHSERAL#
 +.25*GHSERCO#; 6000 N!
 PARA G(SIGMA,CO:CO:AL;0) 298.15 +.85*GHSERCO#
 +.15*GHSERAL#; 6000 N!
 PARA G(SIGMA,TA:CO:AL;0) 298.15 +.6*GHSERTA#+.25*GHSERCO#
 +.15*GHSERAL#; 6000 N!
 PARA G(SIGMA,AL:TA:AL;0) 298.15 +.75*GHSERAL#
 +.25*GHSERTA#; 6000 N!

PARA G(SIGMA,CO:TA:AL;0) 298.15 +.6*GHSERCO#+.25*GHSERTA#
+.15*GHSERAL#; 6000 N!

PARA G(SIGMA,TA:TA:AL;0) 298.15 +.85*GHSERTA#
+.15*GHSERCO#-10000+10*T; 6000 N!

PARAMETER L(SIGMA,AL,TA:AL:TA;0) 298.15 -29268.5+4.1*T; 6000 N REF0 !

PARAMETER L(SIGMA,TA:AL,CO:TA;0) 298.15 -32000; 6000 N !

PARAMETER L(SIGMA,TA:AL,CO:TA;1) 298.15 -8000; 6000 N !

PARAMETER L(SIGMA,TA:TA,CO:TA;1) 298.15 -50000; 6000 N !

PHASE YAL13CO4 % 2 .755 .245 !

CONSTITUENT YAL13CO4 :AL : CO : !

PARAMETER G(YAL13CO4,AL:CO;0) 298.15 -39956.6+7.4808*T
+.755*GHSERAL#+.245*GHSERCO#; 6000 N REF0 !

\$

\$ TERNARY PHASES \$

\$

PHASE L21 % 3 1 2 1 !

CONSTITUENT L21 :AL%,TA :CO :AL,CO,TA% : !

PARAMETER G(L21,AL:CO:AL;0) 2.98150E+02
+2*GHSERAL#+2*GHSERCO#-225260+38.5*T; 6.00000E+03 N !

PARAMETER G(L21,TA:CO:AL;0) 2.98150E+02
+GHSERTA#+2*GHSERCO#+GHSERAL#; 6.00000E+03 N !

PARAMETER G(L21,AL:CO:CO;0) 2.98150E+02
+GHSERAL#+3*GHSERCO#-97150; 6.00000E+03 N !

PARAMETER G(L21,TA:CO:CO;0) 2.98150E+02
+GHSERTA#+3*GHSERCO#+146000; 6.00000E+03 N !

PARAMETER G(L21,AL:CO:TA;0) 2.98150E+02
+GHSERAL#+2*GHSERCO#+GHSERTA#-244781+26.58*T; 6.00000E+03 N !

PARAMETER G(L21,TA:CO:TA;0) 2.98150E+02
+2*GHSERTA#+2*GHSERCO#+150000; 6.00000E+03 N !

\$L3-5

PARAMETER L(L21,AL:CO:CO,TA;1) 2.98150E+02
0; 6.00000E+03 N !

\$L5-6

PARAMETER L(L21,AL,TA:CO:TA;0) 2.98150E+02
-162000-73*T; 6.00000E+03 N !

\$L1-5

PARAMETER L(L21,AL:CO:Al,TA;0) 2.98150E+02
-20000; 6.00000E+03 N !

LIST_OF_REFERENCES

NUMBER SOURCE

!

References (not part of the database)

Al-Co binary description[1]

Al-Ta binary description[2]

Co-Ta binary description[3]

[1] P. Wang et al., “Thermodynamic re-assessment of the Al-Co-W system,” *Calphad Comput. Coupling Phase Diagrams Thermochem.*, 2017.

[2] V. T. Witusiewicz et al., “Experimental study and thermodynamic re-assessment of the binary Al–Ta system,” *Intermetallics*, vol. 18, no. 1, pp. 92–106, Jan. 2010.

[3] G. Cacciamani, G. Roncallo, Y. Wang, E. Vacchieri, and A. Costa, “Thermodynamic modelling of a six component (C-Co-Cr-Ni-Ta-W) system for the simulation of Cobalt based alloys,” *J. Alloys Compd.*, vol. 730, pp. 291–310, Jan. 2018.

Appendix 5: .tdb Thermo-Calc database for the optimised Ti-Fe-Mo description produced in this work

```

ELEMENT /- ELECTRON_GAS      0.0000E+00 0.0000E+00 0.0000E+00!
ELEMENT VA VACUUM           0.0000E+00 0.0000E+00 0.0000E+00!
ELEMENT FE BCC_A2           5.5847E+01 4.4890E+03 2.7280E+01!
ELEMENT MO BCC_A2           9.5940E+01 4.5890E+03 2.8560E+01!
ELEMENT TI HCP_A3           4.7880E+01 4.8240E+03 3.0720E+01!

FUNCTION GHSERTI 298.15 -8059.921+133.615208*T-23.9933*T*LN(T)
-.004777975*T**2+1.06716E-07*T**3+72636*T**(-1); 900 Y
-7811.815+132.988068*T-23.9887*T*LN(T)-.0042033*T**2-9.0876E-08*T**3
+42680*T**(-1); 1155 Y
+908.837+66.976538*T-14.9466*T*LN(T)-.0081465*T**2+2.02715E-07*T**3
-1477660*T**(-1); 1941 Y
-124526.786+638.806871*T-87.2182461*T*LN(T)+.008204849*T**2
-3.04747E-07*T**3+36699805*T**(-1); 4000 N !

FUNCTION GHSERFE 298.15 +1225.7+124.134*T-23.5143*T*LN(T)-.00439752*T**2
-5.8927E-08*T**3+77359*T**(-1); 1811 Y
-25383.581+299.31255*T-46*T*LN(T)+2.29603E+31*T**(-9); 6000 N !

FUNCTION GHSERMO 298.15 -7746.302+131.9197*T-23.56414*T*LN(T)
-.003443396*T**2+5.66283E-07*T**3+65812*T**(-1)-1.30927E-10*T**4; 2896 Y
-30556.41+283.559746*T-42.63829*T*LN(T)-4.849315E+33*T**(-9); 5000 N !

FUNCTION UN_ASS 298.15 +0.0; 300 N !

FUNCTION GLIQFE 298.15 +GHSERFE#+12040.17-6.55843*T-3.67516E-21*T**7;
1811 Y
-10838.83+291.302*T-46*T*LN(T); 6000 N !

FUNCTION GLIQTl 298.15 +4134.494+126.63427*T-23.9933*T*LN(T)
-.004777975*T**2+1.06716E-07*T**3+72636*T**(-1); 900 Y

```

$+4382.601+126.00713*T-23.9887*T*LN(T)-.0042033*T**2-9.0876E-08*T**3$
 $+42680*T**(-1); 1155 Y$
 $+13103.253+59.9956*T-14.9466*T*LN(T)-.0081465*T**2+2.02715E-07*T**3$
 $-1477660*T**(-1); 1300 Y$
 $+369519.198-2554.0225*T+342.059267*T*LN(T)-.163409355*T**2$
 $+1.2457117E-05*T**3-67034516*T**(-1); 1941 Y$
 $-19887.066+298.7367*T-46.29*T*LN(T); 4000 N !$
 FUNCTION GLIQMO 298.15 +GHSERMO#+41831.347-14.694912*T+4.24519E-
 22*T**7;
 2896 Y
 $+3538.963+271.6697*T-42.63829*T*LN(T); 5000 N !$
 FUNCTION GFCCFE 298.15 -236.7+132.416*T-24.6643*T*LN(T)-.00375752*T**2
 $-5.8927E-08*T**3+77359*T**(-1); 1811 Y$
 $-27097.3963+300.252559*T-46*T*LN(T)+2.78854E+31*T**(-9); 6000 N !$
 FUNCTION GFCCTI 298.15 +GHSERTI#+6000-.1*T; 4000 N !
 FUNCTION GFCCMO 298.15 +GHSERMO#+15200+.63*T; 5000 N !
 FUNCTION GHCPFE 298.15 -2480.08+136.725*T-24.6643*T*LN(T)-.00375752*T**2
 $-5.8927E-08*T**3+77359*T**(-1); 1811 Y$
 $-29340.776+304.561559*T-46*T*LN(T)+2.78854E+31*T**(-9); 6000 N !$
 FUNCTION GBCCTI 298.15 -1272.064+134.71418*T-25.5768*T*LN(T)
 $-6.63845E-04*T**2-2.78803E-07*T**3+7208*T**(-1); 1155 Y$
 $+6667.385+105.366379*T-22.3771*T*LN(T)+.00121707*T**2-8.4534E-07*T**3$
 $-2002750*T**(-1); 1941 Y$
 $+26483.26-182.426471*T+19.0900905*T*LN(T)-.02200832*T**2$
 $+1.228863E-06*T**3+1400501*T**(-1); 4000 N !$
 FUNCTION GHCPMO 298.15 +3803.698+131.9197*T-23.56414*T*LN(T)
 $-.003443396*T**2+5.66283E-07*T**3+65812*T**(-1)-1.30927E-10*T**4; 2896 Y$
 $-19006.41+283.559746*T-42.63829*T*LN(T)-4.849315E+33*T**(-9); 5000 N !$
 FUNCTION LFETIB0 298.15 -68448+23.825*T; 6000 N !
 FUNCTION LFETIB1 298.15 +5467-5.083*T; 6000 N !
 FUNCTION LFETIB2 298.15 +25262-15.83*T; 6000 N !

FUNCTION GFETI 298.15 -76147-46.603*T+8.663*T*LN(T)-.007151*T**2
 +1.121169E-06*T**3; 6000 N !

FUNCTION GFE2TI 298.15 -78627+326.7*T-60.471*T*LN(T)-.031*T**2
 +5.715108E-06*T**3+73193*T**(-1); 6000 N !

FUNCTION SEVEN 298.15 +7; 6000 N !

FUNCTION ONESEV 298.15 +SEVEN#**(-1); 6000 N !

FUNCTION TWOSEV 298.15 +2*ONESEV#; 6000 N !

FUNCTION THRSEV 298.15 +3*ONESEV#; 6000 N !

FUNCTION FOUSEV 298.15 +4*ONESEV#; 6000 N !

FUNCTION FIVSEV 298.15 +5*ONESEV#; 6000 N !

FUNCTION SIXSEV 298.15 +6*ONESEV#; 6000 N !

FUNCTION FE6MO7 298.15 +GHSERFE#+7*GHSERMO#+23550; 6000 N !

FUNCTION FE6TI7 298.15 +GHSERFE#+7*GHSERTI#; 6000 N !

FUNCTION THREE 298.15 +3; 6000 N !

FUNCTION TRD 298.15 +THREE#**(-1); 6000 N !

FUNCTION TWOTRD 298.15 +2*TRD#; 6000 N !

FUNCTION FE7MO6 298.15 +7*GHSERFE#+6*GHSERMO#-68875+8.955*T; 6000 N
 !

FUNCTION FE7TI6 298.15 +7*GHSERFE#+6*GHSERTI#-230000; 6000 N !

FUNCTION FE8MO5 298.15 +8*GHSERFE#+5*GHSERMO#+100890; 6000 N !

FUNCTION FE8TI5 298.15 +8*GHSERFE#+5*GHSERTI#; 6000 N !

FUNCTION GMUMO 298.15 +GHSERMO#+30380; 6000 N !

FUNCTION GMUTI 298.15 +GBCCTI#+12200; 6000 N !

FUNCTION LBFETIMO 298.15 -8000; 6000 N !

TYPE_DEFINITION % SEQ *!
 DEFINE_SYSTEM_DEFAULT ELEMENT 2 !
 DEFAULT_COMMAND DEF_SYS_ELEMENT VA /- !

PHASE LIQUID:L % 1 1.0 !

CONSTITUENT LIQUID:L :FE,MO,TI : !

PARAMETER G(LIQUID,FE;0) 300 +GLIQFE#; 6000 N REF0 !
PARAMETER G(LIQUID,MO;0) 298.15 +GLIQMO#; 6000 N REF0 !
PARAMETER G(LIQUID,TI;0) 300 +GLIQTI#; 6000 N REF0 !
PARAMETER G(LIQUID,FE,TI;0) 298.15 -76384+17.884*T; 6000 N
REF0 !
PARAMETER G(LIQUID,FE,TI;1) 298.15 +7944-6.071*T; 6000 N REF0 !
PARAMETER G(LIQUID,FE,MO;0) 298.15 -11712+2.917*T; 6000 N REF0 !
PARAMETER G(LIQUID,MO,TI;0) 298.15 -17494.7-3.57111*T; 6000 N
REF0 !
PARAMETER G(LIQUID,MO,TI;1) 298.15 -463.9+9.0476*T; 6000 N
REF0 !
PARAMETER G(LIQUID,FE,MO,TI;0) 298.15 +17000; 6000 N
REF0 !

TYPE_DEFINITION & GES A_P_D BCC_A2 MAGNETIC -1.0 4.00000E-01 !

PHASE BCC_A2 %& 1 1.0 !

CONSTITUENT BCC_A2 :FE,MO,TI : !

PARAMETER G(BCC_A2,FE;0) 300 +GHSEFE#; 6000 N REF0 !
PARAMETER TC(BCC_A2,FE;0) 300 +1043; 6000 N REF0 !
PARAMETER BMAGN(BCC_A2,FE;0) 300 +2.22; 6000 N REF0 !
PARAMETER G(BCC_A2,MO;0) 298.15 +GHSEMO#; 6000 N REF0 !
PARAMETER G(BCC_A2,TI;0) 300 +GBCCTI#; 4000 N REF0 !
PARAMETER G(BCC_A2,FE,TI;0) 298.15 +LFETIB0#; 6000 N REF0 !
PARAMETER G(BCC_A2,FE,TI;1) 298.15 +LFETIB1#; 6000 N REF0 !
PARAMETER G(BCC_A2,FE,TI;2) 298.15 +LFETIB2#; 6000 N REF0 !
PARAMETER TC(BCC_A2,FE,TI;0) 298.15 +637.79; 6000 N REF0 !

PARAMETER TC(BCC_A2,FE,MO;0) 298.15 +334; 6000 N REF0 !
 PARAMETER TC(BCC_A2,FE,MO;1) 298.15 +531; 6000 N REF0 !
 PARAMETER G(BCC_A2,FE,MO;0) 298.15 +38849-9.539*T; 6000 N REF0 !
 PARAMETER G(BCC_A2,FE,MO;1) 298.15 -8988; 6000 N REF0 !
 PARAMETER G(BCC_A2,FE,MO,TI;0) 298.15 -20000+17*T; 6000 N REF0 !
 PARAMETER G(BCC_A2,MO,TI;0) 298.15 +3383.4-10.0774*T; 6000 N
 REF0 !
 PARAMETER G(BCC_A2,MO,TI;1) 298.15 -56704.6+32.12*T; 6000 N
 REF0 !
 PARAMETER G(BCC_A2,MO,TI;2) 298.15 -15172.4; 6000 N REF0 !

\$ THIS PHASE HAS A DISORDERED CONTRIBUTION FROM BCC_A2

TYPE_DEFINITION ' GES AMEND_PHASE_DESCRIPTION BCC_B2 DIS_PART
 BCC_A2,,,'!

TYPE_DEFINITION (GES A_P_D BCC_B2 MAGNETIC -1.0 4.00000E-01 !
 PHASE BCC_B2 %'(2 .5 .5 !

CONSTITUENT BCC_B2 :FE%,MO%,TI% : FE%,MO%,TI : !

PARAMETER G(BCC_B2,FE:FE;0) 298.15 +0.0; 6000 N REF0 !
 PARAMETER G(BCC_B2,MO:FE;0) 298.15 +0.0; 6000 N REF0 !
 PARAMETER G(BCC_B2,TI:FE;0) 298.15 +.5*GFETI#; 6000 N REF0 !
 PARAMETER TC(BCC_B2,TI:FE;0) 298.15 -1325; 6000 N REF0 !
 PARAMETER G(BCC_B2,FE:MO;0) 298.15 +0.0; 6000 N REF0 !
 PARAMETER G(BCC_B2,MO:MO;0) 298.15 +0.0; 6000 N REF0 !
 PARAMETER G(BCC_B2,TI:MO;0) 298.15 +0.0; 6000 N REF0 !
 PARAMETER G(BCC_B2,FE:TI;0) 298.15 +.5*GFETI#; 6000 N REF0 !
 PARAMETER TC(BCC_B2,FE:TI;0) 298.15 -1325; 6000 N REF0 !
 PARAMETER G(BCC_B2,MO:TI;0) 298.15 +0.0; 6000 N REF0 !
 PARAMETER G(BCC_B2,TI:TI;0) 298.15 +0.0; 6000 N REF0 !
 PARAMETER G(BCC_B2,FE,TI:FE;0) 298.15 -10953; 6000 N REF0 !

PARAMETER G(BCC_B2,FE,TI:FE;1) 298.15 -13719; 6000 N REF0 !
 PARAMETER G(BCC_B2,FE:FE,TI;0) 298.15 -10953; 6000 N REF0 !
 PARAMETER G(BCC_B2,FE:FE,TI;1) 298.15 -13719; 6000 N REF0 !
 PARAMETER G(BCC_B2,MO,TI:FE;0) 298.15 +800; 6000 N REF0 !
 PARAMETER G(BCC_B2,MO:FE,TI;0) 298.15 +LBFETIMO#; 6000 N REF0 !
 PARAMETER G(BCC_B2,TI:FE,TI;0) 298.15 -6097; 6000 N REF0 !
 PARAMETER G(BCC_B2,TI:FE,TI;1) 298.15 +12256; 6000 N REF0 !
 PARAMETER G(BCC_B2,TI:FE,MO;0) 298.15 +2000; 6000 N REF0 !
 PARAMETER G(BCC_B2,FE,TI:MO;0) 298.15 +LBFETIMO#; 6000 N REF0 !
 PARAMETER G(BCC_B2,FE:MO,TI;0) 298.15 +800; 6000 N REF0 !
 PARAMETER G(BCC_B2,FE,TI:TI;0) 298.15 -6097; 6000 N REF0 !
 PARAMETER G(BCC_B2,FE,TI:TI;1) 298.15 +12256; 6000 N REF0 !
 PARAMETER G(BCC_B2,FE,MO:TI;0) 298.15 +2000; 6000 N REF0 !

TYPE_DEFINITION) GES A_P_D FCC_A1 MAGNETIC -3.0 2.80000E-01 !

PHASE FCC_A1 %) 1 1.0 !

CONSTITUENT FCC_A1 :FE,MO,TI : !

PARAMETER G(FCC_A1,FE;0) 300 +GFCCFE#; 6000 N REF0 !
 PARAMETER TC(FCC_A1,FE;0) 300 -201; 6000 N REF0 !
 PARAMETER BMAGN(FCC_A1,FE;0) 300 -2.1; 6000 N REF0 !
 PARAMETER G(FCC_A1,MO;0) 298.15 +GFCCMO#; 6000 N REF0 !
 PARAMETER G(FCC_A1,TI;0) 300 +GFCCTI#; 6000 N REF0 !
 PARAMETER G(FCC_A1,FE,TI;0) 298.15 -55592+8.644*T; 6000 N REF0 !
 PARAMETER G(FCC_A1,FE,TI;1) 298.15 +4352-4.014*T; 6000 N REF0 !
 PARAMETER G(FCC_A1,FE,TI;2) 298.15 +28697-12.022*T; 6000 N
 REF0 !
 PARAMETER G(FCC_A1,FE,MO;0) 298.15 +20978-11.843*T; 6000 N
 REF0 !
 PARAMETER G(FCC_A1,MO,TI;0) 298.15 -23224.5; 6000 N REF0 !

TYPE_DEFINITION * GES A_P_D HCP MAGNETIC -3.0 2.80000E-01 !
PHASE HCP %* 1 1.0 !

CONSTITUENT HCP :FE,MO,TI : !

PARAMETER G(HCP,FE;0) 300 +GHCPFE#; 6000 N REF0 !
PARAMETER G(HCP,MO;0) 298.15 +GHCPMO#; 6000 N REF0 !
PARAMETER G(HCP,TI;0) 300 +GHSERTI#; 4000 N REF0 !
PARAMETER G(HCP,FE,TI;0) 298.15 +16370-13.261*T; 6000 N
REF0 !
PARAMETER G(HCP,MO,TI;0) 298.15 +14250.8; 6000 N REF0 !

TYPE_DEFINITION + GES A_P_D LAVES_C14 MAGNETIC -3.0 2.80000E-01 !
PHASE LAVES_C14 %+ 2 2 1 !

CONSTITUENT LAVES_C14 :FE%,MO,TI : FE,MO%,TI : !

PARAMETER G(LAVES_C14,FE:FE;0) 298.15 +3*GHSERFE#+15000; 6000 N
REF0 !
PARAMETER G(LAVES_C14,MO:FE;0) 298.15
+2*GHSERMO#+GHSERFE#+50443
-7.289*T; 6000 N REF0 !
PARAMETER G(LAVES_C14,TI:FE;0) 298.15
+GHSERFE#+2*GHSERTI#+30000
-GFE2TI#; 6000 N REF0 !
PARAMETER G(LAVES_C14,FE:MO;0) 298.15 +2*GHSERFE#+GHSERMO#-
20443
+7.289*T; 6000 N REF0 !
PARAMETER G(LAVES_C14,MO:MO;0) 298.15 +3*GHSERMO#+15000; 6000 N
REF0 !
PARAMETER G(LAVES_C14,TI:MO;0) 298.15
+2*GHSERTI#+GHSERMO#+60000;
6000 N REF0 !

PARAMETER G(LAVES_C14,FE:TI;0) 298.15 +GFE2TI#; 6000 N REF0 !
 PARAMETER TC(LAVES_C14,FE:TI;0) 298.15 +273.88; 6000 N REF0 !
 PARAMETER BMAGN(LAVES_C14,FE:TI;0) 298.15 +1.417; 6000 N REF0 !
 PARAMETER G(LAVES_C14,MO:TI;0) 298.15
 +2*GHSERMO#+GHSERTI#+60000;
 6000 N REF0 !
 PARAMETER G(LAVES_C14,TI:TI;0) 298.15 +3*GHSERTI#+15000; 6000 N
 REF0 !
 PARAMETER G(LAVES_C14,FE:FE,MO;0) 298.15 +70000; 6000 N REF0 !
 PARAMETER G(LAVES_C14,FE:FE,TI;0) 298.15 +3498; 6000 N REF0 !
 PARAMETER G(LAVES_C14,FE,MO:MO;0) 298.15 +59450; 6000 N REF0 !
 PARAMETER G(LAVES_C14,FE:MO,TI;0) 298.15 +0.0; 6000 N REF0 !
 PARAMETER G(LAVES_C14,FE:MO,TI;1) 298.15 +3000; 6000 N REF0 !
 PARAMETER G(LAVES_C14,FE,TI:TI;0) 298.15 +11807; 6000 N REF0 !
 PARAMETER G(LAVES_C14,FE,MO:TI;0) 298.15 -30000; 6000 N REF0 !

PHASE MU_PHASE % 4 6 2 4 1 !

CONSTITUENT MU_PHASE :FE%,MO,TI : FE,MO%,TI% : MO%,TI% : FE,MO,TI :
 !

PARAMETER G(MU_PHASE,FE:FE:MO:FE;0) 298.15
 +9*GHSERFE#+4*GHSERMO#
 +74090-76.677*T; 6000 N REF0 !
 PARAMETER G(MU_PHASE,MO:FE:MO:FE;0) 298.15
 +3*GHSERFE#+10*GHSERMO#
 +445950; 6000 N REF0 !
 PARAMETER G(MU_PHASE,TI:FE:MO:FE;0) 298.15 +3*GHSERFE#+6*GHSERTI#
 +4*GHSERMO#+445950; 6000 N REF0 !
 PARAMETER G(MU_PHASE,FE:MO:MO:FE;0) 298.15 +FE7MO6#; 6000 N REF0 !
 PARAMETER G(MU_PHASE,MO:MO:MO:FE;0) 298.15
 +GHSERFE#+12*GHSERMO#
 +340960; 6000 N REF0 !

PARAMETER G(MU_PHASE,TI:MO:MO:FE;0) 298.15
 +GHSERFE#+6*GHSERMO#
 +6*GHSERTI#+340960; 6000 N REF0 !

PARAMETER G(MU_PHASE,FE:TI:MO:FE;0) 298.15 +TWOTRD#*FE7MO6#
 +TRD#*FE7TI6#; 6000 N REF0 !

PARAMETER G(MU_PHASE,MO:TI:MO:FE;0) 298.15
 +GHSERFE#+10*GHSERMO#
 +2*GHSERTI#+340960; 6000 N REF0 !

PARAMETER G(MU_PHASE,TI:TI:MO:FE;0) 298.15 +GHSERFE#+8*GHSERTI#
 +4*GHSERMO#+340960; 6000 N REF0 !

PARAMETER G(MU_PHASE,FE:FE:TI:FE;0) 298.15 +9*GHSERFE#+4*GHSERTI#
 -215000; 6000 N REF0 !

PARAMETER G(MU_PHASE,MO:FE:TI:FE;0) 298.15
 +3*GHSERFE#+6*GHSERMO#
 +4*GHSERTI#+445950; 6000 N REF0 !

PARAMETER G(MU_PHASE,TI:FE:TI:FE;0) 298.15 +3*GHSERFE#+10*GHSERTI#
 +445950; 6000 N REF0 !

PARAMETER G(MU_PHASE,FE:MO:TI:FE;0) 298.15 +TRD#*FE7MO6#
 +TWOTRD#*FE7TI6#; 6000 N REF0 !

PARAMETER G(MU_PHASE,MO:MO:TI:FE;0) 298.15
 +GHSERFE#+8*GHSERMO#
 +4*GHSERTI#+340960; 6000 N REF0 !

PARAMETER G(MU_PHASE,TI:MO:TI:FE;0) 298.15 +GHSERFE#+10*GHSERTI#
 +2*GHSERMO#+340960; 6000 N REF0 !

PARAMETER G(MU_PHASE,FE:TI:TI:FE;0) 298.15 +FE7TI6#; 6000 N REF0 !

PARAMETER G(MU_PHASE,MO:TI:TI:FE;0) 298.15 +GHSERFE#+6*GHSERTI#
 +6*GHSERMO#+340960; 6000 N REF0 !

PARAMETER G(MU_PHASE,TI:TI:TI:FE;0) 298.15 +GHSERFE#+12*GHSERTI#
 +340960; 6000 N REF0 !

PARAMETER G(MU_PHASE,FE:FE:MO:MO;0) 298.15 +FE8MO5#; 6000 N REF0 !

PARAMETER G(MU_PHASE,MO:FE:MO:MO;0) 298.15
 +2*GHSERFE#+11*GHSERMO#
 +484770; 6000 N REF0 !

PARAMETER G(MU_PHASE, TI:FE:MO:MO;0) 298.15
 +2*GHSERFE#+6*GHSERTI#
 +5*GHSERMO#+484770; 6000 N REF0 !

PARAMETER G(MU_PHASE, FE:MO:MO:MO;0) 298.15 +FE6MO7#; 6000 N REF0 !

PARAMETER G(MU_PHASE, MO:MO:MO:MO;0) 298.15 +13*GMUMO#; 6000 N
 REF0 !

PARAMETER G(MU_PHASE, TI:MO:MO:MO;0) 298.15 +7*GMUMO#+6*GMUTI#;
 6000 N
 REF0 !

PARAMETER G(MU_PHASE, FE:TI:MO:MO;0) 298.15 +TWOSEV#*FE6MO7#
 +FIVSEV#*FE6TI7#; 6000 N REF0 !

PARAMETER G(MU_PHASE, MO:TI:MO:MO;0) 298.15
 +11*GMUMO#+2*GMUTI#; 6000 N
 REF0 !

PARAMETER G(MU_PHASE, TI:TI:MO:MO;0) 298.15 +5*GMUMO#+8*GMUTI#;
 6000 N
 REF0 !

PARAMETER G(MU_PHASE, FE:FE:TI:MO;0) 298.15 +.2*FE8MO5#+.8*FE8TI5#;
 6000 N REF0 !

PARAMETER G(MU_PHASE, MO:FE:TI:MO;0) 298.15
 +2*GHSERFE#+4*GHSERTI#
 +7*GHSERMO#+484770; 6000 N REF0 !

PARAMETER G(MU_PHASE, TI:FE:TI:MO;0) 298.15 +2*GHSERFE#+GHSERMO#
 +10*GHSERTI#+484770; 6000 N REF0 !

PARAMETER G(MU_PHASE, FE:MO:TI:MO;0) 298.15 +FOUSEV#*FE6MO7#
 +THRSEV#*FE6TI7#; 6000 N REF0 !

PARAMETER G(MU_PHASE, MO:MO:TI:MO;0) 298.15 +9*GMUMO#+4*GMUTI#;
 6000 N
 REF0 !

PARAMETER G(MU_PHASE, TI:MO:TI:MO;0) 298.15 +3*GMUMO#+10*GMUTI#;
 6000 N
 REF0 !

PARAMETER G(MU_PHASE, FE:TI:TI:MO;0) 298.15 +SIXSEV#*FE6MO7#
 +ONESEV#*FE6TI7#; 6000 N REF0 !

PARAMETER G(MU_PHASE,MO:TI:TI:MO;0) 298.15 +7*GMUMO#+6*GMUTI#;
6000 N

REF0 !

PARAMETER G(MU_PHASE,TI:TI:TI:MO;0) 298.15 +GMUMO#+12*GMUTI#;
6000 N

REF0 !

PARAMETER G(MU_PHASE,FE:FE:MO:TI;0) 298.15 +.2*FE8TI5#+.8*FE8MO5#;
6000 N REF0 !

PARAMETER G(MU_PHASE,MO:FE:MO:TI;0) 298.15 +2*GHSERFE#+GHSERTI#
+10*GHSERMO#+484770; 6000 N REF0 !

PARAMETER G(MU_PHASE,TI:FE:MO:TI;0) 298.15
+2*GHSERFE#+4*GHSERMO#

+7*GHSERTI#+484770; 6000 N REF0 !

PARAMETER G(MU_PHASE,FE:MO:MO:TI;0) 298.15 +ONESEV#*FE6MO7#
+SIXSEV#*FE6TI7#; 6000 N REF0 !

PARAMETER G(MU_PHASE,MO:MO:MO:TI;0) 298.15 +12*GMUMO#+GMUTI#;
6000 N

REF0 !

PARAMETER G(MU_PHASE,TI:MO:MO:TI;0) 298.15 +6*GMUMO#+7*GMUTI#;
6000 N

REF0 !

PARAMETER G(MU_PHASE,FE:TI:MO:TI;0) 298.15 +FOUSEV#*FE6MO7#
+THRSEV#*FE6TI7#; 6000 N REF0 !

PARAMETER G(MU_PHASE,MO:TI:MO:TI;0) 298.15 +10*GMUMO#+3*GMUTI#;
6000 N

REF0 !

PARAMETER G(MU_PHASE,TI:TI:MO:TI;0) 298.15 +4*GMUMO#+9*GMUTI#;
6000 N

REF0 !

PARAMETER G(MU_PHASE,FE:FE:TI:TI;0) 298.15 +FE8TI5#; 6000 N REF0 !

PARAMETER G(MU_PHASE,MO:FE:TI:TI;0) 298.15
+2*GHSERFE#+6*GHSERMO#

+5*GHSERTI#+484770; 6000 N REF0 !

PARAMETER G(MU_PHASE,TI:FE:TI:TI;0) 298.15 +2*GHSERFE#+11*GHSERTI#
 +484770; 6000 N REF0 !

PARAMETER G(MU_PHASE,FE:MO:TI:TI;0) 298.15 +TWOSEV#*FE6MO7#
 +FIVSEV#*FE6TI7#; 6000 N REF0 !

PARAMETER G(MU_PHASE,MO:MO:TI:TI;0) 298.15 +8*GMUMO#+5*GMUTI#;
 6000 N
 REF0 !

PARAMETER G(MU_PHASE,TI:MO:TI:TI;0) 298.15 +2*GMUMO#+11*GMUTI#;
 6000 N
 REF0 !

PARAMETER G(MU_PHASE,FE:TI:TI:TI;0) 298.15 +FE6TI7#; 6000 N REF0 !

PARAMETER G(MU_PHASE,MO:TI:TI:TI;0) 298.15 +6*GMUMO#+7*GMUTI#;
 6000 N
 REF0 !

PARAMETER G(MU_PHASE,TI:TI:TI:TI;0) 298.15 +13*GMUTI#; 6000 N REF0 !

PARAMETER G(MU_PHASE,FE:FE,MO:MO:FE;0) 298.15 -137510+105.096*T; 6000
 N
 REF0 !

PARAMETER G(MU_PHASE,FE:MO,TI:MO:FE;0) 298.15 -83000+28*T; 6000 N REF0
 !

PARAMETER G(MU_PHASE,FE:MO:MO,TI:FE;0) 298.15 -166000+56*T; 6000 N
 REF0 !

PARAMETER G(MU_PHASE,FE:TI:MO,TI:FE;0) 298.15 -166000+56*T; 6000 N
 REF0 !

PARAMETER G(MU_PHASE,FE:MO,TI:TI:FE;0) 298.15 -83000+28*T; 6000 N REF0 !

PHASE R_PHASE % 3 32 18 3 !

CONSTITUENT R_PHASE :FE : MO : FE,MO : !

PARAMETER G(R_PHASE,FE:MO:FE;0) 298.15
+35*GHSERFE#+18*GHSERMO#
+50909-177.308*T; 6000 N REF0 !

PARAMETER G(R_PHASE,FE:MO:MO;0) 298.15
+32*GHSERFE#+21*GHSERMO#
-91498-83.151*T; 6000 N REF0 !

PHASE SIGMA % 2 10 20 !

CONSTITUENT SIGMA :FE,MO : FE,MO : !

PARAMETER G(SIGMA,FE:FE;0) 298.15 +226500+30*GHSERFE#; 6000 N
REF0 !

PARAMETER G(SIGMA,MO:FE;0) 298.15 +20*GHSERFE#+10*GHSERMO#
+487900; 6000 N REF0 !

PARAMETER G(SIGMA,FE:MO;0) 298.15 +10*GHSERFE#+20*GHSERMO#
+31407-43.882*T; 6000 N REF0 !

PARAMETER G(SIGMA,MO:MO;0) 298.15 +486900+30*GHSERMO#; 6000 N
REF0 !

PARAMETER G(SIGMA,FE:FE,MO;0) 298.15 -48114; 6000 N REF0 !

LIST_OF_REFERENCES

NUMBER SOURCE

!

References (not part of the database)

Fe-Mo binary description[1]

Fe-Ti binary description[2]

Mo-Ti binary description[3]

[1] H.-J. Chung, J.-H. Shim, and D. Nyung Lee, “Thermodynamic evaluation and calculation of phase equilibria of the Ti–Mo–C–N quaternary system,” *J. Alloys Compd.*, vol. 282, no. 1–2, pp. 142–148, Jan. 1999.

[2] K. Santhy, “Phase Diagram Calculation of Certain Titanium Containing Alloy Systems by Coupling CALPHAD and First-Principle Methods, PhD thesis, IIT Madras.,” 2010.

[3] V. B. Rajkumar and K. C. Hari Kumar, “Thermodynamic modelling of the Fe–Mo system coupled with experiments and ab initio calculations,” *J. Alloys Compd.*, vol. 611, pp. 303–312, Oct. 2014.